The University Of Sheffield.

A study of turbulence and heat transfer in upward pipe flows of supercritical fluids

Jundi He

A thesis submitted in partial fulfilment of the requirements for the degree of

Doctor of Philosophy

The University of Sheffield

Faculty of Engineering

Department of mechanical engineering

Submission Date

29.3.2021

Acknowledgements

I would like to sincerely express the deepest gratitude to my supervisor Prof. Shuisheng He, for his effort and patience in these four years. I cannot finish my PhD study without his support and guidance, and I have learned a lot from him. I am also grateful to my industrial supervisor Dr. Bing Xu, who has supported me with her technical expertise. I acknowledge the scholarship from EDF Energy, my PhD study is fully sponsored.

I appreciate the support of my friends and colleagues at the Heat, Flow, and Turbulence Research group, it is an exciting journey with your company. I would like to thank Mr. Kenneth Chinembiri, Dr. Ran Tian, Dr. Bo Liu, Dr. XiaoXue Huang, Dr. Cosimo Trinca, Dr. Muhsin Mohd Amin, Dr. Oluwadare Benjamin Segun, Dr. Junjie Yan and Dr. Xu Wang, I have overcome lots of difficulties with your help and guidance. I would also like to express my gratitude to Dr. Wei Wang and Dr. Mehdi Seddighi for the help I have received from them.

Last but not least, I would like to thank my mother and father. My mother helped me build the interest in science and encouraged me to try new things. My father inspired me and gave me confidence when I was facing problems. My life is always full of comfort and happiness with your company.

Publication list

[1] Jundi He, Junjie Yan, Wei Wang, and Shuisheng He. Direct numerical simulation study for fluid-to-fluid scaling for fluids at supercritical pressure. In *International Heat Transfer Conference Digital Library*. Begel House Inc., 2018

[2] Jundi He, Shuisheng He, and Bing Xu. Effect of channel distortion and different graphite thermal conductivity models on the prediction of graphite temperatrue. In *6th EDF Energy Nuclear Graphite Conference*, 2018

[3] Shuisheng He, A Lozano-Durán, Jundi He, and Minjeong Cho. Turbulent-turbulent transition of a transient three-dimensional channel flow. In *Center for Turbulence Research–Proceedings of the Summer Program*, pages 257–266, 2018

[4] Jundi He, Shuisheng He, and Bing Xu. CFD studies of effect of fuel channel/stringer eccentricity in the core of an advanced gas-cooled reactor. In *18th International Topical Meeting on Nuclear Reactor Thermal Hydraulics (NURETH-18)*, 2019

[5] Jundi He, Junjie Yan, Wei Wang, and Shuisheng He. A DNS study of turbulence structures of flow of fluid at supercritical pressure. In *11th International Symposium on Turbulence and Shear Flow Phenomena*, 2019

[6] Jundi He, Junjie Yan, Wei Wang, Peixue Jiang, and Shuisheng He. Effects of buoyancy and thermophysical property variations on the flow of supercritical carbon dioxide. *International Journal of Heat and Fluid Flow*, 86:108697, 2020

[7] Jundi He, Ran Tian, Peixue Jiang, and Shuisheng He. Turbulence in a heated pipe at supercritical pressure. *Journal of Fluid Mechanics*, 2021, accepted.

[8] Jundi He, Bing Xu, and Shuisheng He. The effect of conjugate heat transfer on the flow of supercritical carbon dioxide. In *17th UK Heat Transfer Conference*, 2021, accepted.

Abstract

Supercritical fluid has been applied widely as an effective working fluid in engineering systems due to its unique features. In this study, the flow physics of the abnormal laminarisation and re-transition that happen in heated upward pipe flows of supercritical fluids are investigated using Direct numerical simulations (DNS) with an in-house code CHAPSim. It is important to clarify how different factors trigger and affect the reduction and the following regeneration of turbulence in such flows. DNS of supercritical carbon dioxide with one or more effects artificially isolated or eliminated are carried out so as to better understand the complex phenomena. The axial flow development is found to be important during the laminarisation. The effects of the variations of density and viscosity, and buoyancy are found to be similar, in that all of them cause an overall reduction of pressure gradient following a near-wall deficit of downward force, leading by a response of a rising inertia. Based on these findings, a unified approach has been proposed to describe the effect of spatial acceleration, viscosity variation, buoyancy and inertia making use of the concept of pseudo-body forces. With the apparent Reynolds number (ARN) theory applied, a heated upward flow with these effects can be decomposed into an equivalent-pressure-gradient reference flow and a perturbation flow. The turbulent shear stress and axial velocity predicted using the ARN theory agree well with those produced in DNS, suggesting the proposed unified approach and ARN theory successfully characterise the upward heated flow. A new 'full' laminarisation is identified referring to a region where no new vortical structures are generated. This region is found to be akin to the pre-transition region of a boundary layer bypass transition. The structural (direct) effect of the buoyancy on turbulence is initially weak during the laminarisation, but is dominant in the full laminarisation and re-transition region.

Additionally, an assessment of a fluid-to-fluid scaling method proposed in the literature has been carried out using DNS for the first time. Excellent similarities are achieved between the different supercritical fluid flows tested, suggesting the flow and heat transfer of the upward heated flow can be generally characterised by the similarity parameters. The sensitivities of similarity parameters and inlet conditions are also investigated. The Stanton number is found to be better than the Nusselt number, in terms of characterising the similarity for heat transfer.

Finally, the effect of conjugate heat transfer on supercritical fluid flows is studied. For most numerical studies of such flows in the literature, boundary conditions are normally idealised, with a uniform wall heat flux imposed, while in experiments, the redistribution of heat flux and stabilisation of near-wall enthalpy fluctuations exist due to the solid wall conduction. A conjugate heat transfer solver is implemented in the DNS code, and simulations with and without the solid wall are compared. Although the bulk enthalpies are shifted due to the redistribution of wall heat flux hence influencing the entrance effect, Nusselt number away from this region is not largely affected. It is found that the stabilisation effect is limited to a region close to the wall and diminished further away, but the turbulent kinetic energy is significantly affected by the stabilisation.

Contents

List of Figures

List of Tables

Chapter 1

Introduction

For a fluid at a pressure below its critical pressure, when heating is added while the fluid is at the saturation temperature, rapid vaporization happens with phase change from liquid to gas. As shown in the phase diagram Fig. 1.1, while for the fluid above its critical pressure, there are no boundaries between the liquid and gas phases. when temperature is lower than the critical point, the fluid behaves like a liquid and when temperature is above the critical point, the fluid behaves like a gas, with relatively lower density and dynamic viscosity. This is the so-called supercritical fluid, in which thermophysical properties experience non-linear change when temperature rises through its pseudo-critical value. Such special features make supercritical fluids becoming efficient and popular working fluids and they are widely applied in industry processes. Examples of such system include Supercritical-Water-Cooled Reactor (SCWR)—a type of advanced nuclear reactor, supercritical CO_2 power cycles for extracting geothermal energy or the solar energy, carbon capture and storage system and the cooling system of aircraft engines. Therefore it is important to study the fundamental flow and heat transfer features of supercritical fluids.

It is well known that heat transfer deterioration may happen in an upward heated flow of supercritical fluids (buoyancy-aided), while heat transfer enhancement may happen in a downward heated flow (buoyancy-opposed). Buoyancy is considered to be the main reason for such abnormal heat transfer performances, and vast experimental and numerical studies have been carried out to investigate the physics of these phenomena. Empirical correlations have been developed to characterise the heat transfer features for engineering calculations. However, the mechanisms of buoyancy and other factors (e.g., viscosity and density variations) causing the laminarisation are still not clear and fully explained yet. On the other hand, in terms of the fluid-to-fluid scaling for the translation between experiments/flows of different supercritical fluids, and the effect of including conjugate heat transfer on the simulations of flows, no DNS studies

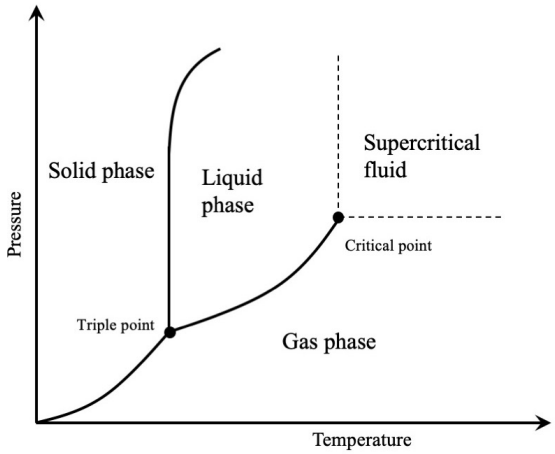

Figure 1.1: Phase diagram of a fluid.

have been conducted. With these motivations, the following objectives are proposed for the present study:

- To investigate the effect of flow development especially under the effects of buoyancy and strong variations of thermophysical properties.
- To develop a unified approach to explain the changes of flow and turbulence in an upward heated flow, and to expand the apparent Reynolds number (ARN) analysis developed in a previous study to such flows. Also to investigate the turbulent structures during the laminarisations and re-transitions in heated flows.
- To test one of the fluid-to-fluid scaling correlations using DNS and carry out sensitivity tests on some of the parameters and inlet conditions. To gain a better understanding on the groups of parameters that characterise the heat transfer and turbulence in upward heated flows of supercritical fluids.
- To study the effects brought by considering conjugate heat transfer in DNS of supercritical fluid flows, that is, the re-distributions of wall heat flux and the stabilization of near-wall enthalpy fluctuations.

1.1 Study overview

The turbulence and heat transfer characteristics of the upward pipe flows of supercritical fluids are investigated in the current study. It is split into four sub-topics: The first studied sub-topic is the mechanisms of buoyancy, viscosity and density variations affecting the flow development and the laminarisation and recovery in the

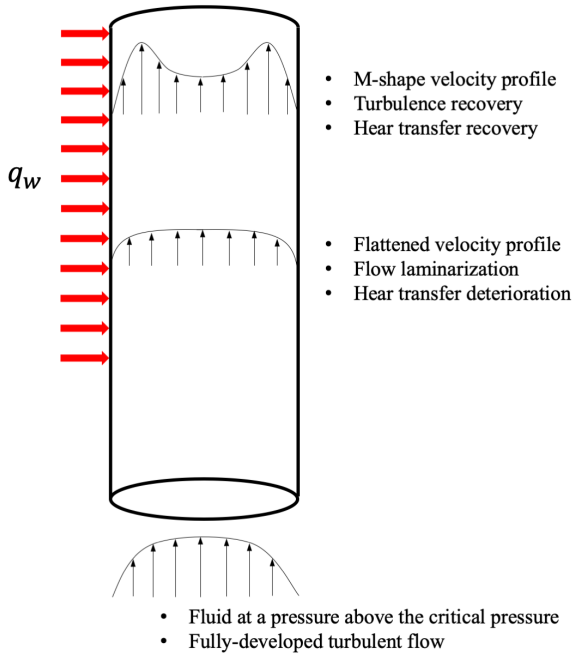

Figure 1.2: The vertical pipe flow of supercritical CO_2 in the present study.

upward heated flows of supercritical carbon dioxide. DNS simulations are carried out, in which one or more thermal properties are artificially frozen to discern the various physical mechanisms from each other so as to better understand the complex phenomena. The concerned flow is illustrated in Fig. 1.2: When a fluid at a pressure above the critical pressure enters a vertical heated pipe, it experiences heat transfer deterioration then recovery. Different from previous similar studies on this topic, this study focuses on the axial flow development resulted from the large variations of thermophysical properties. The processes of buoyancy and viscosity variation effects causing the reduction of pressure gradient and turbulent shear stress are presented and discussed in detail. The inertia terms in the momentum balance of the developing flows are quantified and found to significantly affect the laminarisation process. Further understandings on the combined or individual effects on the laminarisation and recovery are gained from the simulations and discussions on this sub-topic.

The second sub-topic is a further analysis of turbulent characteristics in an upward heated flow using the pseudo-body force concept proposed in an earlier study [13] based on an isothermal flow. The purpose of the research is to provide a new understanding of the turbulence dynamics in a heated turbulent flow of fluid at supercritical pressure (Fig. 1.2). A unified approach has been proposed to explain the laminarisation mechanisms due to the variations of thermophysical properties as well as buoyancy. Spatial acceleration, which plays a significant role in such developing

flows, is treated as a pseudo-body force and its effect on turbulence is explained in the same framework. In the new understanding, the partially laminarising flow is represented by an equivalent-pressure-gradient (EPG) reference flow plus a perturbation flow. The assessment of such correlation against DNS results of several flows with combinations of different effects is presented. A new 'full' laminarisation is identified referring to a region where no new vortical structures are generated. This region is akin to the pre-transition region of a boundary layer bypass transition, and in both cases, the free-stream (or pipe core) turbulence decays exponentially, but elongated streaks are formed in the boundary layer/wall region.

The third sub-topic is on fluid-to-fluid scaling between the upward flows of different supercritical fluids. The purpose of such scaling is to determine groups of non-dimensional parameters that characterise the heat transfer and turbulent behaviour of a heated vertical pipe flow of supercritical fluid, and similarity is expected in two flows with these parameters matched. The pipe flows studied here is akin to that illustrated in Fig. 1.2, with different supercritical fluids, boundary conditions and pipe lengths. With a well-validated scaling correlation developed, surrogate fluids (model fluids) can be used in experiments for another supercritical fluid (prototype fluid), and a similar result could be obtained with lower cost and less technical difficulties. Previous studies on this topic were mostly using empirical correlations or experimental data to validate the scaling correlations. For numerical studies, Reynolds-averaged Navier-Stokes (RANS) simulations were mostly used and none of the studies was using DNS. In the current study, DNS are carried out to validate the fluid-to-fluid scaling method proposed by Ambrosini et al. [14], and the sensitivities of some of the parameters and the inlet conditions are further tested. The purpose of this study is to provide a reliable assessment and sensitivity test for the scaling parameter group that proposed by Ambrosini et al. and to gain further understanding of the reason behind the achievement or failure of similarities between different fluid flows.

On the fourth sub-topic, the effect of including conjugate heat transfer in simulations of supercritical fluid flows is studied. In most of the simulations of supercritical flows, the solid walls were ignored and a uniform heat flux was imposed at the fluid boundaries. Compared to the flows in reality (experiments or industry processes), the enthalpy fluctuations close to the wall were significantly enlarged without considering the solid wall conduction. It is known that the changes in enthalpy fluctuations affect the turbulent heat flux, which affects the heat transfer. Furthermore, the changes in density fluctuations are relevant to the structural effect of buoyancy, that is, changes in buoyancy production, which might affect the turbulent kinetic energy. Such effect

is quantified in the present study, by comparing simulations of vertical pipe flows with and without solid wall considered. The considered flows are akin to that illustrated in Fig. 1.2, with different boundary conditions and a different operating pressure, and a different implementation of heating. Only one previous study on such effect of supercritical flows was carried out [15] using Large eddy simulations (LES), DNS is used in the current study for the first time to provide reliable references and understandings on this topic.

In addition to the fundamental study on the physics of supercritical fluid flows, the author has carried out two numerical studies on nuclear thermal hydraulics during the PhD study. The first one is a numerical study on the effect of fuel channel eccentricity of an Advanced Gas-cooled Reactor (AGR) [4], and the second one is a sensitivity study of applying different irradiated graphite conductivity models [2]. In these two studies, Reynolds-averaged Navier-Stokes (RANS) simulations of a concentric and fully-eccentric fuel channel at different reactor life-time were carried out. The aim is to investigate the effect of fuel channel distortion on the temperature distribution of the main brick.

1.2 Thesis outline

This thesis contains eight chapters, an overview of each chapter is given below:

- **Chapter 1**

  The general introduction of the thesis, including the explanation of the motivation and purpose of the research, and the significance and necessity of the present study.

- **Chapter 2**

  In this chapter, early studies that are relevant to present research topic are collected and reviewed, to present the progress of studies to date. Literature on mixed convection flows, experimental and numerical studies on supercritical fluid flows, developments of the fluid-to-fluid scaling methods for supercritical fluid flows and conjugate heat transfer simulations of supercritical flows are reviewed. A general picture of the studies in this field and the progress that has been made so far are presented in the literature review, the development and implementation of research plans of the current study were based on this.

- **Chapter 3**

  In this chapter, the methodology used to carry out the simulations and data post-processing are introduced in detail. The numerical schemes, including the time and spacial discretizations, the pressure-velocity coupling scheme in the DNS code CHAPSim are presented. Also, the derivations of some important equations used in the post-processing and discussions are also shown. The processing of the raw instantaneous data from the solver, and the calculation of the statistical data are introduced.

- **Chapter 4**

  The study on the effects of buoyancy and thermophysical property variations on the spacial development of the flow of supercritical carbon dioxide are presented in this chapter, including the cases settings and result discussions. The general flow and heat transfer features of the flows are presented, and the mechanisms of buoyancy and viscosity variation causing the laminarisation are analysed through the momentum balance of the corresponding cases.

- **Chapter 5**

  The turbulent characteristics are further analysed using the pseudo-body force concept in this chapter. A unified theory explaining the different property variation and buoyancy effects is proposed. The turbulent structures during the laminarisation and re-transitions are also presented.

- **Chapter 6**

  DNS study of one of the fluid-to-fluid scaling correlations for supercritical fluid flows is included in this chapter. Upward pipe flows of four fluids are scaled to achieve similarity in turbulence and heat transfer. Sensitivity tests on matched parameters and inlet conditions are also investigated.

- **Chapter 7**

  DNS study on the effect of conjugate heat transfer on the flow of supercritical carbon dioxide is presented in this chapter. The laminarisation and heat transfer deterioration processes in the flow with and without solid wall conduction are compared to investigate the effect of the re-distribution of wall heat flux and stabilization of the enthalpy fluctuations.

- **Chapter 8**

  Conclusions drawn from the discussions of the four chapters are included here. Some suggestions for future work are proposed.

Chapter 2

Literature review

2.1 Mixed convection flows

The topic of interest in the present study is heat transfer and turbulent characteristic in flows of fluids at supercritical pressure. It is always useful to firstly review studies of mixed convection flows, followed by the review of the studies on supercritical fluid flows, as the flows of supercritical fluids under heating is one of the scenarios of mixed convection, with relatively strong buoyancy.

Forced and natural convections are important modes of heat transfer: the former is driven by the pressure gradient, while the latter is purely driven by buoyancy. Mixed convection is a combination of forced and natural convection, with significant buoyancy effects, and a good discussion of the concept was provided in a review article by Jackson et al. [16]. Mixed convection is a huge topic and there have been numerous experimental and numerical studies on this topic. Here we will only review a small number of studies to outline the key features of heat transfer and turbulence characteristics in mixed convection. Such effects will be further discussed in the context of flow at supercritical pressure.

Jackson et al. [16] has summarized several experimental studies of mixed convection flows. It is clear from their results, and results of numerous studies that for laminar upward flows, heat transfer is always enhanced, while for turbulent upward flows, heat transfer deterioration happens when buoyancy is modest, and heat transfer is enhanced when buoyancy is strong. Jackson et al. [16] recommended using low-Reynolds number turbulence models to simulate mixed convection flows in numerical studies, as the significant variation of shear stress happens near the wall, which leads to the failure of wall functions used for standard turbulence models. Since then, many more experimental studies on mixed convection flows have been carried out [17, 18, 19, 20] to obtain heat transfer correlations for such flows with different

configurations, and also review work [21, 22] has been published to summarize different heat transfer correlations obtained in early experimental studies and propose optimized correlations with more factors considered.

The rapid development of computing techniques promotes the use of computational fluid dynamic (CFD) simulation as an alternative and efficient method for studies of physics of mixed convection flows. Numerical studies of mixed convection laminar flows have been done to simulate practical flows and investigate the effect of geometries and configurations [23, 24, 25, 26], the Navier-Stokes equations are closed without the need of turbulence models (naturally). Cotton & Jackson [27] simulated the mixed convection turbulent air flow in a vertical pipe (Re=9800), using the Launder and Sharma low-Re $k-\epsilon$ turbulence model [28], with buoyancy modelled by the Boussinesq approximation [29], and the turbulent Prandtl number is fixed at 0.9. Heat transfer deterioration and enhancement could be observed in the simulation results for moderate and very high buoyancy-influenced flows, respectively. The profiles of Nusselt number and streamwise velocity agree well with those from the experiments carried out by Carr et al. [30]. Direct numerical simulations (DNS) of mixed convection air flows in a vertical pipe were carried out by You et al. [31] to study the effect of heat flux. You et al. [31] investigated the difference of buoyancy effect in laminar and turbulent flows, which is often opposite: for example, heat transfer is hindered in downward laminar flow but the opposite is true in a turbulent flow. They discussed the concept of external effect (affects the mean velocity profile) and structural effect (affects the velocity fluctuation) in turbulent flows. Another DNS study of mixed convection flow of air in a vertical pipe with strong heating was carried out by Zhao et al. [32]. Heat transfer deterioration was observed along with turbulence attenuation. Their numerical result suggested that the laminarisation was due to the acceleration close to the wall induced by the buoyancy (external effect) under the flow conditions that they studied. The Fukagata, Iwamoto & Kasagi (FIK) identification of Nusselt number [33, 34] showed that the laminar contribution remained largely unchanged during the heat transfer deterioration. Turbulent and inhomogeneous contributions are mostly responsible for the worsened heat transfer.

Overall, it can be summarised: in buoyancy-opposed flows, e.g., downward flows with heating, heat transfer is always enhanced due to the enhanced turbulence, which is in turn caused by the buoyancy-induced distortion of the mean velocity profile. In buoyancy aiding flows, e.g., upward flows with heating, heat transfer deterioration followed by enhancement could happen depending on the strength of buoyancy. A

moderate buoyancy causes flow laminarisation and accordingly heat transfer deterioration, whereas a very strong buoyancy leads to turbulence to be regenerated and heat transfer recovers. Buoyancy effect is the key to changes of heat transfer in mixed convection turbulent flows, and this effect has not been completely understood yet as far as detailed turbulence behaviour is concerned despite extensive research over many years.

2.2 Supercritical fluid flows

For fluids under the pseudocritical pressure, rapid vaporization (boiling) happens when the enthalpy/temperature is rising through the boiling point, with phase change. While for fluids above the pseudocritical pressure, there is no phase change when enthalpy/temperature increases, but there are significant variations of thermophysical properties when the enthalpy/temperature is close to the critical value.

Variations of density, dynamic viscosity, specific heat and thermal conductivity as functions of temperatures of carbon dioxide (CO_2) at $8.57MPa$ and water (H_2O) at $25MPa$ are shown in Fig. 2.1 (data from the NIST database [35]), with pseudo-critical temperature T^*_{pc} in each fluid is specified by a red dash line. The critical pressures of the two fluids are $7.38MPa$ and $22.1MPa$ respectively. It can be seen that for both fluids (in fact for all fluids at supercritical pressure), when the temperature rises through the pseudo-critical value, density and dynamic viscosity rapidly reduce non-linearly, then remain relatively stable at higher temperatures. Similarly, thermal conductivities of both fluids linearly reduce below the pseudo-critical temperature, then reduce more rapidly right above the critical temperatures, and for specific heat, a peak is formed near the pseudo-critical temperatures. Such drastic non-linear changes of thermophysical properties around the pseudo-critical temperature are the reasons for the abnormal flow and heat transfer phenomena in flows of supercritical fluids.

Recently, supercritical fluids are widely applied in energy and aerospace industry, as an efficient working fluid and coolant due to its special features. Flows of fluids at supercritical pressure (SCP) is a special type of mixed convection flows, with stronger buoyancy and effects of significant variations of thermophysical properties. The changes of flow and heat transfer characteristics are more complicated than "normal" mixed convection flows that introduced in the last section. The focus of the present review is mainly the fundamental studies on the abnormal heat transfer and turbulence in SCP fluid flows, and they were mainly carried out by experiments and numerical simulations which are separately reviewed.

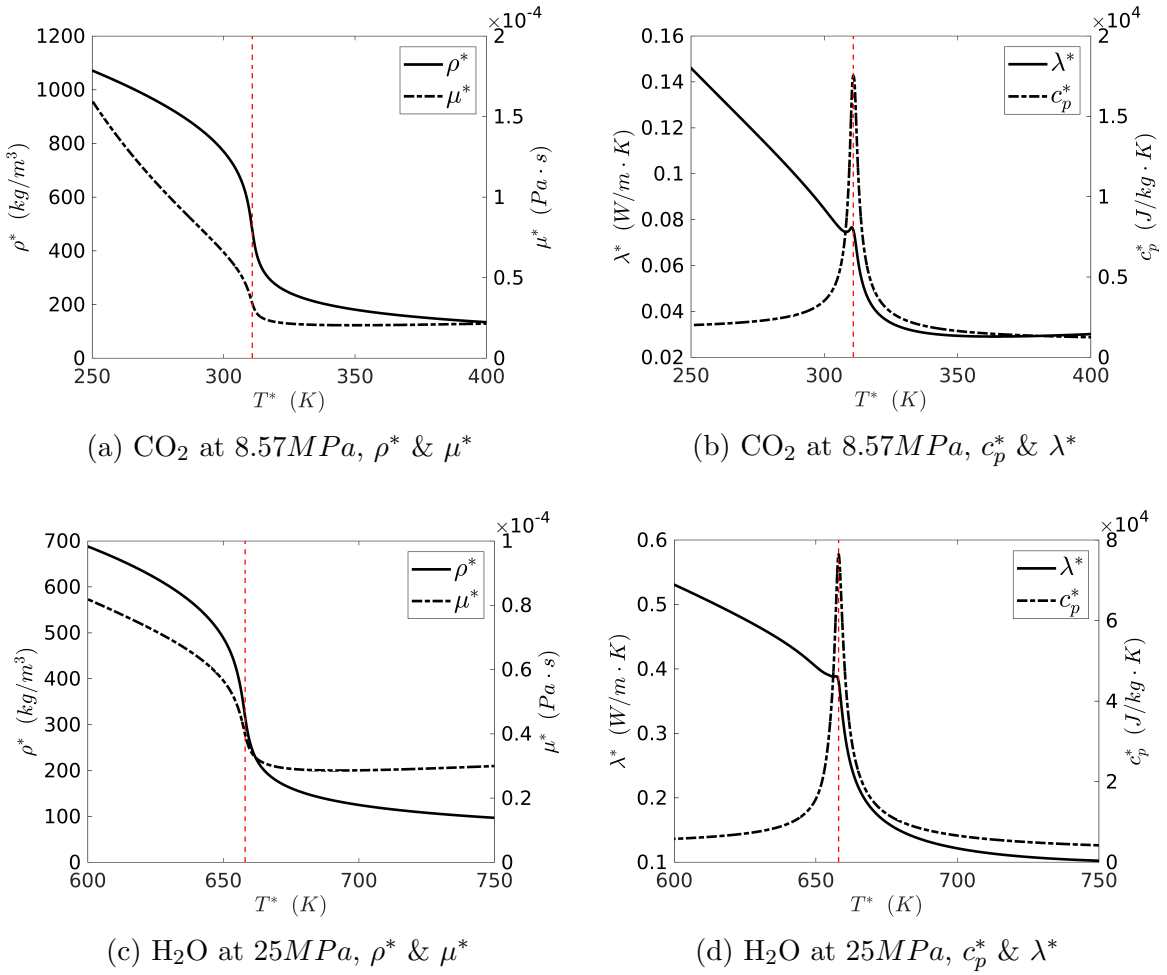

(a) CO_2 at $8.57MPa$, ρ^* & μ^*

(b) CO_2 at $8.57MPa$, c_p^* & λ^*

(c) H_2O at $25MPa$, ρ^* & μ^*

(d) H_2O at $25MPa$, c_p^* & λ^*

Figure 2.1: Variations of ρ^*, μ^*, c_p^* and λ^* against temperature in supercritical CO_2 ($8.57MPa$) and H_2O ($25MPa$).

2.2.1 Experimental studies on supercritical fluid flows

In early experimental studies, flows of different supercritical fluids have been investigated. Bourke et al. [36] carried out a number of experiments on supercritical CO_2 for different conditions and found that in a heated upward flow, heat transfer coefficient was reduced, and suggested that this was linked to the changes of density and viscosity and the effect of buoyancy. By analysing the experimental data, Ackerman [37] suggested that this abnormal heat transfer behaviour is similar to the well-known film boiling. It was found that such heat transfer deterioration is dependent on the flow conditions, some further experiments [38, 9] were carried out to investigate different factors that influence the heat transfer behaviour in vertical pipe flows of supercritical fluids. In these experiments, temperatures were measured by calibrated thermocouples. Shiralkar & Griffith [38] conducted the key experimental

study on the conditions of heat transfer deterioration in pipe flows of supercritical carbon dioxide. It was found that the heat transfer in such flows was characterised by the Reynolds number, the free-convection parameter and a heat-flux parameter. When the effect of buoyancy is relatively weak, i.e., differences between bulk and wall densities are small, heat transfer deterioration is not obvious unless heat flux is very high. Also, the variations in the heat transfer coefficient are found to be sensitive to the variations of pipe diameter, which strongly influences the buoyancy effect according to the Grashof number [39]:

$$Gr_D = \frac{g\beta(T_w - T_c)D^3}{\nu^2}. \tag{2.1}$$

Shiralkar & Griffith clarified the reason for the absence of heat transfer deterioration in previous experiments of supercritical carbon dioxide flows was that the inlet temperature was not low enough, only when the bulk temperature was lower and the wall temperature was higher than the pseudocritical temperature, significant heat transfer deterioration could be observed.

Yamagata et al. [9] carried out experiments of vertical pipe flows of supercritical water at different operating pressures, inlet temperatures, mass flow rates and ranges of wall heat flux. At low heat flux conditions, heat transfer coefficient was enhanced and reached the maximum close to the pseudocritical region, the maximum heat transfer coefficient progressively reduced at higher wall heat flux or operating pressure. For flows with low heat fluxes, a Nusselt number correlation was obtained and validated against experimental data. For flows of a given mass flux, heat transfer deterioration was observed when the heat flux is higher than a critical value. A correlation for such critical limits as a function between wall heat flux q_w^* and mass flow rate $G^* = \rho_b^* u_{z,b}^*$ were also clarified by summarising the experimental data in this study and previous literature, shown in Fig. 2.2. The trend of q_w^* and G^* condition for heat transfer deterioration is of a power-law relationship. When G_w^* is small, a relatively small q_w^* can cause heat transfer deterioration, and vice versa.

Kurganov & Kaptil'ny [40] conducted several experiments of vertical pipe flows of supercritical CO_2 at different Reynolds numbers, with local velocity measurements using Pitot tubes inserted in the flow and local temperature measurements with thermocouples. The results were compared with numerical predictions from the Popov turbulence model [41] with the consideration of the variation of thermophysical properties. Compared to the experimental data, the numerical solutions could not reflect the heat transfer deterioration, which the authors attributed to the failure of the modelling of the turbulence Prandtl number. Jackson et al. [42] reported experiments

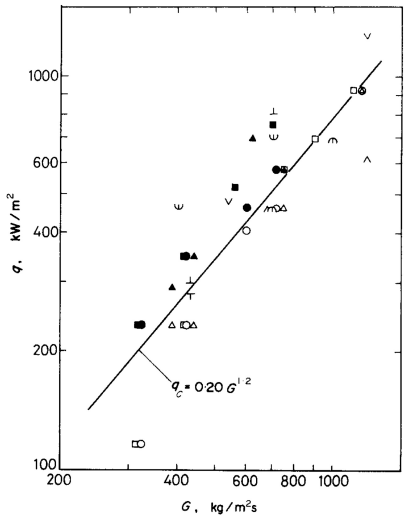

Figure 2.2: The relationship between the critical wall heat flux and mass flow rate for heat transfer deterioration for supercritical water ($P^* = 22.6 \sim 31.0$), adapted from Yamagata et al. [9].

of vertical pipe flows of CO_2 just above and below the critical pressure (supercritical & subcritical CO_2, $\frac{p^*}{p^*_{pc}} = 0.88 \sim 1.12$). Similar to previous experimental studies, the observed condition of local heat transfer deterioration was that wall heat flux was sufficiently high to cause the wall temperature higher than the pseudocritical temperature T^*_{pc}, while the temperature at the core flow is still lower than that. In this circumstance, the near-wall fluid had a much lower density than the core flow, and also significantly different thermophysical properties inside the thermal boundary layer, which affected the turbulence and heat transfer characteristics. For the subcritical CO_2, film boiling happened inside the thermal boundary layer, similar to that of the supercritical CO_2 flows, buoyancy effect is very strong, which caused differences in the heat transfer behaviours in upward and downward flows.

Jackson [10] summarized some experimental work that had been done in his group in the 1960s and 1970s, including those with upward and downward pipe flows of supercritical CO_2. With the previous experimental data summarised, two parameters which they proposed before were discussed to characterise the buoyancy strength for flows with wall temperatures lower and higher than the pseudocritical temperature ($T^*_w < T^*_{pc}$ & $T^*_w > T^*_{pc}$), i.e., $\frac{\overline{Gr_b}}{Re_b^{2.7} Pr_b^{0.5}}$ and $\frac{\overline{Gr_b}}{Re_b^{2.7}}$. With these parameters lower than 10^{-5}, the effect of buoyancy on heat transfer was less than 5%. The correlation of Nusselt number against $\frac{\overline{Gr_b}}{Re_b^{2.7}}$ for flows with $T^*_w > T^*_{pc}$ in upward and downward pipe flows of supercritical CO_2 were also obtained from vast early experimental data, shown in Fig. 2.3. Lower than the criterion ($\frac{\overline{Gr_b}}{Re_b^{2.7}} < 10^{-5}$), the effect of buoyancy

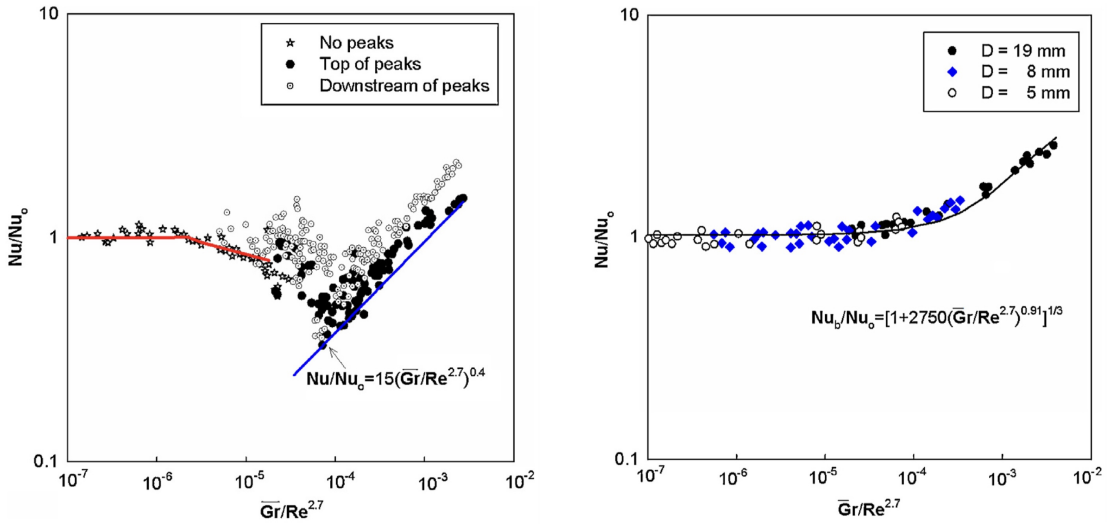

Figure 2.3: Correlations of $\frac{Nu}{Nu_0}$ against $\frac{\overline{Gr_b}}{Re_b^{2.7}}$ for upward (a) and downward (b) pipe flows of supercritical carbon dioxide, adapted from Jackson [10].

on heat transfer was relatively small, Nusselt numbers in upward and downward flows remained the same as that of forced convection Nusselt number ($\frac{Nu}{Nu_0} \approx 1$). With $\frac{\overline{Gr_b}}{Re_b^{2.7}}$ increased, heat transfer was monotonously enhanced in downward flows, while for upward flows, heat transfer deterioration happened first, followed by the enhancement at stronger buoyancy. In the discussion, the different heat transfer behaviours in upward and downward flows were attributed to the different directions of gravity, which appear in the momentum equation. Hence buoyancy affects the heat transfer behaviour through modifying the turbulence, and this was found to be the dominant effect that is more important than the others, e.g., the variations of thermophysical properties.

Literature surveys on early experimental studies were reported by Pioro et al. and Duffey & Pioro [43, 44]. Pioro et al. [43] collected heat transfer correlations from early studies and compared their predictions with experimental data. They have found that only some of the correlations show similar results to the experimental data. Duffey & Pioro [44] went through 450 papers on the experiments of supercritical CO_2. The majority of these experiments were for vertical pipes, and some were for horizontal pipes. The authors re-iterated the classification of the heat transfer modes of heated supercritical fluid flows as normal, deteriorated, and improved heat transfer. Deteriorated heat transfer mode usually appears in higher wall heat flux and lower mass flux flows.

Jiang and his co-workers have carried out vast experimental studies on supercritical fluids for many years. In particular, they studied flows in small and mini tubes

using a variety of different supercritical fluids. Jiang et al. [45] experimentally investigated the effects of inlet temperature, wall heat flux and mass flow rate on turbulent heat transfer of upward flows of supercritical carbon dioxide in mini-tubes and porous mini-tubes. It was found that for flows in porous tubes, the heat transfer coefficients of flows with inlet temperature T_0^* much larger than T_{pc}^* were much lower than those of flows with T_0^* much higher than T_{pc}^*. The variations of Nusselt number in mini-tube flows agree with the heat transfer correlation proposed by Krasnoshchekov [46]. The experimental results also showed that for vertical mini-tube flows of supercritical CO_2, the inlet temperature, wall heat flux and mass flow rate significantly influence turbulent heat transfer. The heat transfer correlation against the buoyancy strength for flows with high heat flux generally agreed with the trend summarised by Jackson [10] (Fig. 2.3a), i.e., turbulent heat transfer becomes worse when buoyancy is increased initially, while a further increase of buoyancy strength results in rising turbulent heat transfer performances. Experimental studies of mini-tube ($D^* = 0.27mm$) flows of supercritical CO_2 at low Reynolds number ($Re_{D,0} = 1900 \sim 2900$) were carried out by Jiang et al. [47] to investigate the effect of inlet temperature, operating pressure, mass flow rate and flow direction. In these experiments, flow direction has a limited effect on heat transfer as buoyancy is relatively weak due to the small tube diameter. When heat flux was small, wall temperature developments in upward and downward flows were both continuous, while for flows with high heat fluxes, the wall temperatures followed the increase-decrease-increase developments in both upward and downward flows. Jiang et al. suggested turbulence and heat transfer are largely affected by the acceleration effect due to the density reduction. Another experimental study of an even smaller diameter tube ($D^* = 0.1mm$) flows of supercritical CO_2 carried out by Jiang et al. [48] at various inlet Reynolds number($Re_{D,0} = 2600 \sim 6700$) also showed that the buoyancy effect on turbulence and heat transfer is not as significant as the acceleration effect. Comparisons of the upward and downward flows showed that they both have similar non-linear developments of wall temperatures due to the acceleration effect.

Experiments of heated pipe flows of supercritical CO_2 at high Reynolds number ($Re_{D,0} = 3800 \sim 20000$) were carried out by Li et al. [49], at various boundary conditions. Similar to those observed in early experiments, at high Reynolds number ($Re_{D,0} = 9000$) but low heat flux, consistent heat transfer behaviours were observed in upward and downward flows, indicating that buoyancy effect was not significant at these flows. For flows with higher heat fluxes and stronger buoyancy, however, heat transfer deterioration followed by recovery happened in upward flow. Li et al. also

applied the Krasnoshchekov correlation [46] and Jackson correlation [50] for mixed convection Nusselt number for the experiment flows with weak and strong buoyancy, good agreements were shown between them. Liu et al. carried out experiments of upward and downward pipe flow ($D^* = 0.95 \sim 2.00mm$) of supercritical n-decane at various conditions. In n-decane flows with operating pressure $p_0^* = 3$MPa and 5MPa, with high inlet Reynolds number $Re_{D,0} = 7000$, even though wall heat flux was relatively large, the effects of buoyancy and acceleration on heat transfer were neglectable. While for flows at lower inlet Reynolds number (2700 and 4000), heat transfer deterioration caused by the strong buoyancy was observed. Two new Nusselt number correlations for forced and mixed convection situations were proposed based on the experimental data in this study, to characterise the variations in heat transfer behaviours of n-decane flows. Apart from studies of heated supercritical fluid flows introduced above, experiments of cooling flow of supercritical CO_2 were also conducted by Jiang et al. [51], variation trends of heat transfer coefficient different from heated flows were observed. For upward flows (buoyancy-opposed), heat transfer coefficient firstly increased then reduced, while for downward flows (buoyancy-aided), heat transfer coefficient firstly decreased then increased. In both upward and downward cooling flows, when bulk temperatures were close to the pseudocritical value, heat transfer coefficient varied significantly.

Studies on other aspects of supercritical fluid flows were conducted by Yan et al. [52] and Jiang et al. [53]. Yan et al. [52] carried out experiments mainly looked at the instability of supercritical fluid flows, and found that the transition to turbulence at the downstream is one of the reasons of the instability. The instability of the flow is weaker at higher pressures, higher mass flow rates, and higher inlet temperatures. Jiang et al. [53] studied the heat transfer features of supercritical n-decane in rotating centrifugal channels, with varied rotating speed, mass flow rate, inlet temperature and heat flux. Jiang et al. [53] found that heat transfer deterioration is weakened by the strong centrifugal force and flow deceleration.

For vertical flows of supercritical fluids, the variations of heat transfer characteristics were studied widely, the effects that cause these changes in turbulence and heat transfer were investigated in detail by conducting experiments with different flow and thermal boundary conditions and using different fluids. On the other hand, for horizontal flows of supercritical fluids, more complicated variations could happen as the flow is not homogeneous at spanwise direction, buoyancy could cause secondary flows at this direction, with mass transfer between the top and bottom regions, which could significantly affect the turbulence and heat transfer in such flows. Studies on

horizontal flows were also conducted to investigate the fundamental physics in such circumstances. Tian et al. [54] carried out experiments of supercritical R134 flows with varying diameter, heat flux and mass flux. It was found that the buoyancy criteria based on supercritical water is not applicable to organic fluids, thus a new parameter was developed and validated against their own experimental data and those from previous literature. A set of experiments of supercritical R134 flows in horizontal pipes was obtained by Tian et al. [55] to provide heat transfer data and correlations for further studies. A non-uniform circumferential wall temperature distribution was observed in these results, which can be attributed to the effect of buoyancy. For the bottom wall, the Dittus-Boelter type correlations [56] are acceptable, implying that the flow behaves as forced convection. For the top surface of the horizontal pipe flows, the authors developed a new correlation based on a buoyancy parameter.

2.2.2 Numerical studies on supercritical fluid flows

In the above discussed experimental studies, limited attempts have been made to gain information on the flow and thermal fields through measurements due to technical difficulties. Computational fluid dynamics (CFD) method provides an alternative, efficient and powerful way for the studies of the abnormal heat transfer and turbulent behaviour in such fluid flows despite that care has to be taken to interpret the simulation results. In CFD studies, more flow details can be accessed with a lower cost compared to experiments. The numerical approach has become increasingly more popular with the advancement of high-performance computers, which provide high-speed computation capabilities. Bellmore & Reid [57] used an early numerical model to predict the wall temperature of an upward pipe flow of para-hydrogen just below the critical pressure. Density fluctuations were taken into consideration in the governing equations for compressible flows, and the turbulence viscosity was modelled by the mixing length theory. The predicted wall and bulk temperatures agreed with the experimental data, and the "M" shaped velocity profiles were reflected in the simulations. Koshizuka et al. [58] carried out CFD simulations of cooled vertical pipe flows of supercritical water using a steady-state solver with the standard $k-\epsilon$ turbulence model. They also considered the variable thermophysical properties. The correlations of mass flux and heat flux obtained from the CFD simulations agreed well with those from the experiments [9]. In these numerical studies, when the heat flux was significantly above the value of the deteriorated heat transfer mode, there were spacial oscillations in the resolved temperature profiles, and the simulations were

highly unstable. Two explanations were proposed to explain the heat transfer deterioration of the heated supercritical flow: (i) low near-wall viscosity leads to lower Prandtl numbers, which leads to thicker thermal boundary layers and smaller Nusselt numbers, and hence heat transfer deteriorated; (ii) the near-wall flow is accelerated due to the strong buoyancy, and then the streamwise velocity profile is flattened with a low wall-normal gradient and thus lower turbulence production. This understanding and explanation of the heat transfer deterioration provide an important reference for further investigations on vertical flows of supercritical fluids. Lee & Howell [59] conducted a similar numerical study using a modified mixing length turbulence model to simulate the convective heat transfer of fluids near the critical point. The numerical model could capture the general feature of supercritical flows and showed good agreement with the experimental data. It was found that one of the effects of property variations is to delay the flow developing process and the flow reaches the fully-developed state in a longer distance.

He et al. [60] used a number of low-Reynolds number eddy-viscosity turbulence models to simulate supercritical CO_2 in a vertical pipe, in which governing equations are the Reynolds-averaged Navier-Stokes (RANS) equations. The simulations reproduced most of the general features observed in previous experiments, and it was found that in a pipe with a small diameter, the buoyancy effect is not significant, but there is still heat transfer deterioration. This is because of the streamwise acceleration caused by a significant reduction in density. In addition, He et al. [60] compared the ability of a number of low Reynolds number turbulence models to predict the supercritical fluid flows. Most of the turbulence models assessed can reproduce the general trend of heat transfer deterioration caused by the buoyancy, but significant quantitative differences between the predictions of these models were observed. The comparison of RANS simulations using a number of low-Reynolds number turbulence models with DNS to assess the ability of the former to predict the heat transfer and turbulence of supercritical flow were carried out [61]. It was found that the V2F [62] model produced the most reliable predictions, and most turbulence models could reproduce the diminished turbulence kinetic energy, but not the recovery of heat transfer. This could be attributed to the applied Simple Gradient Diffusion Hypothesis (SGDH) when the turbulent heat flux is determined. In this method, the turbulent Prandtl number is assumed constant ($Pr_t = 0.9$).

Kim et al. [63] compared the performances of several low-Reynolds number, two-equation and four-equation turbulence models with that of DNS in terms of simulating

vertical pipe flows of mixed convection flows, with buoyancy modelled by the Boussinesq approximation and variations of thermophysical properties neglected. It was found that the indirect effect in buoyancy influenced flows was the most important in terms of causing the laminarization and deterioration of heat transfer, while the direct effect was negligible at this stage. However, the buoyancy production (direct effect) was noticeable during the recovery (re-transition) stage. Early turbulence models (the Launder-Sharma model [28] & the Yang-Shih model [64]) had better performance in reproducing the general trends buoyancy-influenced of flow features. Pucciarelli et al. [65] also tested the performance of several two-equation turbulence models, i.e., the AKN [66] model, the Deng [67] model, and the low-Reynolds $k-\epsilon$ model in solving the heat transfer of supercritical fluids, and found that the three models behaved similarly. All of them were sensitive to the crossing of the critical temperature, and the recovery was not well predicted, because the turbulence production due to buoyancy was not taken into account. Adding the Algebraic Heat Flux Model (AHFM) would help these turbulence models to better predict the recovery phase. The capabilities and limitations of such Algebraic Heat Flux Model were further tested and discussed by Pucciarelli et al. [68], and compared with DNS data. The model prediction agreed reasonably well with DNS, though Pucciarelli et al. [68] pointed out that further improvement could be obtained by selecting a case-specific AHFM parameter for different turbulence models. The recent study by Xu et al. [69] supports the above conclusions drawn by He et al. [61] and Pucciarelli et al. [65]. Recognizing that the inaccurate prediction of turbulence production and the use of constant turbulent Prandtl number are major factors for the failure of RANS turbulence models in solving supercritical fluid flows, Jiang et al. [70] developed a new modified model, with an improved model for buoyancy production and a variable turbulent Prandtl number. The new model was adopted in the AKN $k-\epsilon$ model [66], and showed improved performance in terms of solving supercritical fluid flows with strong heating.

The main concern of RANS simulations in terms of solving supercritical fluid flows is the inaccurate modelling of the reduced turbulent heat flux affected by buoyancy, which, to some extent, increases the uncertainties of the simulation result. The studies based on RANS simulations suggest that low-Reynolds number models such as the V2F model and the large eddy simulations (LES) are more capable in predicting the features of heat transfer and turbulence of supercritical flows. While for high-Reynolds number models, sufficiently accurate results for industry applications could be obtained with some special treatments implemented. The problem concerned for

RANS simulations is whether the increase in turbulence reflects in an enhancement of heat transfer. This problem does not exist in direct numerical simulations (DNS), as the turbulent heat flux is directly resolved in DNS. Compared to DNS, RANS simulations and LES both have limitations in terms of simulating wall bounded flows. In RANS simulations, the governing equation is closed with the turbulent shear stress modelled, and in LES, only the large scale motions are simulated, while the small scale activities are modelled. For wall bounded flows, the small scale activities are important to the turbulent characteristics. In DNS, the large and small scale motions are directly solved without modelling. A key DNS study on heated upward and downward pipe flows of supercritical CO_2 was carried out by Bae et al. [11]. Flows with different buoyancy conditions were simulated and the heat transfer deterioration and recovery were identified, accompanied by the laminarization and regeneration of turbulence. The resolved streamwise velocity profiles in strong buoyancy cases were similar to those resolved in the RANS simulations and observed in experiments, i.e., near-wall acceleration and core-flow deceleration happen and the velocity profiles were firstly flattened, then turned into "M" shape profiles at the later stage. When velocity profiles were flattened, the flow is laminarised, heat transfer is significantly worsened at this stage, and the "M" shape profile corresponded to the stage that turbulence was regenerated and heat transfer was enhanced. The response of the viscous and turbulent shear stress ($-\overline{\tau} = \overline{\mu \frac{\partial u_z}{\partial y}}$ & $\overline{\rho u_z'' u_r''}$) were found to be abnormal. To show this, one of the case (case C) with strong buoyancy is taken as an example, the resolved shear stress profiles at fully laminarised stage (with a flattened velocity profile) and regeneration stage (with an "M" shape velocity profile) are shown in Fig. 2.4. When the flow is fully laminarised, turbulent shear stress is nearly zero at most part and heat transfer is the worst. When velocity gradient rises again due to the M-shaped velocity profile, turbulence was regenerated. Turbulent shear stress is negative at most part, and only positive very close to the wall. While during this process, viscous shear stress remained largely unchanged. Responses of the other turbulent quantities, e.g., turbulent kinetic energy and its production, buoyancy production and turbulent heat flux were also discussed, which presented a detailed picture of the vertical pipe flows of supercritical CO_2. This provides a very useful reference for other studies in this field.

DNS investigations to vertical annular flows with a heated inner wall were also carried out by Bae et al. [71]. It was shown that near the hot wall, the normalised streamwise velocity profiles are not logarithmic any more because the turbulent shear stress near the wall is largely reduced. Another observation was that the high-speed

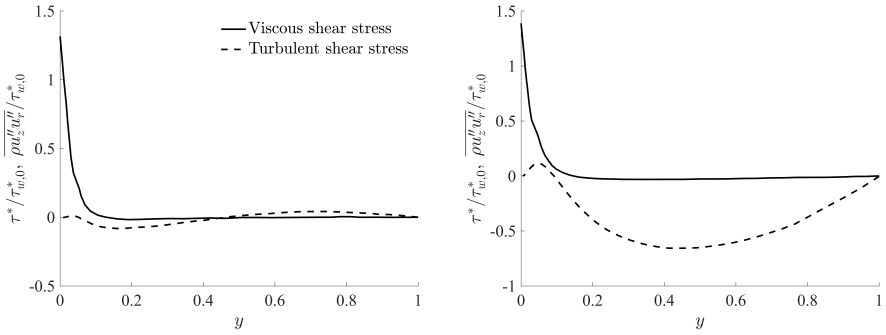

Figure 2.4: Profiles of viscous and turbulent shear stress at fully laminarised (z/D=12.52) and regeneration (z/D=27.52) stages of case C [11].

and low-speed fluctuating velocity streaks disappear at the locations of the heat transfer deterioration, and turbulence activities such as sweep and ejection are largely weakened at this stage of the flow. The DNS of pipe flows of strongly heated air was also conducted by Bae et al. [72] to study the effect of thermophysical property variations. Similar turbulence and heat transfer reduction were observed, and the mean velocity and temperature profiles were found to be dissimilar with each other at down-stream locations. It is of interest to note that low Mach number approximation was applied in the governing equations used by Bae et al. [11], following Accary et al. [73]. This method is different from the incompressible approach where the compressibility is completely ignored. Some other DNS studies of supercritical fluid flows are done by Li et al. [74] and Chu & Laurien [75]. Li et al. [74] simulated channel flows of supercritical carbon dioxide, with a heated and a cooled wall. The flow is similar to that in an annular flow simulated by Bae et al. [71]. The distance between the high- and low-speed streaks in the cooling region increases and turbulence is enhanced. It was found that the compressibility effect linked to the pressure fluctuation and dilatation of velocity fluctuation could be ignored, while the buoyancy production was significant, due to strong density fluctuations. Chu & Laurien [75] simulated a horizontal pipe flow of supercritical carbon dioxide, which confirmed the observations made by Tian et al. [55]. The wall temperature was again found to be higher at the top due to the secondary flow caused by buoyancy. Interestingly, without the buoyancy effect in the streamwise direction, a reduction in turbulence and heat transfer coefficient still happen due to the variations of thermophysical properties. Nemati et al. [76] carried a DNS on the effect of imposing different thermal wall boundary conditions, i.e., with and without enthalpy fluctuations at the pipe wall. It was shown that the heat transfer in supercritical fluids can be significantly influenced by

the thermal boundary conditions. With/without enthalpy fluctuations at the wall, and hence the density and viscosity fluctuations can influence the turbulent shear stress and turbulent heat flux. The review of vast numerical (RANS & DNS) and experimental studies on mixed convection flows of supercritical fluids were carried out by Yoo [77], including various heat transfer correlations summarised in experimental studies. Yoo found that most of the experimental studies focused on heat transfer rather than turbulence, none of the correlations could characterise the heat transfer deterioration and recovery in vertical flows. Yoo suggested further developments of visualization and measurement technique for experimental studies on supercritical fluids. RANS studies were also summarised, it was found that most turbulence models could resolve the laminarization and recovery of turbulence, but unable to reproduce the heat transfer recovery due to the failure of modelling the turbulent heat flux at this stage. This problem can be solved by using DNS, in which more detailed flow and heat transfer features could be resolved, but the time-consuming and expensive required computing resource is another problem for DNS of flows at high Reynolds number.

From the conclusions of previous experimental and numerical studies, the effects that cause the abnormal heat transfer and turbulence behaviour in supercritical fluids in vertical pipes are mainly: (i) buoyancy (non-uniform body force) effect, (ii) acceleration due to density reduction and (iii) effect of other variable thermophysical properties. In the present study, these three effects are investigated using direct numerical simulations (DNS) with artificially varied conditions to eliminate or isolate some effects. Similar research methodology has been seen in a numerical study of heated and cooled annular channel flow of supercritical CO_2 [78]. In that work, simulations with constant thermophysical properties, or with only variable density, or only variable viscosity, or variable thermophysical properties with and without gravity, were carried out to study the effects. The simulations of their study were carried out under the condition of fully developed flows, and hence any entrance effects are excluded. Mean velocity and turbulent shear stress profiles were significantly affected by the variations of density and viscosity. The change of velocity gradient increases the production of turbulent kinetic energy near the cold wall but decreases it near the hot wall. Another DNS study that is relevant to the present study was done by He et al. [13], who studied non-uniform body force (i.e., the buoyancy) effect using an artificially prescribed body force distributions simulating buoyancy. This enables them to study the buoyancy force under an isothermal condition. A new interpretation was proposed for flow laminarisation caused by non-uniform body forces such

as buoyancy. It was found that the turbulent shear stress of a body force influenced flow can be expressed as a summation of that of a flow of the same pressure gradient (EPG) but without any body forces, and an additional shear stress attributed to the body force. We will further discuss this idea together with the analysis of our results in Chapter 4.

The current study aims at investigating the effects of various physical mechanisms/processes on heat transfer and turbulence in an upward pipe flow of supercritical CO_2, it refers to the work conducted by Bae et al. [11]. In Bae et al.'s work, the link between heat transfer deterioration/enhancement and the laminarisation/increase in turbulence is identified, and the behaviours of turbulent shear stress, turbulent heat flux, turbulent kinetic energy and buoyancy production is presented and discussed. However, the changes in turbulence is a result of the combination of several effects, including the variations of viscosity and density, buoyancy and flow development. Their mechanism and how they affect the changes in turbulence is not covered in Bae et al.'s work. The techniques used in Peeters et al. [78] to eliminate or isolate different effects is implemented in the current study. In Peeters's study on an annular channel flow, the inner and outer walls were set to hot and cold respectively and the net heat input to the flow was zero. Consequently, there was no flow development in the axial direction, which significantly simplified the flow phenomena. In this study, we apply a constant heat flux on the pipe wall and the flow development along the pipe is a major characteristic of the flow as in many experiments. We expect significant differences between developing and fully-developed supercritical fluid flows, which is one of the focuses of this study.

2.3 Studies on turbulence in heated flows

It is now well established that turbulence in a heated vertical flow in a pipe or channel is often significantly different from that in an unheated isothermal flow due to the influence of buoyancy [77, 79]. In a heated downward (buoyancy-opposed) flow, buoyancy destabilises the flow enhancing turbulence and heat transfer, whereas the situation is significantly more complex in a heated upward (buoyancy aided) flow. With moderate buoyancy and heat flux, turbulence is suppressed and heat transfer is worsened. When the heat flux is sufficiently large resulting in a strong buoyancy, the flow may be completely laminarised leading to the so-called heat transfer deterioration. With a further increase in heat flux and buoyancy, however, turbulence reappears leading to improved heat transfer. At this stage, the flow is dominated

by natural convection. In addition to buoyancy, the flow in a heated pipe is also complicated by the influences of the variations of thermophysical properties, including viscosity and density (other than the buoyancy), which also contribute to the 'peculiar' behaviours. It is useful to note that many of the flow physics discussed herein in the context of supercritical fluid also occur in the sub-critical fluid systems, although the fact that the system pressure is above the critical value often makes the phenomena more complex and difficult to predict [80].

Bae et al. [11] carried out one of the first DNS of flow of fluid at supercritical pressure in a vertical pipe for a range of conditions including up and downward flows of variable buoyancy influences. The detailed information on the flow and thermal fields enabled the authors to elaborate the physics on the turbulence reduction and recovery in a greater depth than could have been done previously. In particular, they focused on the external (indirect) and structural (direct) effects of buoyancy on turbulence and turbulent heat flux following Petukhov & Polyakov [81]. The former refers to the fact that buoyancy acting as a body force modifies the mean velocity profile, which in turn results in a change in turbulence production. This is known to be the dominating effect of the two and key for the primary understanding of such flows as discussed in the opening paragraphs of this paper. The structural effect on the other hand refers to the effect of the interactions between the fluctuating buoyancy force and velocity, which lead to a direct generation/destruction of turbulence. This is reflected in the budget of turbulence kinetic energy as the buoyancy production. Bae et al's [11] results confirmed that the leading indirect effect could in most cases be used to explain the key features of flow laminarisation and recovery, supporting previous semi-empirical theory. Their data on buoyancy production was however proved to be not entirely expected. While the buoyancy production in a downward flow is always a positive contribution to turbulence kinetic energy as expected since such a flow is akin to an unstable flow so far as buoyancy is concerned, the production in an upward flow is initially negative, but turns to be positive over the rest of the pipe. This was then shown to be the leading factor for turbulence recovery, which is perhaps the main reason that turbulence models are unable to accurately predict turbulence recovery since the buoyancy production is very difficult to predict even with the most sophisticated models [61, 77].

The theme of the structural effects of buoyancy on turbulence has been carried over in some more recent studies. Peeters et al. [78] conducted DNS of supercritical fluid flow in an annular channel with a heated outer wall and a cooled inner wall with zero net heat flux to the flow, which enabled the authors to study buoyancy-aided

and buoyancy-opposed flows simultaneously under an axially fully developed condition. It was shown that the turbulence was significantly decreased near the hot wall but increased near the colder wall, which was only partially attributed to the effect of mean dynamic viscosity and density variations. By analysing the solution of the transport equation for the evolution of the streamwise coherent streak flank strength, the authors demonstrated that near the hot wall, both thermal expansion and buoyancy reduce the streak coherence, while the viscosity gradient that exists across the streaks may interact with the mean shear to either strengthen or weaken the streaks dependent on the radial location. The formation of the streamwise vortices is not directly strongly influenced by the density and viscosity fluctuations, but is hindered by the torque resulted from the kinetic and density gradients. Overall, based on such analyses of the near wall turbulence re-generation cycle, the authors concluded that the instantaneous density and dynamic viscosity fluctuations are (partially) responsible for decreased turbulent motions in heated fluids at supercritical pressure, and the increase on the cold wall. This is consistent with Bae et al's [11] conclusion noting that the buoyancy was moderate in the case of Peeters et al. [78] and the flow was equivalent to the initial phase of Bae et al's developing flow.

In a follow-up study [82], the authors further analysed the data on the annular flow specifically focusing on the direct effects on heat transfer of the variations of thermal properties. Based on the analyses of the budget of the turbulent heat transfer and quadrant analyses, the authors concluded that both the fluctuations and the mean gradients of the density and molecular Prandtl number had a significant influence on the turbulent heat flux. That is, the direct and indirect effects were equally important under the conditions studied. It was also demonstrated that the temperature fluctuations diminished in the regions of high heat capacity close to the pseudo-critical temperature, reducing the direct effect there, but the opposite was true when the heat capacity was smaller.

Azih & Yaras [83] also investigated the structural effect of density variations considering a heated channel subject to either wall normal, or streamwise (opposed) or zero buoyancy. The heated section was relatively short, just over 11 half channel heights and hence the flows are typical of those close to the early entrance region of a heated flow. By analysing the coherent turbulence structures, the authors found that the reduction in density and viscosity in a forced convection promotes the generation of small scale vortices interacting and breaking pre-existing large near-wall structures and hence leading to a reduction in turbulent mixing. In a buoyancy-opposed flow, the baroclinic vorticity generation due to the spanwise density gradient, which was

introduced in an earlier study [84], was shown to promote larger-scale ejections and sweeps leading to additional wall-normal thermal mixing, which is consistent with the findings of previous work under similar conditions [11].

Another interesting recent development in the area of heated flows is the scaling of the mean velocity, turbulence and temperature distributions. It is well tested and documented that for isothermal compressible flows at moderate to high Mach number, the van Driest transformation ($\overline{u}^{\nu D} = \int_0^{\overline{u}/u_\tau} \sqrt{\overline{\rho}/\overline{\rho}_w} d(\overline{u}/u_\tau)$) [85] enables the transformed velocity $\overline{u}^{\nu D}$ of a compressible flow (in which the viscous heating causes non-uniform mean density distribution) to collapse with the law of the wall of an incompressible flow with y^+ used in both the compressible and incompressible flows. The transformation adjusts the velocity gradient by a factor of $\sqrt{\overline{\rho}/\overline{\rho}_w}$ based on dimensional argument. This transformation works well for boundary layers above an adiabatic wall [86, 87]. The success of the density-weighted scaling can be attributed to the success of Morkovins hypothesis, which states that the relationships between the relevant statistical properties of turbulence are unaffected by compressibility if the r.m.s. density fluctuations are small (of order 1/10) compared to the absolute density [86, 88].

For a heated flow where there is a wall-normal gradient of thermal properties, the van Driest law fails. This has been attributed to the elongation and shortening of the near-wall streaks on hot and cold walls, respectively [86, 89, 90]. These streak modifications are quantified in terms of the wall-based viscous units. To overcome the above shortcomings, Huang et al. [87] proposed to use the so-called semilocal scaling, that is, $(y^* = \overline{\rho}(\tau_w/\overline{\rho})^{1/2} y/\overline{\mu})$, which has been found to effectively account for the changes in streak length in the buffer layer [91, 92]. The modified van Driest law have then been successfully applied to various heated/cooled flow scenarios e.g, Coleman et al. [86], even though it clearly does not provide a universal law.

Recently, Trettel & Larsson [93] attempted to develop a universal scaling to consider the influences of variable properties. Their argument was based on the log-layer scaling as well as the near-wall momentum conservation, and introducing velocity and coordinate transformations separately. Their work has resulted in a new velocity transformation accounting for the density and viscosity gradients:

$$\overline{u}^* = \int_0^{\overline{u}/u_\tau} \left(\frac{\overline{\rho}}{\overline{\rho}_w}\right)^{1/2} \left[1 + \frac{1}{2\overline{\rho}}\frac{d\overline{\rho}}{dy}y - \frac{1}{\overline{\mu}}\frac{d\overline{\mu}}{dy}y\right] d(\overline{u}/u_\tau), \tag{2.2}$$

which embodies previously proposed scaling, such as the van Driest and that used by [87].

Patel and colleagues have also studied the effect of variable properties on turbulence structures and scaling about the same time. Patel et al. [92] introduced a semilocal frictional Reynolds number, $Re_\tau^* = Re_\tau \sqrt{(\overline{\rho})/\overline{\rho}_w}/(\overline{\mu}/\overline{\mu}_w)$, which was used to successfully rescale turbulence statistics and the van Driest transformed velocity for variable-property flows. The basic expression can be reorganised to take a similar form as that used in Trettel & Larsson [93] for most flows. Unlike constant property flows, however, the turbulence statistics show a strong dependence on Re_τ^*. For the case when Re_τ^* decreases away from the wall, the streamwise normal Reynolds stress anisotropy increases, which was associated with the stretching of the large-scale low-speed streaks in the buffer layer. The reverse is true for increasingRe_τ^* cases. Later Patel et al. [94] provided a more comprehensive discussion on the effects of the near-wall property gradients on mean velocity scaling, near wall turbulence statistics and turbulence structures. Again Re_τ^*, and in particular, its radial profile, was shown to characterise the modifications of turbulence structures. This was used to explain the way turbulence anisotropy is affected by wall heating and cooling. Additionally, it was found that the viscous shear stress is a universal function in the inner layer when expressed in the semi-local parameter,$(h/Re_\tau^*)du^{\nu D}/dy$. It was later showed in Patel et al. [95] that the statistics of a scaler (such as temperature) can also be scaled using the semi-local Reynolds number and a semi-local Pr* defined as $Pr^* = Pr_w(\overline{\mu}/\mu)/(\overline{\lambda}/\lambda)$. The above idea was further used in Pecnik & Patel [96] to derive a so-called semi-local scaled transport equation for turbulence kinetic energy, in which the viscous terms are scaled with Re_τ^* and the turbulence production is governed by the gradient of the van Driest velocity. They then successfully used this equation in conjunction with a turbulence model to simulate several fully developed turbulent flows, ranging from volumetrically heated flows at low Mach (Ma) numbers to a fully compressible case of $Ma = 4$ in a channel with isothermal walls.

The above scaling work has been based on ordinary fluid (that is fluids at sub-critical pressure). More recently these scaling theories have been tested for flows at trans-critical and super-critical pressures [97, 98, 99], though all of them only considered forced convection neglecting the effect of buoyancy. Wan et al. [98] found that the semi-local scaling (Re_τ^*) correlated both the mean velocity and temperature field very well for a spatially fully developed channel flow with a heated and a cooled wall. Liu et al. [99] considered a more challenging case where the flow is developing spatially in a heated pipe under forced convection condition. It was found that the mean velocity in the logarithmic region could be well scaled by the semi-local scaling, but the temperature could be better scaled with the modified van Driest

transformation. Ma et al. [97] considered a flow in a heated/cooled channel with a very high temperature difference (200K) at a pressure just above the critical value. This hence resulted in a density difference up to 18 times in the flow and therefore even greater a challenge for scaling. It was shown that whereas the semi-local scaling was suitable for one wall, but not the other where the density fluctuations are very high, with $STD(\rho'/\rho) > 40\%$, and hence the condition for the Morkovins hypothesis is not satisfied.

Finally, we briefly discuss the recent work by He et al. [13] which provides much of the foundation of the discussion presented herein. In that work, DNS were carried out to study the effect of non-uniform body force (including for example buoyancy force) on turbulence using a prescribed linear or step change body force near the wall. The flow was isothermal. It was established that, in contrast to common perception, the turbulence is not modified by such body forces when compared with that in an equivalent pressure gradient (EPG) flow, which can be seen as a suitable reference for corresponding body force-influenced flows. In this theory, the so-called laminarisation represented as a reduction in the apparent Reynolds number which can be estimated once the body force itself is known. The detail of the theory is further discussed in the results session. More recently, the apparent Reynolds number concept was used in Marensi et al. [100] to produce a Reynolds number-heating phase diagram, showing if a flow is expected to be turbulent or laminar (or convection driven flow) for a heated upward flow using the Boussinesq approximation for density effect. The phrase diagram agrees well with DNS results and analysis based on the linear stability.

In the present study, we aim to establish a unified approach to explain the mechanisms of laminarisation due to the effects of buoyancy, and variations of density and viscosity in a heated vertical flow at supercritical pressure. The unified theory also explains the effect of inertia in such a spatially developing flow, which is treated as a pseudo-body force and its effect is explained in a similar way for other effects. Additionally, we study the region of "full" laminarisation and show that in this region turbulence in the core of the pipe decays in an exponential manner similar to that of a grid generated turbulence. Near the wall however streaks are generated which leads to an increase in streamwise turbulent fluctuations (and hence turbulence kinetic energy) but new turbulence (the transverse fluctuating components and turbulence spots) is generated only in a later re-transition region.

2.4 Fluid-to-fluid scaling for supercritical fluids

For some experiments of supercritical fluids, the cost for increasing and maintaining the pressure of the fluid of interest (prototype fluid), and heating up the fluid could be high. Under such circumstances, surrogate fluids (model fluid) could be used to save the cost and reduce technical difficulties. The heat transfer behaviour of the prototype fluid can be obtained from converting the experiment result obtained using the model fluid, with the support of fluid-to-fluid scaling correlations. Required by the fluid-to-fluid scaling laws, the flow configurations of the model fluid need to be carefully chosen, to scale some of the chosen non-dimensional parameters which characterize the heat transfer and flow performance.

Early technique on fluid-to-fluid scaling was developed for the demand of studying the heat transfer behaviour in boiling-water-cooled reactor (BWR) using modelled fluid to save experimental cost. A generalized modelling technique was developed by Ahmad [101] using non-dimensional analysis. The fluid-to-fluid scaling method for boiling water was well tested by experiments for different boiling conditions and geometries. Fluid-to-fluid scaling technique was well applied in nuclear thermohydraulic studies to model the complicated heat transfer in flows with phase change. A downscaled model was developed by Van et al. [102] to study the Dodewaard BWR using freon-12 as the modelling fluid. The downscaled model only consumes 2% energy of the original BWR reactor, with most of the system parameters fixed. Phase change number and sub-cooling number were used to scale the heat flux and inlet enthalpy.

The main task to achieve similarity among supercritical fluids is to establish a group of non-dimensional parameters to characterize the heat transfer and flow behaviour, then by scaling the boundary conditions of the model and prototype fluids, to ensure these non-dimensional parameters be the same in the model and prototype fluids. Several groups of non-dimensional numbers characterizing the heat transfer behaviour and stability of supercritical fluid flows were proposed and discussed in some recent studies [103, 104, 105]. A brief review on fluid-to-fluid scaling was carried out by Pioro & Duffey [106], three dimensionless parameters are used to scale the flow:

$$(\frac{P}{P_c})_M = (\frac{P}{P_c})_P \tag{2.3}$$

$$(\frac{T_b}{T_c})_M = (\frac{T_b}{T_c})_P \tag{2.4}$$

$$(\frac{\rho_b U_b D}{\mu_b})_M = (\frac{\rho_b U_b D}{\mu_b})_P \tag{2.5}$$

Early fluid-to-fluid scaling law for supercritical fluids was developed by Jackson & Hall[107]. They analysed the non-dimensional governing equation and identified twelve non-dimensional parameters to achieve complete similarity in two systems that are free of buoyancy effect. It is impossible to satisfy all the twelve parameters in two systems, and 5 non-dimensional parameters were chosen to be scaled, to achieve similarity of the development of Nusselt number: $Nu_b = f(\frac{z*}{D*},\ \frac{P_0^*}{P_c^*},\ Re_b,\ Pr_b,\ \frac{q^*D^*}{\lambda_b^* T_b^*})$. This scaling method is for forced convection systems with the same fluid. Based on this scaling law, Zwolinski et al. [108] has developed a modified version of Jackson's scaling law, to achieve similarity between supercritical CO_2 and H_2O. The five non-dimensional parameters to determine the Nusselt number are

$$Nu_b = f(\frac{z*}{D*},\ \frac{P_0^*}{P_c^*},\ \frac{T_0^*}{T_c^*},\ Re_0,\ \frac{q^*D^*}{\lambda_0^* T_0^*}). \tag{2.6}$$

Also, this modified method is again only for forced convection flow systems.

Another scaling method for supercritical flows was proposed by Cheng et al. [109], who introduced a new parameter $\theta = \frac{T_b^* - T_{pc}^*}{T_{pc}^* - T_c^*}$ to achieve similar non-dimensional fluid properties development trends in two different supercritical fluids. Rather than using the Reynolds number to scale the mass flux, Cheng used an empirical expression including the Reynolds and Prandtl number to achieve similarity of the developments of Nusselt number. In Cheng's law, Nusselt number is determined by four non-dimensional parameters: $Nu_b = f(\frac{P_0^*}{P_c^*},\ \frac{T_b^* - T_{pc}^*}{T_{pc}^* - T_c^*},\ Re_b Pr_b^{5/12},\ \frac{q^*D^*}{\lambda^*(T_{pc}^* - T_c^*)})$. A less straight forward method was used to validate the scaling method: the experimental data of the model fluid was transferred to the equivalent condition of the prototype fluid using the scaling correlation, then the heat transfer behaviour of the prototype fluid in this equivalent condition was calculated using the empirical correlation obtained from early studies. The results were accurately matched, which shows good reliability of this scaling method. Cheng's scaling method was numerically tested for different fluids by Tejaswini et al. [110], who used supercritical CO_2 and R134a to downscale the flow of supercritical H_2O. The scaling law is tested by simulations using the standard $k - \epsilon$ turbulence model. The comparison was not only based on the development of Nusselt number, but also the temperature and density. It was found that the profiles of CO_2 agree better with those of H_2O than those of the R134a.

To avoid the singularity when temperature reaches the critical point, Zahlan et al. [111] used $\frac{T_b^*}{T_{pc}^*}$ to achieve similarity in developing trends of fluid properties. Zahlan et al. has proposed two other scaling laws based on Cheng's similarity correlation. Same as that of Cheng's, empirical expression $RePr^{2/5}$ was used

to achieve similarity of heat transfer coefficients in two fluids. The Nusselt numbers in the two proposed correlation expressions were determined in a new manner: $Nu_b = f(\frac{P^*}{P_c^*},\ \frac{T_b^*}{T_{pc}^*},\ \frac{q^*D^*}{\lambda_b^* T_{pc}^*},\ Re_b Pr_b^{5/12})$ and $Nu_b = f(\frac{P^*}{P_c^*},\ \frac{T_b^*}{T_{pc}^*},\ \frac{T_w^*}{T_{pc}^*},\ Re_b Pr_b^{5/12})$. Zahlan et al. tested the two new correlations together of the two earlier correlations (modified Jackson's correlations, Cheng's correlations) using experimental data of supercritical CO_2 and heat transfer empirical correlation of supercritical H_2O, in a large range of flow conditions. They mostly discussed the similarity in heat transfer coefficient. The two early laws were found to overestimate the heat transfer coefficient, and the two new laws have lower uncertainties.

Recently there were two new scaling proposed and tested by Yu et al. [112] and Tian et al. [113]. Yu et al. proposed a new scaling method by introducing a new non-dimensional parameter, relative enthalpy rise factor $En = \frac{4q^*}{G^* D^* (h^*_{T_{pc}} - h^*_{T_c})}$. Scaling En is to ensure the similarity in experimental condition and fluid type. In Yu's method, Nusselt number was determined by 6 non-dimensional parameters: $Nu_b = f(\frac{P^*}{P_c^*},\ \frac{T^*}{T_{pc}^*},\ \frac{\Delta P^*}{\rho^* \nu^{*2}},\ Re_b, Pr_b, En)$. Supercritical R134a was used to downscale the flow of supercritical H_2O and CO_2, experimental data and empirical correlations were used to validate the new scaling method. Good agreement was shown in the scaling result. Tian et al. [113] has developed a new scaling law for the similarity of mixed convection supercritical flows. A new non-dimensional parameter $Re^{-0.9}\frac{\beta_{pc}^* q^*}{c_{p,pc}^* G^*}$ was used to scale the heat transfer coefficient. It was found from vast early experimental data of mixed convection supercritical fluid flows, Nusselt number and $Re^{-0.9}\frac{\beta_{pc}^* q^*}{c_{p,pc}^* G^*}$ are strongly correlated, so that $Re^{-0.9}\frac{\beta_{pc}^* q^*}{c_{p,pc}^* G^*}$ can be used to characterize the heat transfer behaviour. The new scaling correlation was tested using RANS simulations with $k-\omega$ turbulence model. R134a was used to model the flow of water and the heat transfer behaviours agreed well between the model and prototype fluids. The study extended fluid-to-fluid scaling of supercritical fluids to mixed convection.

Another group of non-dimensional parameters were introduced by Ambrosini [105] to characterize the stability and heat transfer of the supercritical upward pipe flow with uniform heating. These non-dimensional parameters were reconsidered by [14], Reynolds averaged Navier-Stokes (RANS) simulation was used to test the performance of the fluid-to-fluid scaling correlation. More simulations and detailed discussion were carried out by Ambrosini [114]. In this scaling method, the non-dimensional inlet enthalpy N_{SPC} and wall heat flux N_{TPC} are set to be the same for both the model and prototype fluids:

$$N_{SPC} = (h_{pc}^* - h_0^*)\frac{\beta_{pc}^*}{C_{p,pc}^*} \tag{2.7}$$

Table 2.1: Non-dimensional groups of different fluid-to-fluid scaling laws for supercritical fluids.

Fluid-to-fluid scaling correlation	Nusselt number determination
Jackson et al. [107]	$Nu_b = f(\frac{z*}{D*},\ \frac{P_0^*}{P_c^*},\ Re_b,\ Pr_b,\ \frac{q^*D^*}{\lambda_b^*T_b^*})$
Jackson et al. (modified) [108]	$Nu_b = f(\frac{z*}{D*},\ \frac{P_0^*}{P_c^*},\ \frac{T_0^*}{T_c^*},\ Re_0,\ \frac{q^*D^*}{\lambda_0^*T_0^*})$
Cheng et al. [109]	$Nu_b = f(\frac{P_0^*}{P_c^*},\ \frac{T_b^*-T_{pc}^*}{T_{pc}^*-T_c^*},\ Re_bPr_b^{5/12},\ \frac{q^*D^*}{\lambda^*(T_{pc}^*-T_c^*)})$
Ambrosini et al. [14]	$Nu_b = f(\frac{q^*\beta_{pc}^*}{\dot{m}c_{p,pc}^*},\ (h_{pc}^*-h_0^*)\frac{\beta_{pc}^*}{c_{p,pc}^*},\ Re_{b,pc},\ Pr_{b,pc},\ \frac{U_0^{*2}}{gL^*})$
Zahlan et al. [111]	$Nu_b = f(\frac{P^*}{P_c^*},\ \frac{T_b^*}{T_{pc}^*},\ \frac{q^*D^*}{\lambda_b^*T_{pc}^*},\ Re_bPr_b^{5/12})$ & $Nu_b = f(\frac{P^*}{P_c^*},\ \frac{T_b^*}{T_{pc}^*},\ \frac{T_w^*}{T_{pc}^*},\ Re_bPr_b^{5/12})$
Yu et al. [112]	$Nu_b = f(\frac{P^*}{P_c^*},\ \frac{T^*}{T_{pc}^*},\ \frac{\Delta P^*}{\rho^*\nu^{*2}},\ Re_b, Pr_b, En)$
Tian et al. [113]	$Nu_b = f(\frac{P^*}{P_c^*},\ (h^*-h_{pc}^*)\frac{\beta_{pc}}{c_{p,pc}^*},\ \frac{q^*D^*}{\lambda_b^*(T_{pc}^*-T_c^*)},\ Re^{-0.9}\frac{\beta_{pc}^*q^*}{c_{p,pc}^*G^*})$

$$N_{TPC} = \frac{q}{\dot{m}}\frac{\beta_{pc}^*}{C_{p,pc}^*} \tag{2.8}$$

This ensures that the starting points and change rates of the streamwise developments of the non-dimensional bulk enthalpies in the two fluids are the same. The method requires that the pressure of the model and prototype fluids to be tuned to achieve a similarity between the non-dimensional fluid properties. The local Reynolds number calculated by the local bulk properties should also be kept the same, ideally. According to the discussion in Ambrosini & De Rosa [14], it is impossible to achieve the same bulk Prandtl number between two supercritical fluids, and the Peclect number appears in the non-dimensional energy equation cannot be the same after scaling the Reynolds number. The operating pressures of the model and prototype fluids are tuned to achieve the same maximum Prandtl number at the critical point, suggested by Rohde & Van [115]. Similarity of the heat transfer behaviour is given by RANS simulation especially in data sets with lower inlet enthalpy. The non-dimensional parameters to determine the heat transfer in supercritical flow in different fluid-to-fluid scaling methods are listed in table 2.1.

The study described in Chapter 6 will test the fluid-to-fluid scaling method proposed by Ambrosini [14], among four different supercritical fluids, i.e., carbon dioxide, water, ammonia, and fluoroform using direct numerical simulations (DNS). Early studies of fluid-to-fluid scaling for supercritical fluids are mainly based on experimental data, empirical correlations, and RANS simulations. DNS has not been used for

such a purpose before. The result of DNS is able to provide good reference and further understanding of the theory of fluid-to-fluid scaling for supercritical fluids. In chapter 6, the comparisons of variations in turbulence in the different fluids are also of interest, which is directly relevant to the change of the heat transfer.

2.5 Conjugate heat transfer of supercritical fluid flows

Most numerical studies of supercritical fluids only carried out simulations of the fluid domain, with thermal boundary conditions based on a constant heat flux or a constant temperature on the wall. However, the thermal boundary conditions in experiments are different, in most cases, the fluid is heated by the solid pipe, which is heated by electric current. In such experiments, the heat flux through the fluid-solid interface can rather non-uniform due to axial solid conduction. Such redistribution could be intensified when there are strong axial or circumferential variations of heat transfer characteristic.

As discussed in the previous sections, for vertical flows of supercritical fluids under strong heating, when the pseudo-critical temperature is between the bulk and wall temperatures, there are strong changes of heat transfer and turbulent characteristic due to the effect of buoyancy and thermophysical property variations. For horizontal flows, there may be horizontal thermal stratifications due to buoyancy. It can be expected that, for vertical flows, heat flux through the fluid-solid interface maybe redistributed in axial direction, and for horizontal flows, heat flux maybe redistributed in both axial and circumferential directions. It is necessary to use conjugate heat transfer in numerical studies of supercritical fluid flows to quantify the differences brought by considering/neglecting solid conduction in simulations. Such a study was carried out by Pucciarelli & Ambrosini [15] for the first time for channel flows of water at supercritical pressure (25MPa) simulated by large eddy simulations (LES), with and without the steel solid wall. In this study, the thickness of the steel wall was taken to be the half channel height ($1mm$) and the inlet Reynolds number was 3868. According to the result, different types of thermal boundary conditions cause significant difference in terms of heat transfer and turbulence. The fluctuations of temperature were much smaller after considering conjugate heat transfer, which were linked to the fluctuations of thermophysical properties, such fluctuations affect the turbulence characteristics. When the flow was partly and fully laminarised, the near-

wall peak of turbulent kinetic energy reduced by about 50% to 40%, and radial turbulent heat flux reduces by about 30% after including the solid wall conduction.

By considering conjugate heat transfer, two effects are brought in, i.e., the stabilization of temperature (enthalpy) fluctuation and redistribution of heat flux on the fluid-solid interface. The first effect was investigated by Nemati et al. [76] in a DNS study, by studying forced convection pipe flows of carbon dioxide ($Re_\tau = 360$) at supercritical pressure with two thermal boundary conditions, i.e., uniform wall heat flux and fixed wall enthalpy. After eliminating the fluctuation of the wall enthalpy (the latter thermal boundary condition), the magnitude of viscous diffusion, dissipation and production of turbulent kinetic energy budget are all slightly smaller, especially near the wall. Also, the FIK decompositions of Nusselt number [33, 34] show that the laminar and inhomogeneous contributions largely remain the same when the wall enthalpy fluctuations were eliminated, while the turbulent contribution was slightly reduced, which was the main reason for the reduction of Nusselt number. Nemati et al. [76] has quantified the contributions of wall enthalpy fluctuations to heat transfer and turbulence in an example of forced convection, which helps to provide further understanding of the effect of the wall enthalpy (temperature) fluctuations.

Some RANS numerical studies of supercritical fluid flows also considered conjugate heat transfer. Zhou & Krishnan [116] simulated the flows of supercritical sulfur hexafluoride ($Re = 650$) in a T-shape channel with low-Reynolds number $k-\epsilon$ (Chien) turbulence model [117], and validated the numerical result against experiments. Conjugate heat transfer was considered, and the heat flux across the fluid-solid interface was achieved to couple the fluid and solid part. It is found that the wall temperature from the experiment reached the peak value earlier than that resolved numerically. The comparisons of the general trend of horizontal and upward flows were satisfactory against experiments, with the wall temperature reasonable well predicted. Wang et al. [118] carried out conjugate heat transfer simulations of supercritical cryogenic methane flows in rectangular cooling channels using the standard $k - \epsilon$ model to study the effects of solid thermal conductivity. It was found that the variation of solid thermal conductivity significantly affected the redistribution of heat flux to the fluid, and a new empirical Nusselt number correlation was established based on the Jackson & Hall [119] correlation.

Zhao et al. [120, 121] carried out conjugate heat transfer simulations of vertical annular channel flows of supercritical CO2, using the AKN [122, 66], V2F [62], YS [123] turbulence models, and compared their results against experiments. The result

shows the three models can largely reproduce the general trend of the wall temperature, and the wall temperature obtained by the AKN model has the best agreement with the experimental result. Zhao et al. [124] investigated the conjugate heat transfer of supercritical CO2 in a membrane helical coiled heat exchanger, which was more complicated than channel or pipe flows. Abnormal heat transfer behaviour was found: the wall temperature and heat transfer coefficient of the inner surface reduced and increased periodically, but such phenomena disappeared when the Reynolds number or the inlet temperature were increased. Sun et al. [125] studied the supercritical aviation kerosene (RP-3) flows in a horizontal tube using conjugate heat transfer simulation. They used the standard $k-\epsilon$ turbulence model with the modified wall treatment to carried out simulations at different Reynolds number, heat fluxes and tube diameters, and found that the buoyancy effect is stronger at lowered Reynolds numbers, higher wall heat fluxes and larger diameters. By using conjugate heat transfer, the heat flux at the top and bottom of the tube was redistributed, circumferential stratification can also be observed. Xu et al. [126] carried out conjugate heat transfer simulations of supercritical RP-3 flows in a ribbed tube to study the effect of ribs. It was found that the heat transfer was effectively enhanced due to the presence of the ribs, especially at the inlet region. The pyrolytic reaction was increased downstream due to a much higher bulk temperature. Numerical simulations of developing laminar flows of supercritical CO2 in multi micro-channel, with conjugate heat transfer, have also been carried out [127, 128]. It was found that the friction factor and heat transfer coefficient were significantly affected by the strong change of thermophysical properties, and such effect diminished when the temperature or pressure was further above the pseudo-critical value. When the pressure was higher than the critical value, the heat transfer deterioration was weakened, but the Nusselt number was not affected by the Reynolds number in laminar regime.

To shorten simulation running time and reduce necessary computing resources, modelling work has been done to develop simplified models for conjugate heat transfer of supercritical fluids. Pizzarelli et al. [129] and Zima & Nowak-Ocłoń [130] developed similar 1/2-D models to predict the wall temperature of the supercritical methane flows in a rocket engine cooling channel and the heating of the waterwall tubes in steam boilers, respectively. These models both have a 1-D mesh for the mass conservation and momentum balance, and a 2-D mesh for the energy balance, coupled with the solid wall. The turbulent heat flux, skin friction and heat transfer coefficient were calculated using empirical correlations. These models have been validated against CFD solvers and experimental data and proved to be able to capture

the general trend of wall temperatures, and provided useful estimation for industry and other practical applications.

The literature survey on studies of conjugate heat transfer of supercritical fluids indicates that there are few numerical studies on this topic. Most of the simulations in these studies were carried out using the Reynolds-averaged Navier-Stokes (RANS) approach, with the eddy viscosity modelled, and only one [15] used LES. None of them used DNS, which is able to resolve the flow at small scales without modelling to reflect the real physics and mechanisms. Two effects are brought by including conjugate heat transfer in the simulations of supercritical fluid flows, i.e., significant reductions of near-wall enthalpy (temperature) fluctuations and the redistribution of the fluid wall heat flux due to conduction in the solid wall. In RANS simulations, only the redistribution of the heat flux can be reflected. The effect of wall enthalpy (temperature) fluctuations cannot be modelled, because the enthalpy (or temperature) in the energy equation is in Reynolds averaged form, and the fluctuations are not resolved. In the DNS study done by Nemati et al. [76], the effect of elimination of the enthalpy fluctuations was investigated, but the redistribution of heat flux and the effect of buoyancy were not considered. It is necessary to carry out DNS of conjugate heat transfer of supercritical flows to establish further understanding on two effects. Such a study is described in Chapter 7.

Chapter 3

Methodology

More and more studies of flow and/or heat transfer are carried out using numerical methods. Compared to experiments, computational fluid dynamics (CFD) simulations can predict the flow and thermal characteristic reasonably and accurately, with lower costs. In experiments at high pressure and temperature, it is always a challenges to measure velocities and temperatures. Both intrusive methods (pitot tubes) and optical approaches (e.g., LDV or PIV) are difficult to be deployed for such flow/thermal conditions. In comparison, it is more convenient to access the detailed flow and thermal field, at any time and location of the flow domain with the help of CFD. A more complete picture of the flow physics can be presented, and visualizations of turbulent vortexes and activities, energy spectra at different scales become possible. Moreover, CFD simulations can help reducing risks and costs for studies of flows at extreme conditions, e.g., coolant flows at nuclear reactor cores, high temperature ejection flows, etc. Popular CFD types include the Reynolds-averaged Navier-Stokes (RANS) simulations, large eddy simulations (LES) and direct numerical simulations (DNS) were widely applied in solving different problems. Simulations carried out in the current study are direct numerical simulations (DNS), of which the numerical schemes will be introduced in this chapter. Also, the concepts of Reynolds-averaged Navier-Stokes (RANS) equations, Favre-averaged Navier-Stokes (FANS) equations that are relevant to the result discussions in this study, and the post-processing algorithm will be introduced in detail in this chapter.

In this chapter, numerical schemes of the direct numerical simulations in the current study and some background theory are introduced.

3.1 Navier-Stokes equations and DNS code CHAPSim

3.1.1 Navier-Stokes equations

Navier-Stokes equations were derived by French physicists Claude-Louis Navier and Geoge Gabriel Stokes in the 19th century, to describe the conservation of mass, momentum and energy in fluid motions. The conservative and non-dimensional form of continuity (Eq. 3.1), momentum (Eq. 3.2) and energy (Eq. 3.3) equations that describe an incompressible flow in Cartesian coordinate can be written:

$$\frac{\partial \rho u_i}{\partial x_i} = 0 \tag{3.1}$$

$$\frac{\partial \rho u_i}{\partial t} + \frac{\partial \rho u_i u_j}{\partial x_j} = -\frac{\partial p}{\partial x_i} + \frac{1}{Re_0}\frac{\partial}{\partial x_j}\Big(\mu\big(\frac{\partial u_i}{\partial x_j} + \frac{\partial u_j}{\partial x_i}\big)\Big) - \frac{\rho}{Fr_0^2} \tag{3.2}$$

$$\frac{\partial \rho h}{\partial t} + \frac{\partial \rho u_i h}{\partial x_i} = \frac{1}{Re_0 Pr_0}\frac{\partial}{\partial x_i}\big(\frac{\lambda}{c_p}\frac{\partial h}{\partial x_i}\big), \tag{3.3}$$

where Re_0, Fr_0, Pr_0 are the inlet Reynolds number, Froude number and Prandtl number defined as:

$$Re_0 = \frac{u^*_{z,0} R^*}{\nu^*_0} \quad Fr_0 = \frac{u^*_{z,0}}{\sqrt{g^* R^*}} \quad Pr_0 = \frac{c^*_{p,0}\mu^*_0}{\lambda^*_0} \tag{3.4}$$

Fluid flows in reality satisfy the Navier-Stokes at every instant and thus the instantaneous flow/thermal field can be obtained by solving the Navier-Stokes equations. Direct numerical simulation (DNS) is a numerical method solving these equations without introducing empirical modelling and is hence a popular tool for fundamental studies of turbulent flows. DNS reproduces the turbulent structures and small scale flow features, using fine meshes and small time steps. Simulations in the present study are DNSs, carried out using CHAPSim [131, 132, 133], which is an in-house solver for incompressible flows. In this section, the numerical schemes in CHAPSim and a new implementation for conjugate heat transfer by the author are introduced.

3.1.2 Governing equations for pipe flows

Upward pipe flows of fluids at supercritical pressure are simulated in the current study. The governing equations are the conservative Navier-Stokes equations and the energy equation in cylindrical coordinate.
The continuity equation:

$$\frac{\partial \rho}{\partial t} + \frac{\partial\left(\rho u_z\right)}{\partial z} + \frac{1}{r}\frac{\partial\left(r\rho u_r\right)}{\partial r} + \frac{1}{r}\frac{\partial\left(\rho u_\theta\right)}{\partial \theta} = 0, \tag{3.5}$$

The momentum equations:

$$\begin{aligned}\frac{\partial(\rho u_z)}{\partial t}+\frac{\partial(\rho u_z u_z)}{\partial z}+\frac{1}{r}\frac{\partial(r\rho u_r u_z)}{\partial r}+\frac{1}{r}\frac{\partial(\rho u_\theta u_z)}{\partial \theta}&=-\frac{\partial p}{\partial z}-\frac{\rho}{Fr_0^2}\\ +\frac{1}{Re_0}\left(\frac{\partial \tau_{zz}}{\partial z}+\frac{1}{r}\frac{\partial(r\tau_{rz})}{\partial r}+\frac{1}{r}\frac{\partial \tau_{\theta z}}{\partial \theta}\right),&\end{aligned} \tag{3.6}$$

$$\begin{aligned}\frac{\partial(\rho u_r)}{\partial t}+\frac{\partial(\rho u_z u_r)}{\partial z}+\frac{1}{r}\frac{\partial(r\rho u_r u_r)}{\partial r}+\frac{1}{r}\frac{\partial(\rho u_\theta u_r)}{\partial \theta}+\frac{\rho u_\theta u_\theta}{r}&=-\frac{\partial p}{\partial r}\\ +\frac{1}{Re_0}\left(\frac{\partial \tau_{rz}}{\partial z}+\frac{1}{r}\frac{\partial(r\tau_{rr})}{\partial r}+\frac{1}{r}\frac{\partial \tau_{r\theta}}{\partial \theta}-\frac{\tau_{\theta\theta}}{r}\right),&\end{aligned} \tag{3.7}$$

$$\begin{aligned}\frac{\partial(\rho u_\theta)}{\partial t}+\frac{\partial(\rho u_z\cdot u_\theta)}{\partial z}+\frac{1}{r}\frac{\partial(r\cdot\rho u_r\cdot u_\theta)}{\partial r}+\frac{1}{r}\frac{\partial(\rho u_\theta\cdot u_\theta)}{\partial \theta}+\frac{\rho u_r\cdot u_\theta}{r}&=-\frac{1}{r}\frac{\partial p}{\partial \theta}\\ +\frac{1}{Re_0}\left(\frac{\tau_{\theta z}}{\partial z}+\frac{1}{r^2}\frac{\partial(r^2\tau_{r\theta})}{\partial r}+\frac{1}{r}\frac{\partial \tau_{\theta\theta}}{\partial \theta}\right),&\end{aligned} \tag{3.8}$$

in which the viscous stress tensor is written as:

$$\begin{aligned}&\tau_{zz}=\mu\left(2\frac{\partial u_z}{\partial z}-\frac{2}{3}\Psi\right),\quad \tau_{zr}=\mu\left(\frac{\partial u_z}{\partial r}+\frac{\partial u_r}{\partial z}\right),\quad \tau_{z\theta}=\mu\left(\frac{1}{r}\frac{\partial u_z}{\partial \theta}+\frac{\partial u_\theta}{\partial z}\right),\\ &\tau_{rr}=\mu\left(2\frac{\partial u_r}{\partial r}-\frac{2}{3}\Psi\right),\quad \tau_{r\theta}=\mu\left(\frac{1}{r}\frac{\partial u_r}{\partial \theta}+r\frac{\partial}{\partial r}\Big(\frac{u_\theta}{r}\Big)\right),\quad \tau_{\theta\theta}=\mu\left(2\Big(\frac{1}{r}\frac{\partial u_\theta}{\partial \theta}+\frac{u_r}{r}\Big)-\frac{2}{3}\Psi\right).\end{aligned} \tag{3.9}$$

The divergence of velocity vector Ψ is written:

$$\Psi=\frac{\partial u_z}{\partial z}+\frac{1}{r}\frac{\partial\,(ru_r)}{\partial r}+\frac{1}{r}\frac{\partial u_\theta}{\partial \theta}, \tag{3.10}$$

The energy equations:

$$\begin{aligned}\frac{\partial \rho h}{\partial t}&=-\frac{\partial \rho u_z h}{\partial z}-\frac{\partial \rho u_r h}{\partial r}-\frac{1}{r}\frac{\partial \rho u_\theta h}{\partial \theta}\\ &+\frac{1}{Re_0 Pr_0}\left(\frac{\partial}{\partial z}\Big(\lambda\frac{\partial T}{\partial z}\Big)+\frac{1}{r}\frac{\partial}{\partial r}\Big(r\lambda\frac{\partial T}{\partial r}\Big)+\frac{1}{r}\frac{\partial}{\partial \theta}\Big(\lambda\frac{\partial T}{\partial \theta}\Big)\right).\end{aligned} \tag{3.11}$$

In the above equations, velocities, temperature and thermophysical properties are normalised by their inlet values:

$$u_i=\frac{u_i^*}{u_0^*},\quad T=\frac{T^*}{T_0^*},\quad \rho=\frac{\rho^*}{\rho_0},\quad \mu=\frac{\mu^*}{mu_0^*},\quad \lambda=\frac{\lambda^*}{\lambda_0^*}, \tag{3.12}$$

and lengths are normalised by the radius, the pressure is normalised by $\rho^* u_0^* u_0^*$, the enthalpy is shifted by a reference enthalpy h_{ref}^*:

$$z=\frac{z^*}{R^*},\quad r=\frac{r^*}{R^*},\quad r\theta=\frac{r^*\theta^*}{R^*},\quad p=\frac{p^*}{\rho_0^* u_0^* u_0^*},\quad h=\frac{h^*-h_{ref}^*}{c_{p,0}^* T_0^*} \tag{3.13}$$

The enthalpy at $T_0^* + 350K$ is chosen here as h_{ref}^*, so that the curve of $\rho h - h$ can be smooth, to increase the numerical stability of the simulation.

The velocities of flows concerned in the present study are in the order of 1 m/s, which is significantly lower than the sound speed of the order of 100 m/s. According to this, a low-March number approximation is applied to the full-compressible Navier-Stokes equations, with the acoustic interactions and compressibility effects eliminated. This is to avoid the severe time step restriction when the full compressible Navier-Stokes equations are solved. Such typical treatment was applied in some early DNS studies on supercritical fluid flows [11, 12, 78]. For the concerned incompressible flow, although density does not change with pressure, it varies with temperature, so that the time evolution of density is kept in the continuity equation.

In the simulations, thermophysical properties are enthalpy dependent, the NIST property database [35] is used to obtain these properties in the simulation. In CHAPSim, the variable groups ρu_z, ρu_r, ρu_θ, ρh (rather the u_z, u_r, u_θ and h) are solved. When the thermophysical properties are obtained by looking up the NIST database, the thermodynamic pressure is held constant (same as the operating pressure). With the pressure assumed constant [11, 12, 78], the thermophysical properties only change with enthalpy. The enthalpy is firstly obtained using a function $h = f(\rho h)$ obtained from the property database. Then the thermophysical properties (ρ, μ, c_p & λ) are obtained by their functions with the enthalpy. These new thermophysical properties will be used in the solution at the next time step.

The spacial and time discretizations will be introduced in the next two sections.

3.1.3 Spacial discretization scheme

In CHAPSim [131, 132, 133], finite difference scheme is used in spacial discretization, with structured mesh used. A staggered mesh is used for variable storage. That is, the velocities are defined at the cell faces that they are normal to, and the scalars such as the pressure, temperature, enthalpy and thermophysical properties are defined at the cell center. A simple diagram of the structured pipe mesh is shown in Fig. 3.1, with $4 \times 4 \times 8$ cells in streamwise, radial and spanwise direction, as an example to present the mesh scheme for cylindrical coordinate. For simulations in the present study, the mesh qualities are much finer than this.

A second order central difference scheme is used for the spacial discretization in the solver. The numerical expressions of the second convection term and the second diffusion term of the streamwise momentum equation (Eq. 3.6) are shown as examples for the spacial discretization.

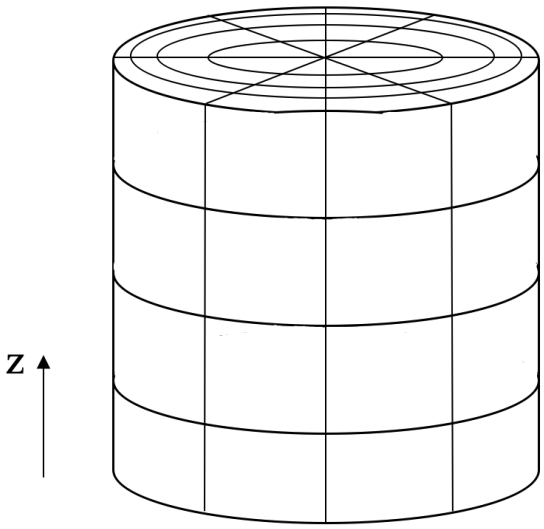

Figure 3.1: Diagram of the example structured pipe mesh in CHAPSim ($4 \times 4 \times 8$).

The first example is the numerical expression of $-\frac{1}{r}\frac{\partial r\rho u_r u_z}{\partial r}$ at location with streamwise and radial indexes i and j, i.e., $\Big(-\frac{1}{r}\frac{\partial r\rho u_r u_z}{\partial r}\Big)_{i,j}$. As shown in the $z-r$ cross section view of the mesh (Fig 3.2), the mesh is uniform at streamwise direction, and non-uniform at radial direction, as finer wall-normal mesh is needed near the wall. The streamwise velocity u_z and mass flux ρu_z (arrows with dash lines) are defined at the red faces that they are normal to, while the radial velocity u_r and mass flux ρu_r (arrows with solid lines) are defined at the blue faces that they are normal to. The streamwise momentum equation term $\Big(-\frac{1}{r}\frac{\partial r\rho u_r u_z}{\partial r}\Big)_{i,j}$, can be discretized using the central difference scheme:

$$\Big(-\frac{1}{r}\frac{\partial r\rho u_r u_z}{\partial r}\Big)_{i,j} = -\frac{1}{r_j}\frac{\big(r\rho u_r u_z\big)_{i,j'+1} - \big(r\rho u_r u_z\big)_{i,j'}}{\Delta r_j} \tag{3.14}$$

The two terms in the right hand side of Eq. 3.14 can be written as:

$$\begin{aligned}\big(r\rho u_r u_z\big)_{i,\,j'+1} &= r_{j'+1}\big(\rho u_r\big)_{i,\,j'+1}\; u_{z,\,i,\,j'+1}\\ \big(r\rho u_r u_z\big)_{i,\,j'} &= r_{j'}\big(\rho u_r\big)_{i,\,j'}\; u_{z,\,i,\,j'}\end{aligned} \tag{3.15}$$

in which $\big(\rho u_r\big)_{i,\,j'+1}$ and $\big(\rho u_r\big)_{i,\,j'}$ are calculated by averaging two neighbouring values:

$$\begin{aligned}\big(\rho u_r\big)_{i,\,j'+1} &= \frac{\big(\rho u_r\big)_{i',\,j'+1} + \big(\rho u_r\big)_{i'-1,\,j'+1}}{2}\\ \big(\rho u_r\big)_{i,\,j'} &= \frac{\big(\rho u_r\big)_{i',\,j'} + \big(\rho u_r\big)_{i'-1,\,j'}}{2}\end{aligned} \tag{3.16}$$

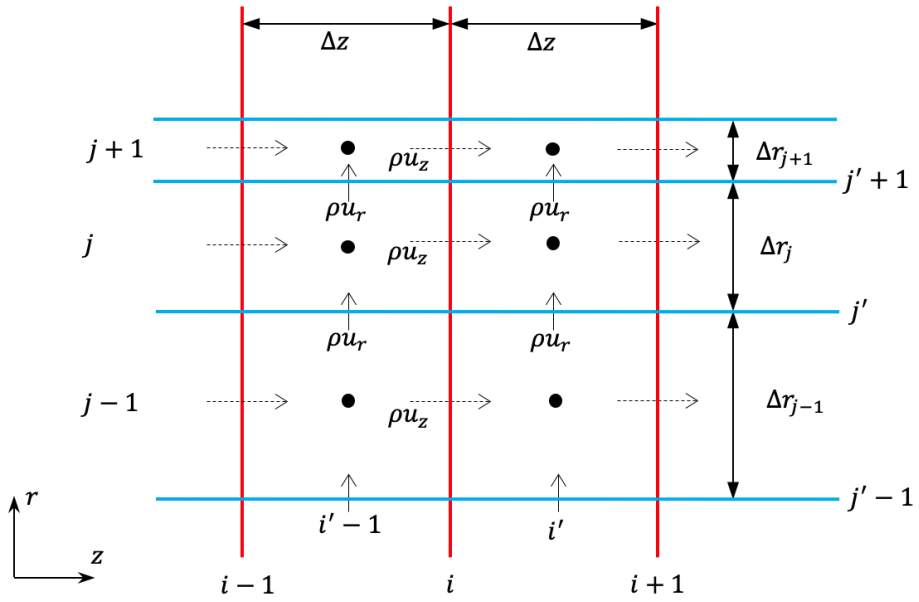

Figure 3.2: Staggered mesh grids and mass flux vectors.

And streamwise velocities $u_{z,\,i,\,j'+1}$ and $u_{z,\,i,\,j'}$ can be obtained by interpolation:

$$\begin{aligned} u_{z,\,i,\,j'+1} &= \big(1 - \frac{\Delta r_{j+1}}{\Delta r_j}\big) u_{z,\,i,\,,j+1} + \frac{\Delta r_{j+1}}{\Delta r_j} u_{z,\,i,\,j} \\ u_{z,\,i,\,j'} &= \big(1 - \frac{\Delta r_j}{\Delta r_{j-1}}\big) u_{z,\,i,\,,j} + \frac{\Delta r_j}{\Delta r_{j-1}} u_{z,\,i,\,j-1} \end{aligned} \tag{3.17}$$

Thus the numerical expression for $-\frac{1}{r}\frac{\partial r \rho u_r u_z}{\partial r}$ at the location $(i,\ j)$ is written:

$$\begin{aligned} &\Big(-\frac{1}{r}\frac{\partial r \rho u_r u_z}{\partial r}\Big)_{i,j} \\ &= -\frac{1}{2 r_j \Delta r_j}\Bigg(r_{j'+1}\Big((\rho u_r)_{i',\,j'+1} + (\rho u_r)_{i'-1,\,j'+1}\Big)\Big((1 - \frac{\Delta r_{j+1}}{\Delta r_j}) u_{z,\,i,\,,j+1} + \frac{\Delta r_{j+1}}{\Delta r_j} u_{z,\,i,\,j}\Big) \\ &\qquad - r_{j'}\Big((\rho u_r)_{i',\,j'} + (\rho u_r)_{i'-1,\,j'}\Big)\Big((1 - \frac{\Delta r_j}{\Delta r_{j-1}}) u_{z,\,i,\,,j} + \frac{\Delta r_j}{\Delta r_{j-1}} u_{z,\,i,\,j-1}\Big)\Bigg) \end{aligned} \tag{3.18}$$

The second example to show the spacial discretization is the numerical expression of the second diffusion term, i.e., $\frac{1}{Re_0}\frac{1}{r}\frac{\partial}{\partial r}\left[r \cdot \mu\left(\frac{\partial u_r}{\partial z} + \frac{\partial u_z}{\partial r}\right)\right]$ at the location $(i,\ j)$. This is still based on the mesh of the $z - r$ cross section in Fig. 3.2. The diffusion term can be discretized using the central difference scheme:

$$\left(\frac{1}{Re_0}\frac{1}{r}\frac{\partial}{\partial r}\Big(r\mu\big(\frac{\partial u_z}{\partial r} + \frac{\partial u_r}{\partial z}\big)\Big)\right)_{i,\,j} = \frac{1}{Re_0}\frac{1}{r_j}\frac{\Big(r\mu\big(\frac{\partial u_z}{\partial r} + \frac{\partial u_r}{\partial z}\big)\Big)_{i,\,j'+1} - \Big(r\mu\big(\frac{\partial u_z}{\partial r} + \frac{\partial u_r}{\partial z}\big)\Big)_{i,\,j'}}{\Delta r_j} \tag{3.19}$$

The two terms in the right hand side of Eq. 3.19 can be written:

$$\begin{aligned}\Big(r\mu\big(\frac{\partial u_z}{\partial r}+\frac{\partial u_r}{\partial z}\big)\Big)_{i,\,j'+1} &= r_{j'+1}\mu_{i,\,j'+1}\Big(\big(\frac{\partial u_z}{\partial r}\big)_{i,j'+1}+\big(\frac{\partial u_r}{\partial z}\big)_{i,j'+1}\Big)\\ \Big(r\mu\big(\frac{\partial u_z}{\partial r}+\frac{\partial u_r}{\partial z}\big)\Big)_{i,\,j'} &= r_{j'}\mu_{i,\,j'}\Big(\big(\frac{\partial u_z}{\partial r}\big)_{i,j'}+\big(\frac{\partial u_r}{\partial z}\big)_{i,j'}\Big)\end{aligned} \tag{3.20}$$

The velocity gradients in the right hand side of Eq. 3.20 can be discretized using central difference:

$$\begin{aligned}\Big(\frac{\partial u_z}{\partial r}\Big)_{i,j'+1} &= \frac{u_{z,\,i,\,j+1}-u_{z,\,i,\,j}}{r_{j+1}-r_j}\\ \Big(\frac{\partial u_z}{\partial r}\Big)_{i,j'} &= \frac{u_{z,\,i,\,j}-u_{z,\,i,\,j-1}}{r_j-r_{j-1}}\\ \Big(\frac{\partial u_r}{\partial z}\Big)_{i,j'+1} &= \frac{u_{r,\,i',\,j'+1}-u_{r,\,i'-1,\,j'+1}}{\Delta z}\\ \Big(\frac{\partial u_r}{\partial z}\Big)_{i,j'} &= \frac{u_{r,\,i',\,j'}-u_{r,\,i'-1,\,j'}}{\Delta z}\end{aligned} \tag{3.21}$$

Viscosities in the right hand side of Eq. 3.20 can be obtained using interpolation:

$$\begin{aligned}\mu_{i,\,j'+1} &= \Big(1-\frac{\Delta r_{j+1}}{\Delta r_j}\Big)\frac{\mu_{i',\,j+1}+\mu_{i'-1,\,j+1}}{2}+\frac{\Delta r_{j+1}}{\Delta r_j}\frac{\mu_{i',\,j}+\mu_{i'-1,\,j}}{2}\\ \mu_{i,\,j'} &= \Big(1-\frac{\Delta r_j}{\Delta r_{j-1}}\Big)\frac{\mu_{i',\,j}+\mu_{i'-1,\,j}}{2}+\frac{\Delta r_j}{\Delta r_{j-1}}\frac{\mu_{i',\,j-1}+\mu_{i'-1,\,j-1}}{2}\end{aligned} \tag{3.22}$$

Thus the discretized diffusion term at the location with index i, j is written:

$$\begin{aligned}&\left(\frac{1}{Re_0}\frac{1}{r}\frac{\partial}{\partial r}\Big(r\mu\big(\frac{\partial u_z}{\partial r}+\frac{\partial u_r}{\partial z}\big)\Big)\right)_{i,\,j}\\ &=\frac{1}{Re_0}\frac{1}{r_j\Delta r_j}\left(r_{j'+1}\mu_{i,\,j'+1}\Big(\frac{u_{z,\,i,\,j+1}-u_{z,\,i,\,j}}{r_{j+1}-r_j}+\frac{u_{r,\,i',\,j'+1}-u_{r,\,i'-1,\,j'+1}}{\Delta z}\Big)\right.\\ &\qquad\left.-r_{j'}\mu_{i,\,j'}\Big(\frac{u_{z,\,i,\,j}-u_{z,\,i,\,j-1}}{r_j-r_{j-1}}+\frac{u_{r,\,i',\,j'}-u_{r,\,i'-1,\,j'}}{\Delta z}\Big)\right)\end{aligned} \tag{3.23}$$

The temporal discretization is introduced in the next section.

3.1.4 Time discretization scheme

To simplify the description, G is used to represent the convection (non-linear) and diffusion (linear) terms at the right hand side of the momentum equations, and the momentum equations can be simply written:

$$\frac{\partial \rho u_i}{\partial t} = G-\frac{\partial p}{\partial x_i}-\rho g \tag{3.24}$$

In the version of CHAPSim used in the present study, third order Runge-Kutta explicit scheme is used for the time discretization [134, 135]. For each time step, local $(\rho u)_i$ is updated in three stages. We assume the current time step is n, and the next time step is $n+1$, and ρu_i at time step n is $(\rho u_i)^n$.
Stage 1:

$$\frac{(\rho u_i)^{n,1} - (\rho u_i)^n}{\Delta t} = a^1 G^n + b^1 G^{n-1} + (a^1 + b^1)(-\frac{\partial p^n}{\partial x_i} - \rho^n g) \tag{3.25}$$

Stage 2:

$$\frac{(\rho u_i)^{n,2} - (\rho u_i)^{n,1}}{\Delta t} = a^2 G^{n,1} + b^2 G^n + (a^2 + b^2)(-\frac{\partial p^{n,1}}{\partial x_i} - \rho^{n,1} g) \tag{3.26}$$

Stage 3:

$$\frac{(\rho u_i)^{n,3} - (\rho u_i)^{n,2}}{\Delta t} = a^3 G^{n,2} + b^3 G^{n,1} + (a^3 + b^3)(-\frac{\partial p^{n,2}}{\partial x_i} - \rho^{n,2} g) \tag{3.27}$$

For each stages, ρu_i is approaching the value at the next time step, and the updated value at the third stage is the final result:

$$(\rho u_i)^{n,3} = (\rho u_i)^{n+1} \tag{3.28}$$

The Runge-Kutta coefficient in the above equations:

$$\begin{aligned} a^1 = \frac{8}{15}, \quad a^2 = \frac{5}{12}, \quad a^3 = \frac{3}{4} \\ b^1 = 0, \quad b^2 = -\frac{17}{60}, \quad b^3 = -\frac{5}{12} \end{aligned} \tag{3.29}$$

The same time discretization is applied for the energy equation, to obtain ρh at the next time step. For every location, the solution of the energy and momentum equation is half a time step staggered with each other. The energy equation is solved at time n, while the momentum equation is solved at time $n+\frac{1}{2}$: at time n, the energy equation is first solved using the flow and thermophysical property field at time n to obtain $(\rho h)^{n,1}$. Then h and thermophysical properties are recalculated, and these new properties are used when solving the momentum equation, then $(\rho u_i)^{n,1}$ is obtained. After these two steps, the resolved flow and thermal field satisfy the momentum and energy equations. To also satisfy the continuity equation, the pressure and mass flux corrections are obtained by solving the Poisson equation, which is introduced in the next section.

The time step Δt is chosen according to the Courant–Friedrichs–Lewy (CFL) condition [136]. For explicit time discretization scheme, the CFL number is defined as:

$$C = \frac{u_{max}\Delta t}{\Delta x_{min}}. \tag{3.30}$$

For $C = 1$, Δt represent the duration that the fluid with the maximum velocity travel through the smallest mesh grid. The stability condition for explicit scheme is $C < 1$. In the current study, we chose a time step with $C \approx 0.44$, which is sufficient for the stable condition of the explicit Runge-Kutta scheme.

3.1.5 Pressure-velocity coupling scheme

For each location of a 3-D pipe flow, five variables at the new time step are calculated, i.e., ρu_z, ρu_r, ρu_θ, ρh, and p, with five governing equations (Eq. 3.5-3.11). There are transport equations for the first four variables, and their time evolutions can be obtained numerically, however, there is no transport equation for the pressure. To obtain the pressure at the next time step using the continuity equation, pressure-velocity coupling scheme is needed. The pressure-velocity coupling scheme in CHAPSim is similar to the SIMPLE scheme [137].

For each time step, the obtained instantaneous flow and thermal fields should satisfy all the governing equations (Eq. 3.5-3.11). For each stage of the 3rd order Runge-Kutta process, new ρh, thermophysical properties and ρu_i are obtained using the 'old' pressure to produce a prediction in equation 3.25-3.27. After each RK step, the Poisson equation [138] is solved to correct the mass flux and pressure, so as to satisfy the the mass conservation. The process of calculating the mass flux and pressure corrections in 3rd order Runge-Kutta process for cylindrical coordinate is shown below with the first stage of the Runge-Kutta process taken as an example. The streamwise mass flux and pressure are corrected as written:

$$(\rho u_z)^{n,1} = (\rho u_z)_t^{n,1} + \Delta(\rho u_i) \qquad p^{n,1} = p_t^{n,1} + \Delta p \tag{3.31}$$

in which $(\rho u_z)_t^{n,1}$ is the temporary mass flux obtained using Eq. 3.25:

$$\frac{(\rho u_z)_t^{n,1} - (\rho u_z)^n}{\Delta t} = a^1 G^n + b^1 G^{n-1} + (a^1 + b^1)(-\frac{\partial p^n}{\partial z} - \rho^n g) \tag{3.32}$$

And the corrected mass flux and pressure should satisfy the momentum equation (Eq. 3.24):

$$\frac{(\rho u_z)_t^{n,1} + \Delta(\rho u_z) - (\rho u_z)^n}{\Delta t} = a^1 G^n + b^1 G^{n-1} + (a^1 + b^1)(-\frac{\partial p^n + \Delta p}{\partial z} - \rho^n g) \tag{3.33}$$

And the following equation can be obtained by combining Eq. 3.32 & 3.33:

$$\frac{\Delta(\rho u_z)}{\Delta t} = -\frac{\partial \Delta p}{\partial z} \tag{3.34}$$

Then the two sides are differentiated in z direction:

$$\frac{1}{\Delta t}\frac{\partial \Delta(\rho u_z)}{\partial z} = -\frac{\partial^2 \Delta p}{\partial z^2} \tag{3.35}$$

These calculations are also done to the radial and spanwise momentum equations, then Eq. 3.36 is obtained by combining the three equations:

$$\frac{1}{\Delta t}\Big(\frac{\partial \Delta(\rho u_z)}{\partial z} + \frac{1}{r}\frac{\partial \Delta(r\rho u_r)}{\partial r} + \frac{1}{r}\frac{\partial \Delta(\rho u_\theta)}{\partial \theta}\Big) = \frac{\partial^2 \Delta p}{\partial z^2} + \frac{\partial^2 \Delta p}{\partial r^2} + \frac{1}{r^2}\frac{\partial^2 \Delta p}{\partial \theta} \tag{3.36}$$

In which the correction of mass flux is the difference between the prediction and the corrected values:

$$\begin{aligned} \Delta(\rho u_z) &= (\rho u_z)^{n,1} - (\rho u_z)_t^{n,1} \\ \Delta(r\rho u_r) &= (r\rho u_r)^{n,1} - (r\rho u_r)_t^{n,1} \\ \Delta(\rho u_\theta) &= (\rho u_\theta)^{n,1} - (\rho u_\theta)_t^{n,1} \end{aligned} \tag{3.37}$$

We want the corrected values $(\rho u_z)^{n,1}$, $(r\rho u_r)^{n,1}$ and $(\rho u_\theta)^{n,1}$ satisfy the continuity equation (Eq. 3.5), that is:

$$\frac{\partial (\rho u_z)^{n,1}}{\partial z} + \frac{1}{r}\frac{\partial (r\rho u_r)^{n,1}}{\partial r} + \frac{1}{r}\frac{\partial (\rho u_\theta)^{n,1}}{\partial \theta} = -\frac{\partial \rho}{\partial t} \tag{3.38}$$

By substituting Eq. 3.37 & 3.38 to Eq. 3.36, Eq. 3.39 is acquired:

$$\frac{1}{\Delta t}\Big(\frac{\partial (\rho u_z)_t^{n,1}}{\partial z} + \frac{1}{r}\frac{\partial (r\rho u_r)_t^{n,1}}{\partial r} + \frac{1}{r}\frac{\partial (\rho u_\theta)_t^{n,1}}{\partial \theta} - \frac{\partial \rho}{\partial t}\Big) = \frac{\partial^2 \Delta p}{\partial z^2} + \frac{\partial^2 \Delta p}{\partial r^2} + \frac{1}{r^2}\frac{\partial^2 \Delta p}{\partial \theta} \tag{3.39}$$

The left hand side of Eq. 3.39 is the source term of the Poisson equation, and it can be calculated using the predicted mass flux and the time derivative of density. The right hand side of Eq. 3.39 is the Laplacian of the pressure correction. Δp field can be obtained using the Poisson equation solver, then with this, streamwise mass flux correction $\Delta(\rho u_z)$ can be obtained using Eq. 3.34. Similar to this, corrections for radial and spanwise mass fluxes, i.e., $\Delta(\rho u_r)$, $\Delta(\rho u_\theta)$ can be obtained. With the mass flux and pressure field corrected, the solution satisfies all the governing equations.

3.1.6 Implement of conjugate heat transfer in CHAPSim

The above sections introduce the numerical scheme implemented in CHAPSim, to calculate the time evolution of flow and thermal fields of the fluid domain, from a

given initial field and boundary conditions. To consider thermal conduction of the solid pipe, additional structured mesh for the solid domain is added for the wall of the pipe. For the solid domain, the governing equation is simpler, the momentum equations and the continuity equation are redundant and therefore eliminated, as there is no motion in the solid. Only the energy equation is solved, as shown in Eq. 3.40, without the convection.

$$\rho c_p \frac{\partial T}{\partial t} = \frac{1}{Re_0 Pr_0}\left(\frac{\partial}{\partial z}\left(\lambda\frac{\partial T}{\partial z}\right) + \frac{1}{r}\frac{\partial}{\partial r}\left(r\lambda\frac{\partial T}{\partial r}\right) + \frac{1}{r}\frac{\partial}{\partial \theta}\left(\lambda\frac{\partial T}{\partial \theta}\right) + S_h\right), \tag{3.40}$$

in which S_h is the non-dimensional solid heating source:

$$S_h = S_h^* \frac{R^{*2}}{\lambda_0^* T_0^*} \tag{3.41}$$

Fig. 3.3a shows the sketch of a simple structured mesh of the fluid and solid domains, and the fluid-solid interface is coloured by red. The number of cells at spanwise and streamwise directions are the same in the fluid and solid mesh. The radial mesh for fluid is non-uniform, while that for the solid is uniform.

In simulations without considering the solid wall, the fluid domain is heated by the imposed thermal boundary condition at the wall (uniform heat flux). With conjugate heat transfer considered, the solid is heated by a volumetric heating source, which is conducted into the fluid via the solid-fluid interface. At each time step, local heat flux through the fluid-solid interface is obtained using information in both the solid and fluid domain from last time step as explained below. This heat flux will then be imposed as the thermal boundary condition for both the fluid and solid domains, to ensure the energy conservation between the two.

Figure 3.3b is the $z-r$ cross section view of the solid and fluid meshes near the interface, the temperature and thermal conductivity of both the solid and fluid are defined at the cell center. The interface is specified by the red dash line. The temperature and thermal conductivity at the first solid cell are T_s and λ_s, and those for the first fluid cell are T_f and λ_f. The blue arrow denotes the heat flux that leaves the first solid cell, the red arrow denotes the heat flux received by the first fluid cell, and the green arrow denotes the heat flux through the fluid-solid interface. Assume the temperature and thermal conductivity at the interface are T_w and λ_w. The three heat fluxes can be expressed numerically:

$$q_s = \lambda_s \frac{T_s - T_w}{\Delta y_s/2}, \qquad q_f = \lambda_f \frac{T_w - T_f}{\Delta y_f/2}, \qquad q_w = \lambda_w \frac{T_s - T_f}{(\Delta y_f + \Delta y_s)/2} \tag{3.42}$$

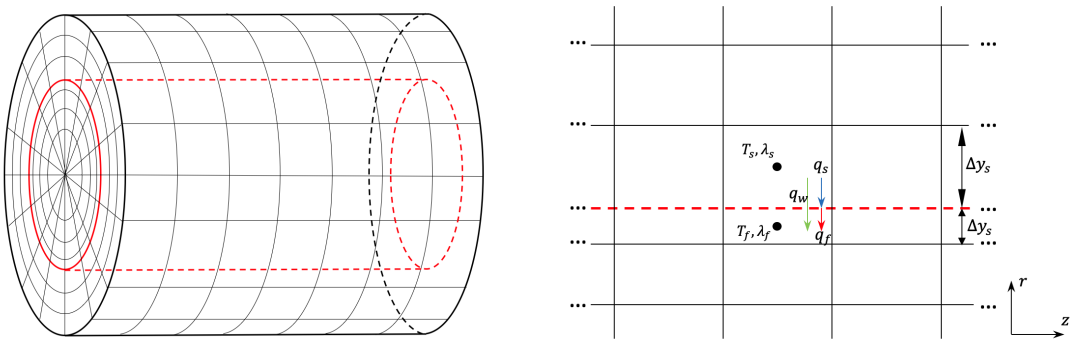

(a) a (b) b

Figure 3.3: Example structured mesh for fluid and solid domains, with fluid mesh size of $7 \times 4 \times 16$ (streamwise $\times$ radial $\times$ spanwise), and solid mesh size of $7 \times 4 \times 16$ (a), and the $z - r$ cross section view of the mesh near the fluid-solid interface.

To satisfy the energy conservation between the solid and fluid domain (assuming no axial conduction in both domains and additionally the convection in the fluid domain is also negligible), the three heat fluxes are the same:

$$\begin{gathered} q_s = q_f = q_w \\ \lambda_s \frac{T_s - T_w}{\Delta y_s/2} = \lambda_f \frac{T_w - T_f}{\Delta y_f/2} = \lambda_w \frac{T_s - T_f}{(\Delta y_f + \Delta y_s)/2} \end{gathered} \tag{3.43}$$

The expression of λ_w can be obtained by rearranging Eq. 3.43:

$$\lambda_w = \frac{(\Delta y_s + \Delta y_f)\lambda_s \lambda_f}{\lambda_f \Delta y_s + \lambda_s \Delta y_f} \tag{3.44}$$

And q_w can be written:

$$q_w = \frac{2\lambda_s \lambda_f (T_s - T_f)}{\lambda_f \Delta y_s + \lambda_s \Delta y_f} \tag{3.45}$$

Thus the local wall heat flux can be explicitly calculated using the temperatures and thermal conductivities of the first cell next to the interface. For each time step, q_w is calculated using the information from last time step, then it is imposed to both the fluid and solid domain as thermal boundary conditions. By doing this, the continuity of heat flux and temperature through the fluid-solid interface, and the energy conservation between the two domains can be ensured.

3.2 Validation of CHAPSim

To validate the capability of CHAPSim in solving the turbulent pipe flow, an isothermal turbulent pipe flow chosen from the simulations done by Khoury et al. [139]

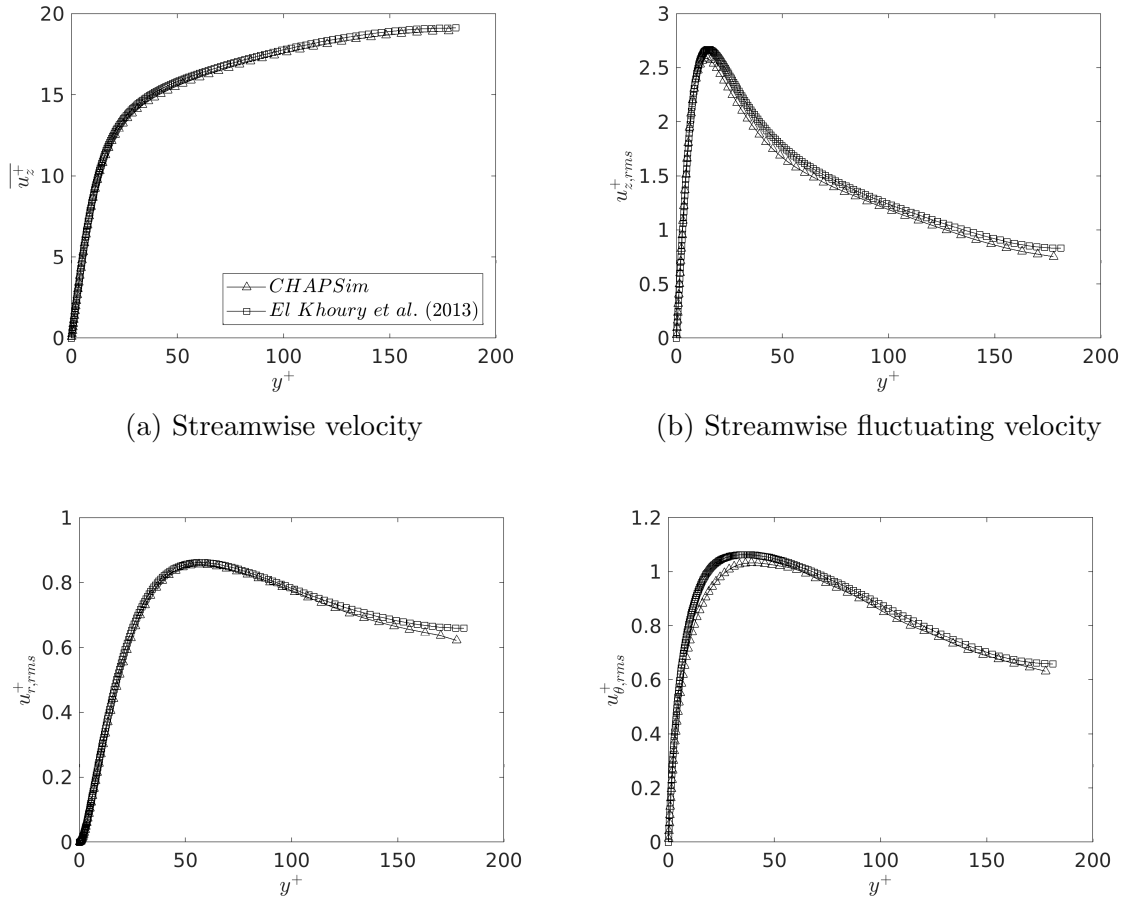

(a) Streamwise velocity

(b) Streamwise fluctuating velocity

(c) Radial fluctuating velocity

(d) Spanwise fluctuating velocity

Figure 3.4: Comparisons of streamwise velocities, root mean square of fluctuating velocities at streamwise, radial, and spanwise directions of a isothermal pipe flow ($Re_\tau = 180$), results obtained by code CHAPSim and Khoury et al.

for a DNS database, was reproduced by CHAPSim. It is a fully developed flow at $Re_\tau = 180$ ($Re_D \approx 5300$), with constant thermophysical properties. For the mesh at radial direction, Δy^+ range of the simulation done by Khoury et al is $0.14 - 3.86$, in our simulation of CHAPSim, the mesh is slightly coarser, Δy^+ range is $0.17 - 7.42$. Comparisons between the two, including the time averaged streamwise velocity $\overline{u}_z^+$, and the root mean square of fluctuating velocities u_{rms}^+ components in three directions agree very well with those from the above reference (figure 3.4). For additional validation, please see the study of Seddighi [131].

The validation of CHAPSim in terms of solving SCP fluid flows is shown next. Two cases with strong heating and buoyancy from the simulations of Bae et al. [11] (case B and D) have been chosen to be reproduced by CHAPSim. These two cases have also been reproduced by Nemati et al. [12], using another DNS code, the results

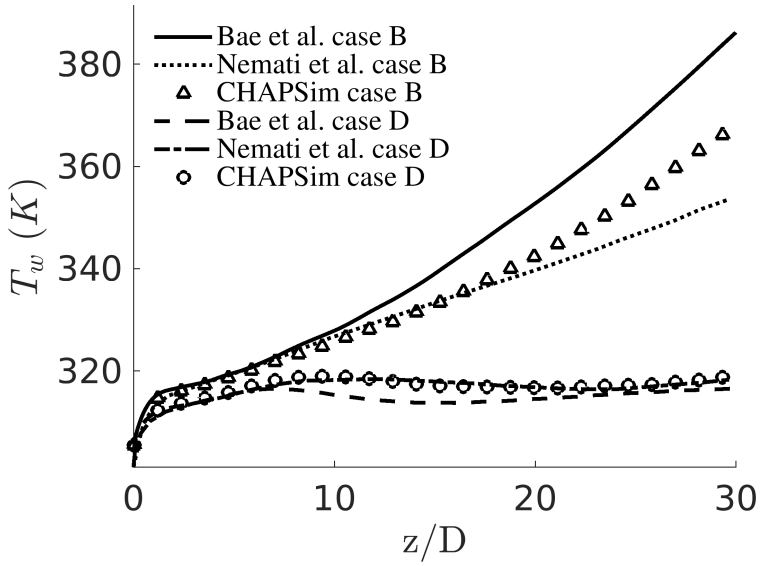

Figure 3.5: Comparison of wall temperature predictions obtained by CHAPSim against results obtained by Bae et al. and Nemati et al.

of which are also presented here for code-to-code comparison. These two cases are upward pipe flows of carbon dioxide at $8MPa$ with uniform wall heat fluxes, and with $Re_D = 5400$ and $T_0^* = 301.15K$ ($T_{pc}^* = 307.85K$). The pipe diameter of case B is $1mm$, and that of case D is $3mm$. The wall heat flux for case B is $61.74kW/m^2$, and that for case D is $20.85kW/m^2$. For the simulations of cases B and D carried out by Bae et al. [11], the mesh size was $769 \times 69 \times 129$ in streamwise, radial and spanwise direction, and the reproduction done by [12] had a mesh size of $768 \times 68 \times 128$, while the cases reproduced by CHAPSim has a the mesh of $768 \times 64 \times 128$.

The comparison of the predictions of the wall temperature is shown in Fig. 3.5. It can be seen that the results of the Nemati et al's and ours agree very well for both cases, whereas both are somewhat lower than those of Bae et al's for case B. Fig. 3.6 show further comparison between the turbulent shear stresses predicted by Nemati et al. and using our mesh at a number of streamwise locations. The agreement is again good in both cases.

3.3 Favre-averaged transport equation for Reynolds normal stresses

The transport equations for the Reynolds normal stresses will be used in the discussion of the current study. The derivation of the transport equation of $\widetilde{u_z'' u_z''}$ is shown herein

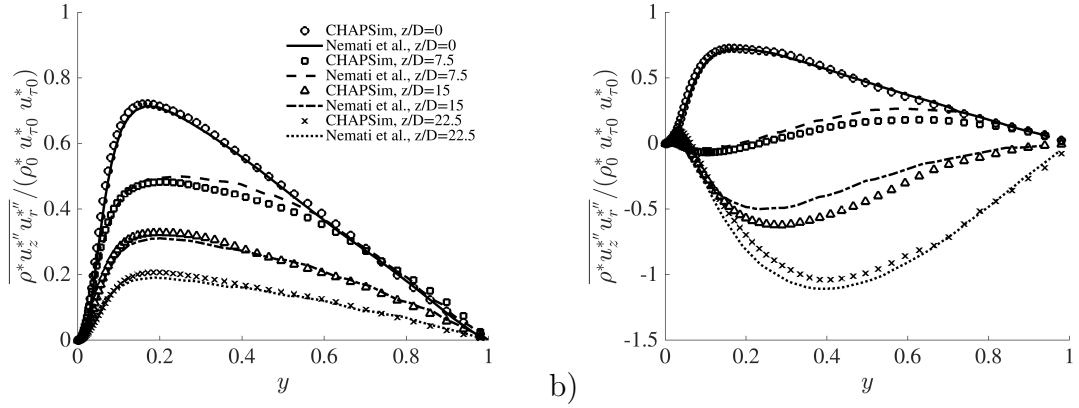

Figure 3.6: Turbulent shear stresses in Bae et al's (a) case B and (b) case D - comparison between predictions of Nemati et al. [12] and those of CHAPSim.

as an example, which begins from the streamwise momentum equation, assume all the right-hand-side terms of the momentum equation are η_z, the momentum equation can be simplified:

$$\frac{\partial \rho u_z}{\partial t} = \eta_z \tag{3.46}$$

The transport equation of $\widetilde{u_z'' u_z''}$ can be obtained by multiplying both sides of equation 3.46 by $2u_z''$:

$$\overline{2u_z'' \frac{\partial \rho u_z}{\partial t}} = \overline{2u_z'' \eta_z} \tag{3.47}$$

Equation 3.47 can be expanded by substituting $\widetilde{u}_i + u_i''$ to u_i and rearranging each terms. The expansion of the left-hand-side can be written:

$$\begin{aligned} \overline{2u_z'' \frac{\partial \rho u_z}{\partial t}} &= \overline{2u_z'' \rho \frac{\partial u_z}{\partial t}} + \overline{2u_z'' u_z \frac{\partial \rho}{\partial t}} \\ &= \overline{2u_z'' \rho \frac{\partial}{\partial t}\left(\widetilde{u}_z + u_z''\right)} + \overline{2u_z'' u_z \frac{\partial \rho}{\partial t}} \\ &= \underbrace{\frac{\partial \overline{\rho} \widetilde{u_z'' u_z''}}{\partial t}}_{\text{Time evolution}} \underbrace{\overline{u_z'' u_z'' \frac{\partial \rho}{\partial t}} - 2\overline{u_z u_z'' \frac{\partial \rho}{\partial t}}}_{\text{Additional terms, A1}} \end{aligned} \tag{3.48}$$

$$
\begin{aligned}
\overline{-2u_z''\frac{\partial \rho u_z u_z}{\partial z}} &= -2\overline{\rho u_z u_z''\frac{\partial u_z}{\partial z}} - 2\overline{u_z u_z''\frac{\partial \rho u_z}{\partial z}} \\
&= -2\overline{\rho\Big((\widetilde{u}_z + u_z'')\frac{\partial(\widetilde{u}_z + u_z'')}{\partial z}u_z''\Big)} - 2\overline{u_z u_z''\frac{\partial \rho u_z}{\partial z}} \\
&= -2\overline{\rho u_z'' u_z''}\frac{\partial \widetilde{u}_z}{\partial z} - \overline{\frac{\partial \rho u_z'' u_z'' \widetilde{u}_z}{\partial z}} - \overline{u_z'' u_z''\frac{\partial \rho \widetilde{u}_z}{\partial z}} - \overline{\frac{\partial \rho u_z'' u_z'' u_z''}{\partial z}} - \overline{u_z'' u_z''\frac{\partial \rho u_z''}{\partial z}} \\
&= \underbrace{-2\overline{\rho u_z'' u_z''}\frac{\partial \widetilde{u}_z}{\partial z}}_{\text{Production}} \underbrace{-\frac{\partial \overline{\rho u_z'' u_z'' \widetilde{u}_z}}{\partial z}}_{\text{Convection}} \underbrace{-\frac{\partial \overline{\rho u_z'' u_z'' u_z''}}{\partial z}}_{\text{Turbulent transport}} \underbrace{+\Big(\overline{u_z'' u_z''\frac{\partial \rho u_z}{\partial z}} - 2\overline{u_z u_z''\frac{\partial \rho u_z}{\partial z}}\Big)}_{\text{Additional terms, A2}}
\end{aligned}
\tag{3.49}
$$

$$
\begin{aligned}
\frac{2}{Re_0}\overline{\frac{u_z''}{r}\frac{\partial \tau_{zz}}{\partial z}} &= 2\overline{u_z''}\frac{\partial \overline{\tau_{zz}}}{\partial z} + 2\overline{u_z''\frac{\partial \tau_{zz}'}{\partial z}} \\
&= \underbrace{2\overline{u_z''}\frac{\partial \overline{\tau_{zz}}}{\partial z}}_{\text{Additional term}} \underbrace{+2\frac{\partial \overline{u_z''\tau_{zz}'}}{\partial z}}_{\substack{\text{Viscous} \\ \text{diffusion}}} \underbrace{-2\overline{\tau_{zz}'\frac{\partial u_z''}{\partial z}}}_{\text{Dissipation}}
\end{aligned}
\tag{3.50}
$$

As shown in Eq. 3.6, η_z contains three convection terms, three diffusion terms, a pressure gradient term and a gravity term. To present the expansion of $\overline{2u_z''\eta_z}$, the expansions of the streamwise convection and streamwise diffusion terms are taken as examples, shown in Eq. 3.49 & 3.50. The expansion of the streamwise convection term contains the shear production, convection, turbulent transport terms of Reynolds normal stress $\widetilde{u_z'' u_z''}$ and an additional terms $A2$, the expansion of the radial viscous diffusion term contains the viscous diffusion and dissipation terms of $\widetilde{u_z'' u_z''}$, and an additional term. The expansion of other convection and viscous diffusion terms are similar, shown in Eq. 3.51 to 3.54.

$$
\begin{aligned}
&-2\overline{\frac{u_z''}{r}\frac{\partial r\rho u_z u_r}{\partial r}} \\
&= \underbrace{-2\overline{\rho u_z'' u_r''}\frac{\partial \widetilde{u}_z}{\partial r}}_{\text{Production}} \underbrace{-\frac{1}{r}\frac{\partial r\overline{\rho u_z'' u_z''}\widetilde{u}_r}{\partial r}}_{\text{Convection}} \underbrace{-\frac{1}{r}\frac{\partial r\overline{\rho u_z'' u_z'' u_r''}}{\partial r}}_{\text{Turbulent transport}} \underbrace{+\overline{u_z'' u_z''}\frac{1}{r}\frac{\partial r\rho u_r}{\partial r} - 2\overline{u_z u_z''}\frac{1}{r}\frac{\partial r\rho u_r}{\partial r}}_{\text{Additional terms, A3}}
\end{aligned}
\tag{3.51}
$$

$$
\begin{aligned}
&-2\overline{\frac{u_z''}{r}\frac{\partial \rho u_\theta u_z}{\partial \theta}} \\
&= \underbrace{-\frac{2}{r}\overline{\rho u_z'' u_\theta''}\frac{\partial \widetilde{u}_z}{\partial \theta}}_{\text{Production}} \underbrace{-\frac{1}{r}\frac{\partial \overline{\rho u_z'' u_z'' \widetilde{u}_\theta}}{\partial \theta}}_{\text{Convection}} \underbrace{-\frac{1}{r}\frac{\partial \overline{\rho u_z'' u_z'' u_\theta''}}{\partial \theta}}_{\text{Turbulent transport}} \underbrace{+\overline{u_z'' u_z''}\frac{1}{r}\frac{\partial \rho u_\theta}{\partial \theta} - 2\overline{u_z u_z''}\frac{1}{r}\frac{\partial \rho u_\theta}{\partial \theta}}_{\text{Additional term, A4}}
\end{aligned}
\tag{3.52}
$$

$$
\frac{2}{Re_0}\overline{\frac{u_z''}{r}\frac{\partial r\tau_{rz}}{\partial r}} = \underbrace{\frac{2}{Re_0}\frac{\overline{u_z''}}{r}\frac{\partial r\overline{\tau_{zr}}}{\partial r}}_{\text{Additional term}} \underbrace{+\frac{2}{Re_0}\frac{1}{r}\frac{\partial r\overline{u_z''\tau_{zr}'}}{\partial r}}_{\text{Viscous diffusion}} \underbrace{-\frac{2}{Re_0}\overline{\tau_{zr}'\frac{\partial u_z''}{\partial r}}}_{\text{Dissipation}}
\tag{3.53}
$$

$$\frac{2}{Re_0}\overline{\frac{u_z''}{r}\frac{\partial\tau_{z\theta}}{\partial\theta}} = \underbrace{\frac{2}{Re_0}\frac{\overline{u_z''}}{r}\frac{\partial\overline{\tau_{z\theta}}}{\partial\theta}}_{\text{Additional term}} \underbrace{+\frac{2}{Re_0}\frac{1}{r}\frac{\partial\overline{u_z''\tau_{z\theta}'}}{\partial\theta}}_{\text{Viscous diffusion}} \underbrace{-\frac{2}{Re_0}\overline{\tau_{z\theta}'\frac{\partial u_z''}{\partial\theta}}}_{\text{Dissipation}} \tag{3.54}$$

The expansion of the pressure gradient term includes the buoyancy production, pressure diffusion and pressure strain terms, shown in Eq. 3.55.

$$\begin{aligned}
-2\overline{u_z''\frac{\partial p}{\partial z}} &= -2\overline{\left(\frac{\partial\overline{p}}{\partial z}u_z'' + \frac{\partial p'}{\partial z}u_z''\right)} \\
&= -2\left(\frac{\partial\overline{p}}{\partial z}\overline{u_z''} + \frac{\partial\overline{p'u_z''}}{\partial z} - \overline{p'\frac{\partial u_z''}{\partial z}}\right) \\
&= \underbrace{-2\frac{\partial\overline{p}}{\partial z}\overline{u_z''}}_{\substack{\text{Buoyancy}\\\text{production}}} \underbrace{-2\frac{\partial\overline{p'u_z''}}{\partial z}}_{\substack{\text{Pressure}\\\text{diffusion}}} \underbrace{+2\overline{p'\frac{\partial u_z''}{\partial z}}}_{\substack{\text{Pressure}\\\text{strain}}},
\end{aligned} \tag{3.55}$$

while the expansion of the gravity term is zero:

$$\begin{aligned}
-2\overline{u_z''\frac{\rho}{Fr_0^2}} &= -\frac{2}{Fr_0^2}\overline{\rho u_z''} \\
&= -\frac{2}{Fr_0^2}\overline{\rho(u_z - \widetilde{u_z})} \\
&= 0
\end{aligned} \tag{3.56}$$

The four additional terms in the expansions of the time evolution and three convection terms can be cancelled using the continuity equation (Eq. 3.5):

$$\begin{aligned}
&\underbrace{-\left(\overline{u_z''u_z''\frac{\partial\rho}{\partial t}} - 2\overline{u_zu_z''\frac{\partial\rho}{\partial t}}\right)}_{\text{Additional terms, A1}} \underbrace{+\left(\overline{u_z''u_z''\frac{\partial\rho u_z}{\partial z}} - 2\overline{u_zu_z''\frac{\partial\rho u_z}{\partial z}}\right)}_{\text{Additional terms, A2}} \\
&\underbrace{+\left(\overline{u_z''u_z''\frac{1}{r}\frac{\partial r\rho u_r}{\partial r}} - 2\overline{u_zu_z''\frac{1}{r}\frac{\partial r\rho u_r}{\partial r}}\right)}_{\text{Additional terms, A3}} \underbrace{+\left(\overline{u_z''u_z''\frac{1}{r}\frac{\partial\rho u_\theta}{\partial\theta}} - 2\overline{u_zu_z''\frac{1}{r}\frac{\partial\rho u_\theta}{\partial\theta}}\right)}_{\text{Additional term, A4}} \\
&= 0
\end{aligned} \tag{3.57}$$

The transport equation for $\widetilde{u_z''u_z''}$ is obtained by expanding and rearranging Eq. 3.47, which is the combination of Eq. 3.48 to 3.56. The full expression is shown in Eq. 3.58.

$$
\begin{aligned}
\underbrace{\frac{\partial \overline{\rho}\widetilde{u_z''u_z''}}{\partial t}}_{\substack{\text{Time}\\ \text{evolution}}} =& \underbrace{-2\overline{\rho u_z''u_z''}\frac{\partial \widetilde{u}_z}{\partial z} - 2\overline{\rho u_z''u_r''}\frac{\partial \widetilde{u}_z}{\partial r} - \frac{2}{r}\overline{\rho u_z''u_\theta''}\frac{\partial \widetilde{u}_z}{\partial \theta}}_{\text{Production}} \\
& \underbrace{-\frac{\partial \overline{\rho u_z''u_z''}\widetilde{u}_z}{\partial z} - \frac{1}{r}\frac{\partial r\overline{\rho u_z''u_z''}\widetilde{u}_r}{\partial r} - \frac{1}{r}\frac{\partial \overline{\rho u_z''u_z''}\widetilde{u}_\theta}{\partial \theta}}_{\text{Convection}} \\
& \underbrace{-\frac{\partial \overline{\rho u_z''u_z''u_z''}}{\partial z} - \frac{1}{r}\frac{\partial r\overline{\rho u_z''u_z''u_r''}}{\partial r} - \frac{1}{r}\frac{\partial \overline{\rho u_z''u_z''u_\theta''}}{\partial \theta}}_{\text{Turbulent transport}} \underbrace{-2\frac{\partial \overline{p}}{\partial z}\overline{u_z''}}_{\substack{\text{Buoyancy}\\ \text{production}}} \underbrace{-2\frac{\partial \overline{p'u_z''}}{\partial z}}_{\substack{\text{Pressure}\\ \text{diffusion}}} \underbrace{+2\overline{p'\frac{\partial u_z''}{\partial z}}}_{\substack{\text{Pressure}\\ \text{strain}}} \\
& \underbrace{+\frac{1}{Re_0}\left(2\frac{\partial \overline{u_z''\tau_{zz}'}}{\partial z} + \frac{2}{r}\frac{\partial r\overline{u_z''\tau_{zr}'}}{\partial r} + \frac{2}{r}\frac{\partial \overline{u_z''\tau_{r\theta}'}}{\partial \theta}\right)}_{\text{Viscous diffusion}} \\
& \underbrace{+\frac{1}{Re_0}\left(-2\overline{\tau_{zz}'\frac{\partial u_z''}{\partial z}} - 2\overline{\tau_{zr}'\frac{\partial u_z''}{\partial r}} - \frac{2}{r}\overline{\tau_{z\theta}'\frac{\partial u_z''}{\partial \theta}}\right)}_{\text{Dissipation}} \\
& \underbrace{+\frac{1}{Re_0}\left(2\overline{u_z''}\frac{\partial \overline{\tau_{zz}}}{\partial z} + \frac{2}{r}\overline{u_z''}\frac{\partial r\overline{\tau_{zr}}}{\partial r} + \frac{2}{r}\overline{u_z''}\frac{\partial \overline{\tau_{z\theta}}}{\partial \theta}\right)}_{\text{Additional terms due to velocity fluctuation}}
\end{aligned}
\tag{3.58}
$$

The derivation of the transport equation of Reynolds normal stress $\overline{u_z'u_z'}$ is similar to that of $\widetilde{u_z''u_z''}$, except the expansion of the pressure gradient and gravity term. The expansions of the pressure gradient term and gravity term for the transport equation of $\overline{u_z'u_z'}$ are shown in Eq. 3.59 & 3.56.

$$
\begin{aligned}
-2\overline{u_z'\frac{\partial p}{\partial z}} &= -2\overline{u_z'\Big(\frac{\partial \overline{p}}{\partial z} + \frac{\partial p'}{\partial z}\Big)} \\
&= -2\overline{u_z'}\frac{\partial \overline{p}}{\partial z} - 2\overline{u_z'\frac{\partial p'}{\partial z}} \\
&= \underbrace{-2\frac{\partial \overline{p'u_z'}}{\partial z}}_{\text{Pressure diffusion}} \underbrace{+2\overline{p'\frac{\partial u_z'}{\partial z}}}_{\text{Pressure strain}}
\end{aligned}
\tag{3.59}
$$

$$
\begin{aligned}
-2\overline{u_z'\frac{\rho}{Fr_0^2}} &= -\frac{2}{Fr_0^2}\overline{\rho u_z'} \\
&= -\frac{2}{Fr_0^2}\overline{u_z'\big(\overline{\rho} + \rho'\big)} \\
&= \underbrace{-\frac{2\overline{\rho' u_z'}}{Fr_0^2}}_{\substack{\text{Buoyancy}\\ \text{production}}}
\end{aligned}
\tag{3.60}
$$

3.4 Post-processing algorithm

3.4.1 Time and spanwise average

After running the simulations, post-processing is carried out to visualise and present the data for further discussions, which are based on two types of result data in the current study, i.e., statistical and instantaneous data. During DNS simulations, instantaneous flow and thermal fields are resolved at each time step, which are the chaotic instantaneous data, e.g., $u_z(z, r, \theta, t)$, $\rho(z, r, \theta, t)$, etc. Herein average can be done in the homogeneous dimensions, e.g., spanwide direction of vertical pipe flows, transverse direction of transversely periodic channel flows, time in the stationary flows, etc, to filter out the oscillations and obtain the mean flow/thermal features over a larger scale.

The flows of interest in the current study are vertical pipe flows after reaching stationary state, therefore a mixed average at spanwise direction and time can be implemented. The time average of variable ϕ at spacial coordinate $\xi = (z_1, r_1, \theta_1)$ between time index m and n is defined as:

$$\begin{aligned}\overline{\phi}^t(z_1, r_1, \theta_1) &= \frac{\phi(z_1, r_1, \theta_1, t(m)) + \phi(z_1, r_1, \theta_1, t(m+1)) + ... + \phi(z_1, r_1, \theta_1, t(n))}{(n-m)+1} \\ &= \frac{\sum_{i=m}^{n} \phi_\xi^i}{(n-m)+1},\end{aligned} \tag{3.61}$$

in which "m" is the time index after the flow reaching stationary state, $(n-m)+1$ is the time step count from time index m to n. A sketch of time development of example variable ϕ is shown in Fig. 3.7, with a transient stage (1 to m) at the begin, and finally reaches stationary state ($i > m$). Time averaged ϕ_ξ between time step m and n is specified by the red line.

Similarly, spanwise average of variable ϕ (at location (z_1, r_1) and time t_1) from spanwise coordinate index l to k is defined as:

$$\begin{aligned}\overline{\phi}^\theta(z_1, r_1, t_1) &= \frac{\phi(z_1, r_1, \theta(l), t_1) + \phi(z_1, r_1, \theta(l+1), t_1) + ... + \phi(z_1, r_1, \theta(k), t_1)}{(k-l)+1} \\ &= \frac{\sum_{j=l}^{k} \phi_{(z_1, r_1, j)}^{t1}}{(k-l)+1},\end{aligned} \tag{3.62}$$

The flows in the current study are homogeneous at spanwise direction and time, spanwise and time average is implemented to obtain statistically averaged flow/thermal

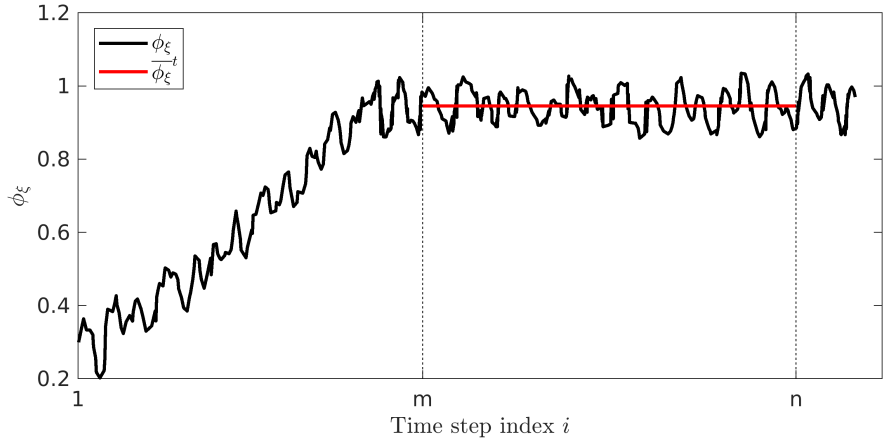

Figure 3.7: Sketch of time development of variable ϕ at location ξ, and its time averaged value at stationary state.

fields:

$$\overline{\overline{\phi}^{\theta}}^{t}(z,r) = \frac{\sum_{i=m}^{n}\sum_{j=l}^{k}\phi(z,r,\theta(j),t(i))}{(m-n+1)(k-l+1)}, \tag{3.63}$$

and the fluctuation of ϕ at location (z,r) and time t is defined as the difference between the local instantaneous and averaged values:

$$\phi'(z,r,t) = \phi(z,r,\theta,t) - \overline{\overline{\phi}^{\theta}}^{t}(z,r) \tag{3.64}$$

The root mean square of fluctuations of ϕ is normally used to characterise the level of fluctuation between two time points, which is defined as:

$$\phi'_{rms}(z,r) = \sqrt{\frac{\phi'^2(z,r,t(m)) + \phi'^2(z,r,t(m+1)) + ... + \phi'^2(z,r,t(n))}{n-m+1}} \tag{3.65}$$

The properties of Reynolds-average are also satisfied in the time and spanwise average values, as they are both obtained by the summation of sampling points divided by the counting number, the properties are listed in Eq. 3.66.

$$\begin{aligned} \overline{\alpha'} &= 0 \\ \overline{\alpha+\beta} &= \overline{\alpha} + \overline{\beta} \\ \overline{\alpha\beta} &= \overline{(\alpha+\alpha')(\beta+\beta')} \end{aligned} \tag{3.66}$$

In the current study, all average calculations are time and spanwise average, to simplify the discussions, $\overline{\overline{\phi}^{\theta}}^{t}$ is named averaged ϕ in later discussions, and it is denoted by an over-bar, as it has the same properties as the Reynolds-averaged:

$$\overline{\phi} = \overline{\overline{\phi}^{\theta}}^{t} \tag{3.67}$$

3.4.2 Calculation of key variables

The calculations of some key parameters/variables are presented herein as references.

Firstly, the definition of bulk enthalpy is shown below, in which $\int_R^0 \overline{\rho u_z} r dr$ is the mass flow rate at each cross section.

$$h_b = \frac{\int_0^R \overline{\rho u_z h} r dr}{\int_0^R \overline{\rho u_z} r dr} \tag{3.68}$$

In the current post-processing, the above calculation is implemented numerically:

$$h_b(z) = \frac{\sum_{j=1}^{n} \overline{\rho u_z h}\Big|_{z,r(j)} r(j)\Delta r(j)}{\sum_{j=1}^{n} \overline{\rho u_z}\Big|_{z,r(j)} r(j)\Delta r(j)}, \tag{3.69}$$

in which j is the index of radial mesh cells, n is the total number of radial mesh cells. With h_b obtained, the bulk temperatures, bulk thermophysical properties can be obtained by looking up their functions against the enthalpy in the property database:

$$T_b = f_1(h_b), \quad \rho_b = f_2(h_b), \quad \mu_b = f_3(h_b), \; etc \tag{3.70}$$

With the bulk density, the bulk streamwise velocity can be calculated as follow (analytical and numerical expressions):

$$\begin{aligned} u_{z,b} &= \frac{G_b}{\rho_b} = \frac{\int_0^R \overline{\rho u_z} r dr}{\rho_b \pi R^2} \\ u_{z,b}(z) &= \frac{G_b(z)}{\rho_b(z)} = \frac{\sum_{j=1}^{n} \overline{\rho u_z}\Big|_{z,r(j)} r(j)\Delta r(j)}{\rho_b(z)\pi R^2}, \end{aligned} \tag{3.71}$$

in which G_b is the bulk mass flux at different locations. With $u_{z,b}$ and the bulk thermophysical properties obtained, the bulk Reynolds number and Prandtl number can be calculated as follow:

$$Re_b = \frac{u^*_{z,b} D^*}{\nu^*_b} \quad Pr_b = \frac{c^*_{p,b}\mu^*_b}{\lambda^*_b} \tag{3.72}$$

In CHAPSim, various Reynolds averaged of the instantaneous quantities (e.g., u_i, p, ρ) are calculated and output. In post-processing, the statistics of the fluctuations of these quantities (e.g., $u_i^{'}$, $u_i^{''}$, $p^{'}$, $p^{''}$) are calculated using the CHAPSim output statistics of the instantaneous quantities as explained below. In the derivations and discussions of the transport equations (momentum, energy, turbulent kinetic energy,

etc), some of the terms include $\overline{\mu u_i^{''}}$, $\overline{\mu u_i^{''} u_j^{''}}$ or $\overline{\rho u_i^{''}}$, $\overline{\rho u_i^{''} u_j^{''}}$ and $\overline{\rho u_i^{''} u_j^{''} u_k^{''}}$, etc. They are obtained by substituting $u_i^{''}$ with $u_z - \widetilde{u}_i$ then rearranging the equations. The calculations of these terms using the output statistical (time and spanwise averaged) data are presented below:

$$\overline{u_i^{''}} = \overline{u_i - \widetilde{u}_i} = \overline{u_i} - \widetilde{u}_i \tag{3.73}$$

$$\overline{u_i^{''} u_j^{''}} = \overline{u_i u_j - u_i \widetilde{u}_j - \widetilde{u}_i u_j + \widetilde{u}_i \widetilde{u}_j} = \overline{u_i u_j} - \overline{u_i}\widetilde{u}_j - \widetilde{u}_i \overline{u_j} + \widetilde{u}_i \widetilde{u}_j \tag{3.74}$$

$$\overline{\mu u_i^{''}} = \overline{\mu u_z - \mu \widetilde{u_z}} = \overline{\mu u_z} - \overline{\mu}\widetilde{u}_z \tag{3.75}$$

$$\overline{\mu u_i^{''} u_j^{''}} = \overline{\mu u_i u_j - \mu u_j \widetilde{u}_i - \mu u_i \widetilde{u}_j + \mu \widetilde{u}_i \widetilde{u}_j} = \overline{\mu u_i u_j} - \overline{\mu u_i}\widetilde{u}_j - \overline{\mu u_j}\widetilde{u}_i + \overline{\mu}\widetilde{u}_i \widetilde{u}_j \tag{3.76}$$

$$\overline{\rho u_i^{''}} = \overline{\rho u_i + \rho \widetilde{u}_i} = 0 \tag{3.77}$$

$$\overline{\rho u_i^{''} u_j^{''}} = \overline{\rho u_i u_j - \rho u_i \widetilde{u}_j - \rho u_j \widetilde{u}_i + \rho \widetilde{u}_i \widetilde{u}_j} = \overline{\rho u_i u_j} - \frac{\overline{\rho u_i}\ \overline{\rho u_j}}{\overline{\rho}} \tag{3.78}$$

$$\overline{\rho u_i^{''} u_j^{''} u_k^{''}} = \overline{\rho (u_i - \widetilde{u}_i)(u_j - \widetilde{u}_j)(u_k - \widetilde{u}_k)}$$
$$= \overline{\rho u_i u_j u_k} - \overline{\rho u_i u_j}\widetilde{u}_k - \overline{\rho u_i u_k}\widetilde{u}_j - \overline{\rho u_j u_k}\widetilde{u}_i + \overline{\rho u_i}\widetilde{u}_j \widetilde{u}_k + \overline{\rho u_j}\widetilde{u}_i \widetilde{u}_k + \overline{\rho u_k}\widetilde{u}_i \widetilde{u}_j - \overline{\rho}\widetilde{u}_i \widetilde{u}_j \widetilde{u}_k \tag{3.79}$$

$$\overline{\phi' u_i^{''}} = \overline{\phi u_i - \overline{\phi} u_i - \phi \widetilde{u}_i + \overline{\phi}\widetilde{u}_i} = \overline{\phi' u_i'} \tag{3.80}$$

Chapter 4

Effects of buoyancy and thermophysical property variations on the spatial development of the flow of supercritical carbon dioxide

In this chapter, the flow and heat transfer behaviours of fluids at supercritical pressure are studied using direct numerical simulations (DNS), in which one or more thermal properties are artificially frozen to discern the various physical mechanisms from each other so as to better understand the complex phenomena. The studied vertical pipe flow is illustrated in Fig. 1.2 in Chapter 1. Further understandings of the mechanism of laminarisation and recovery affected by the buoyancy and thermophysical property variations are achieved. Comparisons between cases with different effects will be presented, and it shows that buoyancy effect is the key effect in terms of forming the flipped velocity and turbulent shear stress profiles. The mechanism of viscosity variation and buoyancy effects causing the laminarization is presented through the variations of momentum balance in these cases. Most part of this chapter is published in He et al. [6].

4.1 Simulation case settings

According to the reviewed studies, the factors that influence the heat transfer behaviours and turbulence characteristics for a vertical flow of supercritical fluid are mainly the buoyancy and the variations of thermophysical properties. The latter can be split into: the acceleration caused by density reduction and the variations of viscosity (and other properties). The main purpose of the current study is to investigate the contributions of these effects, both their individual and combined effects. The

particular interest is the response of the momentum budgets and and its influences on turbulence reduction and regeneration. The second purpose is to further understand the variations of turbulent structures during this process, and the quantification of the body force effect with the developed correlations. For this purpose, several simulations of upward pipe flows of supercritical carbon dioxide are designed and listed in table 4.1, to isolate or eliminate some of the effects of interest for investigation.

Table 4.1: Simulation case setting

Case	Flow condition	Convection type
A	Supercritical CO_2 (base case)	Mixed convection
B	Supercritical CO_2 (forced convection)	Forced convection
C	Supercritical CO_2 (only density varies)	Mixed convection
D	Supercritical CO_2 (only density constant)	Forced convection
E	Supercritical CO_2 (Boussinesq approximation)	Mixed convection
F	Supercritical CO_2 (isothermal)	Forced convection

Case A is a reference case for an upward pipe flow of supercritical carbon dioxide, with strong and non-linear variations of thermophysical properties under strong heating. Case B is the same as case A, except that the gravity (and hence the buoyancy) is removed, that is, the flow is forced convection. In case C, all the thermophysical properties except density, are constant. Consequently, in this case, only the effects linked to density variations are included (buoyancy and acceleration effects). In case D density is made constant but all other thermophysical properties are enthalpy dependent as in case A. Case E is based on the Boussinesq assumption, that is, all properties are constant except the density in the gravity which is dependent on the enthalpy. Case F is another reference case with all the thermophysical properties set constant.

The numerical implementation of the concerned upward pipe flows is illustrated in Fig. 4.1. The mesh size for all cases is $1024 \times 64 \times 128$ (streamwise$\times$radial$\times$spanwise), the mesh resolutions are shown in table 4.2, those from Bae et al. [11] and Nemati et al. [12] are also included as references. It is an empirical guideline to use the viscous scale (y^+, z^+...) to measure the mesh size in numerical simulations. With the mesh matching the guideline, turbulent motions at Kolmogorov scale are captured in the simulation. They also ensure the streaks to be reasonably well resolved. Compared with the two reference studies, the mesh resolutions in the current study are sufficient to capture the small scale turbulent activities. A mesh sensitivity test is conducted to assess the grid independence of the current mesh size. In the test, the results resolved

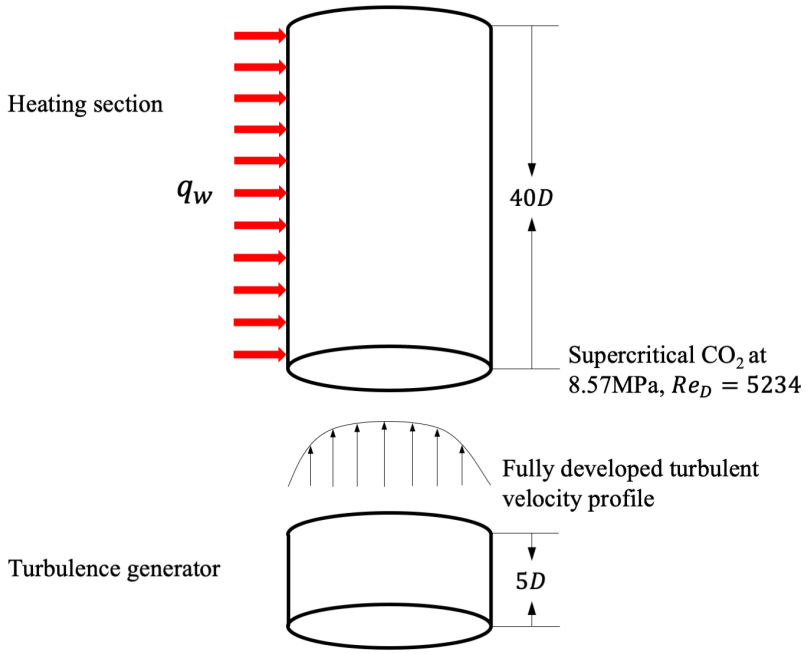

Figure 4.1: Schematic diagram of the heated vertical pipe flow of supercritical CO_2.

using the current mesh and a refined mesh is compared, and they agree well (shown in the appendix).

A turbulence generator with a length of 5D is set to provide fully-developed turbulent velocity profile for the heating section. The turbulence generator is axially periodic, and it solves the isothermal flow with the set Reynolds number. It has the same mesh resolution as the heating section, i.e., $128 \times 64 \times 128$ in this case. The turbulence generator (or a developing section in experiments) is a common approach in the studies of supercritical fluid flows [11, 12, 78, 76] to avoid the influences of the initial flow development. The turbulence generator is also included in the other simulations in this thesis (those in Chapter 5, 6 & 7), to guarantee a fully-developed velocity profile at the inlet of the heating section.

The same inlet and boundary conditions are imposed for all the cases. The inlet pseudocritical pressure is $8.57MPa$, and the inlet temperature is $301.15K$, and for comparison, the critical temperature at this pressure is 310.9 K. The inlet Reynolds number is 2617 (or 5234 based on the diameter), and the inlet Prandtl number is 2.86. A uniform heat flux of $30870W/m^2$ is applied on the wall.

Table 4.2: Mesh resolutions

Case	Δy^+	$\Delta r\theta^+$	Δz^+
A	$0.17 \sim 7.46$	8.91	14.19
B	$0.16 \sim 7.42$	7.56	12.04
C	$0.16 \sim 7.20$	8.61	13.70
D	$0.18 \sim 7.90$	9.44	15.04
E	$0.17 \sim 7.66$	9.15	14.57
F	$0.17 \sim 7.44$	8.89	14.15
Bae et al.	$0.18 \sim 5.34$	9.14	14.55
Nemati et al.	$0.55 \sim 4.31$	3.93	6.25

4.2 Results and discussions

The investigation and discussions of the changes caused by the buoyancy, acceleration due to density reduction and viscosity variation effects are presented in this section. Section 4.2.1 is the overview of the only physical case (case A), while section 4.2.2 is the comparisons between cases with different effects. These two sections shows the buoyancy is the key effect that causing the laminarization and recovery, the viscosity variation effect also has certain contribution to the changes of turbulence and heat transfer, while the acceleration effect is relatively minor. The mechanisms of the flow modification due to viscosity variation and buoyancy effects are discussed in section 4.2.3 and 4.2.4 respectively.

4.2.1 Overview of flow and heat transfer behaviours in a supercritical CO_2 flow (case A)

In this section, the flow and heat transfer feature of case A will be presented and discussed. This is the only case in which a physical pipe flow of SCP CO_2 under heating is simulated. In all other cases, there are always some selected effects that are eliminated or isolated artificially. Early experimental and numerical studies indicate that in an upward pipe flow of SCP fluids, heat transfer deterioration often takes place, which is then followed by recovery. Such heat transfer behaviour can be largely related to flow laminarisation followed by turbulence regeneration. The result of case A simulation exhibits such behaviours. Figure 4.2a shows the streamwise development of wall and bulk temperatures. The pseudo-critical temperature is about $310.9K$. After a short distance from the inlet, the wall temperature is above the critical value, while the bulk temperature is still below that. Right after the inlet, the Nusselt number reduces rapidly in a short distance, while the wall temperature increases rapidly. This

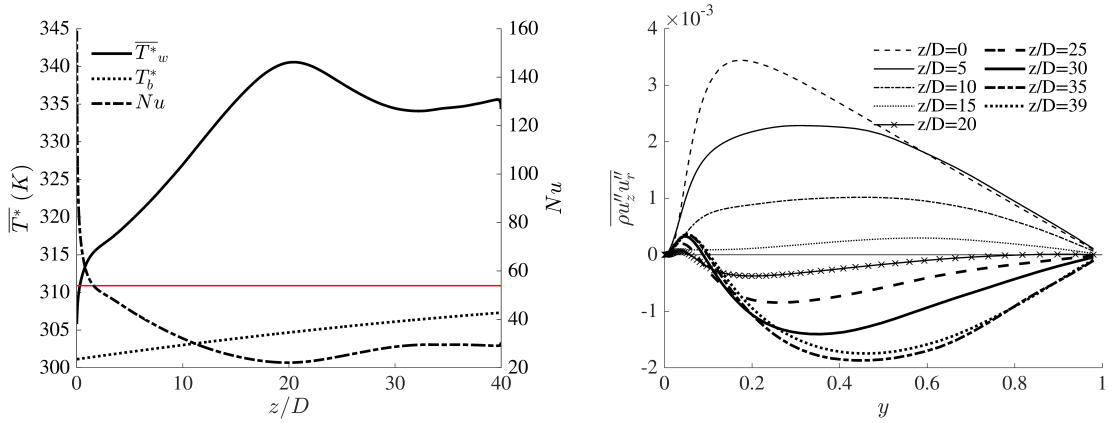

Figure 4.2: Streamwise distributions of wall temperature, bulk temperature, and Nusselt number in case A (a), pseudo-critical temperature is marked by a red solid line. Radial profiles of Favre averaged normalised turbulent shear stress $\overline{\rho u_z'' u_r''}$ at several streamwise locations in case A (b).

is due to the entrance effect, where a thermal boundary layer is formed, which grows rapidly in this region. After the entrance region, the Nu continues reducing, and T_w increases, all at a rate slower than before. T_w reaches the peak at about the same streamwise location as Nu reaches the minimum value, at around $z/D = 20$. After this location, Nu starts to increase and heat transfer improves, thus the wall temperature reduces even as the bulk temperature is still growing linearly. These trends agree with those observed from early experimental and numerical studies. The radial profiles of Favre averaged turbulent shear stress at several streamwise locations are plotted in figure 4.2b. Before $z/D = 15$, the turbulent shear stress reduces with distance from the entrance. At around $z/D = 15$, turbulent shear stress is nearly zero at most part, which suggests that the flow is fully laminarised at this location. This is strongly linked to the heat transfer deterioration. After $z/D = 15$, the magnitude of turbulent shear stress rises again, but in most part, the turbulent shear stress is negative, different from that of the isothermal pipe flow. Under this condition, turbulence is mostly produced in a region away from the wall where the velocity gradient has changed sign due to the M-shape as shown below.

The radial profiles of streamwise velocity, temperature, density, and dynamic viscosity at several streamwise locations are shown in figure 4.3. The development of the streamwise velocity is key to the variations of turbulence and heat transfer. At the inlet, the velocity profile is one of a typical fully-developed turbulent profile. Due to a number of reasons to be discussed later, the near-wall fluid accelerates, and that

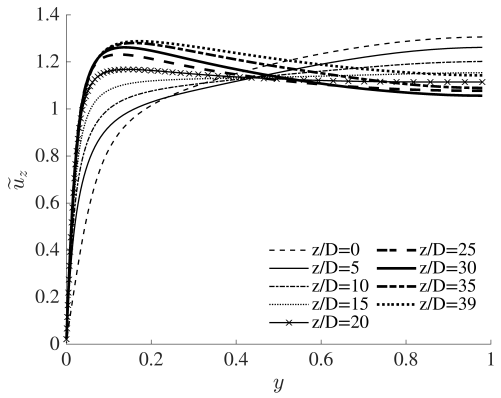

(a) Streamwise velocity

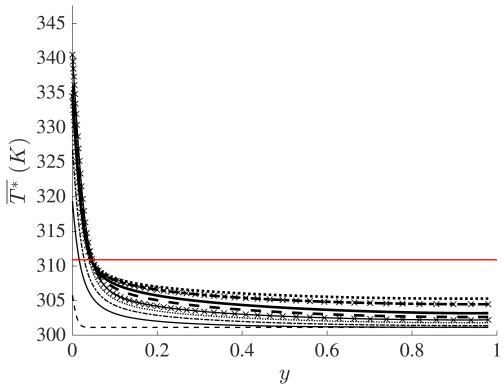

(b) Temperature

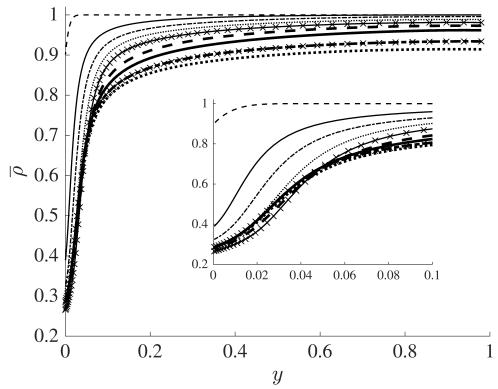

(c) Density

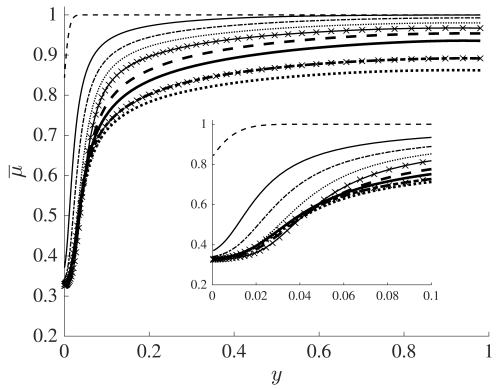

(d) Dynamic viscosity

Figure 4.3: Radial profiles of streamwise velocity (a), temperature (b), density (c), and dynamic viscosity (d) in case A

in the core decelerates relatively. As a result, the velocity profiles become increasingly flattened in the core of the flow. This continues until $z/D = 15$, where the wall-normal velocity gradient is nearly zero everywhere in the flow, except for very close to the wall. The near-wall acceleration and main stream deceleration continue, further downstream, and the velocity profile flips from a flat profile into an "M" shaped one. Here a negative velocity gradient is shown in the central region of the "M" shape profile. Such a flow behaviour is caused by the combination of a number of reasons, including the buoyancy effect, the acceleration due to the density reduction (both local and bulk acceleration), and the rapid and non-uniform (in radial direction) reduction of dynamic viscosity, which will be discussed in the next section.

Also shown in figure 4.3 are the temperature profiles which show that a thermal boundary layer is rapidly developed after the inlet, causing strong variations of temperature near the wall. In the core of the flow, the temperature gradually increases axially, but the radial gradient does not change much. The wall temperature is above the critical temperature, but in the core ($y > 0.1$), the temperature is lower than the pseudo-critical value, which indicates there are significant variations of thermophysical properties between the near-wall and mainstream locations. The profiles of averaged density (figure 4.3c) and dynamic viscosity (figure 4.3d) clearly support this observation. The variations of density and dynamic viscosity profiles are very similar to each other with strong changes in the near-wall region. The lowest density near the wall has dropped to nearly 30% of that at the inlet and the dynamic viscosity has dropped to nearly 35% of that at the inlet. For the properties at the center of the pipe, the reduction is less severe. The density at the outlet is about 90% of the inlet density, and the viscosity is about 85% of the inlet value. The large radial gradient of density causes a strong radially non-uniform buoyancy. The large radial gradient of the dynamic viscosity is another factor, which influences the shear stress especially at the near-wall region.

With such significant changes of thermophysical properties in case A, the flow and heat transfer behaviour is drastically different from that of the isothermal flow, or even that of a heated flow below the pseudocritical pressure.

4.2.2 Comparison of cases with different effects

The overall influences of different thermo-properties and buoyancy on the flow and turbulence are discussed in this section by studying the simulation cases, in which various combinations of property changes are omitted to isolate certain physical phenomenon. The streamwise velocity profiles of cases B to E are shown in figure 4.4,

which can be compared with that in Case A in figure 4.3a. It can be clearly seen that the behaviours of the mean velocity show two strikingly different responses. First, the velocity profiles in Cases B and D are similar to each other but different from those in other cases. In Case D (constant density), the profile becomes flatter in the core of the flow within a short distance ($\Delta z/D < 5$) after the flow is heated and then remains largely unchanged afterwards. This initial change is due to the reduction of viscosity close to the wall as a result of the increase in fluid temperature there. This will be further discussed in the next section. In Case B (forced convection), the velocity profile also becomes flatter in a short distance from the start of the heating. Following this, it increases continuously with distance downstream, though the shape appears to be largely maintained. This increase in bulk velocity is clearly due to the decrease in density as the bulk fluid temperature increases.

On the other hand, the developments of the velocity profiles in Cases C and E are very similar in a qualitative way, to that in Case A, in which the profile first becomes increasingly more flattened. Then at a later stage, it gradually switches to an M-shaped profile, which becomes increasingly more prominent downstream. Noting that these three flows are the only cases with buoyancy, this result implies that buoyancy causes the strongest distortion in velocity distribution and is a necessary condition for the switch of the profile to a M-shape (at least under the conditions studied). Additionally, the switch of the shape of the profile occurs first in Case A ($z/D \sim 15$), then Case C ($z/D \sim 20$) and then Case D ($z/D \sim 30$), which suggests that other effects (viscosity variation and flow acceleration due to the expansion of the fluid) all contribute to the distortion of the velocity profile.

The streamwise developments of the turbulent shear stress for cases B, C, D, and E are shown in figure 4.5. Considering the similarities of streamwise velocity, it is now not surprising to note that the developments in cases B and D are similar to each other but different from those of cases C and E. In Case B, $\overline{\rho u_z'' u_r''}$ reduces gradually over the distance of $z/D < 15$, after which it appears to have reached some equilibrium and remains largely unchanged afterwards. It is somewhat surprising that $\overline{\rho u_z'' u_r''}$ in Case D also reduces significantly in the initial section ($z/D < 15$) which is only slightly smaller than that in Case B, even though the velocity profile in this case does not change following the initial adjustment ($z/D < 5D$). The above result appears to suggest that the variation of viscosity has a stronger effect on turbulence than that of flow acceleration. In cases C and E, $\overline{\rho u_z'' u_r''}$ undergoes the full process of progressively reduction initially, followed by a near all zero distribution over the whole cross-section (full laminarisation) and finally recovery, as in Case A.

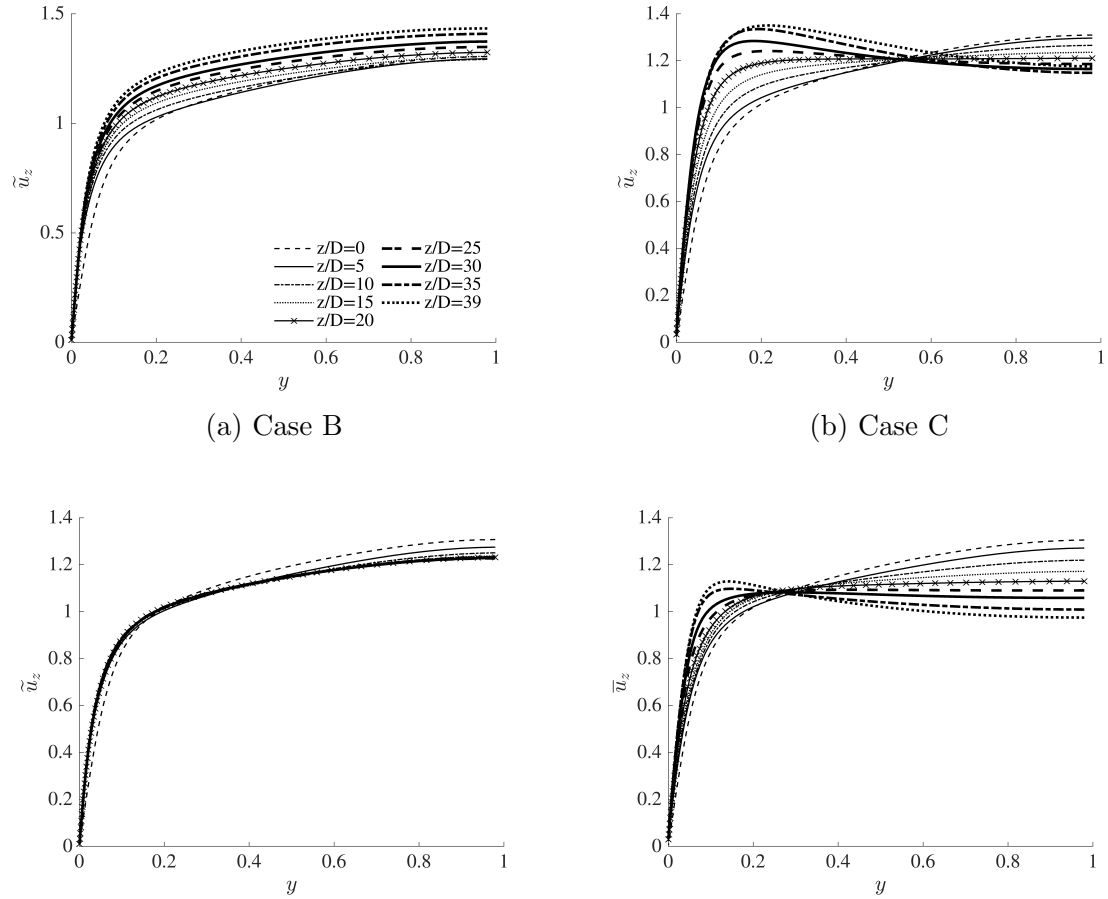

(a) Case B

(b) Case C

(c) Case D

(d) Case E

Figure 4.4: Radial profiles of Favre averaged streamwise velocities of case B (a), case C (b), case D (c), and case E (d).

The location where the flow is fully laminarised approximately corresponds to the location where the velocity profile switches to the M-shape. In addition, the negative value of the $\overline{\rho u_z'' u_r''}$ at the final stage is highest in Case A, then C and then D, again implies that the viscosity and flow acceleration all have an influence on the flow and turbulence, even though the buoyancy is clearly dominating. These results imply that the simulation using Boussineq approximate is able to capture the key phenomenon, including turbulence reduction and heat transfer deterioration, but quantitatively the predictions may suffer from significant uncertainties, predicting a late heat transfer deterioration, for example, which may be undesirable in some applications.

The profiles of the root mean square of the three fluctuating velocity components are shown in figures 4.6 to 4.8. Again the variations of these quantities in Cases B and D are similar to each other, and those in Cases A, C and E are similar. The effects

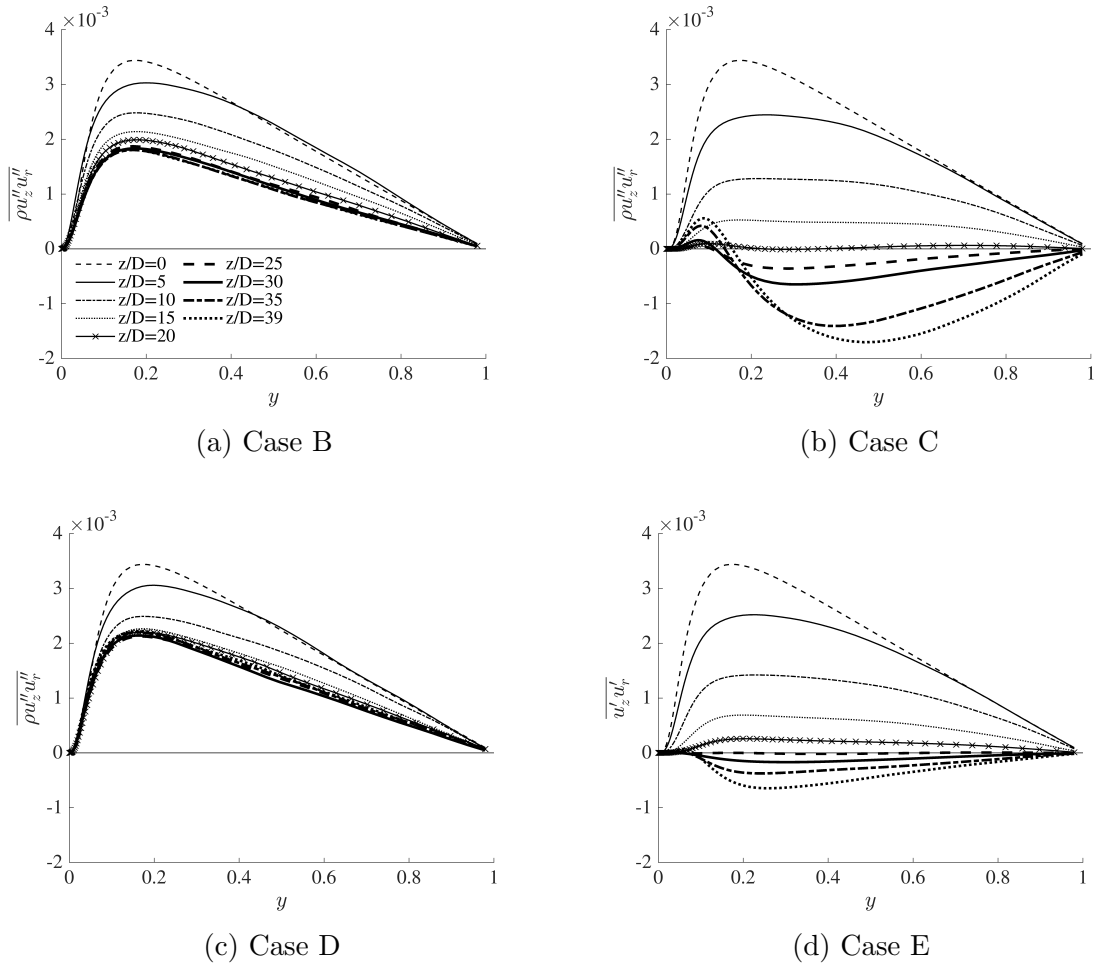

(a) Case B

(b) Case C

(c) Case D

(d) Case E

Figure 4.5: Radial profiles of Favre averaged turbulent shear stress of case B (a), case C (b), case D (c), and case E (d).

of the buoyancy, variation of viscosity and flow acceleration (due to density change) can be observed in a similar way as that in the $\overline{\rho u_z'' u_r''}$ while comparing the results in the various cases, which are not repeated here. However, there are some additional interesting observations which are worthwhile noting. Firstly, the peak value of $u_z^{'}$ in Cases B and D reduces to its lowest values soon after $z/D = 5$, whereas at these locations, $u_r^{'}$ and $u_\theta^{'}$ largely remain unchanged or even with a slight increase in some cases. It takes up to $z/D = 20$ before these quantities reach their final values. This is a reflection of the turbulence structure changes. Secondly, the $u_z^{'}$ in Case D remains largely unchanged shortly after $z/D = 5$ whereas the peak of $u_z^{'}$ in Case B gradually recovers downstream to a value close to its inlet one. This is likely to be linked to the flow acceleration near the wall, but it does not have resonance in $u_r^{'}$ and $u_\theta^{'}$. Finally, all these turbulence quantities reduce initially, reaching a significant lower value at

between $z/D = 15$ and 30 depending on the cases, and then start to recover. It is however important to note that even at the location where $\overline{\rho u_z'' u_r''}$ is near zero, the magnitudes of all the three fluctuating velocities are still very significant. In fact, the peak of $u_z^{'}$ reduces by about half, whereas the reduction of the peaks of the $u_r^{'}$ and $u_\theta^{'}$ is much stronger, to about a third at the lowest point.

The profiles of turbulent kinetic energy (TKE $= \frac{1}{2}\overline{\rho u_i'' u_i''}$) in all cases are shown in Fig. 4.9. The variation of TKE are largely similar to that of $u_{z,rms}^{'}$ for each case. For cases without buoyancy effect (B & D), significant reductions of the peak value close to the wall happen before $z/D = 20$, and maintain after this, while for the main stream, TKE largely remains. In these two cases, the near wall peak of TKE reduces by about 1/2 and 1/3, suggests the acceleration (due to density reduction) has a minor contribution to the laminarization. For cases with the buoyancy effect (A, C & E), the variations of TKE is more complicated: both near-wall and main stream TKE first reduce then increase, however, they reach the lowest value at different locations. For case A, TKE close to the wall reduces to the lowest value at $z/D = 10$, then it starts to increase, while for case C and E, near-wall TKE reach the lowest value at $z/D = 15$ and $z/D = 20$ respectively. In these cases, the recoveries of the main stream TKE happen slightly later (about $\Delta z/D \sim 5$ later) than those near the wall, suggests the early increases of the near-wall peak of TKE are caused by the changes in turbulent structures, this argument is also supported by the faster recovery of near-wall $u_z^{'}$ than $u_r^{'}$ and $u_\theta^{'}$. For cases without the buoyancy effect, TKE profiles at late stage ($z/D > 35$) remain the same shape as the initial profiles (at $z/D = 0$), with a lower peak near the wall, and lower values at the main stream, as the main shear production of TKE is still near the wall. For cases with the buoyancy effect, the shapes of TKE profiles at late stage are totally different from those at the initial stage ($z/D = 0$): the near-wall peaks are lower (about 1/2 or slightly more) than their initial profiles, and the values at the main stream is higher than those of the initial profile, except case E, in which the recovery happens later than the other two cases, it is still the begin of the recovery at $z/D = 35$.

Finally, the influences of the above changes of turbulent characteristics on heat transfer are studied. The streamwise profiles of the wall temperatures and Nusselt numbers in Cases A to E are plotted in figure 4.10. In all cases, the wall temperature increases rapidly within about $z/D = 2$ reflecting the rapid establishment of the thermal boundary layer at the start of the heating, and correspondingly the Nusselt number reduces rapidly from a very high initial value. Note that the top of the Nusselt number plot is clipped off for the benefit of more clearly showing the variations at

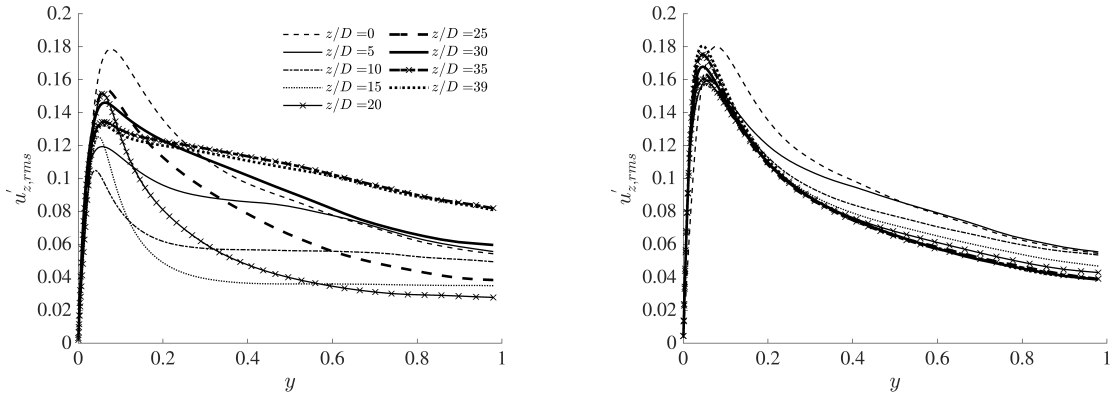

(a) Case A

(b) Case B

(c) Case C

(d) Case D

(e) Case E

(f) Case F

Figure 4.6: Radial profiles of the r.m.s of the streamwise fluctuating velocity in all cases.

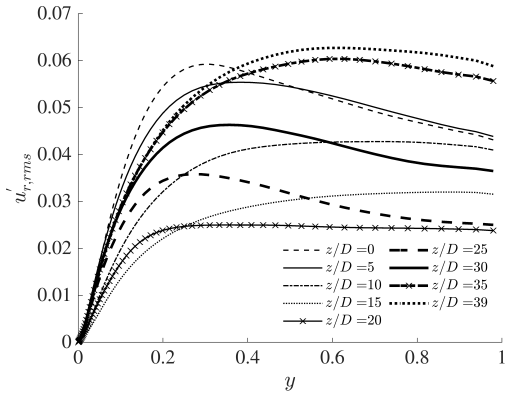

(a) Case A

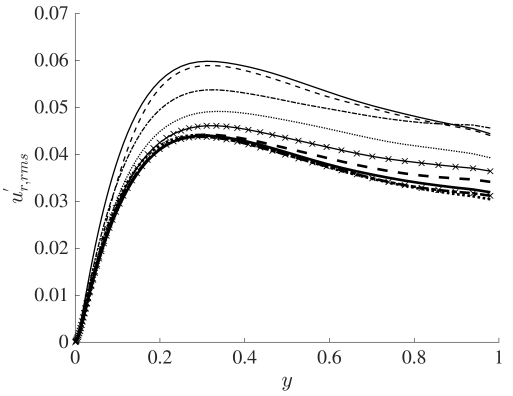

(b) Case B

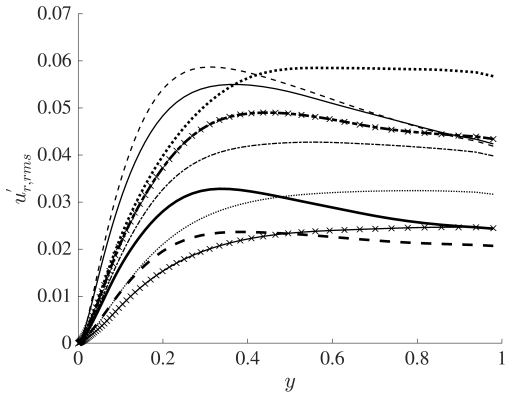

(c) Case C

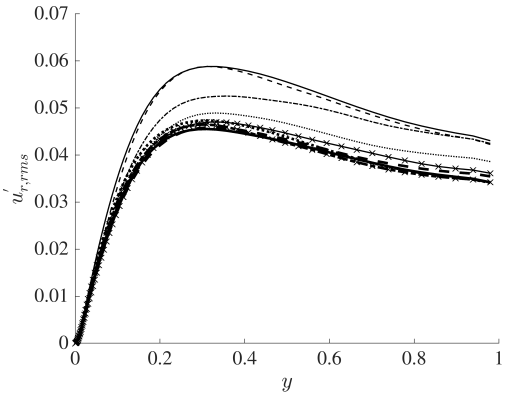

(d) Case D

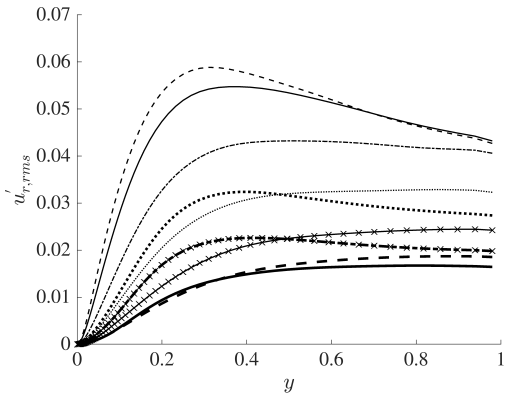

(e) Case E

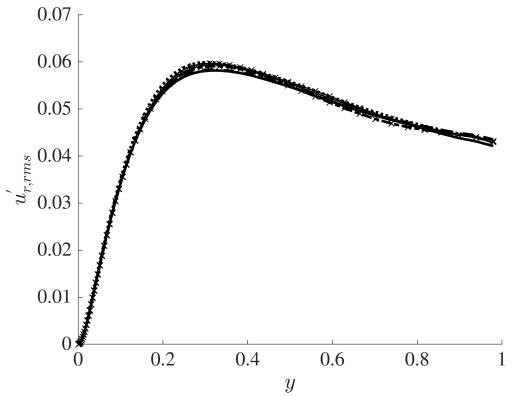

(f) Case F

Figure 4.7: Radial profiles of the r.m.s of the radial fluctuating velocity in all cases.

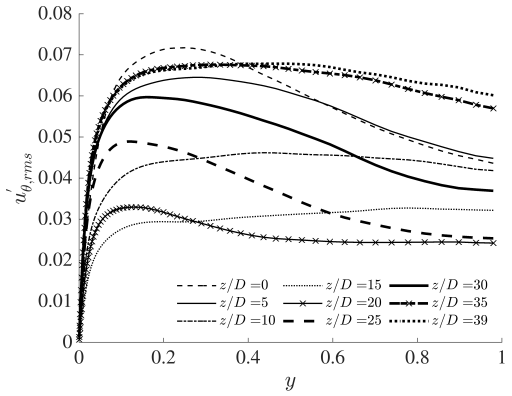

(a) Case A

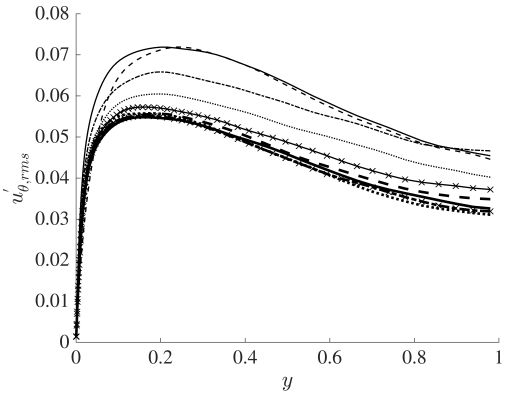

(b) Case B

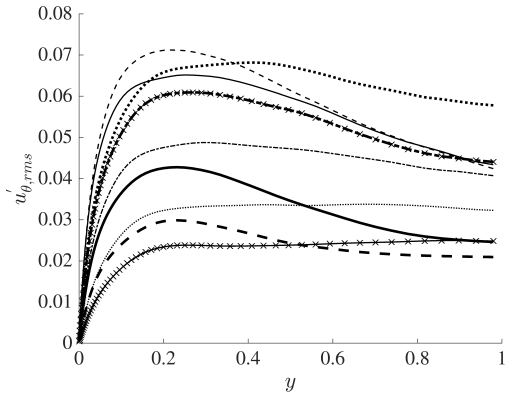

(c) Case C

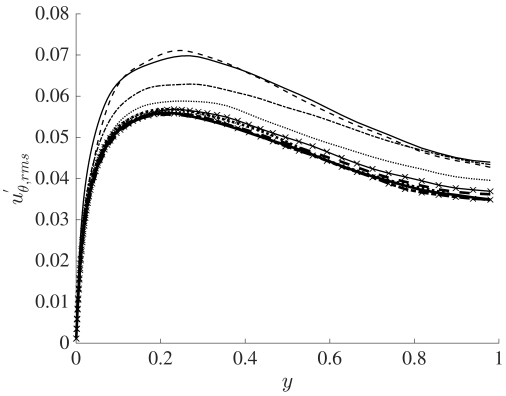

(d) Case D

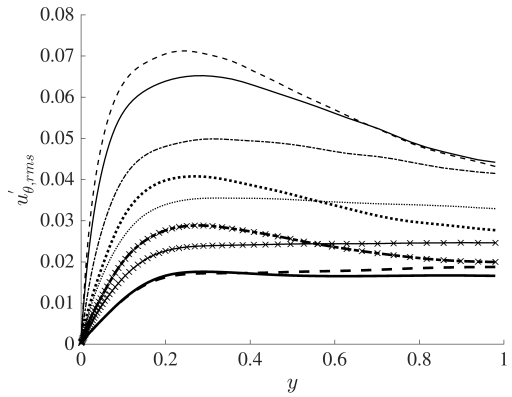

(e) Case E

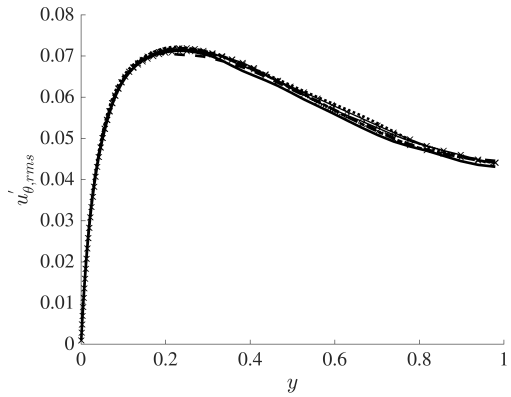

(f) Case F

Figure 4.8: Radial profiles of the r.m.s of the spanwise fluctuating velocity in all cases.

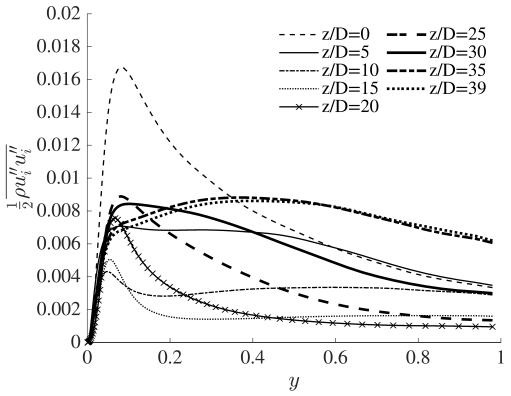

(a) Case A

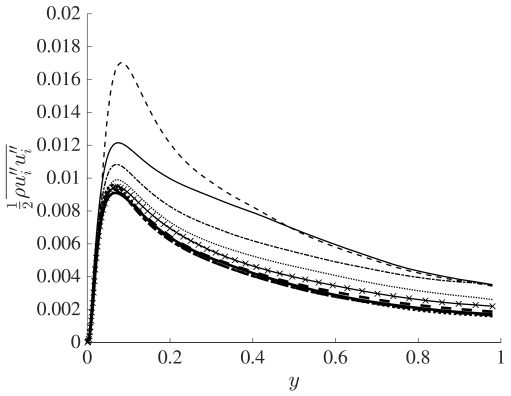

(b) Case B

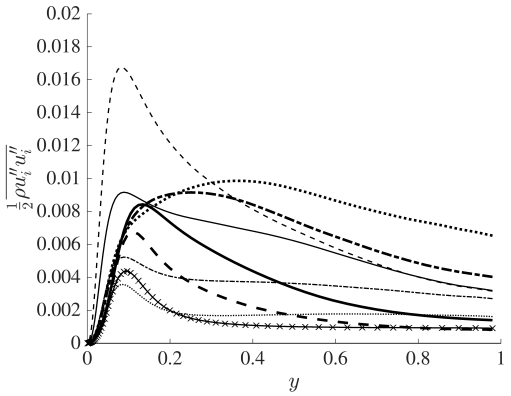

(c) Case C

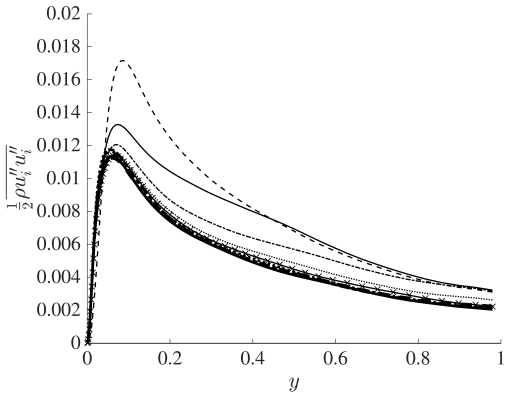

(d) Case D

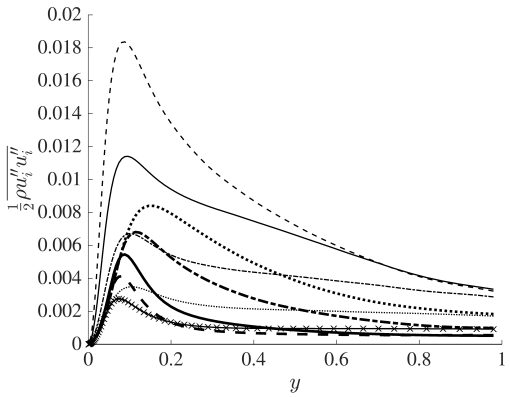

(e) Case E

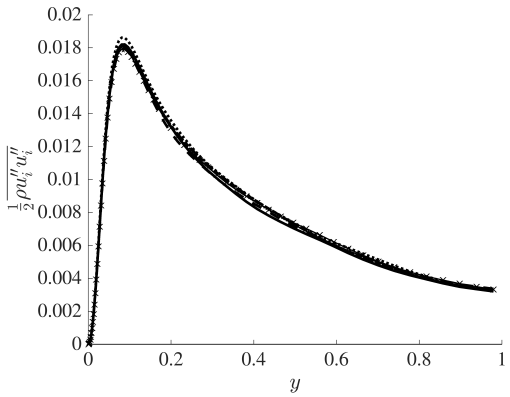

(f) Case F

Figure 4.9: Radial profiles of TKE in all cases.

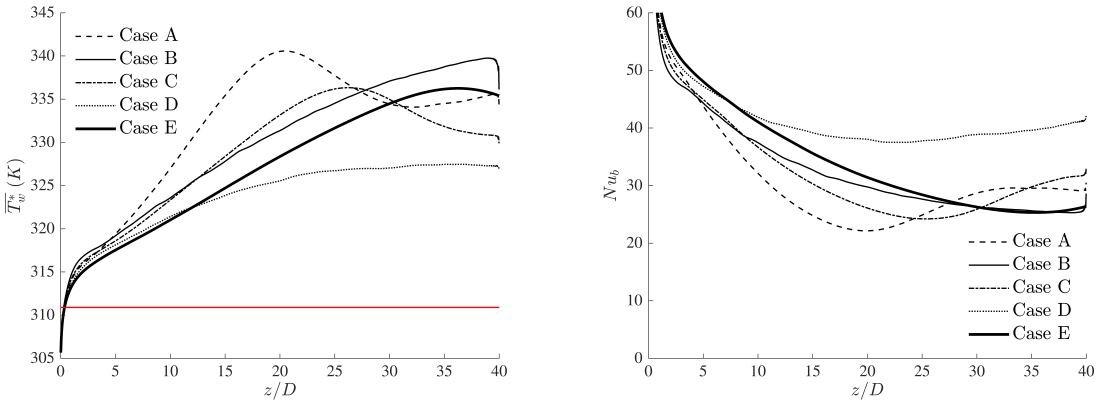

(a) (b)

Figure 4.10: Streamwise distributions of wall temperature (a), pseudo-critical temperature is specified by a red solid line, and Nusselt numbers (b) for case A to E.

later stages. From the wall temperature and Nusselt number profiles, it is clear that cases A, C, and E all experience heat transfer deterioration and recovery, and that case A has the strongest and earliest reduction, followed by case C, then case E. This again suggests that both the variation of thermal property and flow acceleration have some influence on heat transfer although the strongest effect comes from buoyancy. The result of case D indicates that the variation of thermal properties with constant density causes a small reduction in Nusselt number. It is surprising that even though the turbulence is generally speaking much stronger in case B than in Case E, but the variation of the Nusselt number is very similar in the two cases. The variation of thermal conductivity can contribute towards the observation. In case B, when the temperature reaches the pseudo-critical value, there is a significant local reduction in thermal conductivity near the wall, which worsens the heat transfer, while in case E, the thermal conductivity is constant everywhere.

Early RANS studies of supercritical flows [60, 61, 65] indicate the uncertainties in the modelling of turbulent heat flux were attributed to the failure of using a constant turbulent Prandtl number (Pr_t). Turbulent Prandtl number is the ratio between the momentum and thermal turbulent eddy diffusivities, which is required in closing the energy equation. In the Reynolds analogy [140], Pr_t is assumed constant (=1) everywhere. In other studies with experiments carried out or reviewed [141, 142, 143], the range of Pr_t is found to be 0.7 to 0.9 dependent mostly on the flow (turbulence), with an average value of 0.85. In most RANS simulations, constant Pr_t of 1 or 0.85 were used. To show the reliability of these assumptions, the Pr_t (for the radial turbulent heat flux) in case A and E resolved in DNS are discussed herein. The

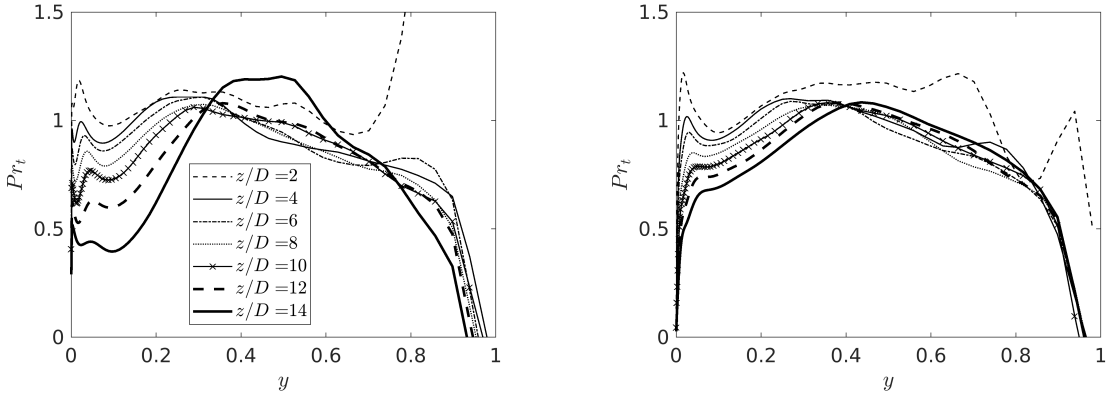

(a) Case A (b) Case E

Figure 4.11: Profiles of the turbulent Prandtl number in case A & E.

turbulent heat flux can be modelled using the eddy viscosity and standard gradient diffusion hypothesis (SGDH) [144, 145] concept as:

$$-\overline{\rho^*}\widetilde{u_r^{*\prime\prime}h^{*\prime\prime}} = \frac{\nu_t^*}{Pr_t}\frac{\partial\overline{h^*}}{\partial r^*}, \tag{4.1}$$

in which ν_t^* is the dimensional eddy viscosity obtained as follow:

$$\nu_t^* = -\frac{\widetilde{u_z^{*\prime\prime}u_r^{*\prime\prime}}}{\frac{\partial\overline{u_z^*}}{\partial r^*}}. \tag{4.2}$$

With Eq. 4.1 rearranged, Pr_t is obtained:

$$Pr_t = -\frac{\nu_t^*\frac{\partial\overline{h^*}}{\partial r^*}}{\widetilde{u_z^{*\prime\prime}u_r^{*\prime\prime}}}. \tag{4.3}$$

The changes in turbulent Prandtl number during the laminarising stage are shown in Fig. 4.11. It is worth noting that when the velocity profile is flattened, $\partial\overline{u_z^*}/\partial r^*$ will approach zero, ν_t^* will not be physical. As shown in Fig. 4.11, at $z/D = 2$ of both cases, Pr_t is around 1 at most locations, which largely satisfies the assumption of the Reynolds analogy. At later locations, Pr_t close to the wall gradually reduce, with a stronger reduction in case A. In the near-wall region of case A, from about $z/D = 12$, Pr_t is below the lower bound that concluded in some experimental studies (0.7). Similar situation happens in case E, that the near-wall Pr_t significantly reduces, and the assumption of constant Pr_t is not applicable in these two cases. Such observation indicates that in most of the RANS models with Pr_t set to be 1, the changes in turbulent heat flux in the flows with strong buoyancy might not be well captured.

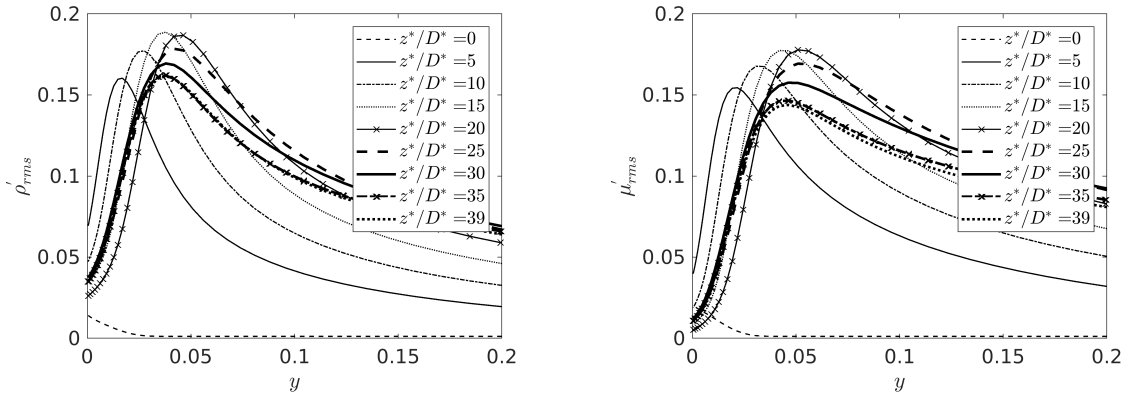

(a) ρ'_{rms}, Case A

(b) μ'_{rms}, Case A

(c) ρ'_{rms}, Case B

(d) μ'_{rms}, Case B

(e) ρ'_{rms}, Case C

(f) μ'_{rms}, Case D

Figure 4.12: Profiles of root mean square of density fluctuation at chosen locations of case A, B and C, and root mean square of dynamic viscosity fluctuation at chosen locations of case A, B and D.

In the cases with variations of thermophysical properties, the fluctuating properties are important factors that influence the turbulent characteristics, e.g., through the buoyancy production of the turbulent kinetic energy. The root mean square of density ρ'_{rms} and dynamic viscosity fluctuations μ'_{rms} near the wall ($y < 0.2$) at chosen locations in the three cases with density variation (case A, B and C) and viscosity variation (case A, B and D) are shown in Fig. 4.12. For all cases, the fluctuations of density and viscosity are mostly zero at the inlet, and rapidly rise everywhere before $z/D = 5$. In every case, the largest fluctuating density/viscosity locates close to the wall, and the peak location slightly vary during the laminarising or recovery stage. Fig. 4.12 shows that the fluctuations of density and viscosity are rather significant, i.e., the peak fluctuations are about 15% of their inlet values.

4.2.3 Turbulence modification due to the viscosity variation (case D)

From the above discussion, it is clear that the buoyancy has the largest effect in the flows with strong thermophysical property variations studied herein, though the changes in other thermal properties can also cause partial laminarisation. The mechanisms of the laminarisation caused by the viscosity variation and buoyancy effects will be investigated in section 4.3 and 4.4. The question we ask is that for a given thermal field (and hence variations of properties and buoyancy), how will the flow and turbulence respond? To answer this question, we study the balances of the terms in the streamwise momentum equation in Cases D, and A & E to understand the evolution of the various terms along the flow. Case D is only affected by the viscosity variation, which causes the flow to be partially laminarised; whereas in cases A (base case) and E (Boussinesq), turbulence is affected by strong buoyancy effect (and other effects in Case A), and the flow undergoes full laminarisation followed by recovery with regeneration of turbulence.

We first focus on Case D to study the effect of viscosity. The axial developments of the radial profiles of the temperature and viscosity are shown in figure 4.13. The wall temperature rises above the critical value ($310.9K$) at an early stage ($z/D < 2$), and the thermal boundary layer is quickly established. After this initial rapid development, the thermal boundary layer appears to largely maintain its shape while the temperature increases very much at the same rate across the radius of the pipe. This implies that the thermal field has achieved some kind of fully-developed state. Due to the strong variation of viscosity with temperature especially around the pseudo-critical point, the viscosity experiences drastic variations close to the wall, in a way

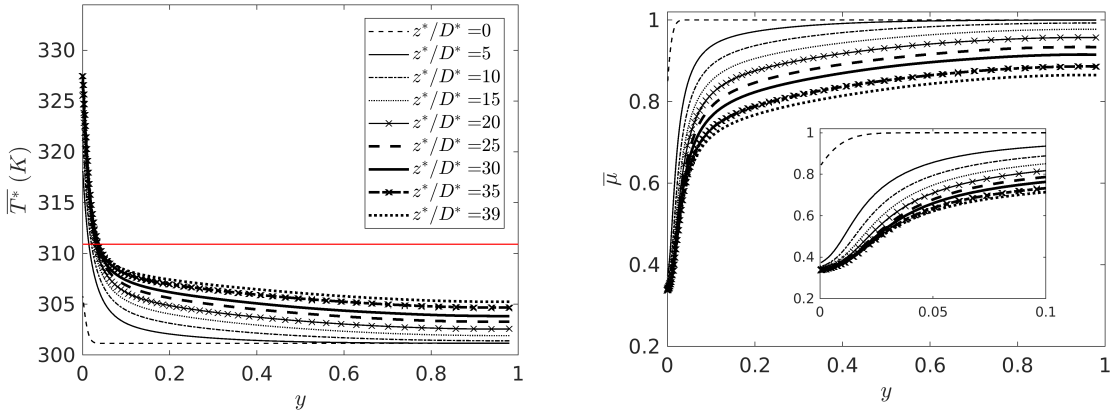

(a) (b)

Figure 4.13: Radial profiles of temperature (pseudo-critical temperature is specified by a red solid line) and normalised dynamic viscosity at several streamwise locations of case D

that mimics the thermal boundary layer. The viscosity at the wall reduces to about 35% of that at the inlet. It is useful to note that even though the viscosity in the core of the flow reduces progressively downstream, the value close to the wall appears to maintain largely unchanged after $z/D = 5$. This is because the viscosity of the fluid passing the pseudocritical point (i.e., the gas-like fluid) does not change significantly with temperature any more as shown in figure 2.1.

We consider the flow to have reached a stationary state and note that the flow is axi-symmetric, and hence the following momentum equation:

$$\begin{aligned}\frac{\partial(\rho u_z)}{\partial t} = &-\frac{\partial(\rho u_z u_z)}{\partial z} - \frac{1}{r}\frac{\partial(r\rho u_r u_z)}{\partial r} - \frac{1}{r}\frac{\partial(\rho u_\theta u_z)}{\partial \theta} \\ &- \frac{\partial p}{\partial z} - \rho g \\ &+ \frac{1}{Re_0}\left(\frac{\partial}{\partial z}\left(2\mu\frac{\partial u_z}{\partial z}\right) + \frac{1}{r}\frac{\partial}{\partial r}\left(r\mu\left(\frac{\partial u_r}{\partial z} + \frac{\partial u_z}{\partial r}\right)\right) + \frac{1}{r}\frac{\partial}{\partial \theta}\left(\mu\left(\frac{\partial u_\theta}{\partial z} + \frac{1}{r}\frac{\partial u_z}{\partial \theta}\right)\right)\right)\end{aligned} \tag{4.4}$$

can be averaged azimuthally and over time. To find the momentum balance over the fluid from the pipe centre to a radius r, we multiply r over both sides of the equation, then integrate every term from the pipe centreline ($r = 0$) to the location (r), then dividing the resultant equation by r. For case D (constant density) and case E (Boussinesq assumption), it follows that the above streamwise momentum equation

becomes:

$$
\begin{aligned}
0 = & \underbrace{-\frac{1}{r}\int_0^r r\frac{\partial(\rho_0\overline{u}_z\ \overline{u}_z)}{\partial z}dr}_{IN1}\ \underbrace{-\rho_0\overline{u}_z\ \overline{u}_r}_{IN2} \\
& \underbrace{-\frac{1}{r}\int_0^r r\frac{\partial(\rho_0\overline{u_z'u_z'})}{\partial z}dr}_{TS1}\ \underbrace{-\rho_0\overline{u_z'u_r'}}_{TS2} \\
& \underbrace{+\frac{1}{Re_0}\Big(\frac{1}{r}\int_0^r r\frac{\partial}{\partial z}\big(2\overline{\mu}\frac{\partial\overline{u}_z}{\partial r}\big)dr}_{VS1}+\underbrace{\overline{\mu}\big(\frac{\partial\overline{u}_r}{\partial z}+\frac{\partial\overline{u}_z}{\partial r}\big)\Big)}_{VS2} \\
& \underbrace{-\frac{r}{2}\frac{\partial P}{\partial z}}_{PG}\ \underbrace{-\frac{1}{r}\int_0^r r(\overline{\rho}-\overline{\rho}_c)gdr}_{Bo}
\end{aligned}
\tag{4.5}
$$

where ρ_0 and ρ_c represent the density at the inlet and the pipe centreline, respectively, and $\frac{\partial P}{\partial z} \equiv (\frac{\partial\overline{p}}{\partial z}+\overline{\rho}_c g)$ is the modified pressure gradient. From left to right, the equation includes, two inertial terms ($IN1$ and $IN2$), two turbulent shear stress terms ($TS1$ and $TS2$), the viscous shear stresses ($VS1$ and $VS2$), and finally the (modified) pressure gradient term (PG) and the buoyancy term (Bo). The terms $TS1$ and $VS1$ have been found to be always negligibly small and are therefore omitted in the following figures and discussion for clarity.

Now let $r = R$ to consider the momentum balance for the entire cross section, in which case the turbulence terms and $IN2$ will disappear. However, unlike a fully developed flow, $IN1$ may not necessarily be zero as will be seen later. Hence:

$$
0 = \underbrace{-\frac{1}{R}\int_0^R r\frac{\partial(\rho_0\overline{u}_z\ \overline{u}_z)}{\partial z}dr}_{IN1} - \underbrace{\frac{\partial P}{\partial z}\frac{R}{2}}_{PG} - \underbrace{\frac{1}{Re_0}\overline{\mu}\big(-\frac{\partial\overline{u}_z}{\partial r}\big)_{r=R}}_{VS2} - \underbrace{\frac{1}{R}\int_0^R r(\overline{\rho}-\overline{\rho}_c)gdr}_{Bo}
\tag{4.6}
$$

The momentum balance (Eq 4.5) for Case D at a number of axial locations are shown in Figure 4.14, in which $y = 0$ is represented by eq. 4.6. The balance for the non-heating section is also shown (in red) for comparison. For such isothermal flows, the only non-zero terms are the viscous ($VS2$) and the turbulent shear stress ($TS2$), and the pressure gradient (PG) and the gravity (Bo). In Case D in which the density is unchanged, Bo is zero.

Let us consider a location soon after the start of the heating (e.g. at $z/D = 5$). The viscosity of the fluid at the wall reduces sharply as shown in figure 4.14, which causes a reduction in frictional resistance on the wall. This directly causes the driving force, pressure gradient, to reduce, which in turn causes the fluid in the core of the flow

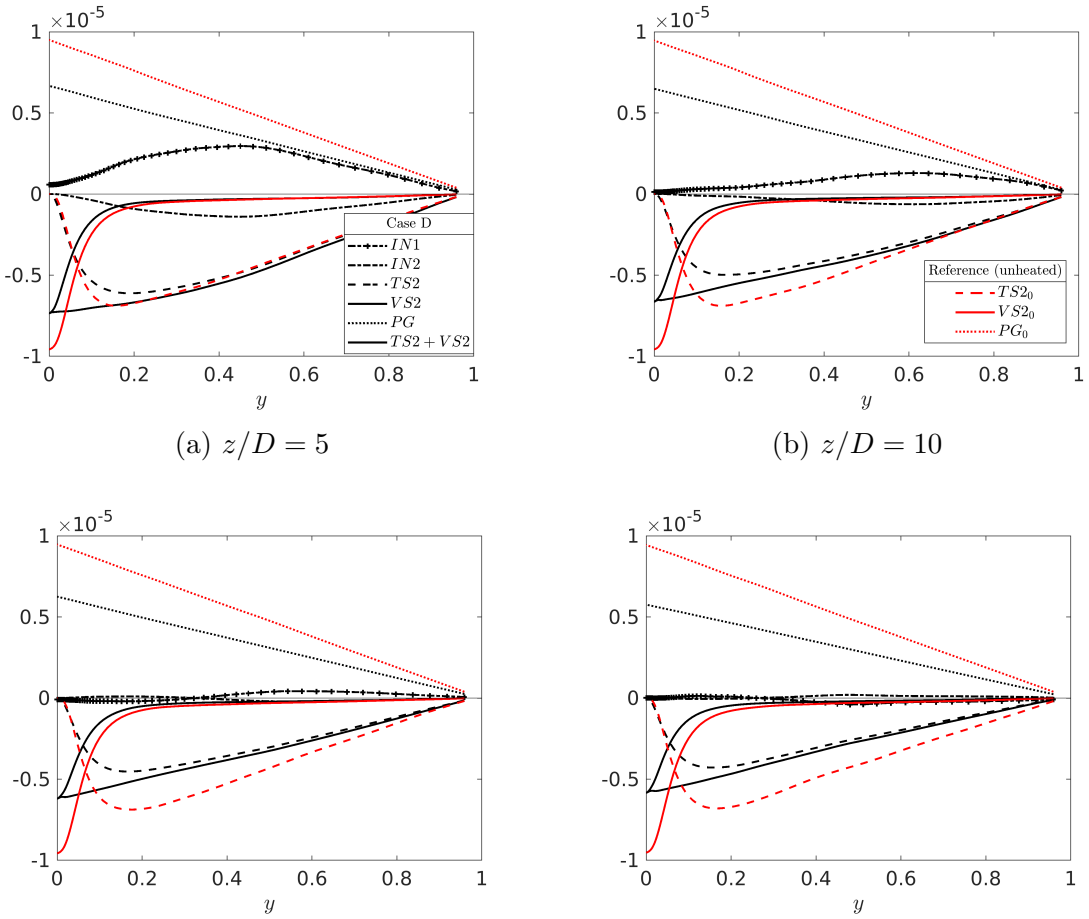

(a) $z/D = 5$ (b) $z/D = 10$

(c) $z/D = 15$ (d) $z/D = 30$

Figure 4.14: Radial profiles of the streamwise momentum equation balance at z/D=5 (a), 10 (b), 15 (c), 30 (d), in case D (black lines), in comparison with the budget profiles before the heating section (red lines).

to decelerate since nothing else (i.e., the viscous or turbulent stresses) has changed at this early stage. In fact, the deceleration directly balances the reduction in pressure gradient. In the region adjacent to the wall however, the reduction in viscous force due to the reduced viscosity prevails the reduction in pressure force and the fluid accelerates. This explains the large values and the distribution of the inertia term $IN1$. The dis-synchronized acceleration/deceleration in the core and wall regions naturally necessitates a net radial flow to maintain continuity, resulting in the second non-zero inertial term ($IN2$). It is useful to note at this point that the large reduction in viscosity on the wall is not completely accommodated by the reduction in pressure gradient. As a result of the non-uniform flow acceleration/deceleration across the radius, the velocity gradient on the wall is significantly increased which compensates the reduction in viscosity to some extent. Hence the actual change in both the wall

shear and the pressure gradient at this location ($z/D = 5$) is less than 30%. It is also interesting to note that the inertial term IN1 is non-zero at the wall due to the redistribution of the velocity profile despite the bulk velocity remains unchanged streamwise.

A consequence of the velocity redistribution is that the velocity profile becomes flatter than in an isothermal flow (see fig 4.4c). This can also be understood knowing that the viscosity is much lower closer to the wall and a large velocity gradient is required to compensate for the reduction in viscosity for the same shear stress. It is well known that a flattened velocity profile will cause a reduction in turbulence production ([11]), which explains the partial flow relaminarisation caused by variable viscosity such as that in Case D. This contrasts the scenario when the viscosity is reduced across the entire pipe, which will lead to an increase in Reynolds number and turbulence.

Next, we recall the fact that much of the reduction in viscosity near the wall occurs within $z/D < 5$, with only small changes later. The velocity, however, takes much longer to adjust due to inertia which is significant over a distance up to around $z/D = 10$. The response of turbulence appears occurs between $z/D = 5$ and $z/D = 15$. This, therefore, suggests that the entrance development is largely governed by the flow characteristics rather than the thermal field, despite the initial cause is the change in viscosity due to temperature variations. The absence of the changes in viscosity downstream explains the significant observation that the flow can reach a fully developed state over most part of the pipe (e.g. $z/D > 15$). This is expected to be a common phenomenon for flows where the wall temperature is above the pseudocritical value. For the flows where the wall temperature is below the T^*_{pc}, the viscosity may vary significantly as the flow and thermal fields develop, which may, in turn, lead to a continuing developing flow.

4.2.4 Laminarisation due to buoyancy and other effects combined (case A, C and E)

We begin with Case E, the momentum balance of which is shown in figure 4.15. Under Boussinesq assumption, all properties are constant except for the density in the gravitational term which varies with temperature. Hence the only effect considered in this case is buoyancy. In figure 4.15, both the modified pressure gradient (PG) and the total body force ($PG + Bo$) are shown to facilitate discussion.

First, again, consider a location at the start of the heating ($z/D = 5$ as an example). Strong buoyancy effects are present near the wall due to the rapid development

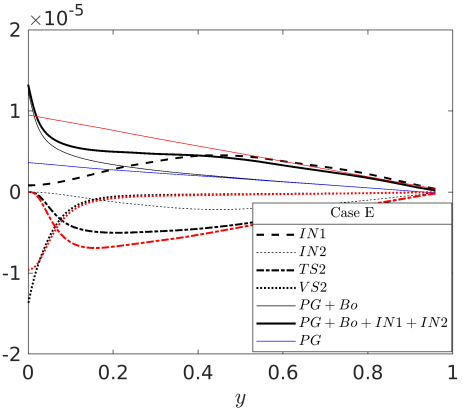

(a) $z/D = 5$

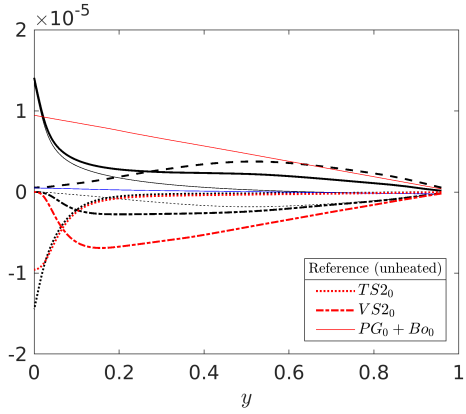

(b) $z/D = 10$

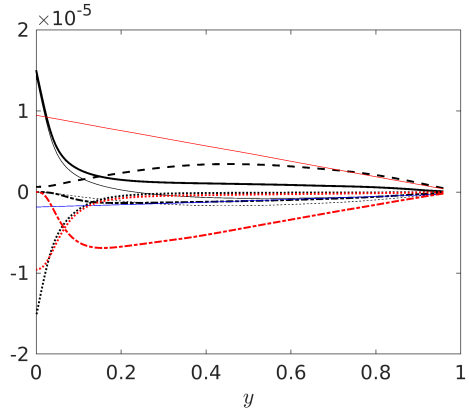

(c) $z/D = 15$

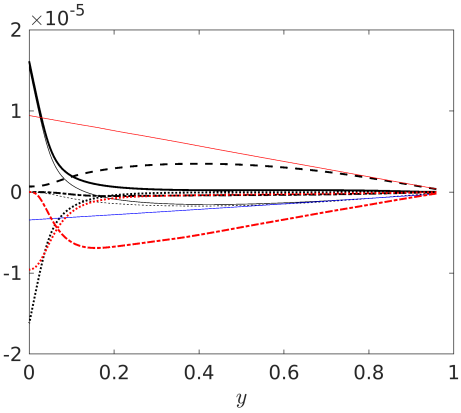

(d) $z/D = 20$

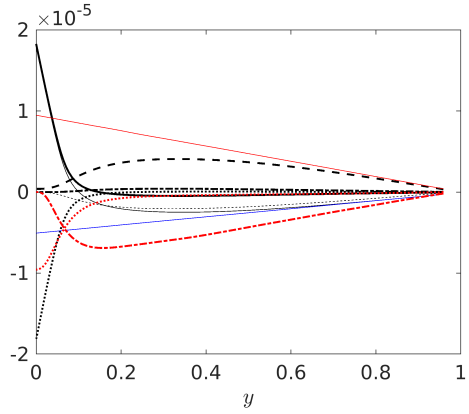

(e) $z/D = 30$

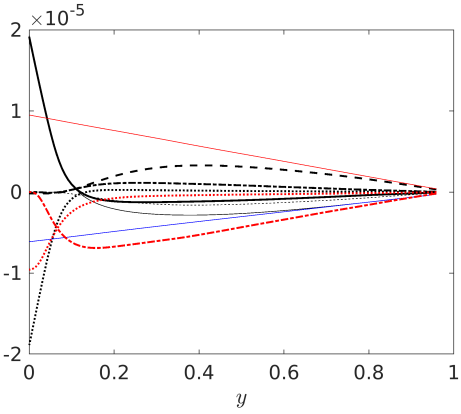

(f) $z/D = 38$

Figure 4.15: Balance of the streamwise momentum equation at several streamwise locations in comparison with the profiles before the heating (red), in case E (black).

of the thermal boundary layer, which accelerates the flow close to the wall. This directly results in a reduction in the pressure gradient under the condition of constant mass flux. Like in Case D, this reduced pressure gradient causes a deceleration in the core region (e.g., $y > 0.5$) since both the viscous and turbulence stresses are still unchanged at this stage. Different from the effect of variable viscosity though, buoyancy-induced flow acceleration near the wall results in an increase in the velocity gradient adjacent to the wall leading to an increase in the wall shear stress.

Further downstream, the buoyancy progressively increases and the modified pressure gradient reduces. In fact, it becomes negative somewhere between $z/D = 15$ and 20. The flow becomes effectively a buoyancy-driven flow and the velocity profile switches to M-shape for $z/D > 20$.

It is useful to note the important role the inertial terms play in this flow. The buoyancy together with the associated change in pressure gradient along the pipe tends to distort the velocity, but this is achieved through flow acceleration/deceleration. Figure 4.15 shows that such effect ($IN1$ and $IN2$) makes a big contribution to the momentum balance at the early stage of the heating section. Unlike in Case D, the effect continues playing a significant role throughout the pipe length. This suggests that any analysis based on 'equilibrium' concept, assuming the flow is fully developed in the flow direction (e.g., [78] & [13]) cannot be directly applied to the spatially developing flow in practice, even though the fundamental understanding can well be used to assist in the analysis. This also explains that the use of the dimensional parameters such as Bo^* based on the local bulk properties may not represent the flow behaviour accurately.

We can, therefore, conclude that in an upwards heated pipe with buoyancy influence-only, the buoyancy effect comes into play through several routes: (i) the non-uniform body force distribution accelerates the flow near the wall; (ii) the pressure gradient reduces as a result of the increasing buoyancy force and hence leading to a relative deceleration in the core of the flow; and (iii) the inertia 'delays'/'lessens' the above effects. The combined effect is that the velocity profile is significantly flattened in the early stage of the heated pipe, which leads to a reduced turbulence production ([11]).

It can be deduced by comparing figures 4.15 and 4.4d that the critical point where the velocity profile turns from an ordinary centre-peaked velocity to an M-shape occurs at the location when the modified pressure gradient approaches roughly zero. Following this point, the pressure gradient is opposing the flow whereas the net forward flow is driven by the buoyancy near the wall. Consequently the peak of the velocity occurs at a location away from the pipe centre. We can further deduce that

the effect of variable viscosity however strong it might be will never turn the flow to M-shape since unlike the flow aiding buoyant force, it will only cause a reduction in the frictional resistance in the near-wall region.

Finally, we study the momentum balance in cases A and C, in which the density varies significantly. Consequently, the corresponding Favre averaged formulation is used for the momentum equation:

$$
\begin{aligned}
0 = & \underbrace{-\frac{1}{r}\int_0^r r\frac{\partial(\overline{\rho}\widetilde{u}_z\,\widetilde{u}_z)}{\partial z}dr}_{IN1}\underbrace{-\overline{\rho}\widetilde{u}_z\,\widetilde{u}_r}_{IN2} \\
& \underbrace{-\frac{1}{r}\int_0^r r\frac{\partial(\overline{\rho u_z'' u_z''})}{\partial z}dr}_{TS1}\underbrace{-\overline{\rho u_z'' u_r''}}_{TS2} \\
& \underbrace{+\frac{1}{Re_0}\Big(\frac{1}{r}\int_0^r r\frac{\partial}{\partial z}\big(2\overline{\mu}\frac{\partial\overline{u}_z}{\partial r}\big)dr}_{VS1}+\underbrace{\overline{\mu}\big(\frac{\partial\overline{u}_r}{\partial z}+\frac{\partial\overline{u}_z}{\partial r}\big)\Big)}_{VS2} \\
& \underbrace{-\frac{r}{2}\frac{\partial P}{\partial z}}_{PG}\underbrace{-\frac{1}{r}\int_0^r r(\overline{\rho}-\overline{\rho}_c)gdr}_{Bo}
\end{aligned}
\tag{4.7}
$$

The general trend of the development of the momentum balance in Case C (figure 4.16) is similar to that observed in Case E, except for that the distributions of the inertial terms. In this case, the dominant inertial term ($IN1$) becomes negative close to the wall which continues up to the wall. In the final station, the term becomes negative throughout the pipe. This implies that the net effect of the velocity profile redistribution is that the momentum increases along with the flow even though the mass flux remains constant. The negative momentum inertia is clearly caused by flow acceleration due to the fluid expansion alongside the increase of the fluid temperature along with the flow.

The development of the momentum balance in Case A again follows a trend very similar to that observed in Case E (figure 4.17), though the changes are clearly stronger and occur earlier. We note the following key points: (i) The reduction of the modified pressure gradient reduces significantly faster under the combined action of all the three effects. Like in the cases discussed earlier, this is the cause for the velocity profile to distort, becoming more flattened in the core. The reduction in pressure also causes even stronger inertial terms, indicating that the flow is significantly different from the 'equilibrium' state, and the flow undergoes strong development axially. (ii) It is interesting to note that the wall shear stress in this flow does not deviate much from that of the isothermal flow. Clearly the effect of the viscosity (reducing the wall

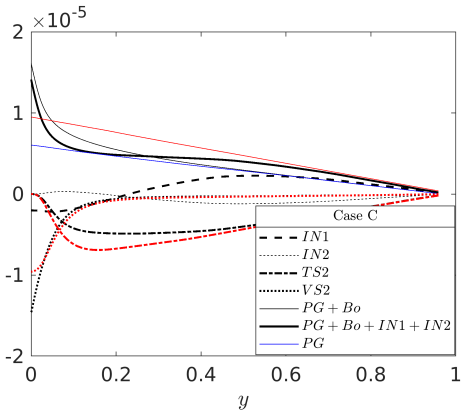

(a) $z/D = 5$

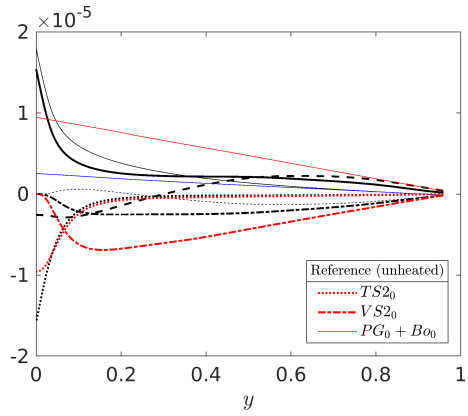

(b) $z/D = 10$

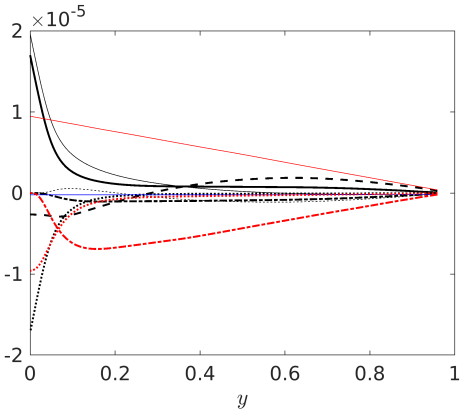

(c) $z/D = 15$

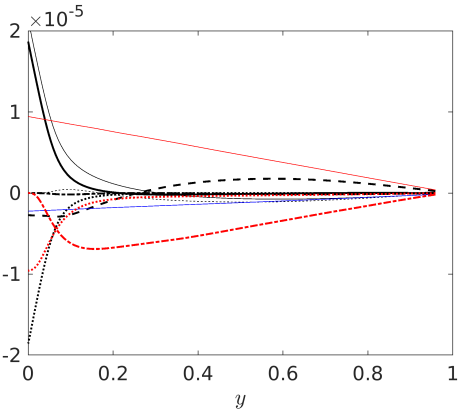

(d) $z/D = 20$

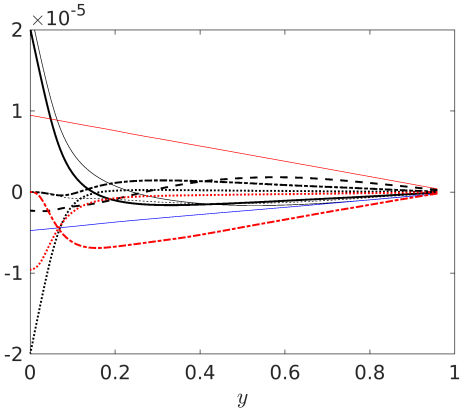

(e) $z/D = 30$

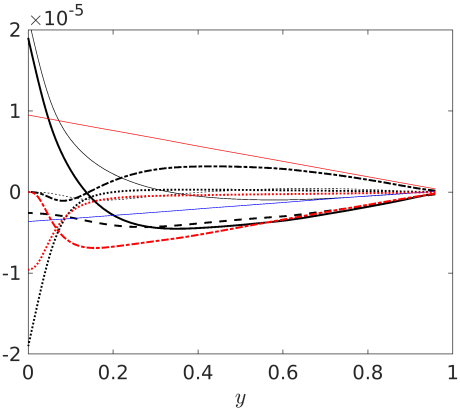

(f) $z/D = 38$

Figure 4.16: Balance of the streamwise momentum equation at several streamwise locations in comparison with the profiles before the heating (red), in case C (black).

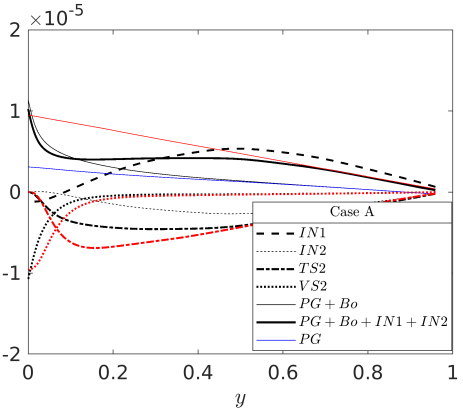

(a) $z/D = 5$

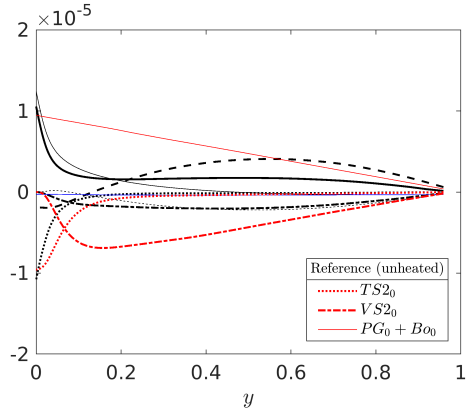

(b) $z/D = 10$

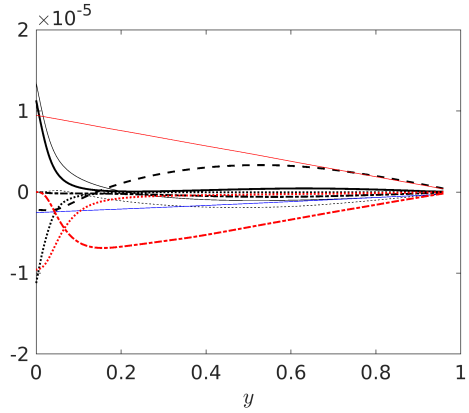

(c) $z/D = 15$

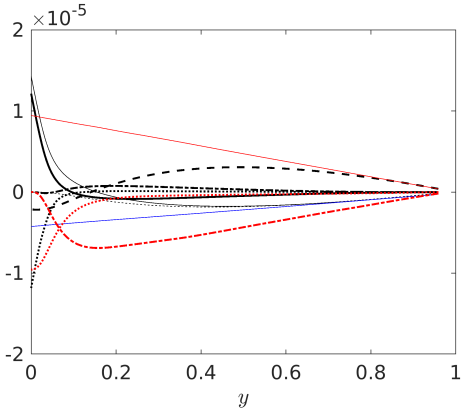

(d) $z/D = 20$

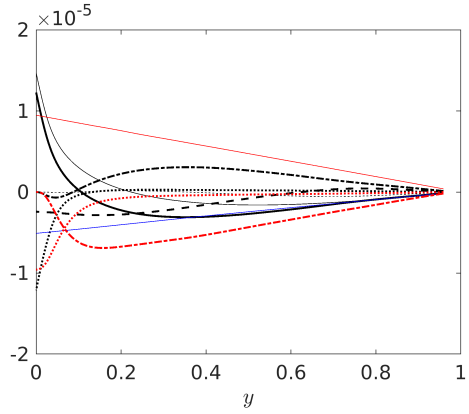

(e) $z/D = 30$

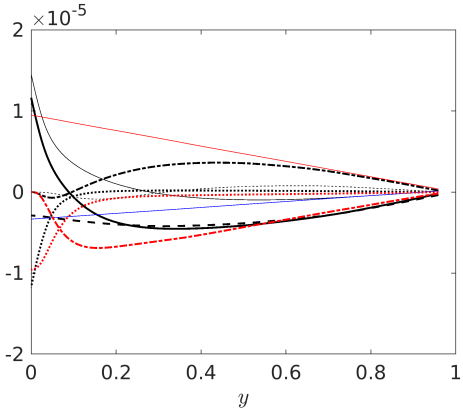

(f) $z/D = 38$

Figure 4.17: Balance of the streamwise momentum equation at several streamwise locations in comparison with the profiles before the heating (red), in case A (black).

shear) and that of buoyancy (increasing the wall shear) have cancelled each other to some extent as far as the wall shear stress, even though their effect on distortion of the velocity profile are in the same direction and reinforce each other. (iii) Similar to that in case C, the dominant inertial term ($IN1$) is negative in Case A even though at the earlier z stations, the region where it is negative is small. It, however, becomes more negative than in case C at later stations. Consequently, again the local acceleration/deceleration of the fluid in the process of distorting the velocity profile has a net effect of flow acceleration in a significant part of the flow.

4.3 Conclusions

In this part of work, a number of simulations have been carried out with one or more thermal properties artificially frozen to isolate or eliminate some physical mechanisms to develop a better understanding of the complex phenomena. Different from previous similar studies on this topic [78, 13], we are particularly interested in the axial developing behaviours resulted from the large variations of thermal properties. The following conclusions can be drawn from the study:

- The flow inertia is significant in the momentum balance throughout the entire length of the pipe in any cases when buoyancy is considered. This is largely due to the local (radially non-uniform) flow acceleration/deceleration caused by the continuously varying buoyancy and viscosity (though the former dominates), leading to a continuously varying velocity profile along the flow. The contribution of the inertia has been quantified by analysing the momentum balance for each case studied.

- The effect of the inertia on momentum in turn impacts on turbulence production, generally delaying flow laminarisation. Such an influence of flow development is non-trivial and cannot be omitted in flow analysis and heat transfer calculations. This suggests that the results of analyses based on a spatial developed flow (such as [78] and [13]) cannot be directly applied to such flows despite they can be very useful in developing fundamental understanding of the physics. Similarly, this also explains that in some cases, buoyancy parameters based on location flow quantities cannot describe heat transfer deterioration accurately.

- The effect of variable viscosity alone can cause turbulence reduction by flattening the velocity profile, but it will not turn the velocity profile to an M-shape, which can only be achieved by buoyancy. If the wall temperature is above

the pseudo-critical temperature, the flow can achieve a fully developed state in which the flow and heat transfer behaviour remain largely unchanged except in the entrance region.

- It has been shown that the use of Boussineq approximation is able to capture the key phenomenon in a heated upward flow of supercritical fluid, including turbulence reduction and heat transfer deterioration. However, there are large quantitative differences between the results of simulations using or not using this approximation, which suggests that the effect of viscosity and other density variation effects (i.e., those in addition to the buoyancy) are also very strong and the use of Boussinesq approximation for the conditions such as those studied herein will cause some uncertainties in the predictions.

In this Chapter, the mechanisms of laminarisation caused by the effects of near-wall reduction of viscosity and buoyancy in a heated vertical pipe flow are discussed. In the next chapter, case A & E will be further discussed using the apparent Reynolds number approach [13], and a unified explanation is established to characterise these effects by pseudo-body forces.

Chapter 5

Further analysis of the supercritical fluid flow using the apparent Reynolds number theory

In the last chapter, the laminarization processes due to the viscosity variation and buoyancy is quantified and investigated, and they have been found to be similar to each other, both begin with a near-wall deficit of downward force (friction or gravity), followed by an overall reduction of the modified pressure gradient PG. In this chapter, a unified theory is proposed to treat the effects of viscosity variation, density variation and buoyancy as pseudo-body forces. Expressions are derived to quantify the body-forces and to characterise their effects on the flow and turbulence. The theory developed in He et al. [13] is extended and applied to the thermal flows in the current study. The changes in turbulent structures during the laminarization and re-transition are investigated, including the forming of coherent streaks and disappearing of multi-scale vortexes during the laminarizing process, and the newly generated turbulent spots and broken down streaks during the re-transition.

5.1 General behaviour and momentum balance of Cases A and E

The two flows with the presence of the buoyancy, Cases E and A from the last chapter are of interest in the current discussion. The general behaviour of the flow can be summarised with reference to figures 5.1 & 5.2, in which the developments of the radial profiles of the velocity and turbulence shear stress for Cases A and E, and profiles of the density, viscosity and temperature for Case A are shown. The two cases show qualitatively similar behaviour. As the fluid is heated in an upward flow,

it becomes lighter near the wall resulting in a buoyant force aiding the flow, which in turn causes the fluid in that region to accelerate relative to the fluid in the core, resulting in a flattened velocity profile. At a later stage, the near-wall fluid accelerates so much that the peak of the profile shifts away from the pipe centre to a location near the wall, and the velocity profile becomes so-called M-shaped. Correspondingly, the turbulence shear stress reduces downstream initially and reaching the lowest level (close to zero everywhere in the pipe) around the time when the velocity profile about to switch its shape. Further downstream, turbulence is regenerated. In comparison with Case E, the turbulence in Case A laminarises stronger and faster in the first stage, and then it recovers also stronger and faster in the later stages, clearly due to the effects of variations of thermophysical properties in addition to buoyancy, which are further discussed later in this chapter.

The phenomenon described above is well-established and has been studied in various investigations [77, 79]. Generally speaking, the flow and turbulence behaviours in such a heated supercritical fluid flow show a clear three-stage development, that is, a partially laminaring flow stage, a full laminarisation stage and a re-transition stage. Both turbulence and heat transfer exhibit distinct characteristics in each of the stages/regions. For the cases considered here, the full laminarisation regions are roughly between $18 < z/D < 28$ and $12 < z/D < 18$, respectively for Cases E and A, which separate the laminarising and re-transition regions before and after it. There may still be strong turbulent kinetic energy in the region of full laminarisation referred to here. The reasons for this and the particular categorisation of the flow regions and the boundaries between them (used above) will become clear later.

We are interested in understanding the mechanisms of flow laminarisation especially with respect to the apparent Reynolds number theory proposed in [13]. The theory is based on the effect of the non-uniform body force, and to understand such forces in the flow concerned herein, we analyse the momentum balances. Integrating the Favre-averaged Navier-Stokes equation from the pipe centre to a radius r yields:

$$\begin{aligned} 0 = &\underbrace{-\frac{1}{r}\int_0^r r\frac{\partial(\overline{\rho}\widetilde{u}_z\,\widetilde{u}_z)}{\partial z}dr}_{IN1}\underbrace{-\overline{\rho}\widetilde{u}_z\,\widetilde{u}_r}_{IN2}\underbrace{-\frac{1}{r}\int_0^r r\frac{\partial(\overline{\rho u_z'' u_z''})}{\partial z}dr}_{TS1}\underbrace{-\overline{\rho u_z'' u_r''}}_{TS2} \\ &\underbrace{+\frac{1}{Re_0}\Big(\frac{1}{r}\int_0^r r\frac{\partial}{\partial z}\big(2\overline{\mu}\frac{\partial\overline{u}_z}{\partial r}\big)dr}_{VS1}\underbrace{+\overline{\mu}\big(\frac{\partial\overline{u}_r}{\partial z}+\frac{\partial\overline{u}_z}{\partial r}\big)\Big)}_{VS2}\underbrace{-\frac{r}{2}\frac{\partial P}{\partial z}}_{PG}\underbrace{+\frac{1}{r}\frac{1}{Fr_0^2}\int_0^r r(\overline{\rho}-\overline{\rho}_c)dr}_{Bo} \end{aligned} \tag{5.1}$$

where ρ_0 and ρ_c are the density at the inlet and the pipe centreline, respectively, and $\frac{\partial P}{\partial z} \equiv (\frac{\partial \overline{p}}{\partial z} + \frac{\overline{\rho}_c}{Fr_0^2})$ is the modified pressure gradient. From left to right, the equation

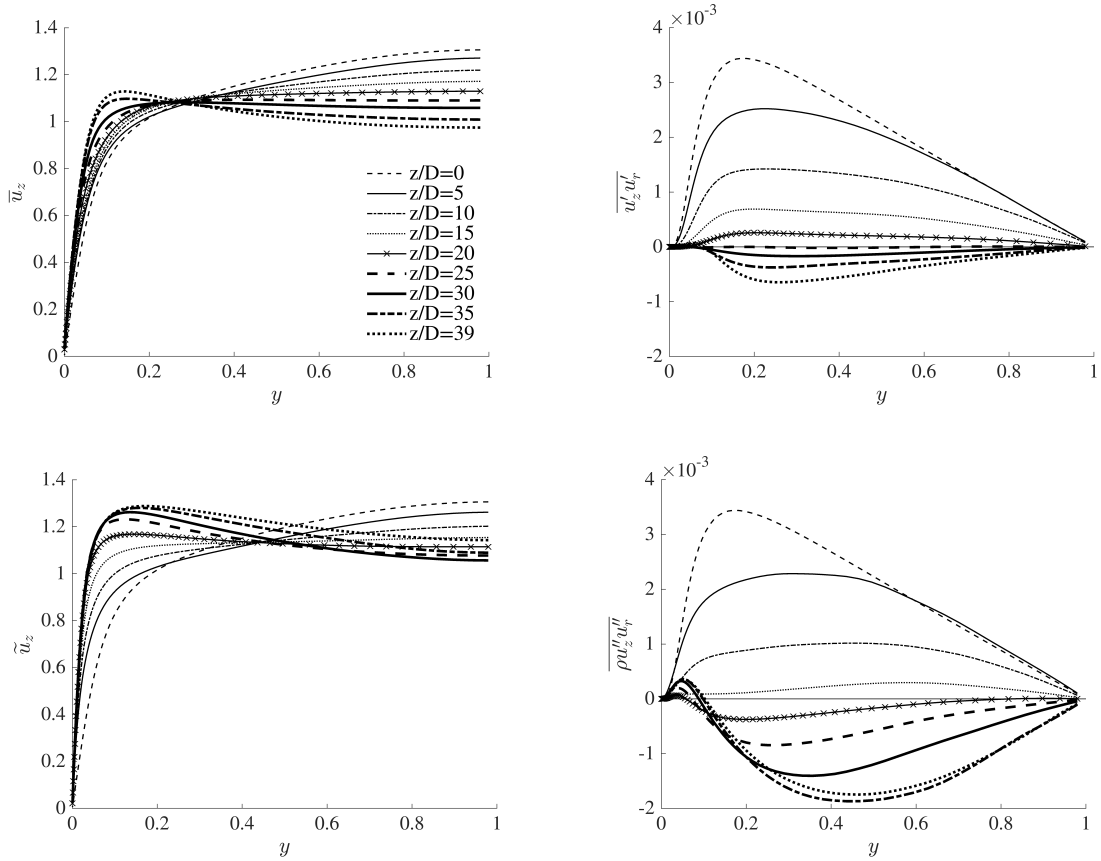

Figure 5.1: Radial profiles of streamwise velocity and turbulent shear stress at chosen locations of Cases E and A.

includes, inertial terms ($IN1$ and $IN2$), turbulent shear stresses ($TS1$ and $TS2$), the viscous shear stresses ($VS1$ and $VS2$), and finally the (modified) pressure gradient (PG) and the buoyancy (Bo). The terms $TS1$ and $VS1$ are always negligibly small and are therefore omitted in the following discussion for clarity. For Case E with the Boussinesq approximation, the Favre averaged velocity and turbulent stresses are replaced by the Reynolds averages and the normalised density and viscosity are both unity.

The momentum balances are shown in Figure 5.3 & 5.4 for two locations in the laminarising region for Cases E and A. Considering Case E first, it is clear that the viscous shear stress remains largely unchanged at both z/D-locations in comparison to the unheated flow except very close to the wall where it is increased significantly. The turbulent shear reduces more strongly at 10D than at 5D as already observed in figure 5.1. The linearly-distributed modified pressure force reduces strongly even at 5D, and becoming close to zero at 10D. The buoyancy is largely zero in most part of core of the pipe but increases sharply near the wall, being much larger at 10D than at

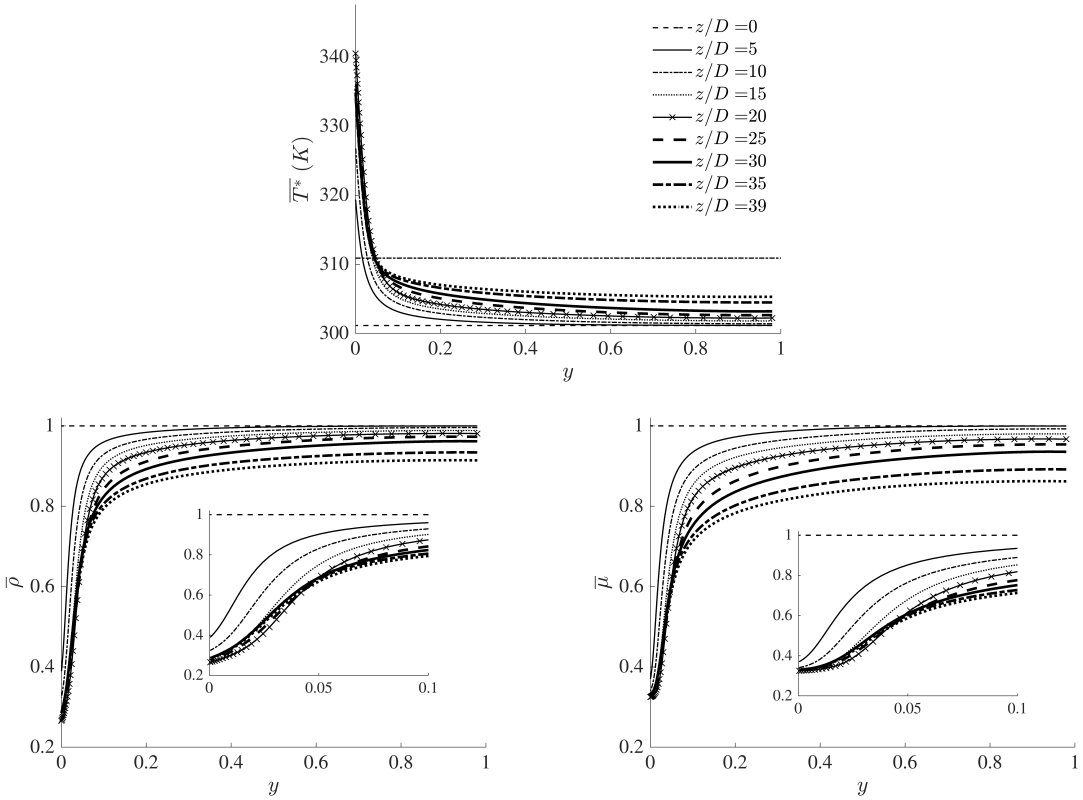

Figure 5.2: Radial profiles of density, temperature and dynamic viscosity at chosen locations of Case A.

5D. Finally, it is interesting to note that the inertia term is very strong in comparison with the rest of the terms, and is largely linear in the pipe core, but reduces rapidly close to the wall.

Before moving to the next section, we briefly discuss the budget of the streamwise turbulent stresses, which are shown in figures 5.5 and 5.6 for Cases E and A, and additionally, the cross-sectional integration in figure 5.7. First it is interesting to note that the buoyancy production (structural effect) is negative but small in the laminarising region. Consequently the turbulence dynamics is largely influenced by the indirect effects. The buoyancy production is however dominant in the full laminarisation and re-transition regions for both Cases A and E. Another point to note is that the convection makes only a small contribution to the overall turbulence budget balance in the flow laminarising region. This is both interesting and significant. Even though the inertia (spatial acceleration) plays a very significant part in the momentum balance in this developing flow as shown above, the turbulence is however largely in equilibrium. It is only insignificantly influenced by the flow up- and down-stream of

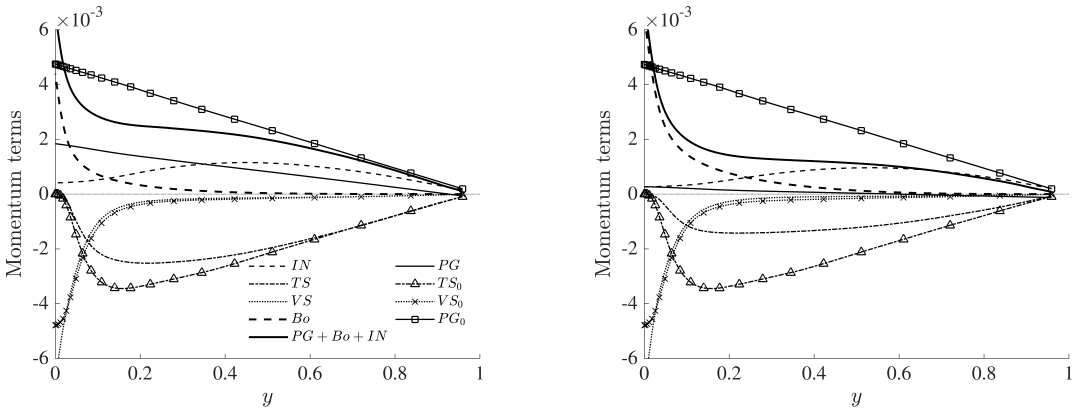

(a) $z/D = 5$ (b) $z/D = 10$

Figure 5.3: Momentum balance at $z/D = 5$ & 10 for Case E.

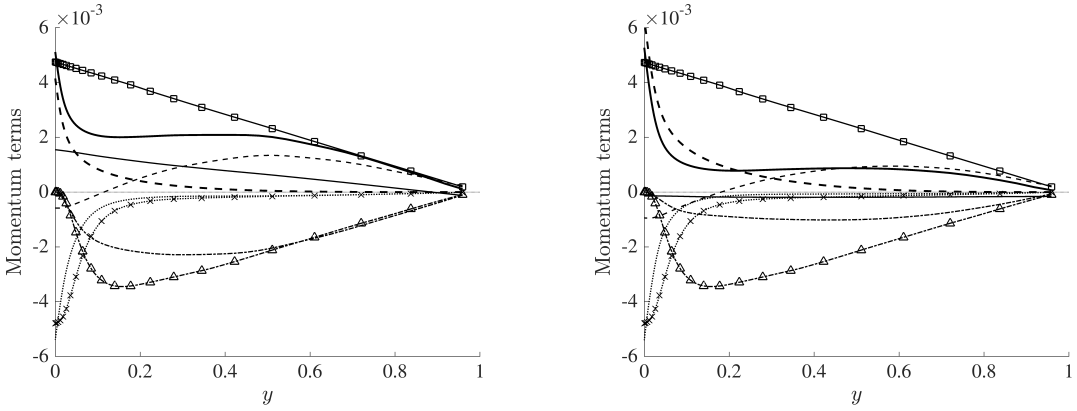

(a) $z/D = 5$ (b) $z/D = 10$

Figure 5.4: Momentum balance at $z/D = 5$ & 10 for Case A.

it. This together with the first point, the buoyancy production being small, provides the foundation for the analysis provided in sections 5.2 to 5.4.

Section 5.2 discusses the apparent Reynolds number concept introduced in He et al. [13] and new hypotheses proposed to extend the theory to the flow concerned herein, the validity of which is evaluated in section 5.3. This is followed by the discussion of a new unified theory in section 5.4. Finally the 'full' laminarisation and re-transition are discussed in section 5.5.

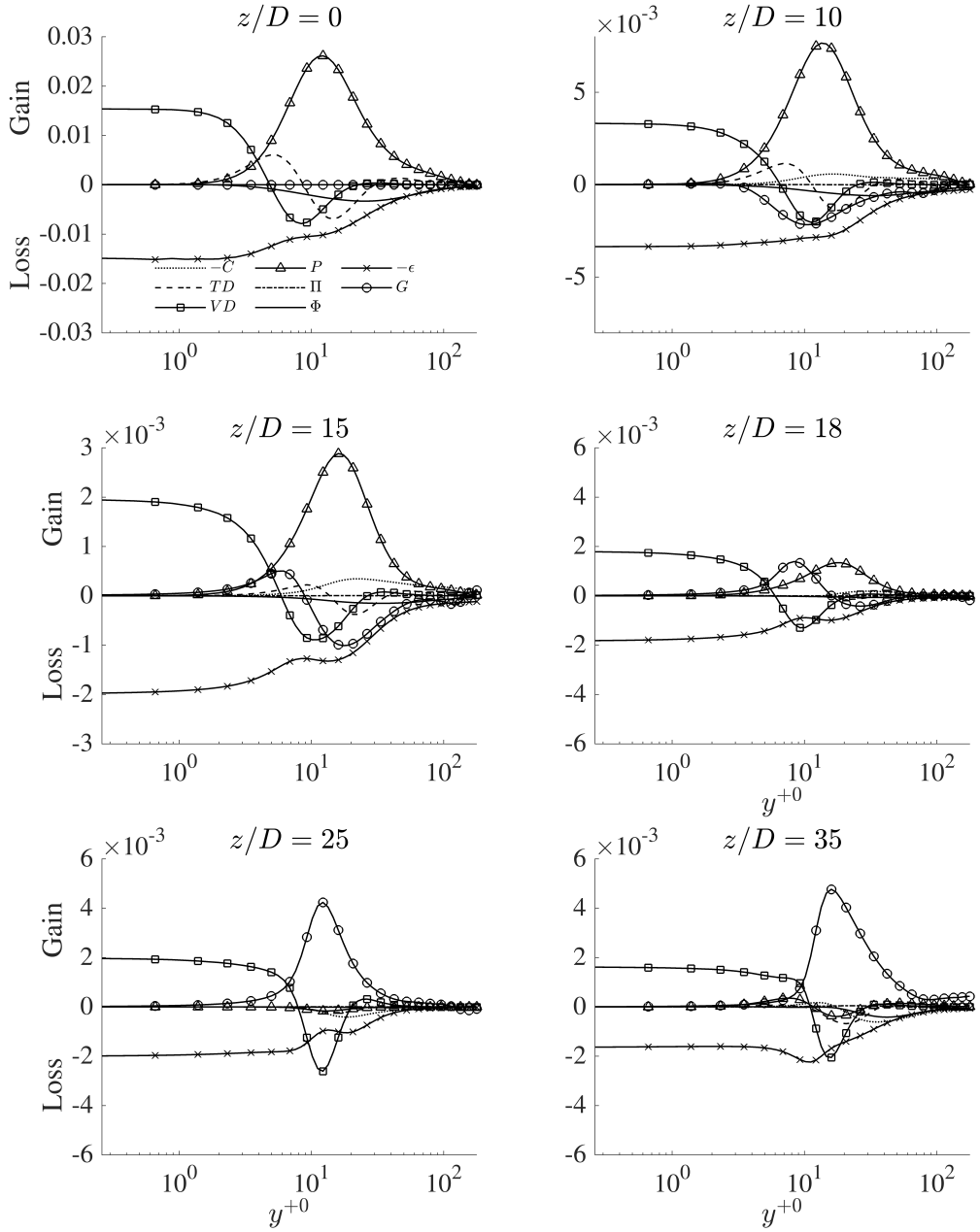

Figure 5.5: The budget of the transport equation for $\overline{u_z' u_z'}$ in Case E. Every three data points are shown for lines with markers for clarity. The budget terms are: Convection (C), viscous diffusion (VD), pressure diffusion (Π), dissipation (ϵ), turbulence diffusion (TD), production (P), pressure strain (Φ) and buoyancy production (G).

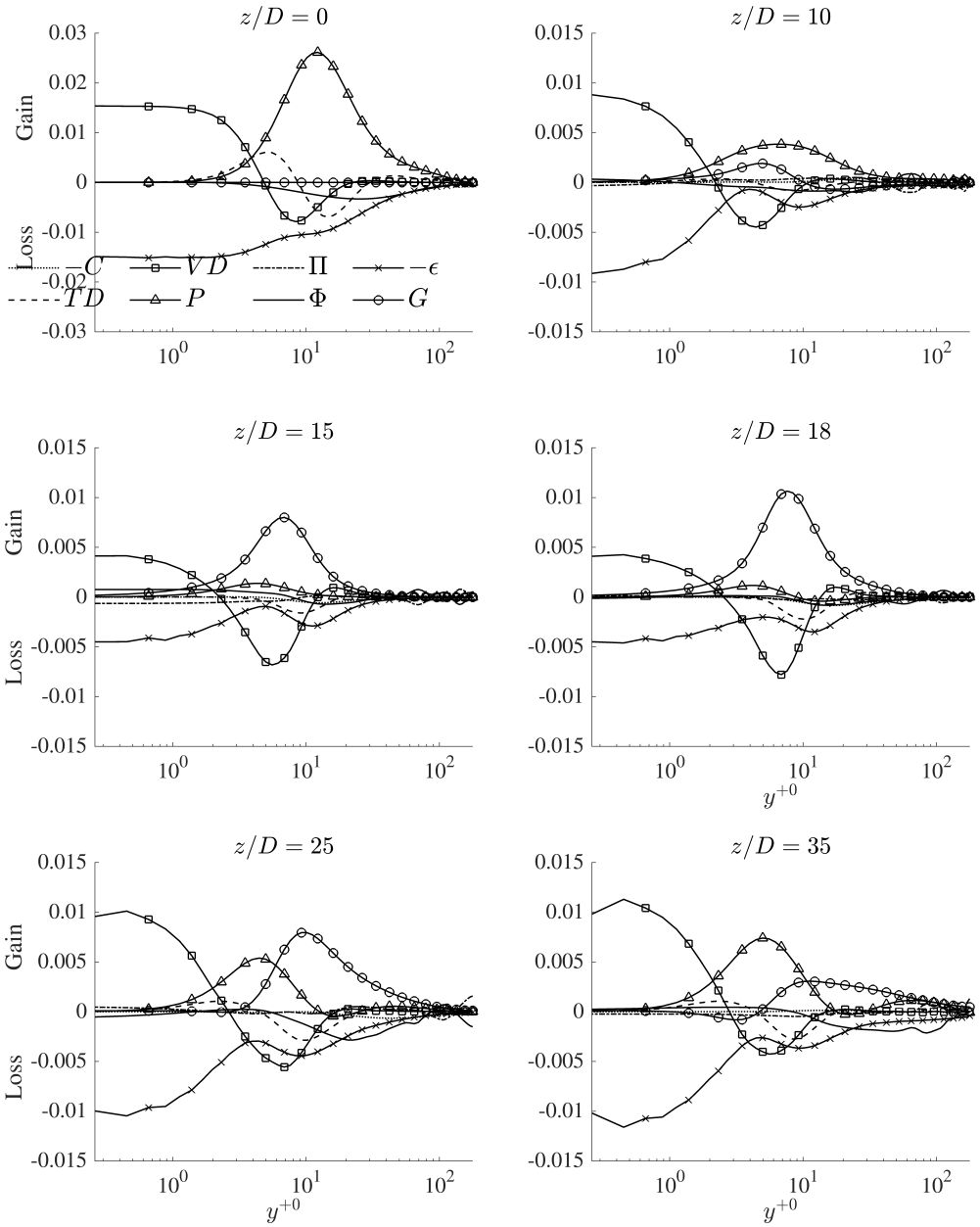

Figure 5.6: The budget of the transport equation for $\overline{\rho u_z'' u_z''}$ in Case A. Every three data points are shown for lines with markers for clarity. The budget terms are: Convection (C), viscous diffusion (VD), pressure diffusion (Π), dissipation (ϵ), turbulence diffusion (TD), production (P), pressure strain (Φ) and buoyancy production (G).

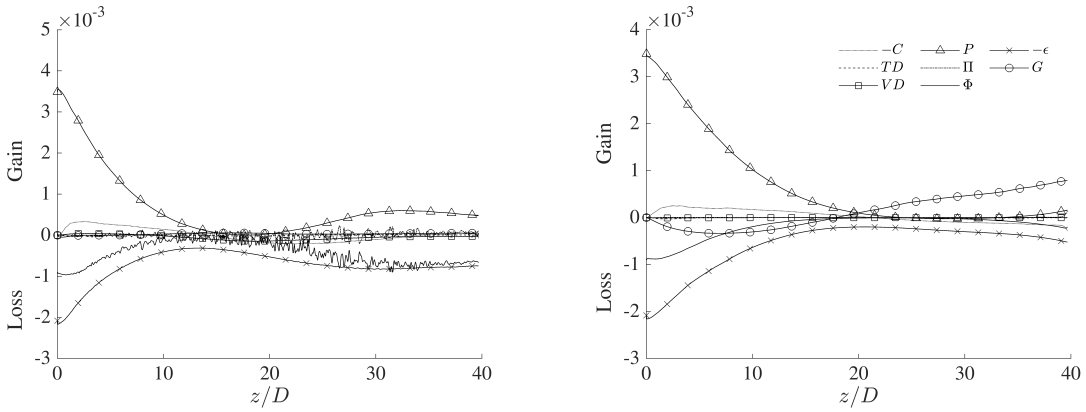

(a) Case A (b) Case E

Figure 5.7: The radial integral of the budget of the transport equation for the streamwise Reynolds normal stress in Case A and E.

5.2 Apparent Reynolds number and pseudo-body forces

He et al. [13] studied a spatially fully developed flow subjected to a prescribed non-uniform body force varying linearly with radius or in a step-change manner to approximate the buoyancy in a heated upward flow using DNS. Not surprisingly, it was found that the idealised body forces cause partial or full laminarisation in a similar manner as the buoyancy does. The intriguing new finding was that the main turbulence characteristics of the body-force influenced flow, including the turbulence mixing represented by the eddy viscosity, are similar to that in a flow with the same pressure gradient without the presence of the body force. This flow was referred to as the equivalent pressure gradient (EPG) reference flow. In other words, applying an additional non-uniform body force does not cause significant changes to the key turbulence characteristics.

Making use of the eddy-viscosity turbulence concept, the Reynolds averaged momentum equation for such a spatially developed flow with constant properties subject to a non-uniform body force (f) can be written as:

$$-\frac{\partial \overline{p}}{\partial z} + \frac{1}{rRe_0}\frac{\partial}{\partial r}\left(r(\nu_t + 1)\frac{\partial \overline{u}_z}{\partial r}\right) + f = 0, \tag{5.2}$$

and its corresponding EPG reference flow is then

$$-\frac{\partial \overline{p}_p}{\partial z} + \frac{1}{rRe_0}\frac{\partial}{\partial r}\left(r(\nu_{tp} + 1)\frac{\partial \overline{u}_{zp}}{\partial r}\right) = 0, \tag{5.3}$$

where $\partial\overline{p}/\partial z = \partial\overline{p}_p/\partial z$ by the definition of EPG flow and the observation of He et al. [13] described above implies that $\nu_t = \nu_{tp}$. Subtracting Eq. 5.3 from 5.2, we have:

$$\frac{1}{rRe_0}\frac{\partial}{\partial r}\left(r(\nu_{tp}+1)\frac{\partial\Delta\overline{u}_z}{\partial r}\right)+f=0, \tag{5.4}$$

where $\Delta u_z = \overline{u}_z - \overline{u}_{zp}$, which is a perturbation caused by the body force. Consequently the heated flow can be represented by the EPG flow plus the body force induced perturbation flow. The authors then defined an apparent friction velocity for the flow based on the pressure gradient, $u^*_{\tau p} = \sqrt{\tau^*_{wp}/\rho^*}$, where $\tau^*_{wp} = -(R^*/2)(\partial\overline{p}^*/\partial z^*)$. Similarly an apparent Reynolds number can be defined as: $Re_{\tau p} = u^*_{\tau p}R^*/\nu^*$. It follows naturally from the observation described above that the flow statistics of body-force influenced flow when normalised by the apparent friction velocity would behave in a similar manner as those in the EPG flow, which was demonstrated by He et al. [13]. The turbulence reduction, or the so-called laminarisation, commonly referred to when compared with a reference flow of the same flow rate (EFR), can then be associated with a reduction in the Reynolds number of the EPG flow (i.e., the $Re_{\tau p}$).

The principal hypothesis of this chapter is that the various flow laminarising mechanisms in a heated flow including the buoyancy, variations of thermophysical properties and even the inertia can be explained with the apparent Reynolds number (ARN) concept.

We first consider the variations of density and viscosity. For this purpose, we consider a stationary, streamwise fully developed flow with non-uniform density and viscosity distributions without the effect of gravity. An example of this is the flow in parallel plates with a heated and a cooled wall on either side as studied by Peeters et al., Wan et al. [78, 98]. The governing equation for the mean flow based on Favre average reads:

$$-\frac{\partial\overline{p}}{\partial z}+\frac{1}{rRe_0}\frac{\partial}{\partial r}\Big(r\big(Re_0\overline{\rho}\widetilde{u''_z u''_r}+\overline{\mu}\frac{\partial\overline{u}_z}{\partial r}\big)\Big)=0, \tag{5.5}$$

which can be re-written as follows after introducing the eddy viscosity modelling concept, $-\widetilde{u''_z u''_r} = \frac{\nu_t}{Re_0}\frac{\partial\overline{u}_z}{\partial r}$,

$$-\frac{\partial\overline{p}}{\partial z}+\frac{1}{rRe_0}\frac{\partial}{\partial r}\left(r(\overline{\rho}\nu_t+\overline{\mu})\frac{\partial\overline{u}_z}{\partial r}\right)=0. \tag{5.6}$$

Consider a new flow with the same/equivalent pressure gradient (EPG), but with uniform and constant density and viscosity distributions,

$$-\frac{\partial\overline{p}_p}{\partial z}+\frac{1}{rRe_0}\frac{\partial}{\partial r}\left(r(\rho_p\nu_{tp}+\mu_p)\frac{\partial\tilde{u}_{zp}}{\partial r}\right)=0 \tag{5.7}$$

where $-\partial\overline{p}_p/\partial z = -\partial\overline{p}/\partial z$ and the subscript 'p' refers to the reference flow condition, which is taken as that at the centreline here. As discussed in the Introduction, the density and viscosity variations have been found to have negligible influence on turbulence dynamics in various previous studies, and that this knowledge has been used in a number of studies as a basis for flow and turbulence scaling [87, 93, 94]. The 'unchanged turbulence dynamics' however can be interpreted in different ways. In the original van Driest analysis for cases where only internal frictional heating was considered, this was taken to be that the mixing length is an invariance in constant and variable density flows. When more complex (heating) conditions are considered in more recent studies (which may involve variations of density and viscosity), additional scaling has been found necessary, including for example the use of the semi-local parameters and a new local Reynolds number (Re^*_τ). Here we follow He et al.'s [13] analysis, assuming the eddy viscosity in the heated flow and its equivalent reference flow are the same, that is, $\nu_t = \nu_{tp}$. Now, subtracting Eq. 5.7 from 5.6,

$$\frac{1}{rRe_0}\frac{\partial}{\partial r}\left(r(\overline{\rho}\nu_{tp}+\overline{\mu})\frac{\partial\Delta\overline{u}_z}{\partial r}\right)+\frac{1}{rRe_0}\frac{\partial}{\partial r}\left(r\big((\overline{\rho}-\rho_p)\nu_{tp}+(\overline{\mu}-\mu_p)\big)\frac{\partial\overline{u}_{zp}}{\partial r}\right)=0, \quad (5.8)$$

which can be re-written with the effects of density and viscosity separated,

$$\frac{1}{rRe_0}\frac{\partial}{\partial r}\left(r(\overline{\rho}\nu_{tp}+\overline{\mu})\frac{\partial\Delta\overline{u}_z}{\partial r}\right)+f_{1b}+f_{1c}=0, \quad (5.9)$$

where

$$f_{1b}=\frac{1}{rRe_0}\frac{\partial}{\partial r}\left(r(\overline{\mu}-\mu_p)\frac{\partial\overline{u}_{zp}}{\partial r}\right) \quad (5.10)$$

and

$$f_{1c}=\frac{1}{rRe_0}\frac{\partial}{\partial r}\left(r(\overline{\rho}-\rho_p)\nu_{tp}\frac{\partial\overline{u}_{zp}}{\partial r}\right). \quad (5.11)$$

We refer to f_{1b} and f_{1c} as the pseudo-body forces due to viscosity and density variations, respectively (Eq. 5.10 & 5.11). They cause a perturbation flow Δu on top of the base (EPG) flow. Like the body-force influenced flow, the heated flow with variable properties can be represented by a constant-property EPG flow plus a perturbation flow i.e., $\overline{u}_z = \overline{u}_p + \Delta\overline{u}_z$. Furthermore the latter (perturbation) is only a function of the non-uniform distributions of the density/viscosity and the eddy viscosity of the EPG flow. In fact, Eq. 5.9 can be rearranged to obtain an explicit expression for the velocity gradient of the perturbation flow as:

$$\frac{\partial\Delta\overline{u}_z}{\partial r}=\left(\frac{(\overline{\rho}-\rho_p)\nu_{tp}+(\overline{\mu}-\mu_p)}{\overline{\rho}\nu_{tp}+\overline{\mu}}\right)\frac{\partial\overline{u}_{zp}}{\partial r}. \quad (5.12)$$

For a general case such as Case A, the flow is also complicated by the spatial development. For the flow away from the immediate start of the heating (say $z/D > 1$), the terms of minor contributions can be neglected and the Favre-averaged streamwise momentum can be written as:

$$-\frac{\partial(\overline{\rho}\widetilde{u}_z\widetilde{u}_z)}{\partial z} - \frac{1}{r}\frac{\partial(r\overline{\rho}\widetilde{u}_r\widetilde{u}_z)}{\partial r} - \frac{\partial \overline{p}}{\partial z} + \frac{1}{rRe_0}\frac{\partial}{\partial r}\left(r(-Re_0\overline{\rho u_z'' u_r''} + \overline{\mu}\frac{\partial \widetilde{u}_z}{\partial r})\right) - \frac{\overline{\rho}}{Fr_0^2} = 0. \tag{5.13}$$

As shown in figure 5.3 & 5.4, the inertia is very significant in the developing flow concerned herein, strongly influencing the flow dynamics. Here, we make a proposition that the inertia can be treated as a pseudo-body force, acting on the flow in a similar way as the buoyancy, and that it does not cause the turbulence to change when compared with the flow of EPG. Under this assumption, we can then group it together with other body forces (pressure and buoyancy) to form the total body force for the flow. Like for the gravity, the inertia can be split into a uniform and a non-uniform component, with the uniform component taken to be the value at the pipe centreline. The total inertial force f_2, its uniform f_{2U} and non-uniform f_{2N} components are then

$$f_2 = -\frac{\partial(\overline{\rho}\widetilde{u}_z\widetilde{u}_z)}{\partial z} - \frac{1}{r}\frac{\partial(r\overline{\rho}\widetilde{u}_r\widetilde{u}_z)}{\partial r}, \tag{5.14}$$

and

$$f_{2U} = f_2(r=0) \text{ and } f_{2N} = f_2 - f_2(r=0). \tag{5.15}$$

The proposition for the linear component is clearly true as physically this implies that the fluid in the entire cross section accelerates as a solid body in response to a uniform body force (pressure or otherwise), without modifying the relative flow (i.e., the strain field). The success of the proposition regarding the non-uniform component and the applicability of the overall non-uniform body effect proposed in He et al. [13] to the flow concerned herein are evaluated in the next section.

Consider all the above analysis together, the heated flow can now be represented by the sum of the EPG flow and a perturbation due to the total body force, which are described by the following equations:

$$-\left(\frac{\partial P}{\partial z}\right)_p + \frac{1}{rRe_0}\frac{\partial}{\partial r}\left(r(\rho_p\nu_{tp} + \mu_p)\frac{\partial \overline{u}_{zp}}{\partial r}\right) = 0 \tag{5.16}$$

and

$$\frac{1}{rRe_0}\frac{\partial}{\partial r}\left(r(\overline{\rho}\nu_{t0} + \overline{\mu})\frac{\partial \Delta\overline{u}_z}{\partial r}\right) + f_T = 0, \tag{5.17}$$

where the total modified pressure gradient is

$$-\left(\frac{\partial P}{\partial z}\right)_p = -\frac{\partial \overline{p}}{\partial z} - \frac{\overline{\rho}_p}{Fr_0^2} + f_{2U}, \tag{5.18}$$

and the total non-uniform body force is

$$f_T = f_{1a} + f_{1b} + f_{1c} + f_{2N}, \tag{5.19}$$

where

$$f_{1a} = (\overline{\rho} - \overline{\rho}_c)/Fr_0^2, \tag{5.20}$$

and the pseudo-body forces are given in Eq. 5.10, 5.11 and 5.15(b). Under the assumptions introduced herein, for any location in the laminarising region of a heated flow, the turbulence dynamics can be approximated by that of the EPG flow (Eq. 5.16), the driving force of which is the total modified pressure gradient (Eq. 5.18). On top of the EPG flow, a perturbation is caused by the combined action of the non-uniform (pseudo-)body forces (Eq. 5.19). In the following section, we evaluate the assumptions introduced above against Cases E and A.

5.3 Evaluation of the apparent Reynolds number analysis of flow laminarization

The profiles of the total shear stresses together with their linear components (extending from the pipe centre) in the laminarising region of Cases A and E are shown in figure 5.8. The total stress were computed from the total apparent body force, $\tau_{tot} = -(r/2)\left(\partial P/\partial z\right)_p + (1/r)\int_0^r r f_T dr$. The first term is the linear component (noted as τ_p), which is used to define the apparent Reynolds number shown in figure 5.9. It is clear that, initially ($z/D < 5$), the apparent Reynolds number ($Re_{\tau p}$) appears to remain largely unchanged, and then it reduces roughly linearly, faster in Case A than in Case E. The $Re_{\tau p}$ reaches around 60 at around $z/D = 15$ and 18 in Cases A and E, where the low Reynolds number would suggest that the flow would approach a laminar state for an equivalent unheated flow.

We first inspect the behaviour of the eddy viscosity to evaluate the applicability of the apparent Reynolds number theory. The distribution of the eddy viscosity in Cases A and E are shown in figure 5.10 against wall unit distance based on three different friction velocity definitions, that is, those based on the unheated flow ($y^{+0} = \overline{\rho}_0 y u_{\tau 0}/\overline{\mu}_0$), the local wall shear stress ($y^{+} = \overline{\rho}_c y u_{\tau}/\overline{\mu}_c$) and the apparent wall shear stress ($y^{+1} = \overline{\rho}_c y u_{\tau p}/\overline{\mu}_c$). Here, $u_{\tau 0} = \sqrt{\tau_{w0}/\overline{\rho}_0}$, $u_{\tau} = \sqrt{\tau_{w}/\overline{\rho}_c}$, and

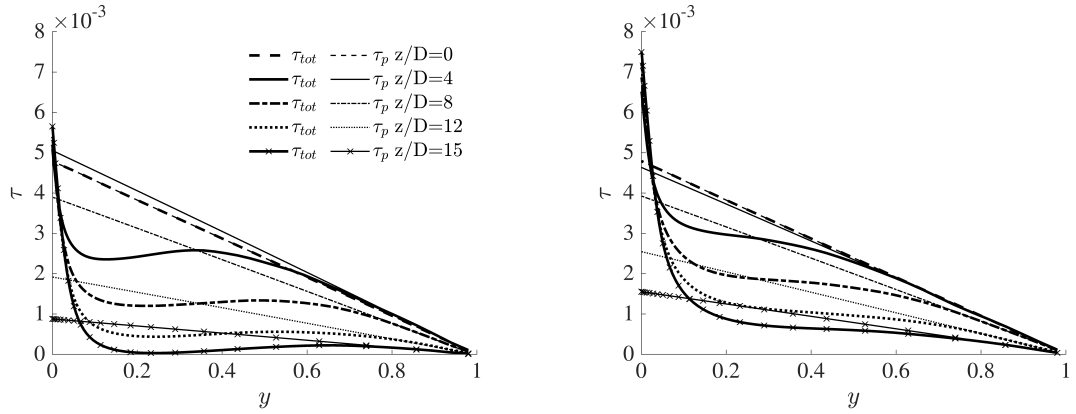

(a) Case A (b) Case E

Figure 5.8: Total body force (including inertia) in Cases A and E.

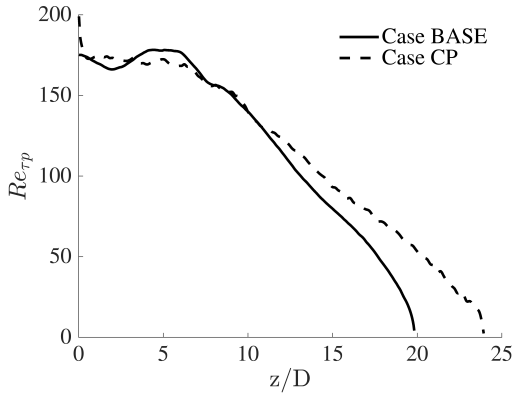

Figure 5.9: The apparent Reynolds number in Cases A and E.

$u_{\tau p} = \sqrt{\tau_{wp}/\overline{\rho}}$, where $\tau_{wp} = -(1/2)(\partial P/\partial z)_p$. The first normalisation shows the absolute changes in eddy viscosity with downstream distance, whereas the second normalisation shows how far the distributions deviate from that of the 'universal' distribution of an unheated flow; and finally the last normalisation would behave as in its corresponding unheated EPG reference flow if the apparent Reynolds number theory applies.

It can be seen from figures 5.10(a and b) that the eddy viscosity at any fixed location in both Cases A and E reduces drastically near the wall. For example, at $y^{+0} = 30$, it reduces from 5.7 to 0.9 in Case E and from 6.8 to 3.0 in Case A. The change is small beyond $y^{+0} = 60$ in Case A, but significant reduction occurs until around $y^{+0} = 100$ in Case E. The behaviour of ν_t versus y^+ is largely the same as that described above though quantitatively the changes are marginally larger due to the increase of the wall shear stresses in the heated pipe. These observations are

consistent with the conventional theory regarding flow laminarisation. The results also show that the flow in the core is less influenced, but the eddy viscosity is of more significance close to the wall where the velocity gradients are larger and the mixing effect due to turbulence is more significant.

In strong contrast, Figures 5.10(e and f) show that ν_t remains largely unchanged in the relaminarising region in both Cases A and E when plotted against y^{+1}. In such low Reynolds number flows, we normally expect that ν_t has some dependence on Reynolds number, that is, it reduces in the core of the flow though it is largely the same close to the wall. To aid discussion, the ν_t in several flows of low Re_τ are shown for comparison. It is clear that close to the wall the ν_t can be reasonably well represented by the apparent Reynolds numbers for both cases. In the core of the flow, however, the ν_t in the heated flow is larger than that in the reference flows, especially in Case A. This is likely a reflection of additional gain due to the convection of turbulence from upstream, and since it largely occurs in the core of the flow, it is not expected to have a significant influence on the overall flow dynamics. Consequently the behaviour of ν_t provides the first evidence supporting the hypothesis that the flow in strongly laminarised flows studied herein can be described by the reduction of the apparent Reynolds number and that the effects of the various factors including variable properties and inertia appear to act in a similar manner, in the form of a (pseudo-)body force.

The normal Reynolds stresses non-dimensionalised using the $u_{\tau 0}$ and $u_{\tau p}$ are shown in figures 5.11 and 5.12 for Cases A and E respectively. The results normalised with $u_{\tau 0}$ are presented for the full pipe length simulated, whereas those normalised by $u_{\tau p}$ are only shown up to the end of the laminraring region where the apparent Reynolds number theory is to be evaluated. It is clear that the Reynolds stresses based on the former normalisation reduce significantly in the laminarizing region in both cases, albeit stronger in Case E than in Case A. The reduction is stronger in the normal and circumferential components than in the streamwise component. For example, the u_r^{+0} and u_θ^{+0} reduce by around 2.5 and 4 times respectively in Case E, but 1.8 and 2.5 times in Case A. When normalised using the local u_τ (not shown), the turbulence reduction is even stronger due to the increase of the wall shear stress in the heated pipe. These results demonstrate that the Reynolds stresses significantly reduce in both absolute terms and when normalised using the wall units as observed in many previous studies (e.g. Bae et al. [11], Peeters et al. [78]).

We now inspect the Reynolds stresses normalised by the apparent wall shear stress and consider Case E first. It is known that the normal and circumferential

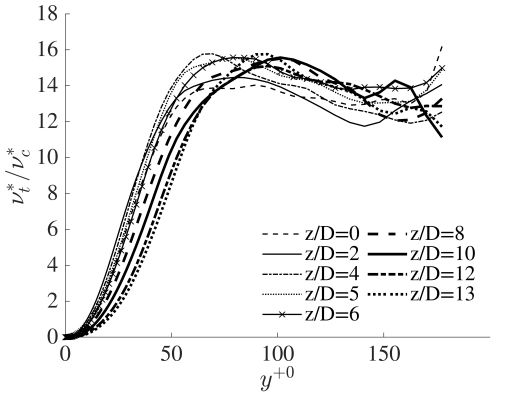

(a) Case A, $\nu_t - y^{+0}$

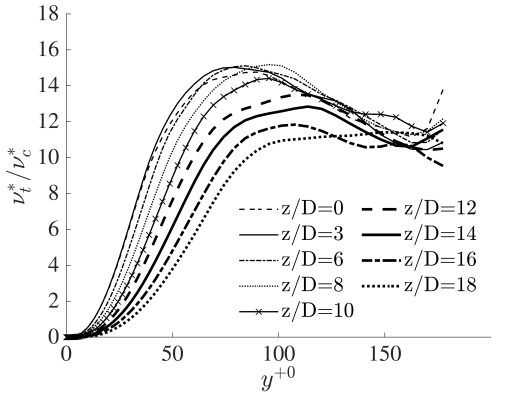

(b) Case E, $\nu_t - y^{+0}$

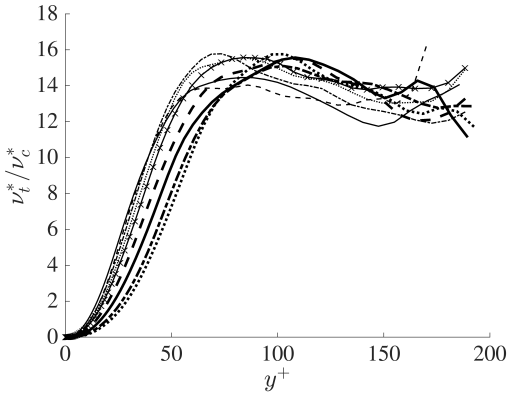

(c) Case A, $\nu_t - y^{+}$

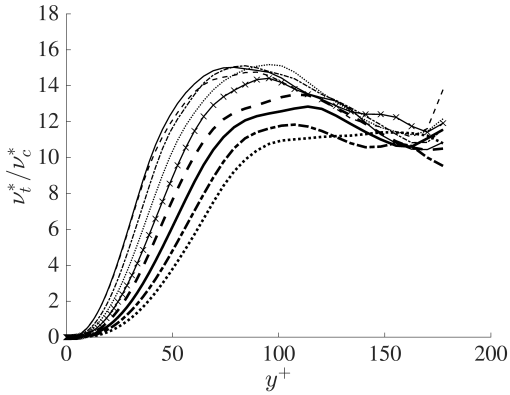

(d) Case E, $\nu_t - y^{+}$

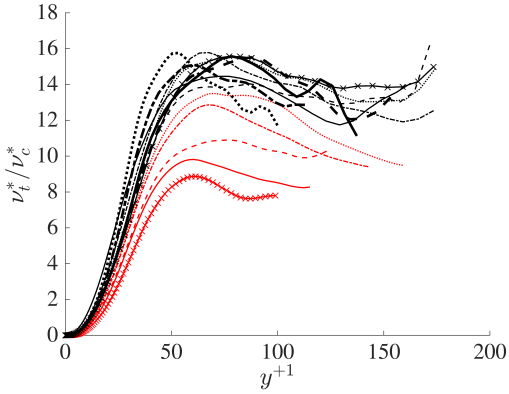

(e) Case A, $\nu_t - y^{+1}$

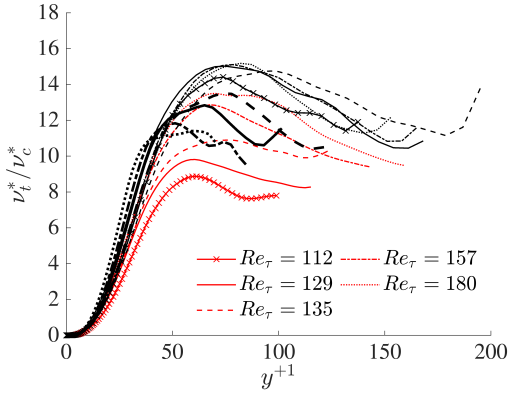

(f) Case E, $\nu_t - y^{+1}$

Figure 5.10: Profiles of the eddy viscosity at chosen locations in Cases A and E.

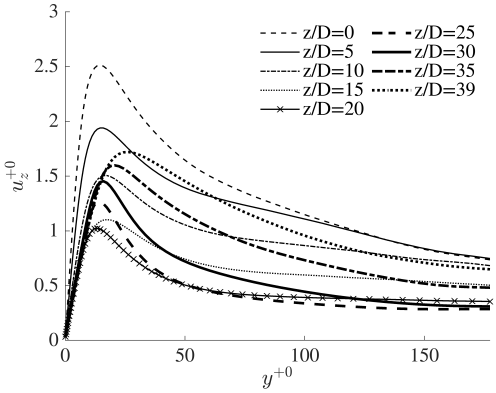

(a) Case E, $u_z^{+0} - y^{+0}$

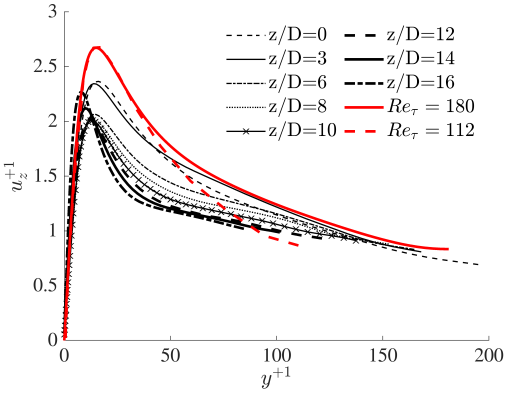

(b) Case E, $u_z^{+1} - y^{+1}$

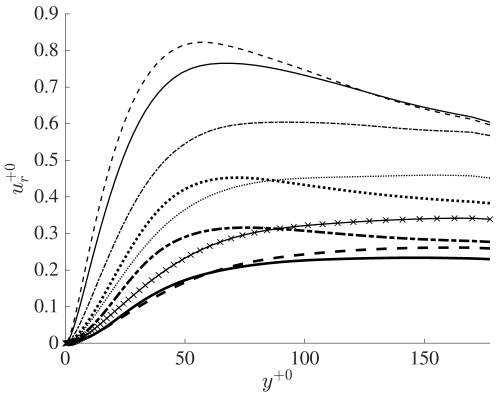

(c) Case E, $u_r^{+0} - y^{+0}$

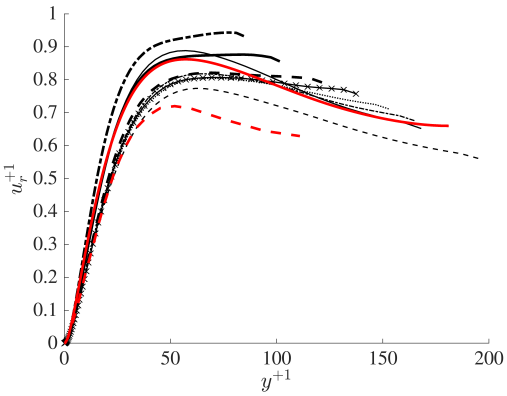

(d) Case E, $u_r^{+1} - y^{+1}$

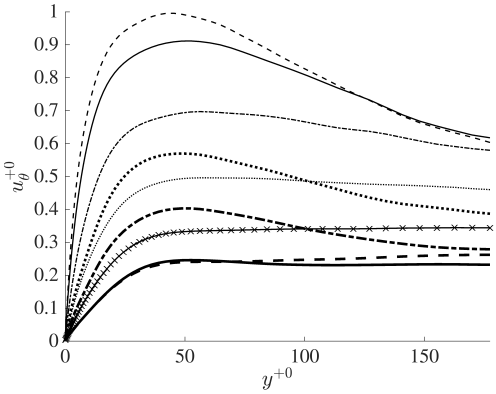

(e) Case E, $u_\theta^{+0} - y^{+0}$

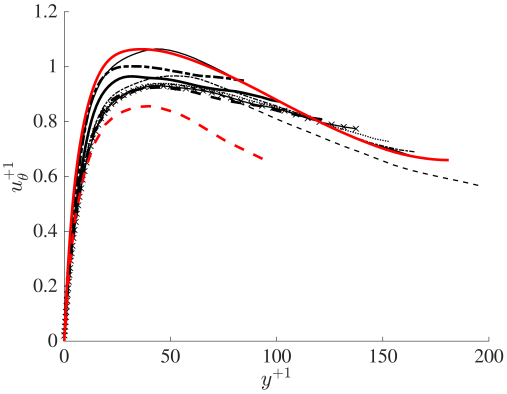

(f) Case E, $u_\theta^{+1} - y^{+1}$

Figure 5.11: The normalized fluctuating velocities in Case E.

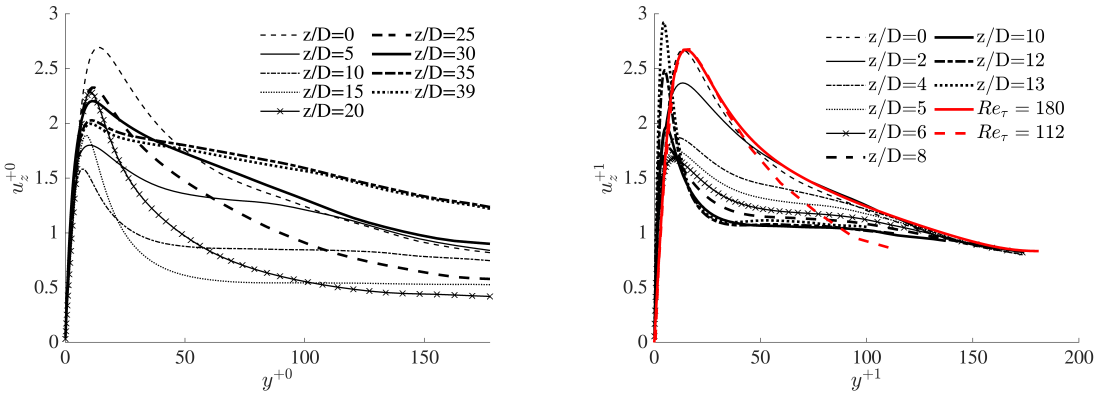

(a) Case A, $u_z^{+0} - y^{+0}$

(b) Case A, $u_z^{+1} - y^{+1}$

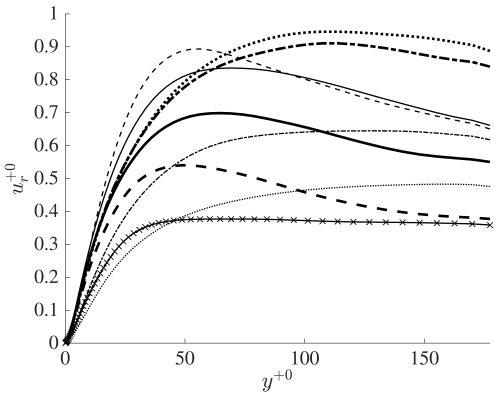

(c) Case A, $u_r^{+0} - y^{+0}$

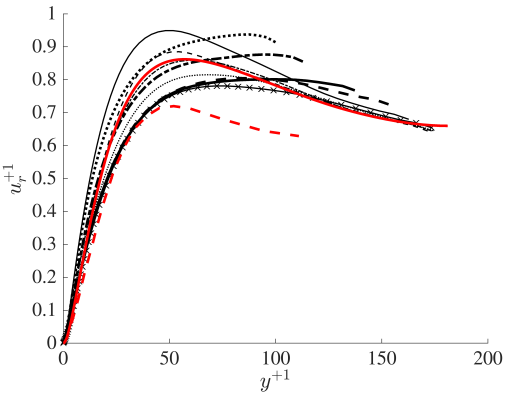

(d) Case A, $u_r^{+1} - y^{+1}$

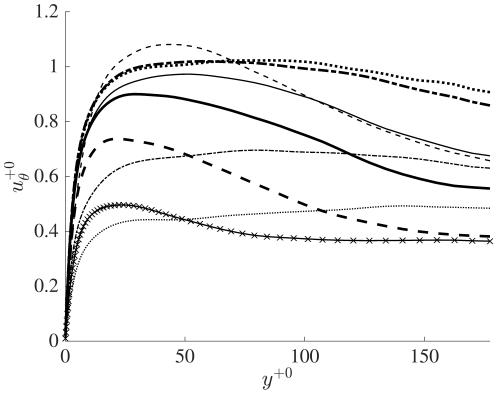

(e) Case A, $u_\theta^{+0} - y^{+0}$

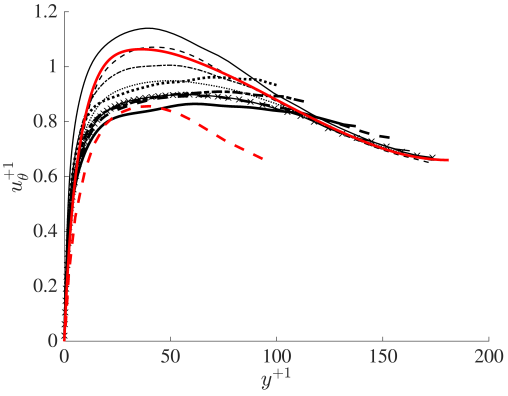

(f) Case A, $u_\theta^{+1} - y^{+1}$

Figure 5.12: The normalized fluctuating velocities in Case A.

stresses reduce slightly with reducing Reynolds number in low Reynolds number flows, but the streamwise component is largely Reynolds number independent. To capture such changes, the profiles for unheated flows at $Re_\tau = 112$ and 180 are shown for comparison. It can be seen from the figure that u_r^{+1} and u_θ^{+1} fluctuate within the bounds of the profiles of the two reference cases, and the changes are within 20%. This is in stark comparison with the drastic reductions observed when normalised by $u_{\tau 0}$ and u_τ discussed above. This finding is in accordance with the findings of He et al. [13], and demonstrates that the two transverse normal stresses normalised by $u_{\tau p}$ can be suitably represented by those of their corresponding EPG flows, and hence again showing that the laminarisation can be represented by a reduction in $Re_{\tau p}$ and all influencing factors represented by pseudo-body forces. In particular, Case E serves to support the conclusion with respect to buoyancy and inertia whereas Case A supports that for all factors combined.

The behaviour of the streamwise component is however different. It reduces with downstream distance even though the peak of the reference results remains unchanged. This trend is opposite to that observed in He et al. [13] in which the streamwise stress is higher than that in the corresponding EPG flow, which was attributed to the generation of streaks. The different behaviours can be attributed to the effect of the inertia which is present in the developing flow concerned here but not in He et al. [13]. As discussed later in section 5.4, the effect of inertia is opposite to other effects reshaping the profile of the non-uniform body forces.

Next we directly evaluate the key statement of the Apparent Reynolds number (ARN), that is, the total flow can be represented by the EPG base flow plus a perturbation induced by the pseudo-body forces, and the latter does not cause any changes to the eddy viscosity. For the flow at any location in the laminarising region concerned here, we can obtain the equivalent pressure gradient via Eq. 5.18, and hence the apparent Reynolds number, which stipulates the EPG flow. Noting that such flows are 'standard' unheated pipe flow, the mean velocity and turbulence statistics of the flow (including the eddy viscosity) can be found from any database available. In addition, the total pseudo-body forces can be calculated (Eq. 5.19) and then the perturbation velocity be estimated via Eq. 5.17. This then enables the total velocity profile to be calculated by simply summing the velocity of the EPG flow and the perturbation velocity. Additionally the perturbation flow induces an additional turbulent shear stress as implied by equation Eq. 5.17, which can be computed as $\Delta\left(\widetilde{u_z'' u_r''}\right) = -\left(\nu_{tp}/Re_0\right)\left(\partial \Delta \overline{u}_z/\partial r\right)$. The total shear stress in the heated flow is then the sum of this and that of the EPG flow.

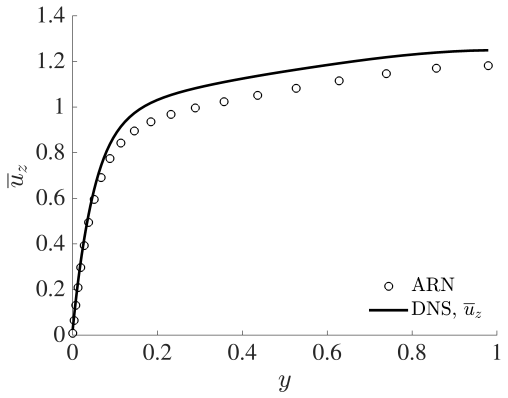

(a) Case E, $z/D = 7.30$

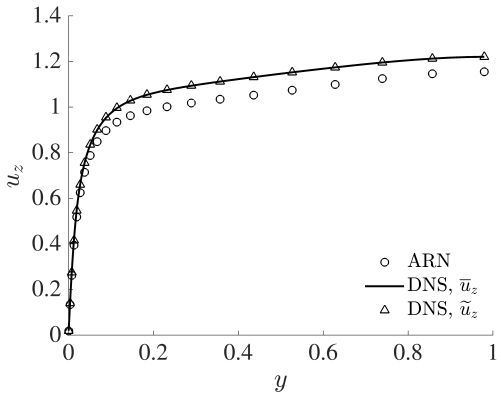

(b) Case A, $z/D = 7.46$

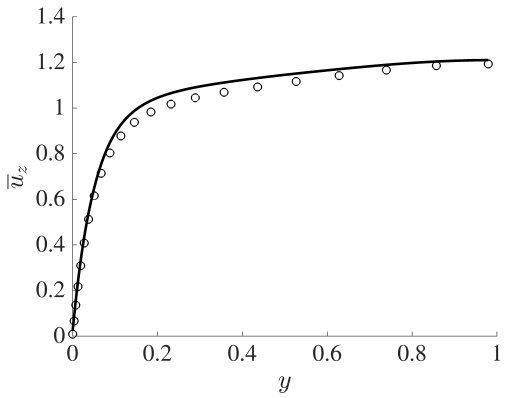

(c) Case E, $z/D = 10.86$

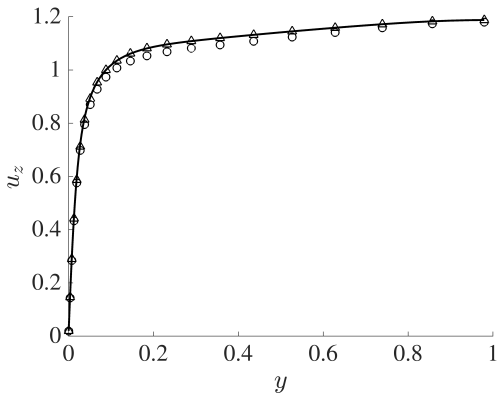

(d) Case A, $z/D = 10.86$

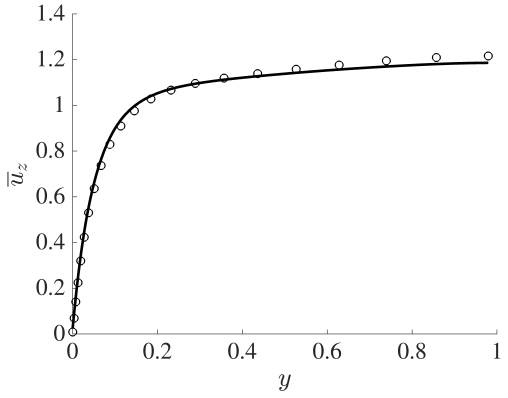

(e) Case E, $z/D = 13.48$

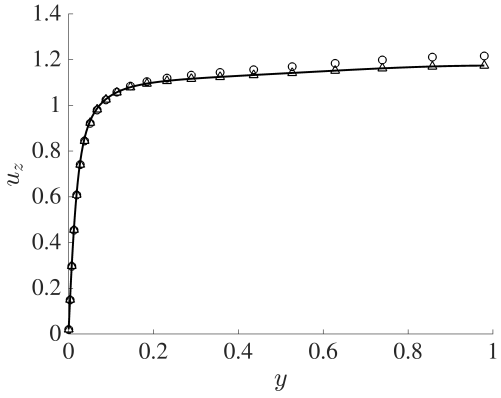

(f) Case A, $z/D = 12.38$

Figure 5.13: Mean velocity in Cases E and A - comparison between the DNS results and the ARN theory predictions at z/D = 7.30, 10.86 and 13.48 in Case E (left column) and 7.46, 10.86 and 12.38 in Case A (right column).

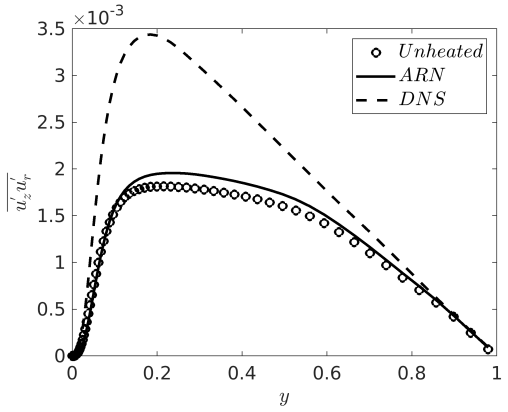

(a) Case E, $z/D = 7.30$

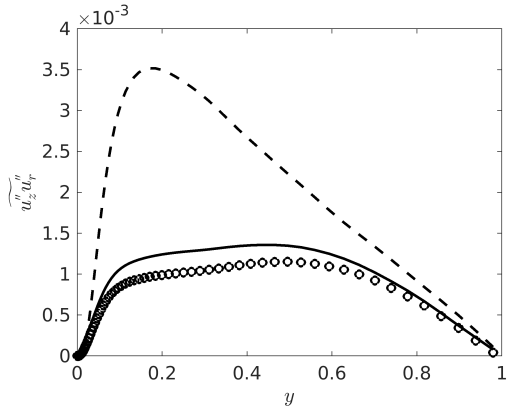

(b) Case A, $z/D = 7.46$

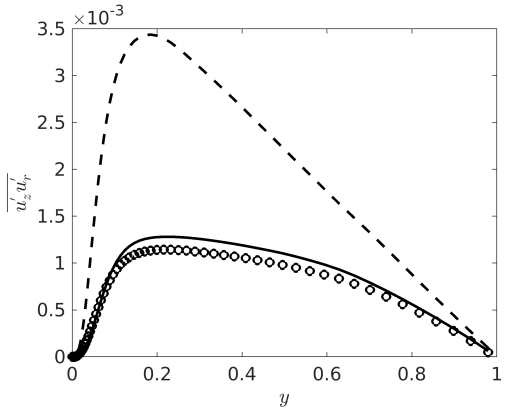

(c) Case E, $z/D = 10.86$

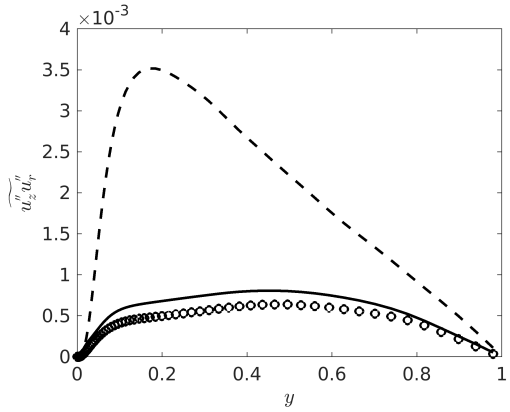

(d) Case A, $z/D = 10.86$

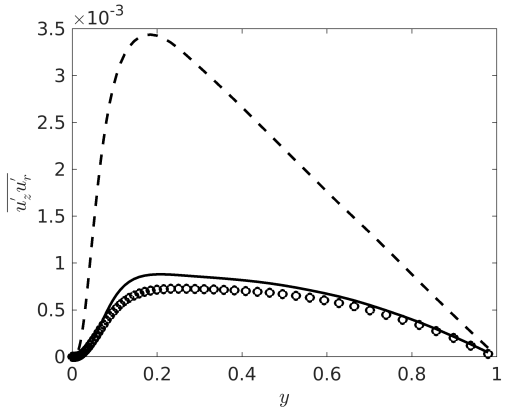

(e) Case E, $z/D = 13.48$

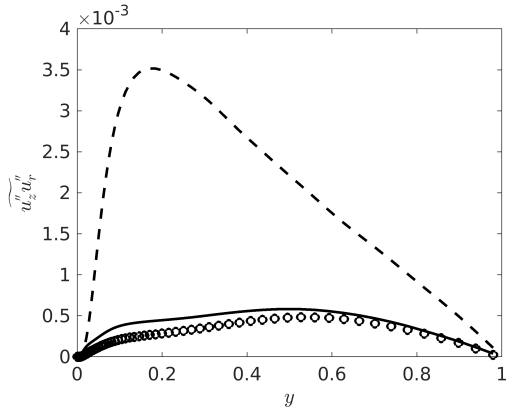

(f) Case A, $z/D = 12.38$

Figure 5.14: The turbulent shear stress in Cases E and A - comparison between the DNS results and ARN theory predictions.

The procedure described above implies that the only information required to 'predict' the mean velocity and turbulence shear stress is the eddy viscosity of the EPG flow having known $\partial P/\partial x$ and f_T of the laminarising flow. Herein the eddy viscosity of unheated reference flow is obtained by interpolation using the data from He et al. [13] for flows at Re_τ between 110 and 180. The EPG and the perturbation velocities are calculated by integrating twice equations 5.16 and 5.17 respectively. The corresponding turbulence shear stresses are then computed from ν_{tp} and the two velocity profiles.

The mean velocity profiles and the turbulent shear stresses calculated using the ARN theory are compared with the DNS data in figures 5.13 and 5.14. It can be seen that the mean velocity of the DNS can be very well represented by the ARN theory at the later locations in both Cases A and E. Larger but still acceptable discrepancies are seen at the earlier position in both cases. The ARN prediction of the turbulence shear stress for Case E agrees very well with the DNS with slightly larger discrepancies away from wall and the pipe centre. The predictions for Case A show larger discrepancies than for Case E, though the strong laminarisation has also been well captured. Overall we consider these results demonstrate that the ARN theory is able to capture the general flow behaviour and laminarisation. It should be noted however that the above exercise does not really provide any predictions of the heated flow, since it uses the thermophysical property distributions and the inertial terms from the DNS. It however provides new insights into the effects of the various factors on turbulence dynamics and flow laminarisation. It is possible to utilise such new understanding in future to improve modelling strategies, for example, following the work by Patel et al. [95].

5.4 A unified approach for the explanation of laminarisation in a heated pipe

The results presented above suggest that the mechanisms of the flow laminarisation due to buoyancy and variations of density and viscosity can potentially be explained in a unified approach using the apparent Reynolds number theory. It also suggests that the flow inertia plays a significant role, and that it can be viewed as a pseudo-body force, the effect of which can also be explained in the same framework. The overall idea is illustrated in figure 5.15, which is discussed in this section. Like in the last two sections, this discussion is for the laminarising stage of the flow and considering only the indirect effect of variable properties on turbulence. The direct

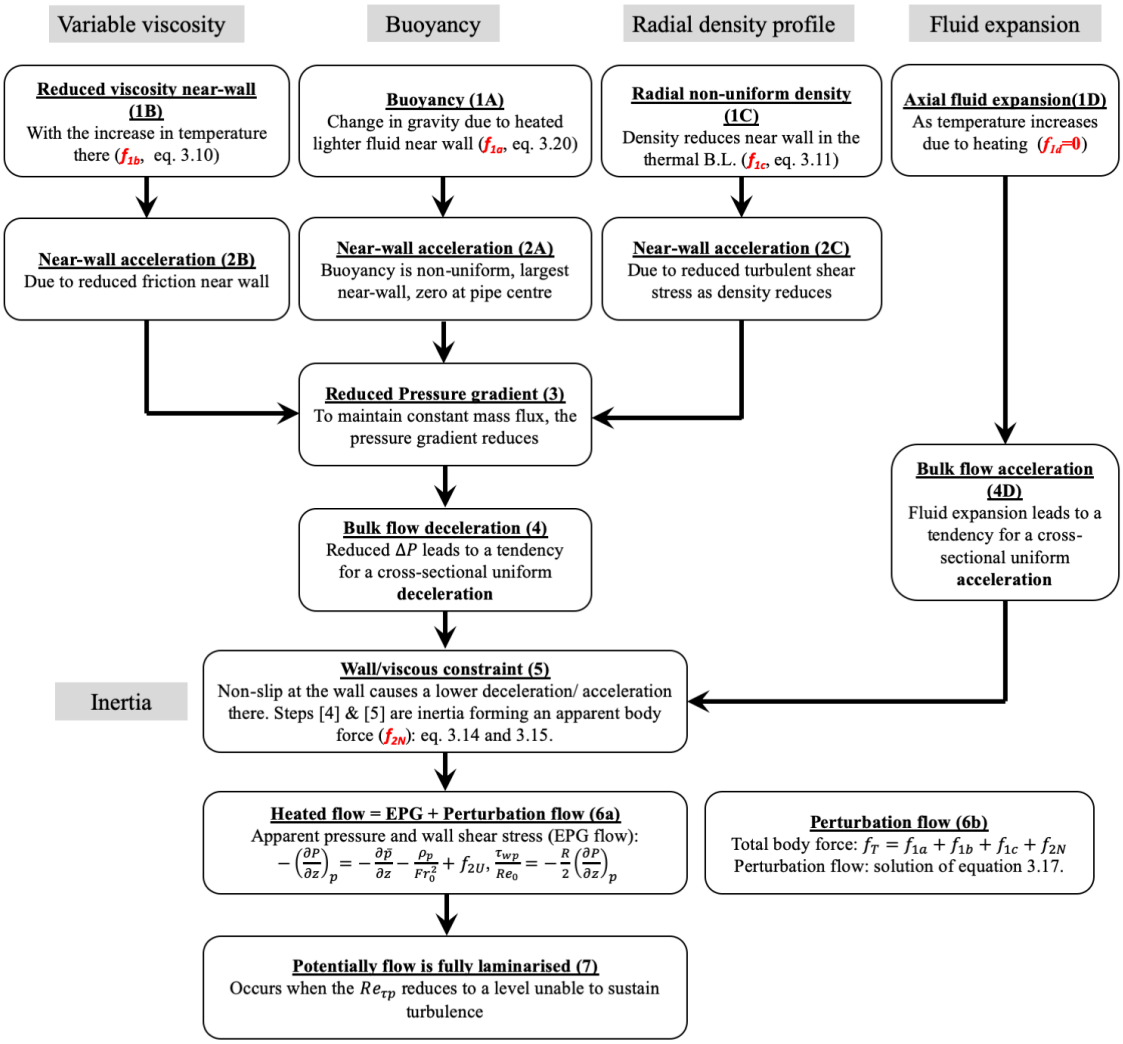

Figure 5.15: A unified theory for flow laminarization in a vertical heated flow

effect will be discussed in the next section and it will be seen that the effect in the laminarising stage is relatively small.

We consider the buoyancy effect first and stages [1A] and [2A] are well known: The heated fluid near the wall becomes lighter resulting in an upward buoyancy force, which in turn causes the fluid there to accelerate in relation to the fluid in the core. Since we are considering a constant mass flux flow, the above two factors necessitate the pressure force (gradient) to reduce [stage 3], which in turn causes the flow tend to decelerate uniform across all radial locations since the pressure is largely uniform radially away from the immediate inlet [stage 4]. The deceleration of the fluid in the region close to the wall is however hindered by viscosity and the no-slip condition on the wall. As a result, the deceleration is uniform in the core of flow but gradually

reduces towards wall and reaching zero on the wall [stage 5]. The region of reduced deceleration is initially limited to a small region close to the wall, but it expands away from the wall with distance downstream.

Consequently, there are two non-uniform body forces involved in a heated developing flow (neglecting other effects for now, e.g., considering Case E), the buoyancy body force f_{1a} and the non-uniform part of inertia, f_{2N}. With the increase of the combined effect of the buoyancy and inertia, the apparent Reynolds number and the corresponding EPG flow reduce, leading to lower turbulence [stage 6]. When the $Re_{\tau p}$ continues reducing and reaching a sufficiently low value, turbulence production may be switched off and the flow is then fully laminarised (see further discussion on 'fully' in the next section) [stage 7].

Next consider viscosity and figure 5.2 shows that it reduces significantly close to the wall along with the increase of the temperature in this region from an early stage following the commencement of heating in Case A [stage 1B in figure 5.15]. This leads to a reduction in frictional resistance in the wall region, and hence a tendency for the fluid to accelerate there [stage 2B]. This is then followed by a process that is very similar to that due to the effect of buoyancy. That is, due to the constant mass flux constraint, the pressure gradient reduces [3], which causes the fluid to decelerate uniformly across the whole cross section [4]; but again the viscosity near the wall restricts the deceleration there [5], and so on. It is clear that both [2B] and [5] causes the velocity profile to be flattened.

Even without considering the structural effects, the (indirect) effects of density variations on flow dynamics are far-reaching, including, buoyancy, flow acceleration caused by fluid expansion and radial non-uniform distribution. These effects can be associated with the buoyancy term, the inertial (spatial acceleration) terms and the turbulent shear stresses of the momentum transport equations (Eq. 5.13). The buoyancy has already been extensively discussed. We now turn our attention to the effect of the flow acceleration, a topic that has been investigated by numerous researchers. It is known that when the hydraulic diameter of the channel is small, flow acceleration effect is often higher than that of buoyancy under strong heating [79, 80]. The effect comes from the fact that the bulk fluid temperature increases with distance downstream due to heating, which results in a density reduction everywhere across the pipe section [stages 1C/4C]. This hence causes the fluid tend to accelerate, stronger near the wall in the entrance region, but mostly uniformly across the radius in downstream locations. The expansion does not directly results in a change in mass flux, and hence unlike in the cases of the buoyancy and viscosity, there is not a direct

consequential reduction in pressure gradient in this case (see figure 5.15). In fact, to cause the flow acceleration, there is a need for an increase in pressure gradient. Again due to the constraint of the wall/viscosity, the near-wall acceleration is hindered and being smaller than in the centre and hence resulting in a flattened velocity profile [5C]. It is worth noting that the inertial/viscous effect in this case is opposite to that in the buoyancy and variable viscosity. That is, the viscous effect near the wall hinders the acceleration (rather than deceleration) of the fluid in the pipe and hence the combined effect of 4C and 5C causes an apparent body force in the direction of the flow.

Unlike the buoyancy and flow acceleration, the radial non-uniform density distribution associated the turbulent shear stress terms is seldom explicitly discussed for heated pipe flow at supercritical pressure. This is however the effect that considered in the van Driest transformation [85], and more recent studies of near wall flow scaling [93, 94]. In all these studies, it is assumed that the density variations do not influence turbulence structures under the condition of small fluctuations (the Morkovins hypothesis), which is interpreted as that the mixing length correlation remains unchanged in the scaling analysis. Under this assumption (or, similarly, the eddy viscosity remains largely unchanged), the significant reduction in density near the wall (figure 1) [Stage 1c] results in a reduction in flow resistance due to the reduced turbulent shear stress (that is, $\widetilde{\overline{\rho}u_z''u_r''}$ reduces because $\overline{\rho}$ reduces strongly whereas the changes of the $\widetilde{u_z''u_r''}$ are minor), and hence a local flow acceleration in that region [stage 2C). This is then followed by a process that is similar to that in the case of buoyancy and viscosity variations: the local flow acceleration necessitates a reduction in pressure gradient [3] under constant mass flux constraint, leading to a whole cross-sectional flow deceleration [4], and so on (figure 5.15).

In summary, the above discussion outlines a unified explanation for the various mechanisms of flow laminarisation in a heated vertical pipe flow. Following a primary cause of change in a heated flow, that is, either the buoyancy, or the variations of density or viscosity, a local change in mass flux occurs near the wall. This then leads to a response in the pressure gradient due to the continuity constraint, which causes a tendency of a uniform bulk fluid acceleration or deceleration balancing the near wall mass flux changes. The no-slip condition on the wall however restrains such changes near the wall resulting in a smaller acceleration/deceleration there, and hence a distortion in velocity profile. These last stages (stages 4 and 5) are the effects of inertia (spatial acceleration) reflected as the so-called entrance effect, or

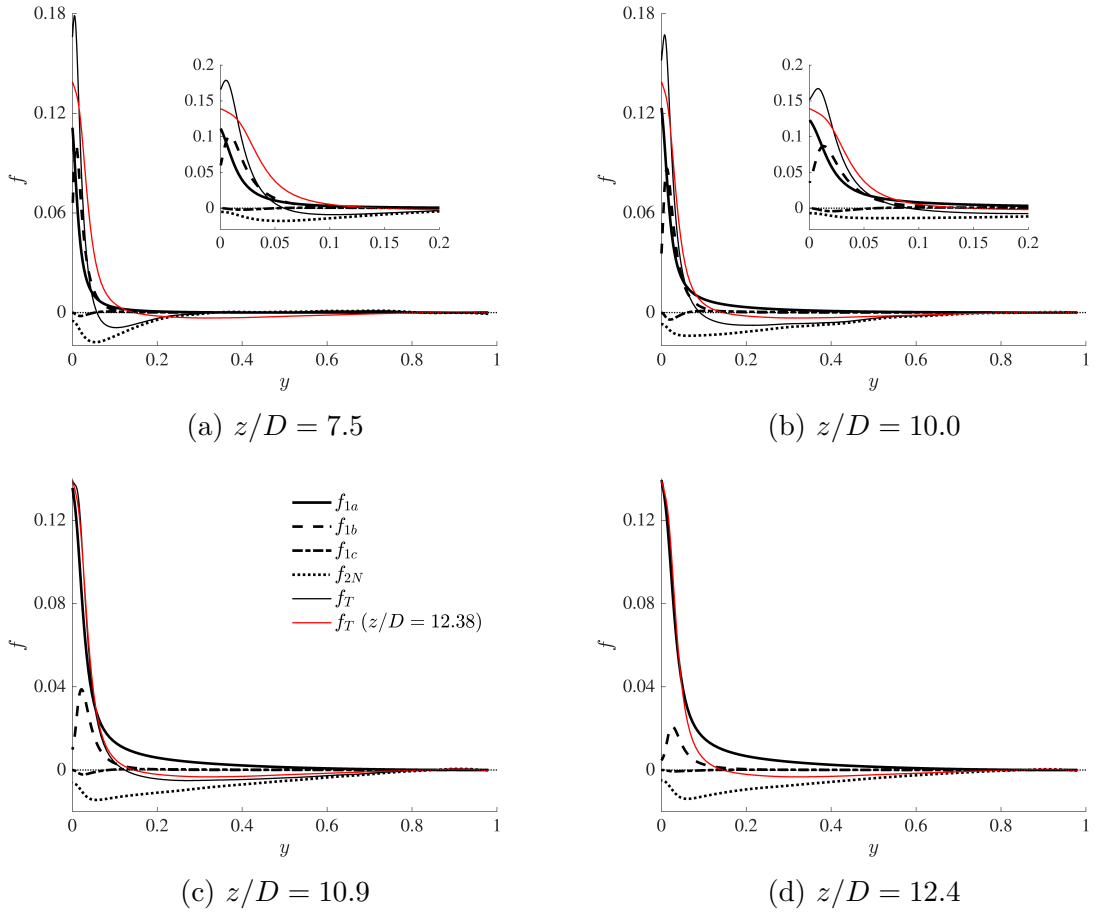

(a) $z/D = 7.5$ (b) $z/D = 10.0$

(c) $z/D = 10.9$ (d) $z/D = 12.4$

Figure 5.16: Comparison between the various pseudo-body forces in Case A at several streamwise locations.

more generally, a spatially developing flow. The effect of the bulk fluid expansion is slightly simpler, directly causing an 'inertial' effect.

Even though we have concluded that the non-uniform body force does not directly cause changes in turbulence, it is clear from the above discussion that they are in fact the reasons for flow laminarisation in a fixed mass flux flow such as this. This is because the total flow comprises the EPG flow plus the non-uniform body force induced perturbation. As the body forces increase, they cause an increase in the perturbation flow; to maintain the total flow, the EPG flow reduces, leading to a reduction in turbulence. Hence the great the non-uniform body forces the stronger the laminarisation.

The (pseudo-)body forces at several streamwise locations in Case A are shown in figure 5.16. Since Eq. 5.17 for the perturbation flow is liner, the different mechanisms act independently and their effects on producing the perturbation flow can simply be

added together. It can be seen that in the flow concerned here (Case A), among the primary causes (first line in figure 5.15), the buoyancy (f_{1c}) is most significant followed by the variable viscosity (f_{1b}). The effect of non-uniform density through turbulence shear (f_1c) is very small. The inertia (f_{2N}) is always strong and it acts against the primary forces, i.e., reducing or delay their effects, which is consistent with our understanding. This also explains the differences between the behaviours of the streamwise turbulence stress in the developing flow considered here and those considered in He et al. [13]. The non-uniform body in the latter causes strong streaks and hence an increase in streamwise turbulence, but the inertia in the flow considered here largely cancel that effect. One can also relate the effects of the positive/negative body forces studied here with the increasing/decreasing Re_τ^* of Patel et al. [94], though it is out of the scope of this study.

5.5 'Full' laminarisation and retransition

In this study, the 'fully' laminarised region is defined such that the start of the region coincides with the location where the streamwise turbulence reaches its minimum and the end of the region coincides with the location where the transverse Reynolds stresses reach their minima. During this period, the pressure strain is minimum as shown in figure 5.6 & 5.5, where the budgets of the streamwise turbulence in Cases A and E are shown. The full laminarisation occupies $12 < z/D < 18$ in Case A and $18 < z/D < 28$ in Case E. It is clear that in this region turbulence kinetic energy still remain very significant in both cases despite much lower than that in the unheated flow. The terminology, 'full' laminarisation, used here refers to the fact that the turbulence regeneration cycle largely ceases despite there being strong generation of low-speed streaks as discussed below.

It can be seen from figure 5.1 that the turbulence shear stress is close to zero everywhere in the cross section towards the end of this period, i.e., at around $z/D = 18$ and 28 in Cases A and E respectively. This is roughly the time when the mean velocity switches from a normal central-peaked profile to an M-shape in which the peak moves away from the pipe centre. The reason that the turbulent shear stress is nearly zero at this stage is that the velocity gradient in most part of the flow is very small except very close to the wall, making the correction $\overline{\rho u_z'' u_r''}$ to diminish to minimum. However, the turbulent activities including mixing for example is still strong at this stage, and the turbulent heat flux is still quite large [11].

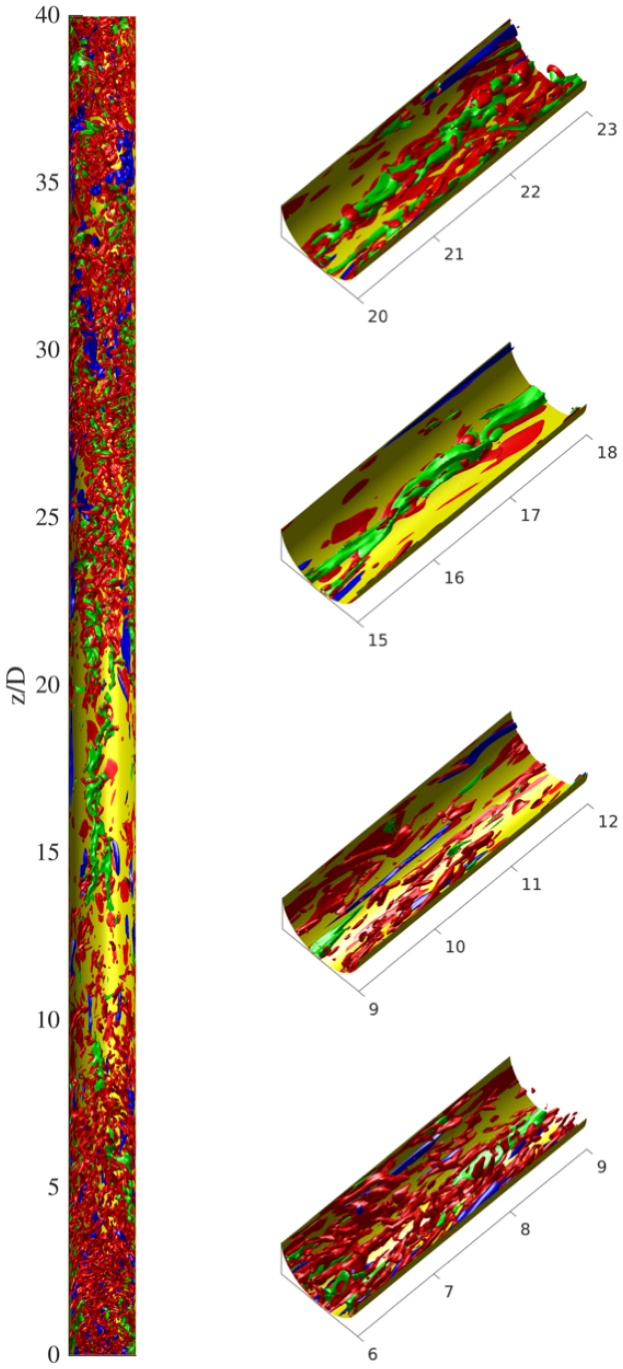

Figure 5.17: Turbulent streaks and vortical structures in Case A ($u'_z = \pm 0.19$ in green and blue respectively, $\lambda_2 = -0.6$ in red). Only half of the pipe is shown and the full-length pipe is shrunk axially.

The shear production remains at a minimum level in the full laminarisation region as can be seen in figure 5.6. In Case A, it approaches zero towards the end of the region, and slowly builds up downstream. Incidentally, there are two peaks now which was observed in various previous studies [11]. The near wall peak is in between the wall and the velocity peak and is stronger. The second peak in the production is in the core of the flow, where both $\overline{\rho u_z'' u_r''}$ and the velocity gradient have changed sign. In Case E, the shear production becomes slightly negative and stays negative for quite some distance ($25 < z/D < 35$). This is mostly in the near wall region. Here, the sign of velocity gradient remains unchanged but $\overline{\rho u_z'' u_r''}$ has changed sign. The negative production implies that in this region the shear extracts energy from the turbulent motions and feeds it back to the mean flow, and hence leading to an inverse cascade. Towards the end of the simulated domain, the shear production becomes mostly positive across the pipe section with also two peaks as in Case A.

For both Cases A and E, the buoyancy production is small and negative (figures 5.6 & 5.5) at the early stages of the heating section (laminarising region). However, it plays a major role in the flow laminarisation and recovery regions, being much stronger than the shear production. Close to the start of the laminarisation stage, the buoyancy production becomes positive, and then increases rapidly with distance, becoming very significant around the point when the shear production is weakest. In the case of A, the peak buoyancy production has maximised at around $z/D = 22$, and then reduces gradually with distance downstream. The peak value becomes lower than that of the shear production around $z/D = 28$. However, the shear production is only significant around the first peak, and is limited to small region ($y^{+0} < 10$). The buoyancy production however peaks at round $y^{+0} = 12$ and is significant over a bigger region towards the core of the pipe. As a result, in terms of the total cross sectional contribution, the buoyancy production maintains roughly a constant value from $z/D = 20$ and is the dominant contributor until the end of the pipe simulated (figure 5.6). In the case of E, the peak of the buoyancy production increases steadily throughout the later part of the pipe. The cross sectional integration increases significantly downstream due to the spread of the region where the production is significant. Consequently these results demonstrate that the buoyancy production is responsible for the re-generation of turbulence and the dominant contributor to the continuing increase of turbulence further downstream.

We now look at the flow from the viewpoint of transition. Similar to the shear production, the production due to buoyancy is only significant in the streamwise Reynolds stress ($\widetilde{u_z'' u_z''}$) and the energy produced is then re-distributed through pressure strain

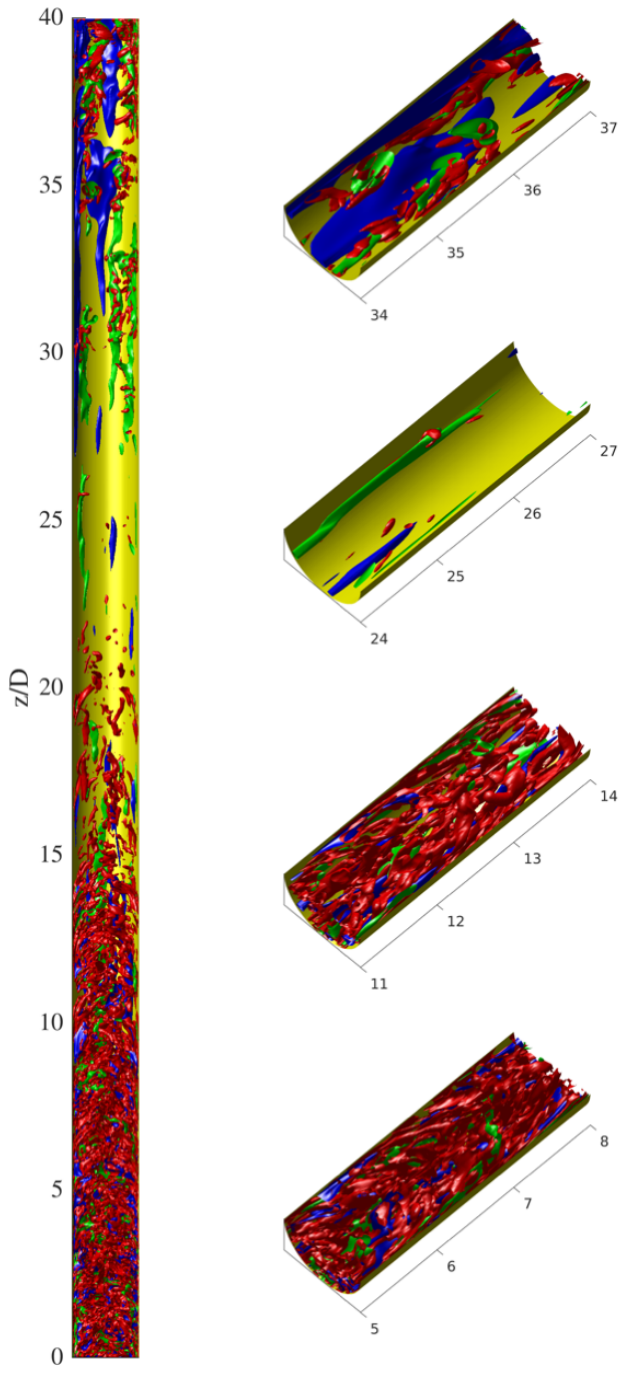

Figure 5.18: Turbulent streaks and vortical structures in Case E ($u'_z = \pm 0.12$ in green and blue respectively, $\lambda_2 = -0.15$ in red). Only half of the pipe is shown and the full-length pipe is shrunk axially.

work to other components. In Case A, the buoyancy production becomes positive at around $z/D = 12$, which is roughly coincident with the location where $\widetilde{u_z'' u_z''}$ is the lowest. The energy in $\widetilde{u_z'' u_z''}$ starts to increase near the wall after this point clearly due to the buoyancy production. The transverse Reynolds stresses ($\widetilde{u_r'' u_r''}$ and $\widetilde{u_\theta'' u_\theta''}$), however, continue to reduce until around $z/D = 18$. This observation is consistent with that in the bypass transition in transient flow (He and Seddighi [132, 146]). Hence, we named this flow stage the 're-transition' stage, which represents the turbulence increases again after being laminarised. The initial generation of $u'_{z,rms}$ ($z/D = 12$ to 18) is likely linked to the formation and elongation of high- and low-speed streaks. Only at around $z/D = 18$, such streaks start breaking down forming turbulent spots where vortices of various small scales are generated. This process can be viewed in figures 5.17 and 5.18, where the isosurface plot of $u'_{z,rms}$ and λ_2 are shown. In Case A, between $z/D = 12$ and 18, even though the $u'_{z,rms}$ increases significantly the turbulence vortices remain the lowest, and they start to appear only after $z/D = 18$. In Case E, the turbulent vortices remain very low over a large section of the pipe and the regeneration of turbulence remains weak even at the end of the simulated domain. Additionally, figure 5.19 shows a quadrants analysis for the turbulent activities in Case A, in which both weak (H=0) and strong events (high H=2, 4) are shown for the ejection (Q2) and sweep events (Q4). Both events reach very low level (especially the strong events) during the full laminarisation stage. However, sweeps appear to reach its minimum at the middle of this region and starts to increase gradually at the second half region, while the ejections only start to recover some distance after the end of this region. For Case E, the buoyancy production becomes positive at around $z/D = 19$, which again coincides with the location where $\widetilde{u_z'' u_z''}$ is the lowest. The $\widetilde{u_z'' u_z''}$ starts to increase rapidly following this but the transverse components continue to reduce until about $z/D = 30$. During all this stage ($z/D > 19$), the shear production is either very low or slightly negative, and turbulence is mostly generated due to buoyancy production.

It can now be concluded that in the 'fully' laminarised flow region, the coupled sequential streaks and vortices generation of the turbulence regeneration cycle associated with the initial shear flow has largely ceased. The pressure-strain also approaches zero, indicating that the vorticity generation has become minimum. Nevertheless, turbulence fluctuations are still in existence. In fact, right from the start of this stage, buoyancy turbulence generation has started in the form of new elongated streaks, which leads to an increase in $\widetilde{u_z'' u_z''}$ in the wall region. Consequently, the region of laminarisation discussed here is not complete consistent with that used commonly in

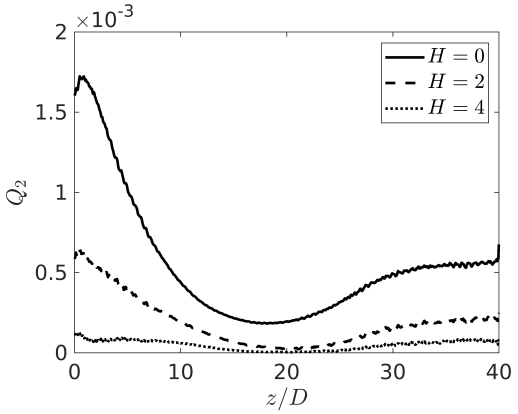

(a) Case A, sweep event ($Q2$), $y^{+0} = 15.3$

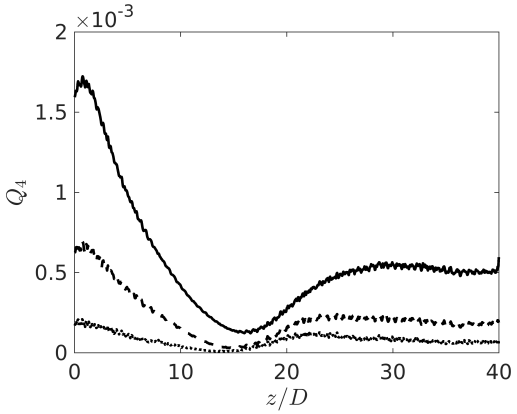

(b) Case A, ejection event ($Q4$), $y^{+0} = 15.3$

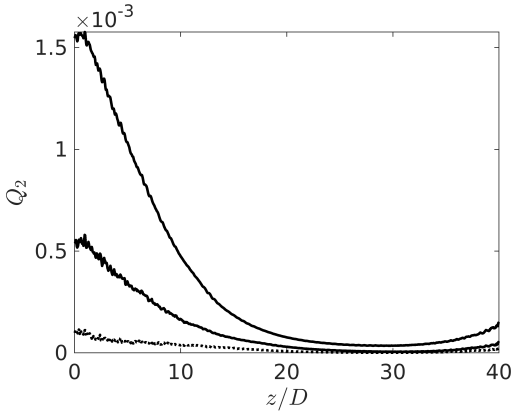

(c) Case E, sweep event ($Q2$), $y^{+0} = 16.5$

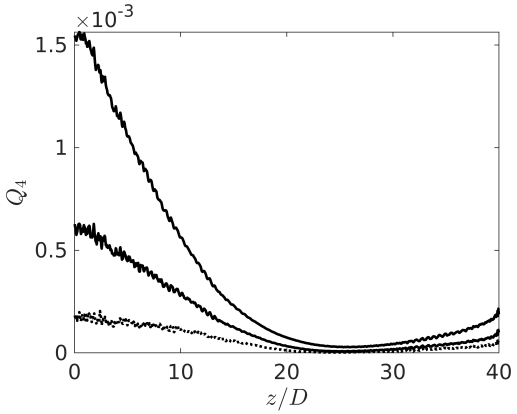

(d) Case E, ejection event ($Q4$), $y^{+0} = 16.5$

Figure 5.19: Variations of sweep and ejection events at near-wall locations of Cases A and E.

the literature in which laminarisation normally refers to zero turbulent kinetic energy or turbulence production. The re-transition considered herein refers to the stage where new turbulence spots and multi-scale vortical structures start appearing, which may be significantly later than the initial recovery of turbulence kinetic energy related to the generation of streaks, an phenomenon occurs at the pre-transition stage. Key observations in the three stages of a heated flow are illustrated by the contour of $(\rho u_z)'$ at a near-wall surface of case E (Fig. 5.21).

During the full laminarisation stage, the energy of streamwise turbulence at locations away from the wall, and the transverse turbulence components everywhere continue decaying. In fact, in the core region, the turbulence behaves in a manner similar to the decay of grid generated homogeneous turbulence, which is known to behave as $k/u_z^2 = c((x - x_0)/M)^{-n}$, where x_0 is the virtual origin and n is between 1.15 and 1.45 [147]. The transport equations for turbulence kinetic energy and its

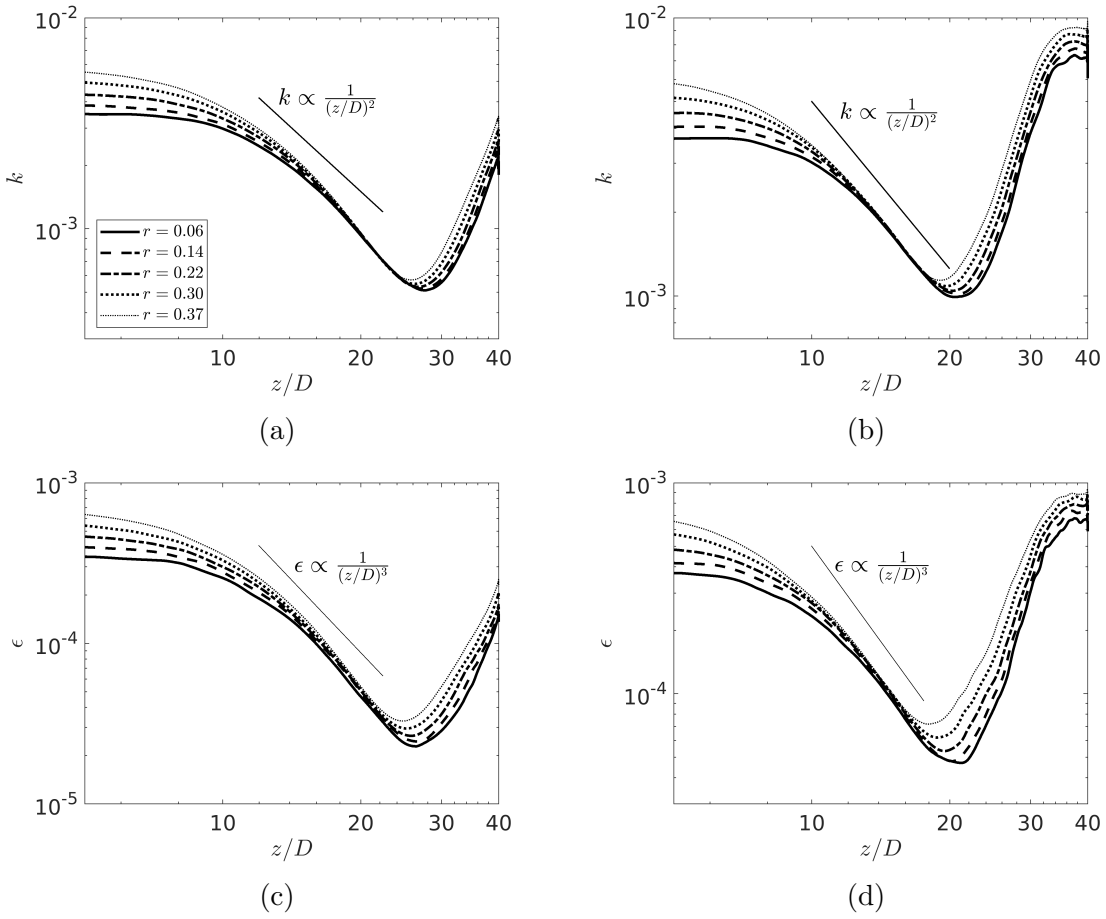

Figure 5.20: Decay of the turbulent kinetic energy and its dissipation rate in Cases A and E.

dissipation for such a flow can be written as:

$$\overline{u}_z \frac{\partial k}{\partial z} = -\epsilon, \overline{u}_z \frac{\partial \epsilon}{\partial z} = -C_{\epsilon 2} \frac{\epsilon^2}{k} \tag{5.21}$$

where $C_{e2} = 1.9$. The above also suggests that $\epsilon \propto x^{-(n+1)}$. It can be seen from figure 5.20 that turbulence kinetic energy in the core of the pipe ($r < 0.4$) during the 'full' laminarisaed region indeed decays in an exponential manner. But the exponent is significantly highly than that of a grid turbulence, being around 2. Consistently, the turbulence dissipation decays also exponentially with an exponent of 3. Additionally, we have computed C_{e2} from Eq. 5.21, (that is assuming a convective decaying turbulence). The value is mostly between 1.5 and 2.0 in the fully laminarised region but being significantly different from this value elsewhere. The observation described above is typical of the pre-transition stage of boundary layer bypass transition in which elongated streaks are formed within the boundary layer whereas the

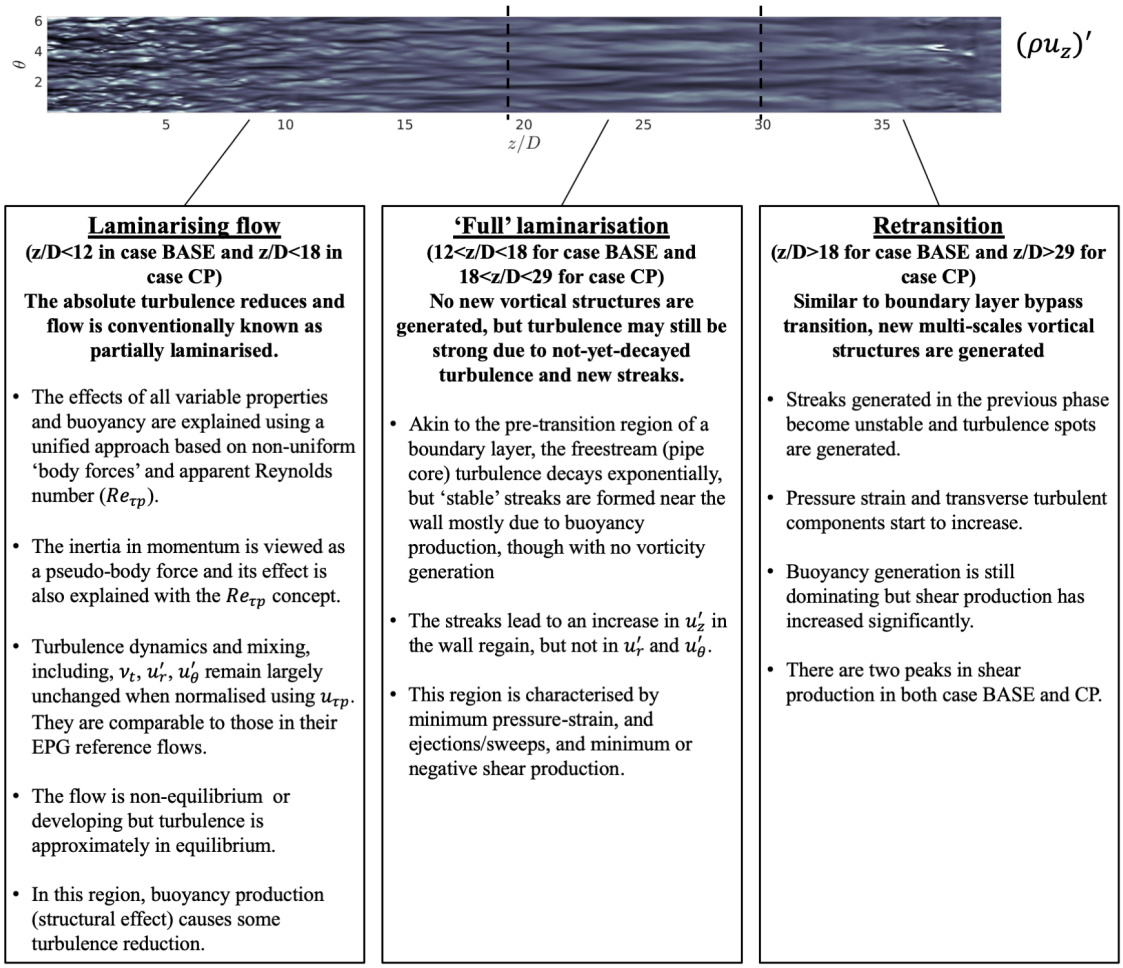

Figure 5.21: Turbulent dynamics in a vertical heated flow.

free-stream turbulence decays exponentially [148, 149, 150].

5.6 Conclusions

Cases A & E from Chapter 4 is further analysed in this part of work, new understanding has been established of the turbulence dynamics with respect to its three-stage development, that is, partially laminarising, full laminarisation and re-transition stages. The main findings are as follows:

- The effects of buoyancy and variations of density and viscosity on turbulence (and laminarisation) together with those of inertia are explained using a unified theory based an apparent Reynolds number (ARN) and a non-uniform pseudo-body force concept. The partially laminarising flow is represented by

an equivalent pressure gradient (EPG) base flow plus a perturbation caused by the various (pseudo-) body forces.

- In this paper, the 'full' laminarisation refers to a region where the turbulence regeneration cycle has ceased, but typically turbulence kinetic energy is still significant in the flow. There can still be strong turbulence generation due to buoyancy production resulting in the generation of high-/low-speed streaks near the wall. Away from the wall, turbulence decays exponentially with downstream distance.

- Transition is marked by the generation of the transverse turbulence components and the associated increase of pressure-strain in Reynolds stress budgets.

The above is further expanded below with the key points illustrated in figure 5.21.

1. **Laminarisating flow**

   The flow laminarising region occupies $z/D < 12$ in Case A and $z/D < 18$ in Case E. The flow at any streamwise location can be represented by its equivalent-pressure-gradient (EPG) flow and a perturbation flow caused by the pseudo-body forces due to the various mechanisms. The stronger the buoyancy or property variations, the greater the pseudo-body forces, which in turn causes a larger perturbation flow. For the flow in a pipe with a fixed mass flux, this means a smaller EPG flow, and hence lower turbulence. When the Reynolds number of the EPG flow (i.e., the $Re_{\tau p}$) reduces to a very low level (say, $Re_{\tau p} < 80$), the flow may be fully laminarised. In this theory, the laminarising flow can be estimated using the knowledge of the EPG flow and the (pseudo-)body forces without solving the non-equilibrium turbulent flow. This theory is based on a hypothesis that the buoyancy, variable properties and the inertia do not alter the key turbulence characteristics including the mixing effect. It then follows straightforwardly that all effects can be expressed as a pseudo-body force. The hypothesis was shown in [13] to be true for non-uniform body forces in an isothermal flow. With regard to the effect of variations of density and viscosity, a similar hypothesis was proposed and used in previous studies, including [87, 93, 94], and the well-known van driest transformation (for density only) [86]. In present study, the hypothesis has been extended to include not only all the physical effects (variable properties and buoyancy), but also the spatial

acceleration, hence establishing a unified theory for the explanation of laminarisation in a heated flow. The hypothesis is demonstrated in section 5.3 to be true using the Boussinesq-assumption based flow and a flow with a full account of all thermophysical property variations.

- There are a number of primary causes (mechanisms) to make a heated vertical flow to be different from an unheated flow, that is, the buoyancy, the variations of viscosity, the flow acceleration due to fluid expansion caused by heating and the radial variation of density resulting in a change in turbulent shear. The way they come into influence on the flow can be seen through the momentum equations: that is, gravitational force, the viscous diffusion terms, the spatial acceleration (convection) terms, and the turbulent shear stresses. Each effect can be represented by a (pseudo-)body force. They all influence the flow in a similar manner but independently to each other and their effects can be linearly added up. Together they cause an overall perturbation flow which can be computed knowing the body forces and the EPG flow. The fluid expansion caused acceleration directly results in a change in the inertia, which is discussed below.
- The spatial acceleration (inertia) is strong in such a developing flow and its effect on turbulence can again be treated as a pseudo-body force. It has two components: The uniform component is a direct response to a change in pressure gradient (effectively 'cancelling' it partially) and this term can be grouped with the pressure and the uniform gravitational component, forming a total modified pressure gradient. The non-uniform component acts like other (pseudo-)body forces having no direct influence on the turbulence but a mean perturbation flow. The inertia is a response of the flow to the primary causes as shown in figure 5.15. The direction of the inertia is opposite to other effects, and is delaying or partially cancelling the reduction of turbulence due to other effects.
- When normalised using the apparent friction velocity, the eddy viscosity and the transverse turbulence components remain largely the same at any locations in the laminarising region. Hence the primary turbulence dynamics and mixing are not modified by the effects of buoyancy, property variations and flow development; and they can be reasonably well represented by those of the EPG reference flow. The turbulent shear stress can

be reasonably well evaluated using the EPG flow statistics. The streamwise turbulent stress normalised in the same way, however, does change with streamwise distance. This is a reflection of the additional production of the high/low-speed streaks due to the perturbation flow caused by the pseudo-body forces.

- The flow is 'non-equilibrium', that is, it is developing with distance and the inertia is a significant contributor to the momentum balance. The turbulence however is approximately in equilibrium and the convection is insignificant, though the turbulence anisotropy may be different from that in an unheated flow due to the generation of streaks.
- In this region, buoyancy production (i.e., the structural effect) causes some turbulence reduction even though it is relatively small in comparison with other budget terms. Incidentally the contributions of the buoyancy production and the convection to turbulence budget are opposite and partly cancel each other making the net effect to be smaller. This, to some extent, contributes to the success of the unified theory which implicitly assumes that turbulence is in equilibrium in the sense that it is not affected by up/down-stream turbulence and the structural effect is insignificant.

2. **'Full' laminarisation**

   This region can be likened to the pre-transition region of boundary layer bypass transition: The freestream/core turbulence decays, but high-/low-speed streaks are formed near the wall with no vorticity generation. This region extends $12 < z/D < 18$ for Case A and $18 < z/D < 29$ for Case E, respectively.

   - Turbulence kinetic energy in the pipe core ($r < 0.4$) reduces exponentially following $k/u_z^2 = c((x - x_0)/M)^{-n}$, similar to that of a grid turbulence but with a greater exponent of $n = 2$ (c.f. 1.15 to 1.45 for grid turbulence). Correspondingly, the dissipation also reduces exponentially with an exponent of 3.
   - The streaks are generated mostly due to buoyancy production but with small shear production at the later stage of this phase. The streaks lead to an increase in the streamwise turbulent stress in the wall regain but not in transverse turbulent stresses.

- The ejections/sweeps and the pressure-strain term reduce to and stay at a minimum. The shear production reaches minimum or even negative. The transverse turbulent stresses reach minimum.
- Here, 'full laminarisation' refers to the fact that there are no new vortical structures (turbulent spots) produced, but the actual turbulence (turbulence kinetic energy and turbulent mixing) can still be strong due to the decaying turbulence and new streaks. In relation to the latter, the total (shear + buoyancy) production of turbulence may be very strong, resulting the streaks but not multi-scale vortices. Consequently, the use of the term 'full laminarisation' here emphasizes the stoppage of the turbulence regeneration cycle, which is different from other common uses, which often refer to no turbulence generation or presence of turbulence kinetic energy.

3. **Re-transition**

   Similar to boundary layer bypass transition, new multi-scale vortical structures are generated due to flow instability potentially linked to streaks, though this is not studied in this paper. This region extends $z/D > 18$ for Case A and $z/D > 29$ for Case E, respectively.

   - The transition is clearly visualised using instantaneous flow data, which show the breakup of streaks and generation of turbulence spots.
   - With respect to the statistics, this process is reflected as an increase in the pressure-strain action and transverse turbulence components.
   - Buoyancy generation is still dominating in this region but shear production has increased significantly. In fact the local peak production is more than double that of the buoyancy towards the end in Case A, though the shear production is still small in Case E.
   - There are two peaks in the shear production in both A and E, but the near-wall peak is far greater than that in the outer region.

Chapter 6

Fluid-to-fluid scaling for supercritical fluid flows

The mechanisms of laminarisation and re-transition in a vertical pipe flow of supercritical fluid are discussed in detailed in the last two chapters, with new understandings established. In this chapter, the similarity between the upward pipe flows of different supercritical fluids is studied, and it is achieved using fluid-to-fluid scaling correlations. The purpose of fluid-to-fluid scaling for supercritical fluid flows is to determine non-dimensional parameter groups that describe the heat transfer characteristics, and with these parameters matched in flows of different fluids, similarity is achieved. The significance of such similarity is that a surrogate fluid can be used in some experiments to avoid the high cost and technical difficulties. In this chapter, the scaling correlation proposed by Ambrosini et al. [14] is investigated using direct numerical simulations (DNS). A successful match between different supercritical fluids has been found and discussed in detail.

6.1 Case settings

An upward pipe flow of CO_2 is chosen as the prototype fluid flow, for which the configuration is the same as Case A defined in section 4.1, while the pipe length is slightly shorter ($L^* = 60R^* = 30D^*$), as it is sufficient to cover the heat transfer deterioration and recovery. The flow and thermal boundary conditions of three other fluids, i.e., water (H_2O), ammonia (NH_3) and fluoroform (R23) are scaled to achieve similarity with the prototype fluid flow. In the current scaling method, similarities in thermophysical properties and non-dimensional parameters are to be achieved [14, 114]. The following points are implemented to achieve similar fluid properties:

- 1.1 Let $N_{SPC} = (h^*_{pc} - h^*_0)\frac{\beta^*_{pc}}{c^*_{p,pc}}$ and $N_{TPC} = \frac{Q^*}{\dot{m}^*}\frac{\beta^*_{pc}}{c^*_{p,pc}}$ to be the same in all flows.
- 1.2 Select the operating pressures to achieve similar thermophysical property functions, e.g., $\rho(h^+)$, $\mu(h^+)$ in different fluids [14].

N_{SPC} and N_{TPC} are the non-dimensional inlet enthalpy and wall heat flow defined by Ambrosini et al. [14], and the definition of the non-dimensional enthalpy h^+ will be explained later. With the above points satisfied, the bulk properties in different fluids will be similar. On the other hand, the following non-dimensional parameters are scaled to achieve similar flow dynamics:

- 2.1 Let $Re_0 = \frac{u^*_{z,0}R^*}{\nu^*_0}$, $Fr_0 = \frac{u^{*2}_{z,0}}{g^*R^*}$, the non-dimensional parameters in diffusion and gravity terms of the momentum equations, to be the same in all flows.
- 2.2 Alternatively let $Pe_0 = Re_0Pr_0$, $Fr_0 = \frac{u^{*2}_{z,0}}{g^*R^*}$, the inlet Peclect number in the diffusion term of the energy equation and the inlet Froude number, to be the same in all flows.

In theory, with all the above points (1.1, 1.2 & 2.1, 2.2) satisfied, the momentum equations and energy equations in all fluids will be the same, and the flow and thermal field will be very similar among these flows. However, it is impossible to satisfy all the points, the current method attempts to satisfy most of them. With 2.1 satisfied, the satisfaction of point 2.2 depends on whether the inlet Prandtl numbers of the different fluids are similar or not (normally they are different), which will be shown later.

It should be noted that the definition of the non-dimensional inlet enthalpy N_{SPC} [14] is different from h defined (Eq. 3.13) in the solver:

$$N_{SPC} = (h^*_{pc} - h^*_0)\frac{\beta^*_{pc}}{c^*_{p,pc}} = -h^+_0 \tag{6.1}$$

Thus a non-dimensional enthalpy h^+ can be defined which will be used in the discussion herein:

$$h^+ = (h^* - h^*_{pc})\frac{\beta^*_{pc}}{c^*_{p,pc}} \tag{6.2}$$

With a spacially uniform and temporally constant non-dimensional heating, i.e., $N_{TPC} = \frac{Q^*}{\dot{m}^*}\frac{\beta^*_{pc}}{c^*_{p,pc}}$, the streamwise distribution of the bulk h^+ at stationary state will be linear, with a starting value of N_{SPC}, and a slope N_{TPC}. Thus the developments of

bulk h^+ in different flows can be ensured to be consistent by fixing N_{SPC} and N_{TPC}. N_{SPC} and N_{TPC} are respectively 0.5669 and 0.1783.

In the current scaling method, Re_0, Fr_0, N_{SPC}, N_{TPC}, L/D of all the fluids (CO_2, H_2O, NH_3, R23) are chosen to be the same, and their pressures are selected to achieve similar $\rho(h^+)$ and $\mu(h^+)$ functions. The tuned pressures are CO_2 at 8.57MPa, H_2O at 25MPa, NH_3 at 12.63MPa, R23 at 5.7MPa. Variations of the non-dimensional density and dynamic viscosity against h^+ of the four fluids at these chosen pressures are shown in Fig. 6.1, with the inlet enthalpy $h^+ = -N_{SPC}$ specified by thin dash lines. Excellent agreements are shown in the variations of ρ, as a result of the carefully chosen pressure, while the differences between the four curves of μ are relatively large. However, the general trends and magnitudes of μ are similar among the four fluids. In conclusion, by satisfying point 1.1 & 1.2, the similarity in the developments of bulk ρ and μ can be reasonably well achieved in the four flows.

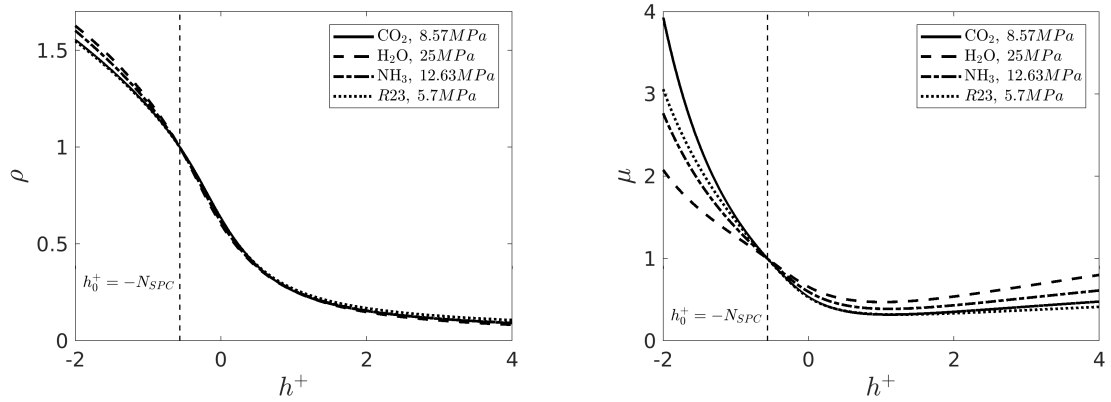

(a) $\rho(h^+)$ (b) $\mu(h^+)$

Figure 6.1: Variations of ρ and μ against h^+ for four fluids at chosen operating pressures.

With 1.1, 1.2 and 2.1 satified, the uncertainties of the similarity come from the inlet Prandtl number Pr_0. The inlet enthalpy h_0 and temperature T_0 for the four model fluids are obtained with a fixed N_{SPC}, thus the inlet Prandtl number $Pr_0 = \frac{c^*_{p,0}\mu^*_0}{\lambda^*_0}$ is already determined. The variations of Pr against h^+ are shown in Fig. 6.2a, with the inlet enthalpy h^+_0 specified by a thin dash line. The general trends of the $Pr(h^+)$ curves in different fluids are similar, which increases before the pseudocritical enthalpy ($h^+ = 0$) and decreases after that. A zoomed in view of the Prandtl numbers at the inlet enthalpy $h^+ = -N_{SPC}$ is also shown, and the inlet Pr for CO_2, H_2O, NH_3 and R23 are 2.86, 1.68, 2.18 and 2.09, respectively. The inlet Pr of NH_3 and R23 are

relatively close to each other and are about 0.76 and 0.73 of that of CO_2, which is 1.7 times of that of H_2O.

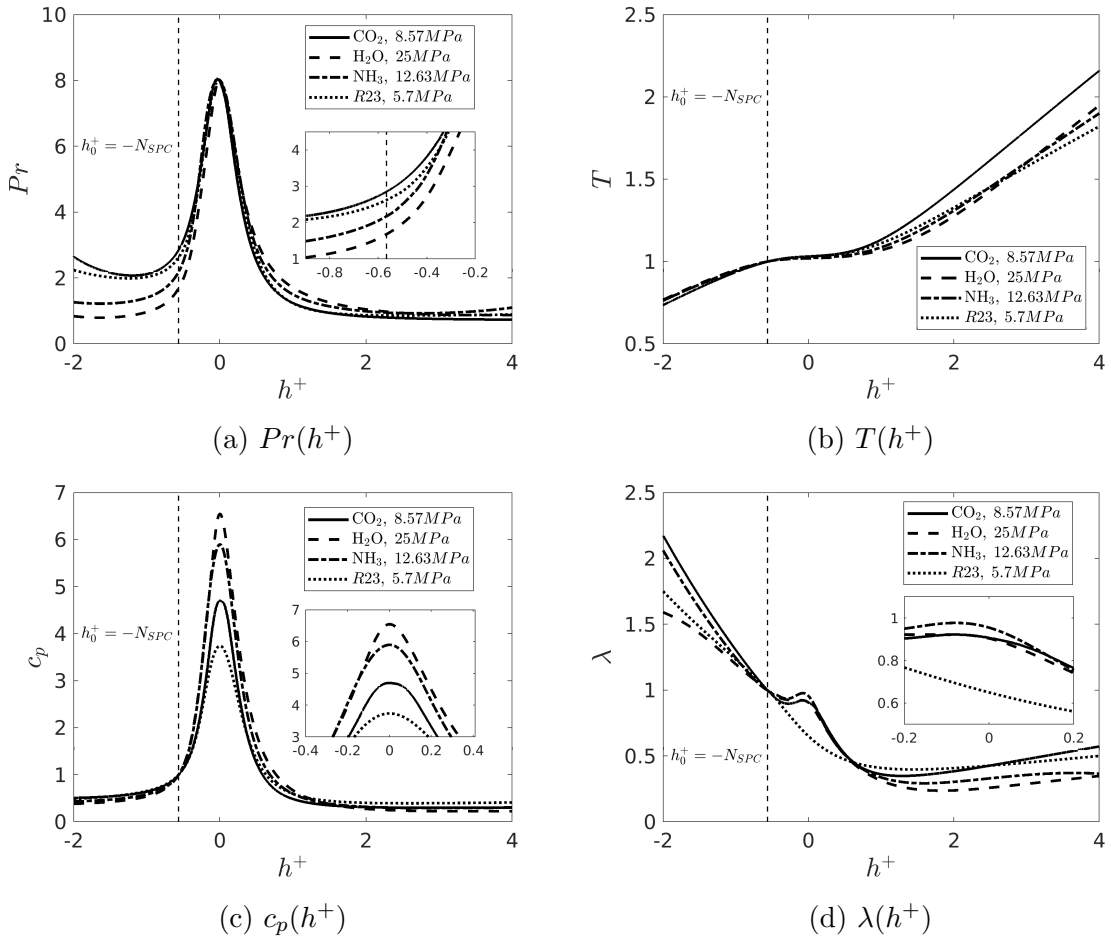

(a) $Pr(h^+)$ (b) $T(h^+)$

(c) $c_p(h^+)$ (d) $\lambda(h^+)$

Figure 6.2: Variations of Pr, T, c_p and λ against h^+ for four fluids at chosen operating pressures.

The variations of T, c_p and λ against h^+ are shown in Fig. 6.2b, 6.2c and 6.2d. The values of them at h_0^+ are 1 as they are all normalized by their inlet values. The $T(h^+)$ profiles in all fluids show a similar trend, the change rate is much smaller around the pseudocritical enthalpy h_{pc}^+, as the specific heat c_p reaches a large peak at h_{pc}^+, which is shown in Fig. 6.2c. Further above h_{pc}^+, the divergences of the $T(h^+)$ profiles of different fluids from each other is larger. Generally, the profiles of $T(h^+)$ of different fluids at these chosen pressures are similar. For the trends of the $c_p(h^+)$ curves, they all increase before h_{pc}^+ and decrease after, however, their peak values are very different: R23 has the lowest peak c_p, while H_2O has the highest, which is 3.81 times of the former. Finally, the comparisons of the $\lambda(h^+)$ profiles are shown, and similar trends and magnitudes among these fluids can be seen. For CO_2, H_2O and

NH_3, there is a small local peak around h^+_{pc}, while for R23, λ monotonically decreases with h^+.

The assessment of the satisfaction of point 1.2 can be assured using the above comparisons. The $T(h^+)$, $c_p(h^+)$ and $\lambda(h^+)$ profiles are generally similar in terms of trends and magnitudes, even though they do not strictly collapse with each other. One consideration is the difference in Pr_0, as it is in the diffusion term of the energy equation, which strongly affects the temperature distributions. It is impossible to ensure both Re_0 and Pr_0 to be the same in the model fluids. Only one of them can be matched. It is obvious that equating Re_0 is more important, as it determines the flow dynamics, which also affects the thermal field. Unable to scale Pr_0 in the model fluid is a sacrifice of similarity in this set of scaling study. In a separate series of study, scaled cases with matched $Pe_0 = Re_0 Pr_0$ (but different Re_0) are also carried out. Cases with Re_0 matched are named "RE", and those with Pe_0 matched are named "PE". The discussions of the current study mainly focus on the "RE" cases because they are expected to achieve better similarity than the "PE" cases, and the purpose of the "PE" cases are to additionally study the effect of parameter Pe_0 through comparisons with the "RE" cases.

Configurations for simulation cases are shown in table 6.1. The inlet Reynolds number for all the "RE" cases are the same, and the inlet Peclect number for all the "PE" cases are the same. All cases are upward pipe flows with a uniform heat flux imposed at the wall. The boundary conditions for the "RE" and "PE" cases are chosen to match non-dimensional parameter groups as explained above. An additional parameter is matched in all cases to determine the pipe length L^*, i.e., $L/D = 30$. This is to achieve the similarity in geometry aspect ratio, so that locations can be corresponded by the non-dimensional distance. It should be noted that Re_0 is calculated using R^* rather than D^*.

Table 6.1: Boundary conditions of simulation cases

Case	q^*_w (W/m^2)	$u^*_{z,0}$ (m/s)	D^* (m)	N_{TPC}	N_{SPC}	Fr	Re_0	Pe_0
CO2	30870	0.220	0.0020	0.1783	0.5669	0.0825	2617	7477
H2O-RE	113739.32	0.245	0.0025	0.1783	0.5669	0.0825	2617	4403
NH3-RE	54050.83	0.251	0.0026	0.1783	0.5669	0.0825	2617	5695
R23-RE	20884.68	0.211	0.0018	0.1783	0.5669	0.0825	2617	5477
H2O-PE	135696.83	0.292	0.0035	0.1783	0.5669	0.0825	4444	7477
NH3-PE	59185.45	0.275	0.0031	0.1783	0.5669	0.0825	3436	7477
R23-PE	23168.41	0.234	0.0023	0.1783	0.5669	0.0825	3573	7477

6.1.1 Determination of boundary conditions

Case "H2O-RE" and "H2O-PE" are taken as examples to show the determination of the scaled boundary conditions for the model fluids. In Case H2O-RE, non-dimensional group Re_0, Fr_0, N_{TPC}, N_{SPC}, L/D are the same as those of Case CO2, while in Case H2O-PE, non-dimensional group Pe_0, Fr_0, N_{TPC}, N_{SPC}, L/D are the same as Case CO2. The following steps are used to determine the boundary conditions in these cases:

Step 1. Choose the operating pressure for different fluids to achieve similar enthalpy dependent properties, e.g., $\rho(h^+)$, $\mu(h^+)$.

- Several operating pressures for water are chosen for examination. For each chosen pressure, an inlet enthalpy h_0^* is obtained, as the $N_{SPC} = -h_0^+$ is fixed to be the same as the prototype fluid flow, i.e., case CO2 here:

$$h_0^* = h_{pc}^* - \frac{N_{SPC} c_{p,pc}^*}{\beta_{pc}^*}, \tag{6.3}$$

- The inlet thermophysical properties, e.g., ρ_0^*, μ_0^*, $c_{p,0}^*$, λ_0^*, etc, are obtained using the property database. The enthalpy dependent properties $\rho(h^+)$, $\mu(h^+)$, $c_p(h^+)$, $\lambda(h^+)$ for each chosen pressure are obtained, and the profiles of these functions are compared with the corresponding profiles of CO_2 at 8.57MPa (the prototype fluid), are shown in Fig. 6.1 & 6.2.

- The operating pressure with the most similar enthalpy dependent properties is chosen for the model fluid (H_2O), if all of them do not match with those of CO_2, other operating pressures are examined and such comparisons are repeated.

Step 2. Once the operating pressure for the H_2O is determined, the inlet and pseudocritical enthalpies are determined. Thermophysical properties at the inlet and pseudocritical enthalpy are obtained using the property database.

Step 3. This step is to determine the inlet velocity $u_{z,0}^*$ and pipe radius R^* using the fixed parameters. For Case H2O-RE, the fixed Re_0 and Fr_0 are used, while for Case H2O-PE, Pe_0 and Fr_0 are used.

- For Case H2O-RE, Re_0 and Fr_0 from Case CO2 (prototype fluid) are used:

$$Re_0 = \frac{\rho^* u_{z,0}^* R^*}{\mu^*}, \quad Fr_0 = \frac{u_{z,0}^{*2}}{g^* R^*} \tag{6.4}$$

With two equations and two unknowns ($u^*_{z,0}$ & R^*), Eq. 6.4 can be solved:

$$u^*_{z,0} = \sqrt[3]{\frac{Fr_0 Re_0 g^* \mu^*_0}{\rho^*_0}}, \quad R^* = \sqrt[3]{\frac{Re_0^2 \mu_0^{*2}}{\rho_0^{*2} g^* Fr_0^*}} \tag{6.5}$$

- For Case H2O-PE, Pe_0 and Fr_0 from Case CO2 (prototype fluid) are used:

$$Pe_0 = Re_0 Pr_0 = \frac{\rho^*_0 u^*_{z,0} R^* c^*_{p,0}}{\lambda^*_0}, \quad Fr_0 = \frac{u^{*2}_{z,0}}{g^* R^*} \tag{6.6}$$

With two equations and two unknowns ($u^*_{z,0}$ & R^*), Eq. 6.6 can be solved:

$$u^*_{z,0} = \sqrt[3]{\frac{Fr_0 Pe_0 g^* \lambda^*_0}{\rho^*_0 c^*_{p,0}}}, \quad R^* = \sqrt[3]{\frac{Pe_0^2 \lambda_0^{*2}}{Fr_0 \rho_0^{*2} c^{*2}_{p,0} g^*}} \tag{6.7}$$

Step 4. Re-write the expression for N_{TPC}:

$$N_{TPC} = \frac{Q^*}{\dot{m}^*} \frac{\beta^*_{pc}}{c^*_{p,pc}} = \frac{2\pi R^* L^* q^*_w}{u^*_{z,0} \rho^*_0 \pi R^{*2}} \frac{\beta^*_{pc}}{c^*_{p,pc}}, \tag{6.8}$$

in which the dimensional pipe length $L^* = 60R^*$. The wall heat flux q^*_w can be obtained by rearranging Eq. 6.8:

$$q^*_w = \frac{N_{TPC} u^*_{z,0} \rho^*_0 c^*_{p,pc}}{120 \beta^*_{pc}} \tag{6.9}$$

With step 1 to 4, the flow and thermal boundary condition for Case H2O-RE and H2O-PE can be obtained. The same process is used to obtain the boundary conditions for the other two fluids (NH_3 & R23).

6.1.2 Mesh criteria

For the RE-series cases, the mesh resolutions for streamwise, radial and spanwise directions are $768 \times 64 \times 128$ and the non-dimensional mesh sizes are shown in table 6.2 in comparison with that of Bae et al. [11]. While for "PE" cases, the Reynolds numbers are larger and finer meshes are used. For Case NH3-PE ($Re_0 = 3436$) and R23-PE ($Re_0 = 3573$), the mesh resolution is $1080 \times 90 \times 128$ (streamwise $\times$ radial $\times$ spanwise directions), and for Case H2O-PE ($Re_0 = 4444$), the mesh resolution is $1440 \times 120 \times 128$. The non-dimensional mesh sizes of the "PE" cases are also shown in table 6.2. Compared to the reference case, the mesh resolutions of the current simulations are sufficient to capture small scale turbulent activities, especially near the wall.

For each case, a turbulence generator is used to provide instantaneous fully-developed (isothermal) turbulent velocity profiles for the inlet to the heating section every simulation instant. The turbulence generator is periodic at streamwise direction, in which the length is $5D^*$ and the same radial and spanwise mesh resolutions are applied, e.g., for Case H2O-PE, the mesh resolution is $240 \times 120 \times 128$ (streamwise $\times$ radial $\times$ spanwise directions).

Table 6.2: Mesh criteria of the base and scaled cases

Case	Δy^+	$R^*\Delta\theta^+$	Δz^+
CO2	$0.17 \sim 7.33$	8.77	13.96
H2O-RE	$0.17 \sim 7.28$	8.71	13.86
NH3-RE	$0.17 \sim 7.33$	8.76	13.95
R23-RE	$0.17 \sim 7.44$	8.89	14.16
H2O-PE	$0.14 \sim 6.13$	11.66	13.73
NH3-PE	$0.15 \sim 6.59$	12.54	11.08
R23-PE	$0.16 \sim 6.90$	13.13	11.60
Bae et al. [11]	$0.18 \sim 5.34$	9.14	14.55

6.2 Results and discussion on RE-series

In this section, the heat transfer and turbulent behaviours in the RE-series cases are compared. In general, although the Peclect number in the energy equation is not strictly scaled, similarity of enthalpy fields is well achieved in all the RE-series cases. It will be shown in this section, similarity is achieved in the developments of Stanton number, suggesting the streamwise variations of heat transfer characteristics (deterioration and recovery) are reproduced by each of the RE-series cases. Furthermore, similarities in flow fields and turbulent characteristics are observed in these flows, with laminarisation and recovery happen at about the same locations. The success of the current scaling correlation indicates the heat transfer and turbulent behaviour is well characterized by the chosen non-dimensional parameters.

6.2.1 Comparison of bulk enthalpies and properties

Firstly, we compare the bulk enthalpies and temperatures in the RE-series cases. As shown in Fig. 6.3a, all four cases consistently show the same streamwise linear growth of dimensionless bulk enthalpy, as a result of the fixed N_{SPC} (starting point) and N_{TPC} (slope). The bulk temperatures in the four cases are shown in Fig. 6.3b, they have a same starting point ($T_{b,0} = 1$) but diverge quickly at later locations. This is due to the differences in $c_p(h^+)$ functions in the four fluids as shown in Fig. 6.2c. The developments of bulk density and dynamic viscosity in the four cases are shown in Fig. 6.3c & 6.3d. In general, they all have a same starting point ($\rho_{b,0} = 1$, $\mu_{b,0} = 1$), and all show a similar variation trend. ρ_b and μ_b in Case H2O-RE and NH3-RE diverge from the other two cases at later locations, while those in Case CO2-RE and R23-RE perfectly agree with each other. Although the bulk enthalpy h_b^+ is fixed in the all cases, some differences in ρ_b and μ_b appear due to the different enthalpy dependence. It is seen in the next section that such differences do not appear to cause significant differences in the flow/heat transfer in the various test cases.

6.2.2 Comparison of general heat transfer behaviours

The developments of the wall enthalpy $\overline{h_w^+}$ in the RE-series cases are shown in Fig. 6.4a. The $\overline{h_w^+}$ profiles in the four cases nearly collapse with each other, which indicates the heat transfer features and h^+ fields in these cases are similar. It is found that $\overline{h_w^+}$ in all cases shows the same variations at corresponding locations. At the initial stage ($\sim z/D < 2$), $\overline{h_w^+}$ rapidly increase as a thermal boundary layer is formed. After this, $\overline{h_w^+}$ increases linearly before $z/D \sim 20$, at which $\overline{h_w^+}$ reaches its peak, then it starts

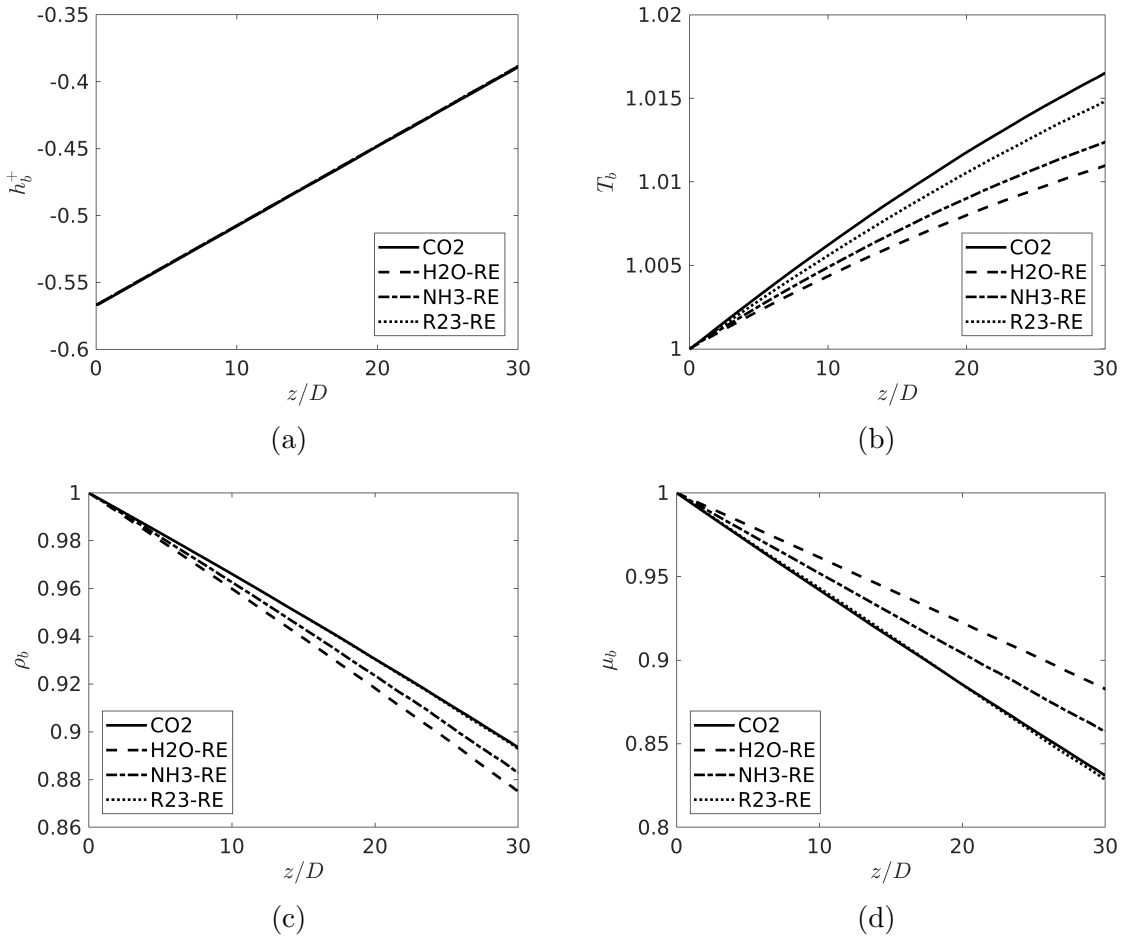

Figure 6.3: Streamwise developments of (a) bulk enthalpy, (b) bulk temperature, (c) bulk density and (d) bulk dynamic viscosity in the RE-series cases.

reducing at later locations. The changes in $\overline{h_w^+}$ reflect the heat transfer deteriorations and enhancements, and their corresponding locations are about the same in the RE-series cases.

The wall temperatures $\overline{T}_w$ in these cases are shown in Fig. 6.4b. The developments of $\overline{T}_w$ is not as similar as those of $\overline{h_w^+}$ as these fluids have different $c_p(h^+)$ functions. Despite the differences in $\overline{T}_w$ developments are larger, they show the same trend as $\overline{h_w^+}$, with peaks appear at similar locations. The above results show that the wall enthalpies in each of the RE-series cases can be accurately predicted by the other cases in the "RE" series. The prediction of wall temperature can then be obtained using the function $T(h^+)$ from property database.

The changes of heat transfer characteristic are reflected in the streamwise developments of Nusselt number and Stanton number, which are shown in Fig. 6.4c &

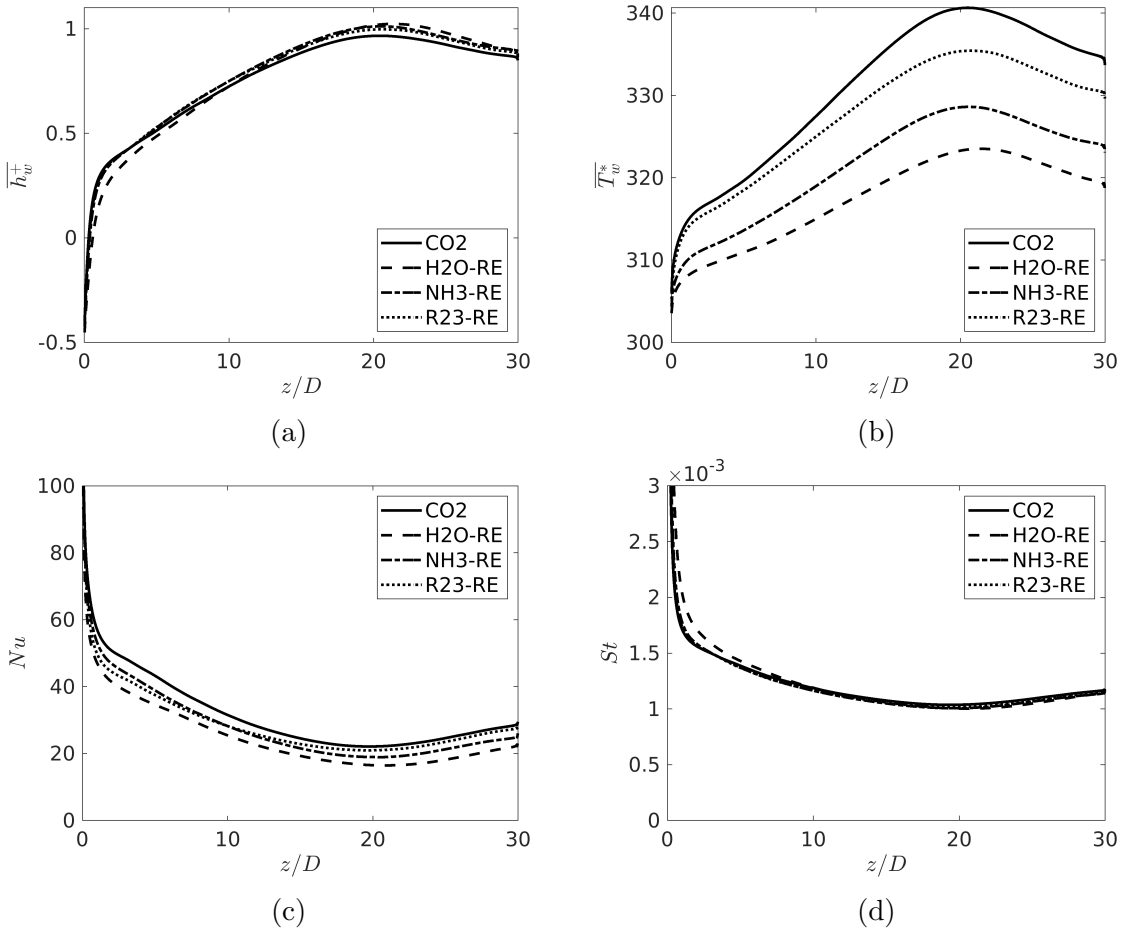

Figure 6.4: Streamwise developments of (a) wall enthalpy, (b) wall temperature, (c) Nusselt number and (d) Stanton number in the RE-series cases.

6.4d. The definitions of these two parameters are written as:

$$Nu = \frac{q_w^* D^*}{\lambda_b^*} = \frac{\overline{\lambda}\frac{\partial \overline{T}}{\partial r}\Big|_w D}{\lambda_b\left(\overline{T_w} - T_b\right)} \quad St = \frac{Nu}{Re_b Pr_b}, \tag{6.10}$$

where Re_b and Pr_b are the local bulk Reynolds and Prandtl numbers:

$$Re_b = \frac{\rho_b^* u_{z,b}^* D^*}{\mu_b^*} \quad Pr_b = \frac{c_{p,avg}^* \mu_b^*}{\lambda_b^*}, \tag{6.11}$$

in which $c_{p,avg}^*$ is the averaged c_p^* in the local cross section [151]:

$$c_{p,avg}^* = \frac{h_w^* - h_b^*}{T_w^* - T_b^*} \tag{6.12}$$

The streamwise developments of the Nusselt number and Stanton number in the RE-series cases are shown in Fig. 6.4c. The RE-series cases show similar trends

of Nusselt and Stanton number developments, with the Stanton numbers perfectly collapse and the Nusselt numbers showing similar trends even though with different values. After the entrance, Nusselt number and Stanton number reduce rapidly in every case due to the rapid development of the thermal boundary layer. To clearly show the variations during heat transfer deterioration and recovery, the top parts of the Nusselt number and Stanton number are clipped off. The Nusselt number of Case H2O-RE is the lowest, and that of Case CO2 is the highest. For the Stanton number, Case H2O-RE has a higher value than the other three cases at the initial streamwise location ($z/D = 10$), but it soon converges to those of the other three at later locations. The Stanton number of the RE-series cases are the same from $z/D = 10$ to 30. Consequently it can be concluded that the changes in heat transfer characteristics are similar in all cases and the worst heat transfer locates at nearly the same location. Furthermore, the Stanton number is found to be better than the Nusselt number in terms of characterising the similar heat transfer features in these cases as also discussed in Pucciarelli et al. [152]. In general, such comparisons demonstrate that an excellent similarity in heat transfer performances has been achieved using the chosen non-dimensional parameters.

To identify and compare different contributions to the Nusselt number across these cases, the FIK decomposition is used. The FIK decomposition of the Nusselt number is firstly established by Fukagata et al. [34], and later Gomez et al. [153] has extended this to compressible flows with thermophysical property variations. FIK identify has been widely used in heat transfer studies [76, 32] as a useful tool to identify the dominant effect on the variation of Nusselt number. The full formula of the FIK decomposition of Nusselt number for vertical pipe flows with property variation can

be written as follow:

$$
\begin{aligned}
Nu_{FIK} = & \\
& \underbrace{\frac{8}{\alpha_b\left(\overline{h_w}-h_b\right)}\int_0^1 r\bar{\alpha}\frac{\partial\bar{h}}{\partial r}rdr}_{Nu_1} \underbrace{-\frac{8Re_{b0}Pr_0}{\alpha_b\left(\overline{h_w}-h_b\right)}\int_0^1 r\overline{\rho h''u_r''}rdr}_{Nu_2} \\
& \underbrace{-\frac{4Re_{b0}Pr_0}{\alpha_b\left(\overline{h_w}-h_b\right)}\int_0^1\left(R^2-r^2\right)\left\langle\frac{1}{r}\frac{\partial r\bar{\rho}\tilde{h}\tilde{u}_r}{\partial r}\right\rangle rdr}_{Nu_3} \underbrace{-\frac{4Re_{b0}Pr_0}{\alpha_b\left(\overline{h_w}-h_b\right)}\int_0^1\left(R^2-r^2\right)\left\langle\frac{\partial\bar{\rho}\tilde{h}\tilde{u}_x}{\partial x}\right\rangle rdr}_{Nu_4} \\
& \underbrace{-\frac{4Re_{b0}Pr_0}{\alpha_b\left(\overline{h_w}-h_b\right)}\int_0^1\left(R^2-r^2\right)\left\langle\frac{\partial\overline{\rho h''u_x''}}{\partial x}\right\rangle rdr}_{Nu_5} \underbrace{+\frac{4}{\alpha_b\left(\overline{h_w}-h_b\right)}\int_0^1\left(R^2-r^2\right)\left\langle\frac{1}{r}\frac{\partial r}{\partial r}\overline{\alpha'\frac{\partial h'}{\partial r}}\right\rangle rdr}_{Nu_6} \\
& \underbrace{+\frac{4}{\alpha_b\left(\overline{h_w}-h_b\right)}\int_0^1\left(R^2-r^2\right)\left\langle\frac{\partial}{\partial x}\left(\bar{\alpha}\frac{\partial\overline{h}}{\partial x}\right)\right\rangle rdr}_{Nu_7} \\
& \underbrace{+\frac{4}{\alpha_b\left(\overline{h_w}-h_b\right)}\int_0^1\left(R^2-r^2\right)\left\langle\frac{\partial}{\partial x}\left(\overline{\alpha'\frac{\partial h'}{\partial x}}\right)\right\rangle rdr}_{Nu_8},
\end{aligned}
\tag{6.13}
$$

in which "$\langle\ \rangle$" represents the following operator:

$$
\langle\phi(r,z)\rangle = \phi(r,z) - \frac{2}{R^2}\int_0^R \phi(r,z)rdr \tag{6.14}
$$

In Eq. 6.13, Nu_1 denotes the laminar contribution. It is therefore named Nu_l. Nu_2 is the contribution from the turbulent heat flux in the radial diffusion term $-\overline{\rho u_r'' h''}$, which is named Nu_t. Nu_3 and Nu_4 are respectively the contributions from the radial and streamwise convection terms, which are shown to be significant in developing flow [32]. Nu_5 is the contribution from the turbulent heat flux in the streamwise diffusion term, i.e., $-\overline{\rho u_z'' h''}$, it has relatively small contribution to the Nusselt number. Nu_6, Nu_7 and Nu_8 are the contributions from the fluctuation of radial heat flux, streamwise conduction and fluctuation of streamwise heat flux. The influence of them are found to be ignorable, which will be proved in the later discussion. Nu_3 and Nu_4 are the inhomogeneous contributions, the summation of them is named Nu_h.

The decompositions of Nusselt number in the RE-series cases are shown in Fig. 6.5. To validate the formula of the decomposition (Eq. 6.13), the Nusselt number in each case, and the summation of the decomposed Nusselt number, i.e., $Nu_{FIK} = Nu_l + Nu_t + Nu_h$ are shown in the same figure. In each case, excellent agreement is

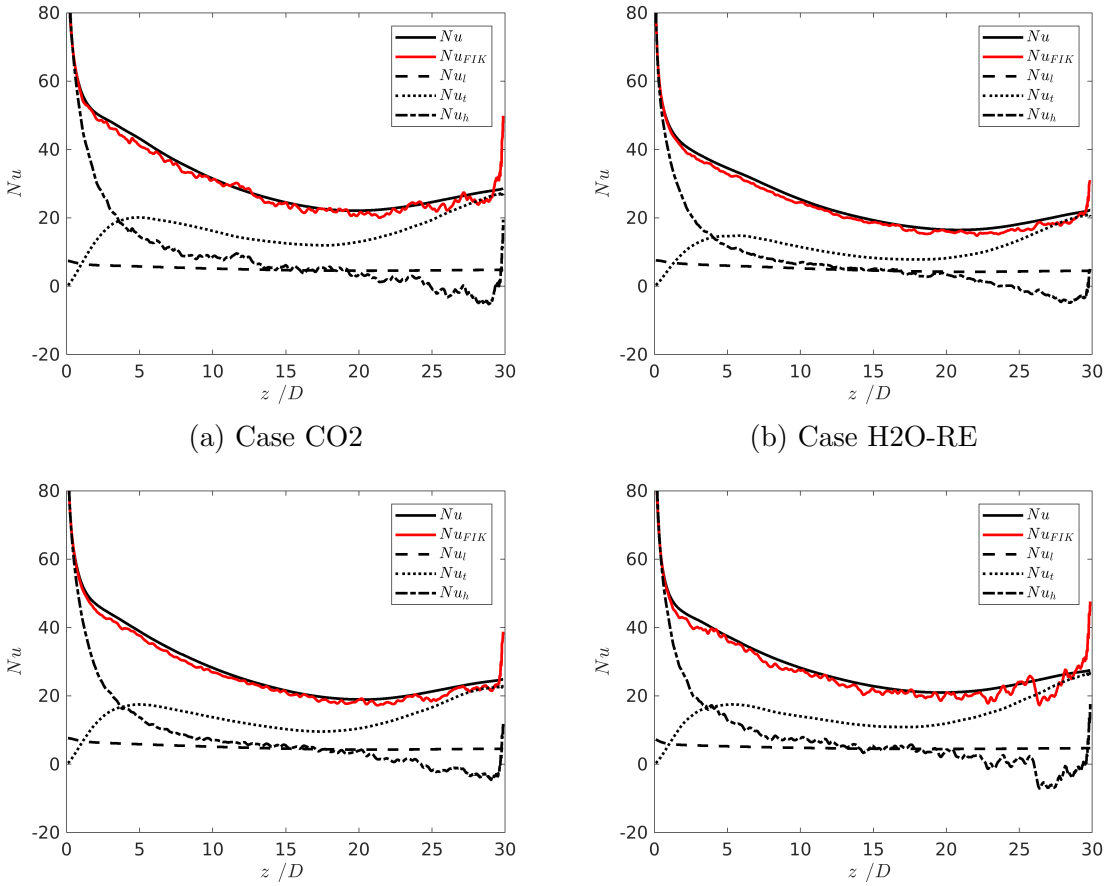

(a) Case CO2

(b) Case H2O-RE

(c) Case NH3-RE

(d) Case R23-RE

Figure 6.5: FIK identify for the Nusselt number in the RE-series cases.

shown between Nu_{FIK} and Nu, suggesting Eq. 6.13 is reliable and the last last three inhomogeneous contributions (Nu_6, Nu_7 and Nu_8) are negligible. The variations of the three contributions (Nu_l, Nu_t and Nu_h) are very similar in each case. At the inlet of each case, the Nu_t is zero, as the fluctuations of enthalpy is still minor, and then Nu_t rises rapidly to a peak at about $z/D = 5$ in each case. Interestingly such early peak of Nu_t are about 20 except Case H2O-RE, which is about 15. After the peak, Nu_t reduces in each case, and reaches the minimum at about $z/D = 20$, then it increases again. In all cases, the changes in Nu_t are strongly linked to the heat transfer deterioration and recovery that discussed previously, which reflect the variations of turbulent mixing effect on heat transfer. Near the outlet of each case, Nu_t is higher than the early peak (at $z/D \sim 5$), suggesting that the impact of turbulence at the recovery stage is stronger than that at the initial stage.

Consistently, Nu_l largely remain constant ($Nu_l \approx 4.6$) in each case, only reduces shortly after the inlet, as a result of the entrance effect. Generally, the contributions

of Nu_l to the total Nusselt number is relatively small in all cases, compared to Nu_t and Nu_h. When the thermal boundary later is formed in each case, the total Nusselt number rapidly reduces before $z/D = 5$, and it is the main contributor to the rapidly reduced Nu_h as shown. At about $z/D \approx 4$ of each case, the Nu_h becomes lower than Nu_t. Then Nu_h keeps reducing at a lower rate. The reduction of Nu during the heat transfer deterioration $z/D = 5$ to 20 is mainly attributed to the reduction of Nu_h and Nu_t. This suggests that heat transfer deterioration is not only due to the laminarization, but also due to the impact from convection, that is the flow/thermal developing effect.

The trends of Nu_l, Nu_t and Nu_h in the "RE" cases agree well with each other, which suggests not only similarity of heat transfer characteristics is achieved, but also the individual contributions during the heat transfer deterioration and recovery are similar.

In the previous discussions, the h_b^+ of the RE-series cases are shown to be the same (Fig. 6.3a) and $\overline{h_w^+}$ profiles are very similar (Fig. 6.4a). These similarities suggest the radial profiles of h^+ in these cases are very similar, and correspondingly, the thermal diffusivity and turbulent heat flux are expected to be similar in these cases. The radial diffusion term of the Favre-averaged energy equation for enthalpy h^+ can be converted from the original diffusion term according to the normalization of h and h^+:

$$\frac{1}{r}\frac{\partial}{\partial r}\Big(\frac{r\overline{\lambda}}{Re_0 Pr_0 \overline{c_p}}\frac{\partial \overline{h}}{\partial r} - r\overline{\rho u_r'' h''}\Big) = \frac{1}{r}\frac{\partial}{\partial r}\Big(\frac{r\overline{\lambda}}{Re_0 Pr_0 \overline{c_p}}\frac{c_{p,pc}^*}{c_{p,0}^* T_0^* \beta_{pc}^*}\frac{\partial \overline{h^+}}{\partial r} - r\overline{\rho u_r'' h^{+\prime\prime}}\frac{c_{p,pc}^*}{c_{p,0}^* T_0^* \beta_{pc}^*}\Big), \tag{6.15}$$

in which the laminar (molecular) and turbulent heat flux are written:

$$q_l = \frac{\overline{\lambda}}{Re_0 Pr_0 \overline{c_p}}\frac{\partial \overline{h}}{\partial r} = \frac{\overline{\lambda}}{Re_0 Pr_0 \overline{c_p}}\frac{c_{p,pc}^*}{c_{p,0}^* T_0^* \beta_{pc}^*}\frac{\partial \overline{h^+}}{\partial r} \tag{6.16}$$

and

$$q_t = \overline{\rho u_r'' h''} = \overline{\rho u_r'' h^{+\prime\prime}}\frac{c_{p,pc}^*}{c_{p,0}^* T_0^* \beta_{pc}^*}. \tag{6.17}$$

The profiles of turbulent heat flux at chosen locations in the four cases are shown in Fig. 6.6. The profiles in each case generally agree well, with the peaks at about the same locations ($y \approx 0.1$). The turbulent heat flux of Case H2O-RE is lower than those of the other three cases during the laminarization ($z/D = 5$, 10 and 17), and excellent agreement is shown between the profiles of Case CO2 and R23-RE at the first two locations. During the laminarization processes in all cases, from $z/D = 5$ to

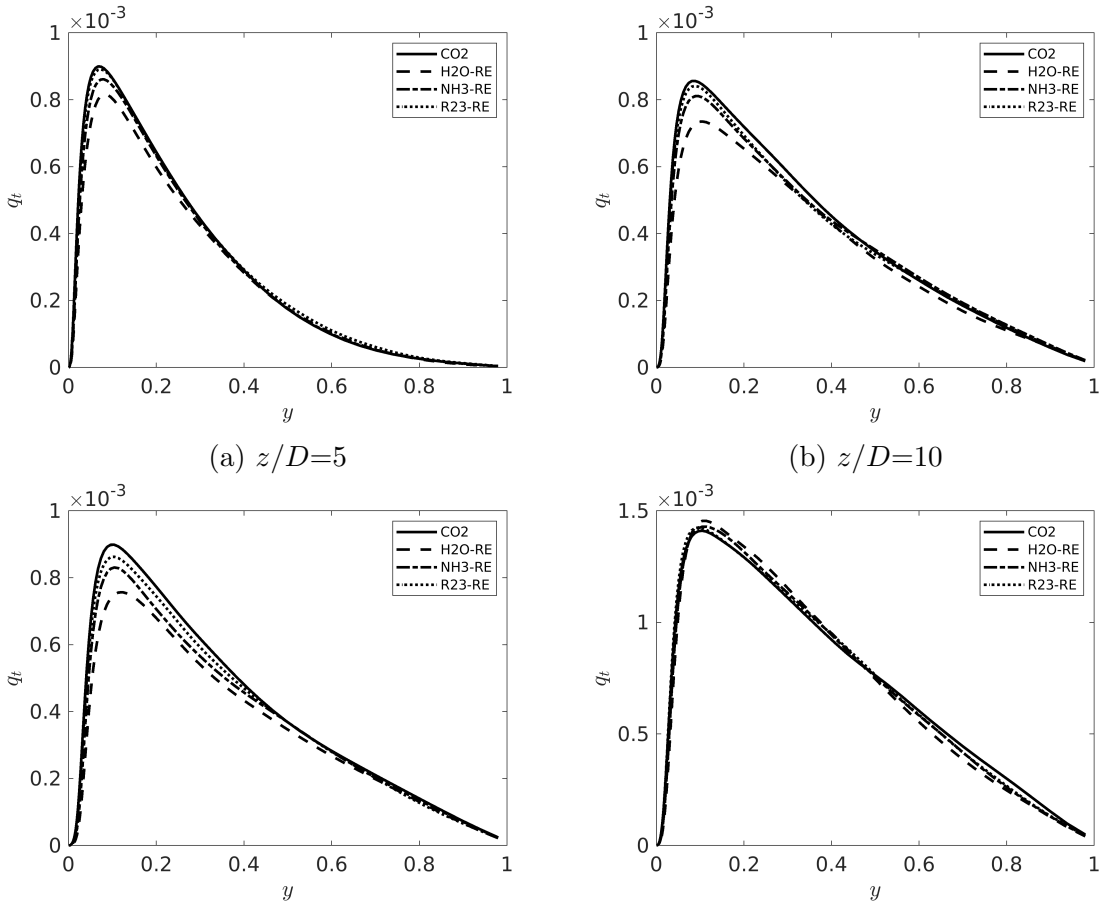

(a) z/D=5 (b) z/D=10

(c) z/D=17 (d) z/D=28

Figure 6.6: Profiles of q_t at chosen locations of all RE-series cases.

17, turbulent heat flux close to the wall in each case does not change much, suggesting the effects of turbulent mixing in these cases are similarly remained.

The profiles of the molecular heat flux are shown in Fig. 6.7. In all cases, q_l is large close to the wall (in the thermal boundary layer) and mostly zero at the core flow where the gradient of enthalpy is much smaller. General trends of q_l in the RE-series cases are very similar, with the main differences locate close to the wall. In all locations, Case R23-RE always has the largest q_l, while Case H2O-RE always has the lowest value, which is about 40% lower than that in Case R23-RE. Consistencies in the laminar and turbulent heat fluxes (q_l & q_t) between the RE-series cases suggest the radial heat transfer features of these cases are very similar, and similar h^+ profiles in these cases are expected.

Comparisons of the radial gradient of enthalpy h^+ are shown in Fig. 6.8. In each case, $\partial h^+/\partial r$ has a peak near the wall, then it rapidly reduces further away. At about $y > 0.2$, above the thermal boundary layer, the enthalpy gradients are zero. In

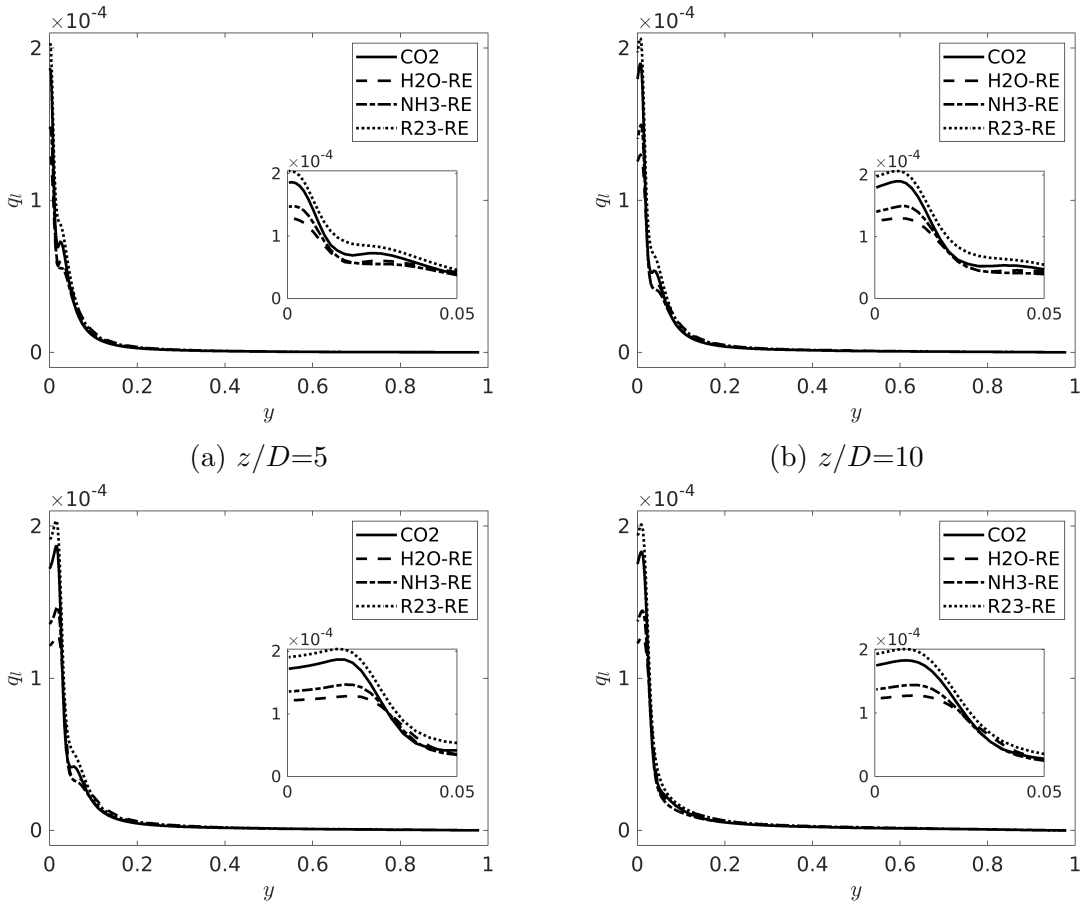

(a) z/D=5 (b) z/D=10

(c) z/D=17 (d) z/D=28

Figure 6.7: Profiles of q_l at chosen locations of the RE-series cases.

all case, the thickness of the thermal boundary layer increase along the streamwise direction similarly. Excellent agreement is shown in the enthalpy gradients of all cases at corresponding locations, which suggests the similar distributions of enthalpy in these cases. It is also seen that the main differences are close to the wall (around the peaks) and minor. The near-wall $\partial h^+/\partial r$ in Case H2O-RE is lower than in the other three cases, which is corresponding to the lower $\overline{h_w^+}$ in this case. In general, a good similarity is achieved in the trends and magnitudes of $\overline{h^+}$ in these cases.

6.2.3 Comparison of turbulent characteristics

In this section, variations of the resolved flow fields and turbulent characteristics in the RE-series cases are compared. It is known that the heat transfer deterioration and recovery is strongly linked to the laminarization and regeneration of turbulence in strong buoyancy-aided mixed convection flows. Also, the FIK decomposition shows

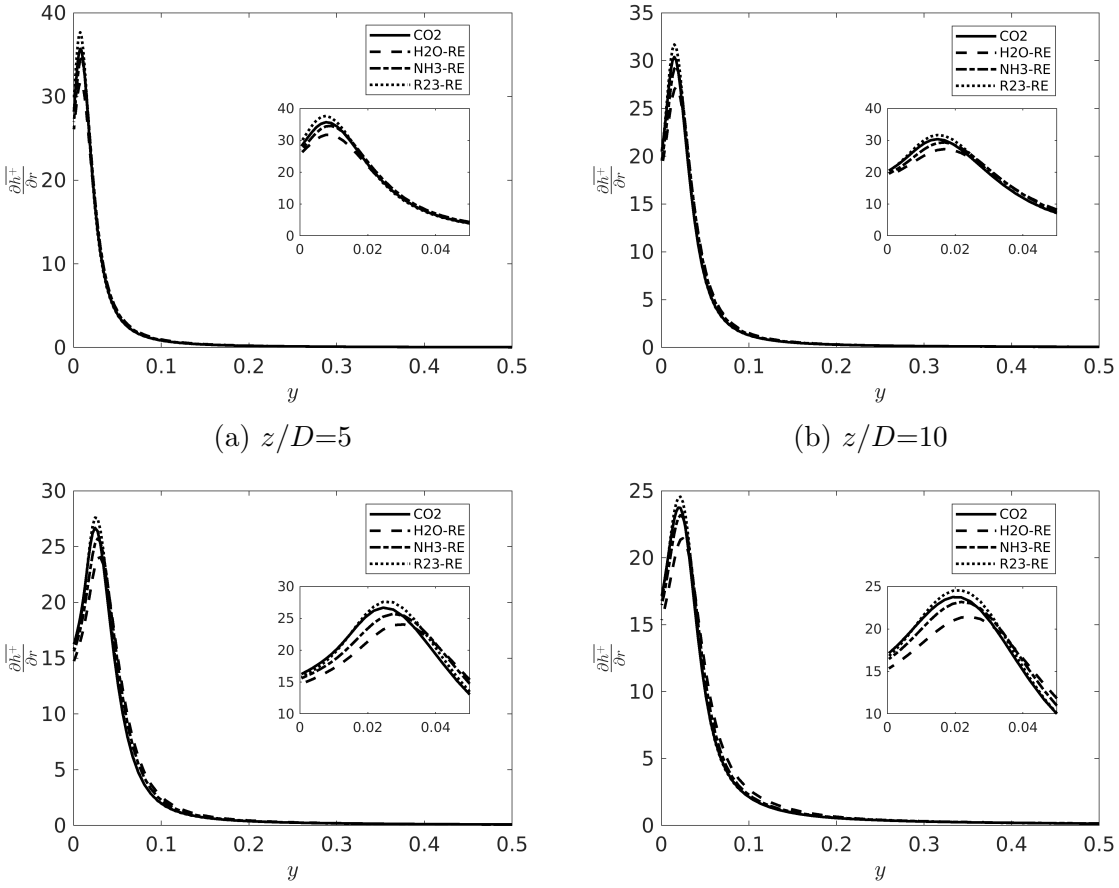

(a) z/D=5 (b) z/D=10

(c) z/D=17 (d) z/D=28

Figure 6.8: Profiles of $\frac{\partial \overline{h^+}}{\partial r}$ at chosen locations of the RE-series cases.

the changes of turbulence is one of the reasons of the reduction in Nusselt numbers. The successful similarity in heat transfer is expected to be due to the similarity in flow field and turbulence. As discussed before, the scaling method of the RE-series cases mainly serves to achieve similarity in the non-dimensional momentum equations: with similar flow fields and turbulent behaviours reproduced in all fluids, similarity in heat transfer can be achieved. In this section, the comparisons of flow fields and turbulent behaviours are presented to further understand the success of the current scaling method.

Firstly the profiles of the non-dimensional streamwise velocity at chosen locations (z/D = 5, 10, 17, 28) of all the four cases are shown in Fig. 6.9. The general development trends of $\overline{u_z}$ profiles agrees with the trends of flows presented by Bae et al. [11] and He et al. [13]. The velocity profiles of the RE-series cases at corresponding locations agree well with each other, which suggests the scaling based on Re_0, Fr_0

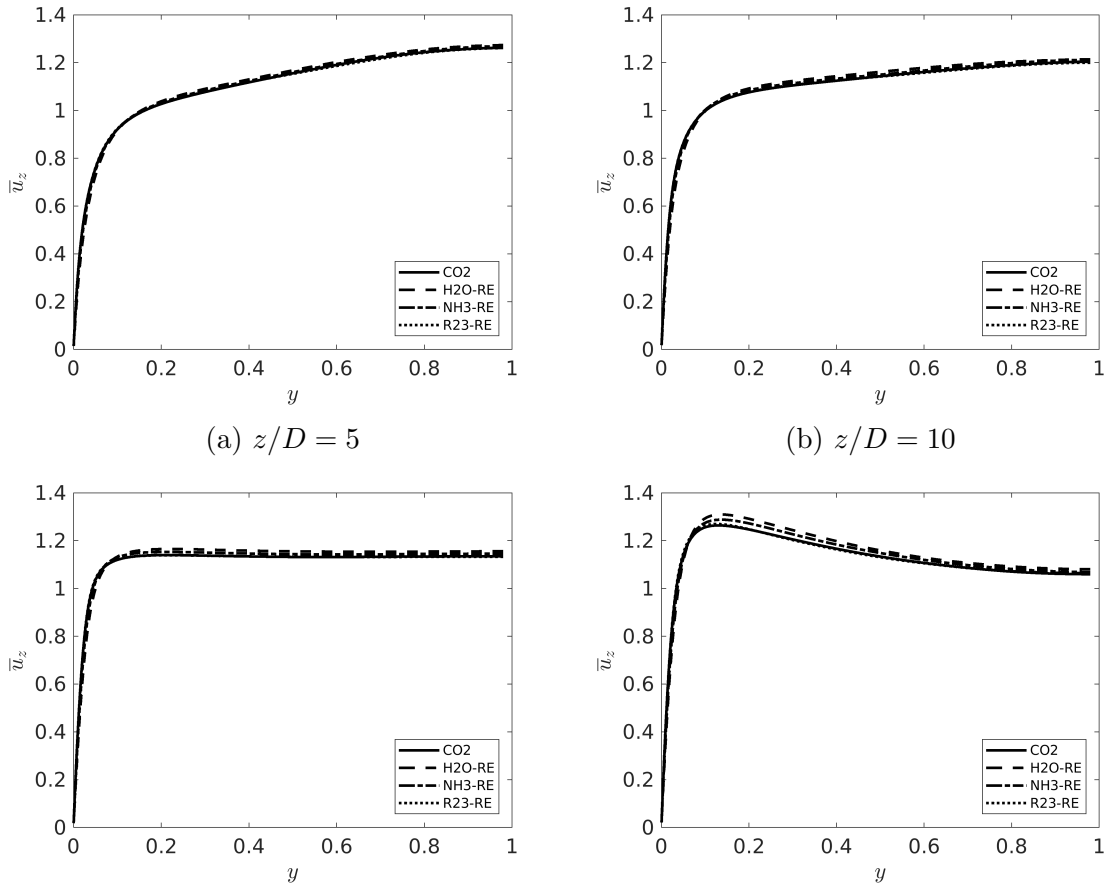

(a) $z/D = 5$ (b) $z/D = 10$

(c) $z/D = 17$ (d) $z/D = 28$

Figure 6.9: Profiles of $\overline{u_z}$ at chosen locations of the RE-series cases.

and bulk fluid properties guarantees the similarity of momentum equations in this case. Excellent agreements between the velocity fields in the RE-series cases is the precondition of the success of the thermal fields presented in the last section. Fig. 6.9 shows that $\overline{u_z}$ profiles in all cases change from fully-developed turbulent profiles ($z/D \sim 0$) to flatten profiles ($z/D \sim 17$), due to several reasons (mainly the buoyancy effect), and then they change to M-shape profiles, with the maximum velocities located near the wall. When the M-shape profiles are formed, the differences across cases are slightly larger, especially for the near-wall peak. Case H2O-RE has a slightly larger peak velocity here.

In addition to $\overline{u_z}$, similarities in the property fields are also required to achieve a similarity in momentum equations. As similar enthalpy fields are found in the RE-series cases in the last section, similarities in $\overline{\rho}$ and $\overline{\mu}$ fields are expected as the $\rho(h^+)$ and $\mu(h^+)$ functions of these fluids are very similar at such flow conditions (Fig. 6.1). Profiles of $\overline{\rho}$ and $\overline{\mu}$ close to the wall ($y < 0.2$) at chosen locations of the RE-series

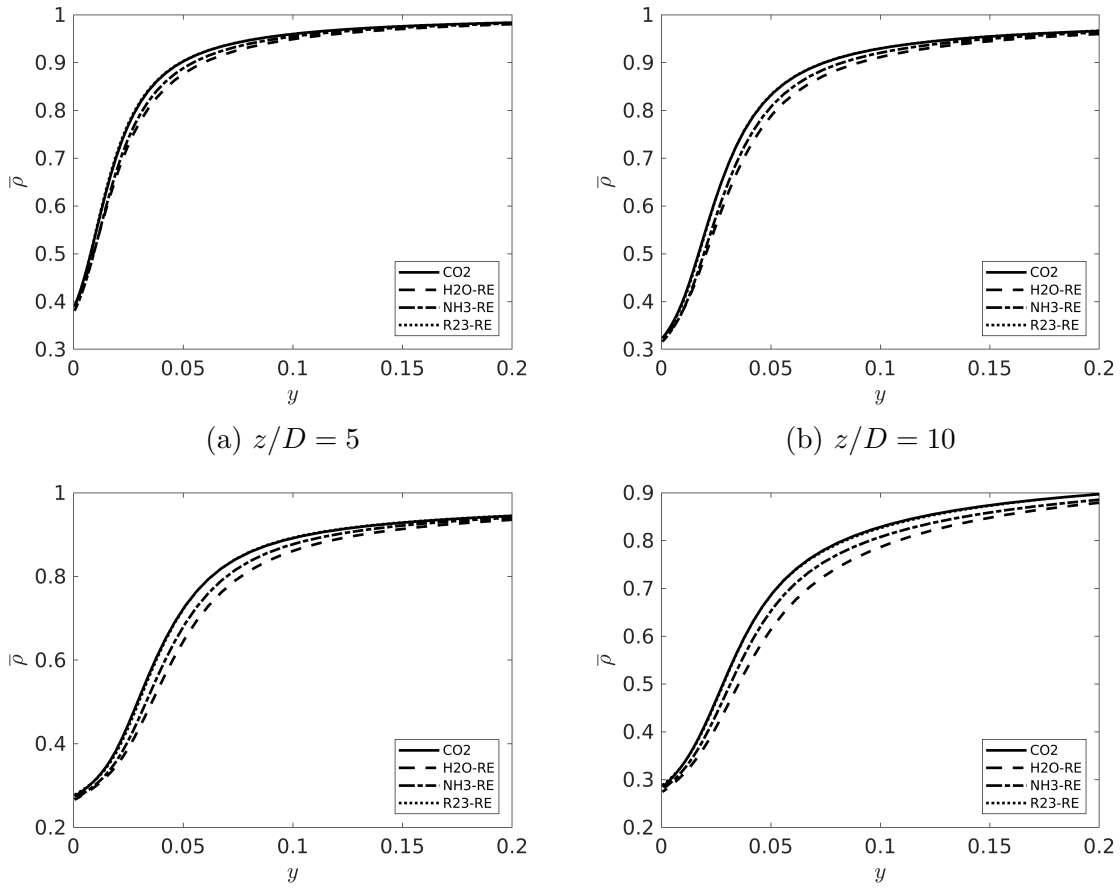

(a) $z/D = 5$ (b) $z/D = 10$

(c) $z/D = 17$ (d) $z/D = 28$

Figure 6.10: Profiles of $\overline{\rho}$ at chosen locations of the RE-series cases.

cases are shown in Fig. 6.10 and 6.11. The $\overline{\rho}$ and $\overline{\mu}$ profiles of the RE-series cases are similar, though the agreements are not as good as that for $\overline{u_z}$. As shown in Fig. 6.10, densities are hugely changed near the wall. At $z/D = 17$ & 28, the density reduces to about 30% of the inlet value. The density profiles of CO2 and R23-RE are nearly collapsed, and both higher than the other two cases. Similar $\overline{\rho}$ profiles in the RE-series cases indicate that the buoyancy force $((\rho_c - \rho)g)$ is roughly similar in these cases. This is the main reason for the similarity in $\overline{u_z}$ profiles as the changes from flattened to M-shape profiles are mainly due to the buoyancy effect. The comparison of buoyancy effect in the RE-series cases will be discussed later using the momentum balance.

Divergence of the $\overline{\mu}$ profiles across these cases are larger than that in $\overline{\rho}$, but the effect of viscosity variations on changes of $\overline{u_z}$ profiles are weaker, according to the discussions in last chapter. The similarity of $\mu(h^+)$ functions in the four fluids is not as good as that of $\rho(h^+)$ functions. When h^+ reaches the pseudocritical enthalpy, μ_{pc}

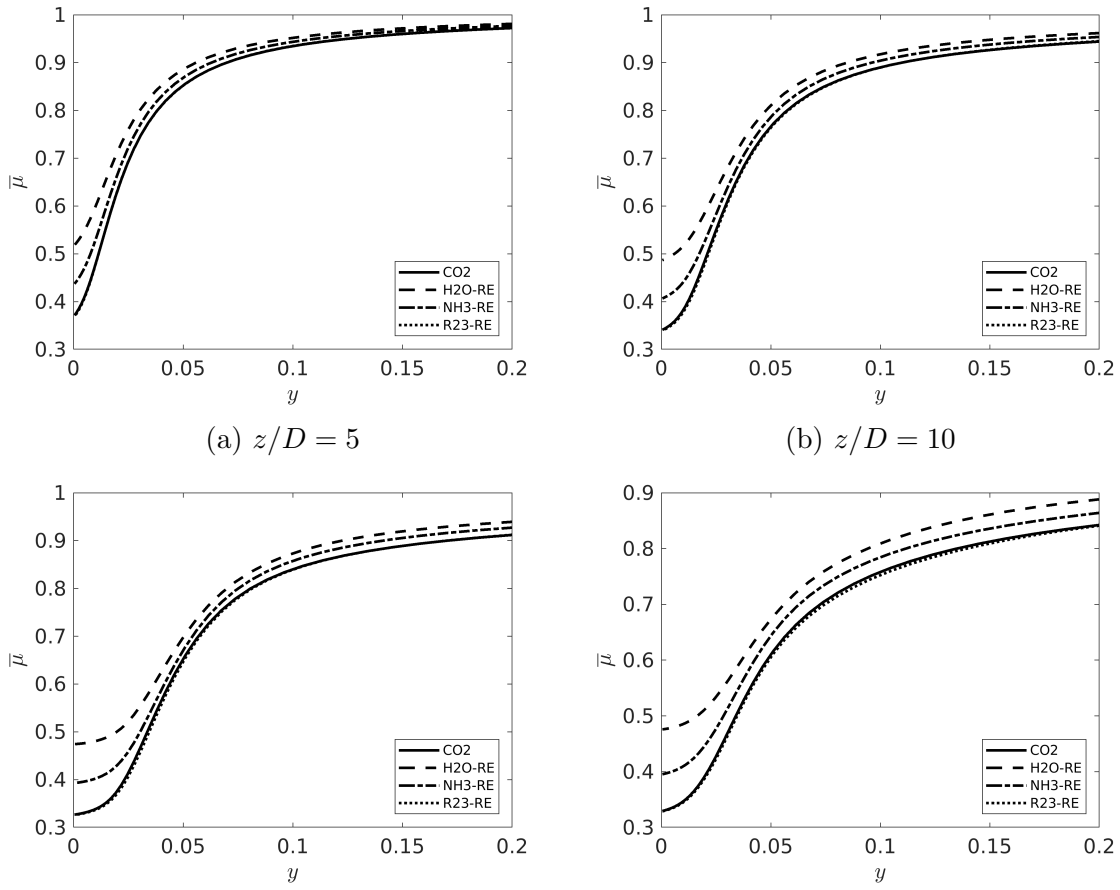

(a) $z/D = 5$ (b) $z/D = 10$

(c) $z/D = 17$ (d) $z/D = 28$

Figure 6.11: Profiles of near-wall ($y < 0.2$) $\overline{\mu}$ at chosen locations of the RE-series cases.

($= \frac{\mu^*_{pc}}{\mu^*_0}$) values of CO_2, H_2O, NH_3 and R23 are respectively 0.54, 0.66, 0.60 and 0.53, while ρ_{pc} ($= \frac{\rho^*_{pc}}{\rho^*_0}$ values are 0.63, 0.60. 0.61 and 0.63. With similar resolved radial profiles of h^+ in the RE-series cases, $\overline{\mu}$ profiles are less similar, especially near the wall, where $\overline{\mu}$ of H2O-RE and NH3-RE is very different from Case CO2. However, in all locations, $\overline{\mu}$ of Case R23-RE is very similar to that of Case CO2, which is due to the consistent $\mu(h^+)$ functions in the two fluids. When the pressures of the RE-series cases are tuned to achieve similarity between the functions of thermophysical properties against h^+, the similarity of $\rho(h^+)$ is the priority to consider as it is more important in determining the flow fields. The viscous shear stress near the wall in Case H2O-RE and NH3-RE is expected to be different from Case CO2 and R23-RE, due to the discrepancies in $\overline{\mu}$ here. Some differences in momentum balance is expected due to the differences in viscous shear stress, and this effect will be quantified and discussed later.

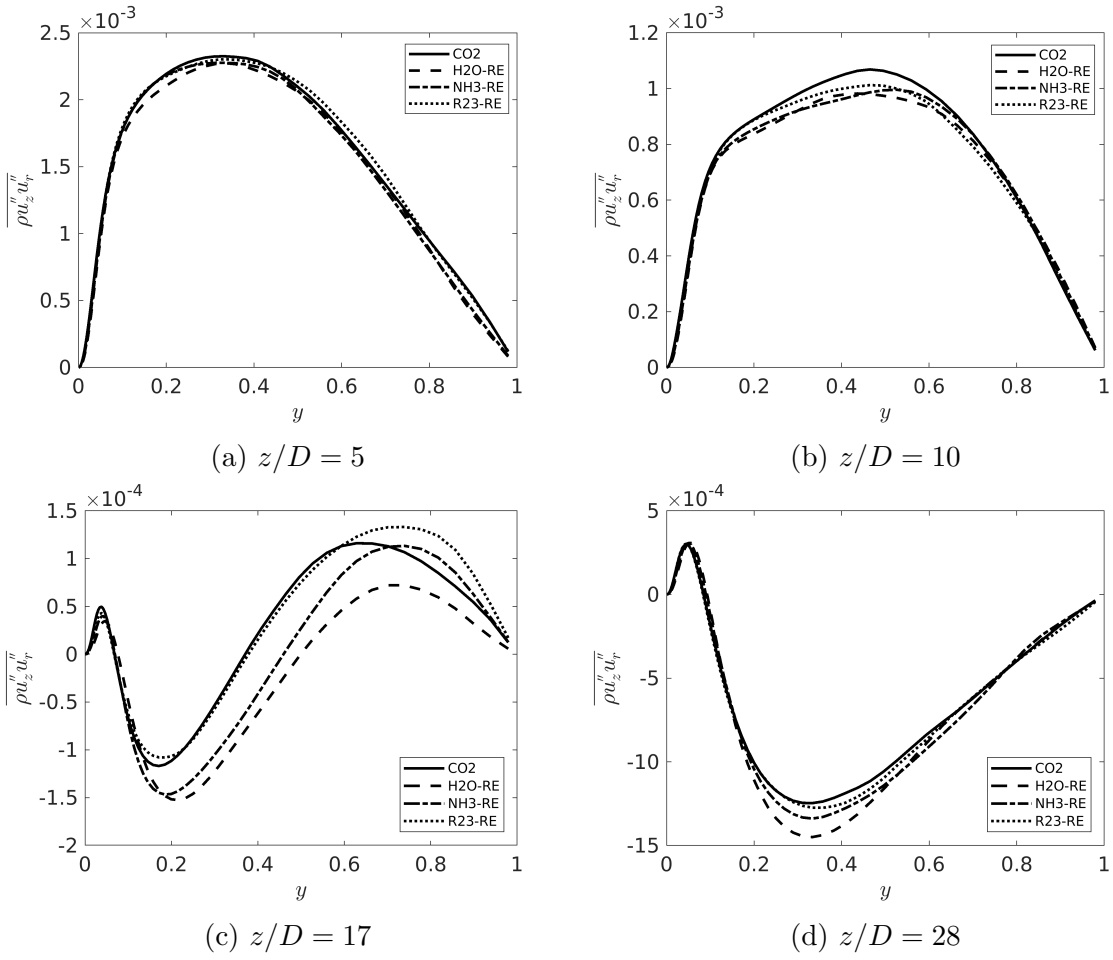

(a) $z/D = 5$ (b) $z/D = 10$

(c) $z/D = 17$ (d) $z/D = 28$

Figure 6.12: Profiles of near-wall ($y < 0.2$) $\overline{\rho u_z'' u_r''}$ at chosen locations of the RE-series cases.

The FIK decompositions of Nu in the last section suggest the laminarization (reduction of turbulence) plays an important role in heat transfer deterioration, and the regeneration of turbulence is also the key reason of the heat transfer enhancement at later locations in all cases. Comparisons of variations in turbulent quantities, i.e., turbulent shear stress $\overline{\rho u_z'' u_r''}$ and turbulent kinetic energy (TKE) $\frac{1}{2}\overline{u_i'' u_i''}$ are shown in Fig. 6.12 and Fig. 6.13 respectively.

As shown in Fig. 6.12, $\overline{\rho u_z'' u_r''}$ in each case rapidly reduces from the inlet to $z/D = 17$, where $\overline{\rho u_z'' u_r''}$ reaches the minimum at most part and these flows are fully laminarized. This is corresponding to (but slightly before) the locations of minimum Nu and St ($z/D \sim 20$). At further down stream, the magnitudes of $\overline{\rho u_z'' u_r''}$ rapidly increases, with positive values at about $y < 0.1$ (corresponding to the locations with negative $\frac{\partial \overline{u_z}}{\partial r}$), and negative values at about $y > 0.1$ (locations with positive $\frac{\partial \overline{u_z}}{\partial r}$). This is corresponding to the forming of M-shape velocity profiles and the regeneration of

turbulence. Generally, the reducing rates of $\overline{\rho u_z'' u_r''}$ in the RE-series cases are all similar to each other. Profiles at $z/D = 10$, 17 and 20 show that $\overline{\rho u_z'' u_r''}$ of the three "RE" cases reduce slightly faster than Case CO2.

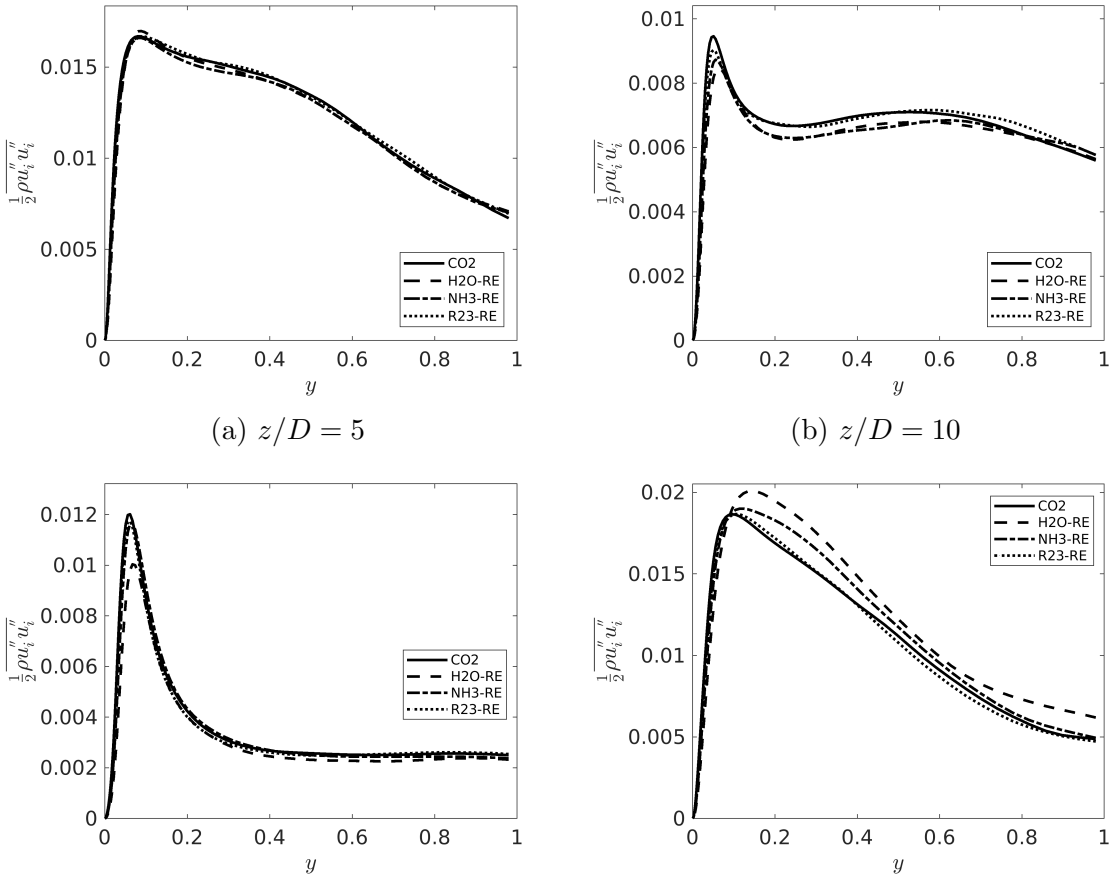

(a) $z/D = 5$ (b) $z/D = 10$

(c) $z/D = 17$ (d) $z/D = 28$

Figure 6.13: Profiles of $\frac{1}{2}\overline{\rho u_i'' u_i''}$ at chosen locations of the RE-series cases.

Similar to $\overline{\rho u_z'' u_r''}$, the $\frac{1}{2}\overline{\rho u_i'' u_i''}$ (TKE) profiles in the RE-series cases agree well with each other at corresponding locations (Fig. 6.13). At $z/D = 5$, TKE profiles of all cases nearly collapse, with a near-wall peak in each case. Later downstream, at $z/D = 10$, the magnitudes of TKE reduce in all cases, while similarities of the profiles are largely remained. The near-wall peak value in each profile is significantly reduced here, and another smaller peak appears at about $y = 0.6$. At $z/D = 17$, when the four flows are fully laminarized, TKE values at the mainstream ($y > 0.4$) are relatively low. At this location, the near-wall peak of TKE in Case H2O-RE is lowered than those of the other three cases, and at $z/D = 28$, TKE of H2O-RE is larger than the other three cases at most part, which suggest the streamwise developments in terms

of laminarization and recovery in Case H2O-RE is faster. Generally, similarity is also achieved in the streamwise variations of TKE.

Similarities are also shown in the variations of turbulent structures, iso-surfaces of $\lambda_2 = -0.4$ in the four cases are shown in Fig. 6.14. λ_2 is the second largest eigenvalue of the symmetric tensor $\boldsymbol{S^2 + \Omega^2}$ ($\boldsymbol{S}$ and $\boldsymbol{\Omega}$ are the symmetric and antisymmetric parts of the velocity gradient tensor $\boldsymbol{\nabla u^*}$).

To compare the variations of the turbulence structures in different cases, iso-surfaces of $\lambda_2 = -0.4$ in each case are shown in figure 6.14. Locations of $\lambda_2 < 0$ represent the core of turbulence vortexes. To clearly visualise the vortexes at different locations, the pipe is halved by a plane through its axis. Iso-surfaces of $\lambda_2 = -0.4$ are coloured by their radial locations, i.e., near-wall vortexes are in grey, vortexes at the core flow are in red, and the vortexes in the middle region are in yellow. λ_2 fields are calculated using the instantaneous velocity fields after these flows reaching stationary state. At the initial regions ($z/D < 5$) of all cases, vortexes are dense and spacially frequent. Consistently, at $z/D = 5$ to 10 of each case, vortexes gradually disappear, and after about $z/D = 13$, vortexes are very sparse, indicating that turbulent activities are largely lessened here due to the laminarization process. At $z/D = 13$ to 20, vortexes remain sparse, but there are few new spots generated at the near-wall and middle region (grey and yellow), and after about $z/D = 25$, vortexes increase again, with higher spacial frequency, corresponding to the regeneration of turbulence. Laminarization and regeneration of turbulence in each case can be clearly visualised by the variation of vortex, which agree with the change of heat transfer characteristics presented in the last section. The behaviours of the turbulent vortexes in all the RE-series cases are very similar, suggesting a similar turbulent behaviour is reproduced in each of these cases.

Contours of streamwise mass flux fluctuations $(\rho u_z)'$ at opened-up wall-parallel surfaces close to the wall in all cases are shown in Fig. 6.15. The y_0^+ ($y_0^+ = (y^* \sqrt{\frac{\tau^*_{w,0}}{\rho^*_0}})/\nu^*$) of the chosen $z - \theta$ surfaces in Case CO2, H2O-RE, NH3-RE and R23-RE are respectively 5.28, 5.40, 5.23 and 5.57. The initial flows of all cases contain short and frequent turbulent spots. The main changes of the fluctuating mass flux in each case happens at about $z/D \approx 13$, where streaks are formed and elongated, and become spacially coarser, corresponding to the fully laminarized region where turbulent vortexes are mostly disappeared. After $z/D \approx 22$, turbulent spots are generated and become more and more at later locations. In all cases, although turbulent is recovered at downstream locations, the behaviour of $(\rho u_z)'$ is different

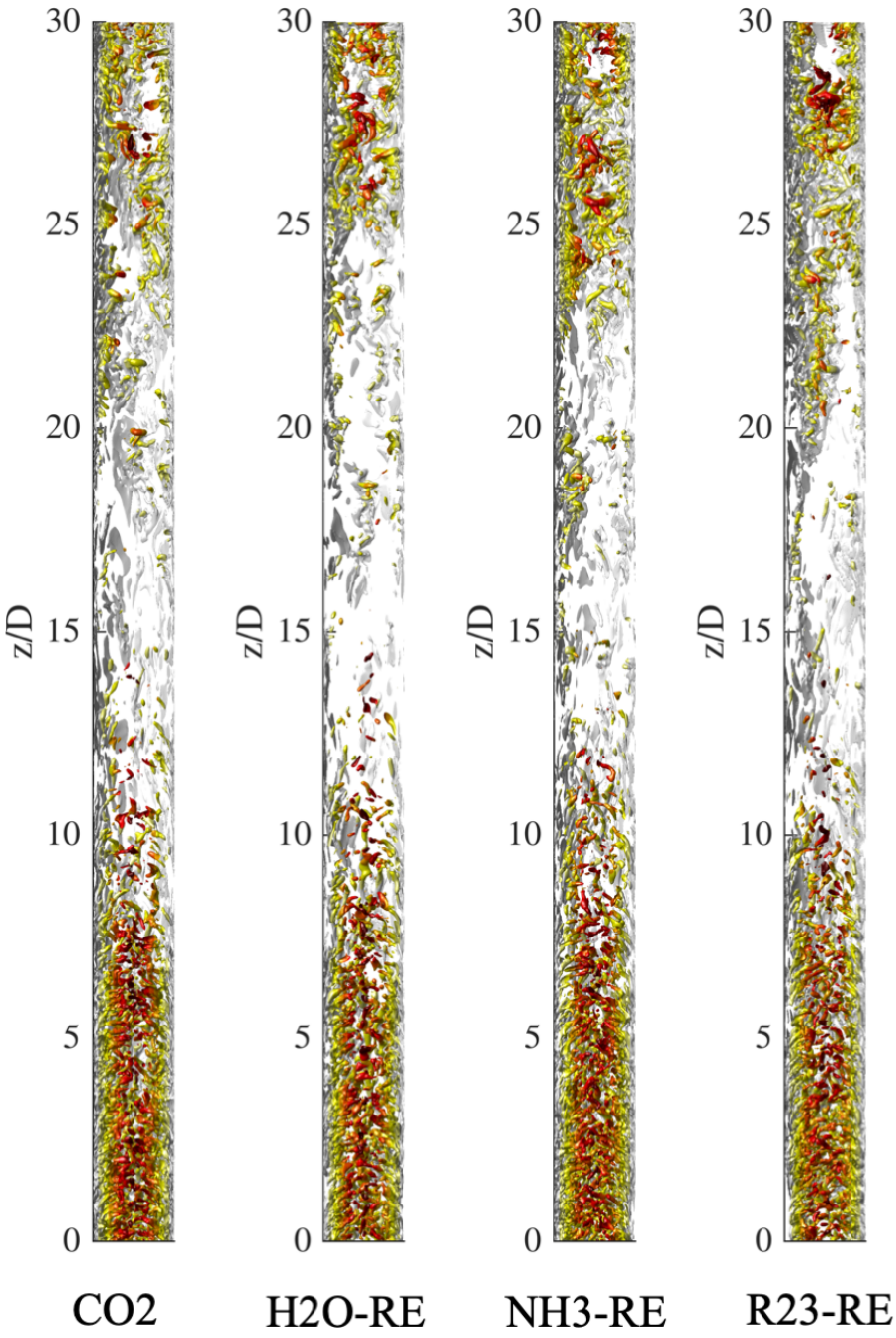

Figure 6.14: Isosurfaces of $\lambda_2 = -0.4$ in the RE-series cases, coloured by the radial location of the vortexes.

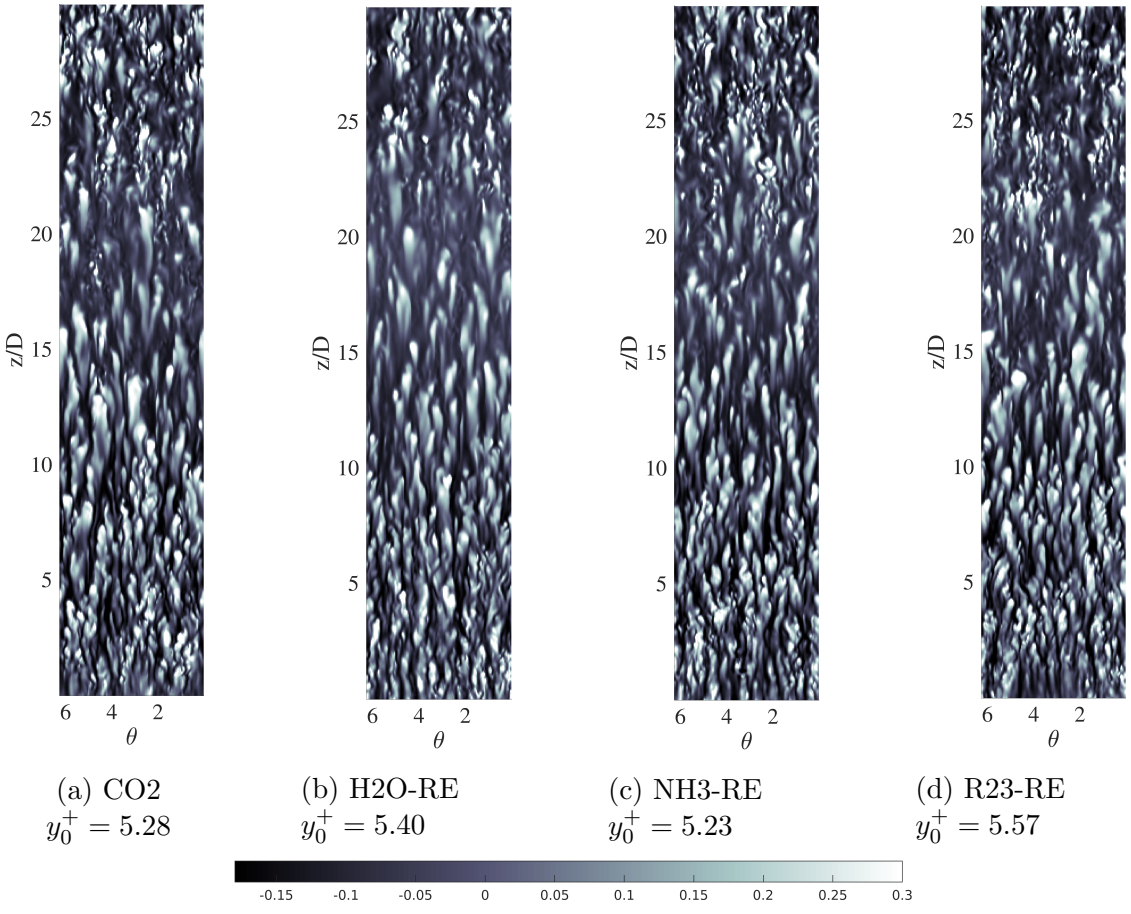

(a) CO2 $y_0^+ = 5.28$ (b) H2O-RE $y_0^+ = 5.40$ (c) NH3-RE $y_0^+ = 5.23$ (d) R23-RE $y_0^+ = 5.57$

Figure 6.15: Contours of instantaneous $(\rho u_z)'$ at near-wall surfaces in the RE-series cases.

from those at the initial locations. Again, similar changes in $(\rho u_z)'$ structures are produced by the RE-series cases, with similar streaks behaviours.

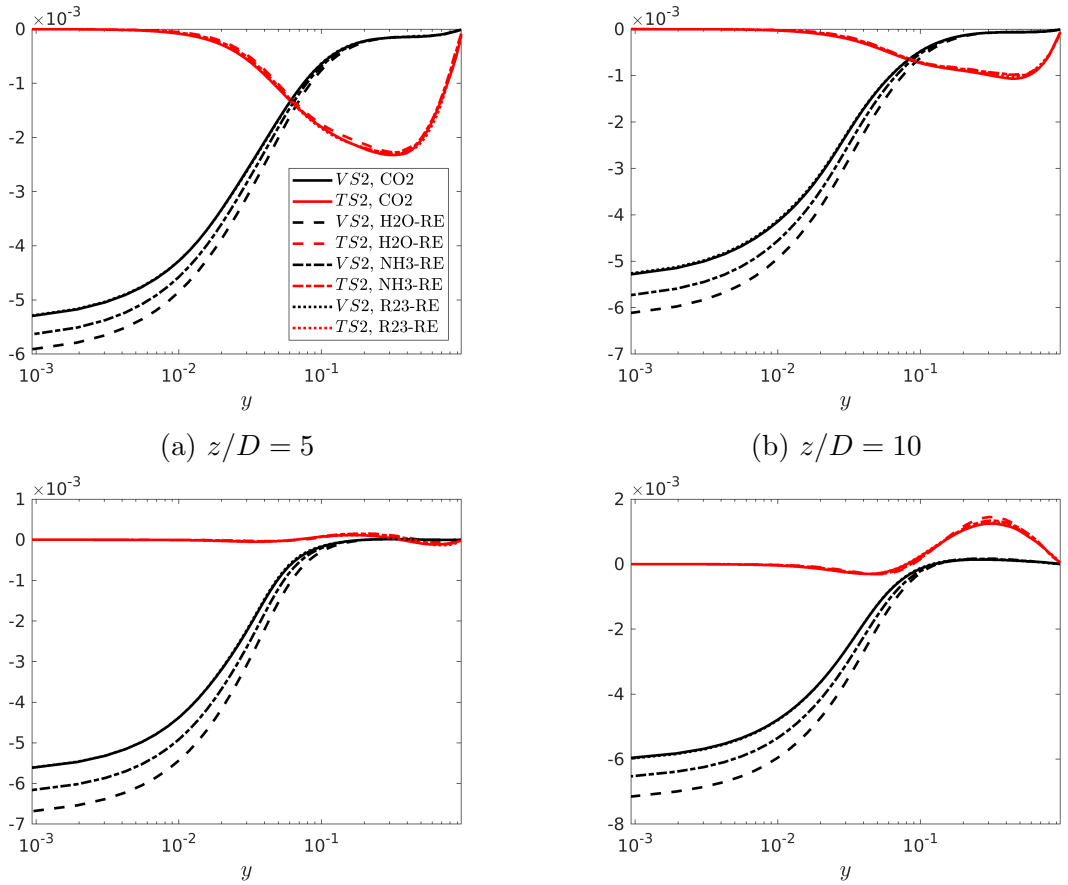

(a) $z/D = 5$ (b) $z/D = 10$

(c) $z/D = 17$ (d) $z/D = 28$

Figure 6.16: Profiles of viscous ($TS2$) and turbulent stress term ($VS2$) of the integrated momentum equation in the RE-series cases.

Similar and spacially synchronous developments of velocity profiles, turbulent quantities ($\overline{\rho u_z'' u_r''}$ & $\frac{1}{2}\overline{\rho u_i'' u_i''}$) are demonstrated in all the RE-series cases. These achieved similar flow fields and turbulent characteristics in the RE-series cases are the reasons behind the successful similarity in enthalpy (h^+) fields and heat transfer characteristics. The similarity of the property functions cannot be fully guaranteed. As shown in Fig. 6.11, the dynamic viscosities of Case H2O-RE and NH3-RE deviate from that of CO2 near the wall, especially at downstream locations ($z/D = 17$ & 28). The differences caused by the the difference in near-wall viscosity is reflected in the changes in momentum balance. However, it is shown that the similarity of turbulent shear stress $\overline{\rho u_z'' u_r''}$ is not strongly affected. To investigate the effect of the divergence in near-wall viscosities, the momentum balances in these cases are compared.

The integrated Favre-averaged streamwise momentum equation for cylindrical coordinate, which is derived in the chapter 4 and describes the stationary vertical pipe flows can be written as follow:

$$
\begin{aligned}
0 = & \underbrace{-\frac{1}{r}\int_0^r r\frac{\partial(\overline{\rho}\widetilde{u}_z\,\widetilde{u}_z)}{\partial z}dr}_{IN1}\underbrace{-\overline{\rho}\widetilde{u}_z\,\widetilde{u}_r}_{IN2} \\
& \underbrace{-\frac{1}{r}\int_0^r r\frac{\partial(\overline{\rho u_z'' u_z''})}{\partial z}dr}_{TS1}\underbrace{-\overline{\rho u_z'' u_r''}}_{TS2} \\
& \underbrace{+\frac{1}{Re_0}\Big(\frac{1}{r}\int_0^r r\frac{\partial}{\partial z}\big(2\overline{\mu}\frac{\partial\overline{u}_z}{\partial r}\big)dr}_{VS1}+\underbrace{\overline{\mu}\big(\frac{\partial\overline{u}_r}{\partial z}+\frac{\partial\overline{u}_z}{\partial r}\big)\Big)}_{VS2} \\
& \underbrace{-\frac{r}{2}\frac{\partial P}{\partial z}}_{PG}\underbrace{-\frac{1}{r}\int_0^r r(\overline{\rho}-\overline{\rho}_c)gdr}_{Bo},
\end{aligned}
\tag{6.18}
$$

which contains two inertia terms ($IN1$ & $IN2$), two turbulent shear stress terms ($TS1$ & $TS2$), two viscous shear stress terms ($VS1$ & $VS2$), the modified pressure gradient term ($PG = -\frac{r}{2}\frac{\partial P}{\partial z} \equiv -\frac{r}{2}\big(\frac{\partial\overline{p}}{\partial z} + \overline{\rho_c}g\big)$) and the buoyancy term (Bo).

The viscous and turbulent shear stress profiles at chosen locations of the RE-series cases are shown in Fig. 6.16. To better view the difference near the wall, logarithmic scale is applied to the horizontal axis. The near-wall viscous shear stress of Case R23-RE and CO2 agree very well, nearly collapse with each other in all locations, shown in Fig. 6.11. In all locations, the magnitudes of the near-wall viscous shear stress in Case H2O-RE is the largest, followed by that of Case NH3-RE, and those of Case CO2 and R23-RE are the lowest. From $z/D = 10$ to 28, the magnitudes of $VS2$ in all cases gradually increases, indicates the upward force (buoyancy force) near the wall is growing larger. Unlike $VS2$, turbulent shear stress profiles $TS2$ of the four cases agree very well.

The profiles of the modified pressure gradient, buoyancy term and the inertial terms in all cases are shown in Fig. 6.17. The buoyancy terms near the wall show divergence which balances with that of $VS2$ terms, i.e., Case H2O-RE has the largest buoyancy force, followed by NH3-RE, then Case CO2 and R23-RE has nearly the same and lowest Bo. Although the densities near the wall are very similar in each case, there are differences in Bo near the wall, and the differences in $VS2$ are responses to those in Bo. The developments of PG is very similar in all cases, during the laminarization and regeneration of turbulence, PG profiles in all cases keep reducing at very similar rates, which are largely determined by the non-uniform gravity force,

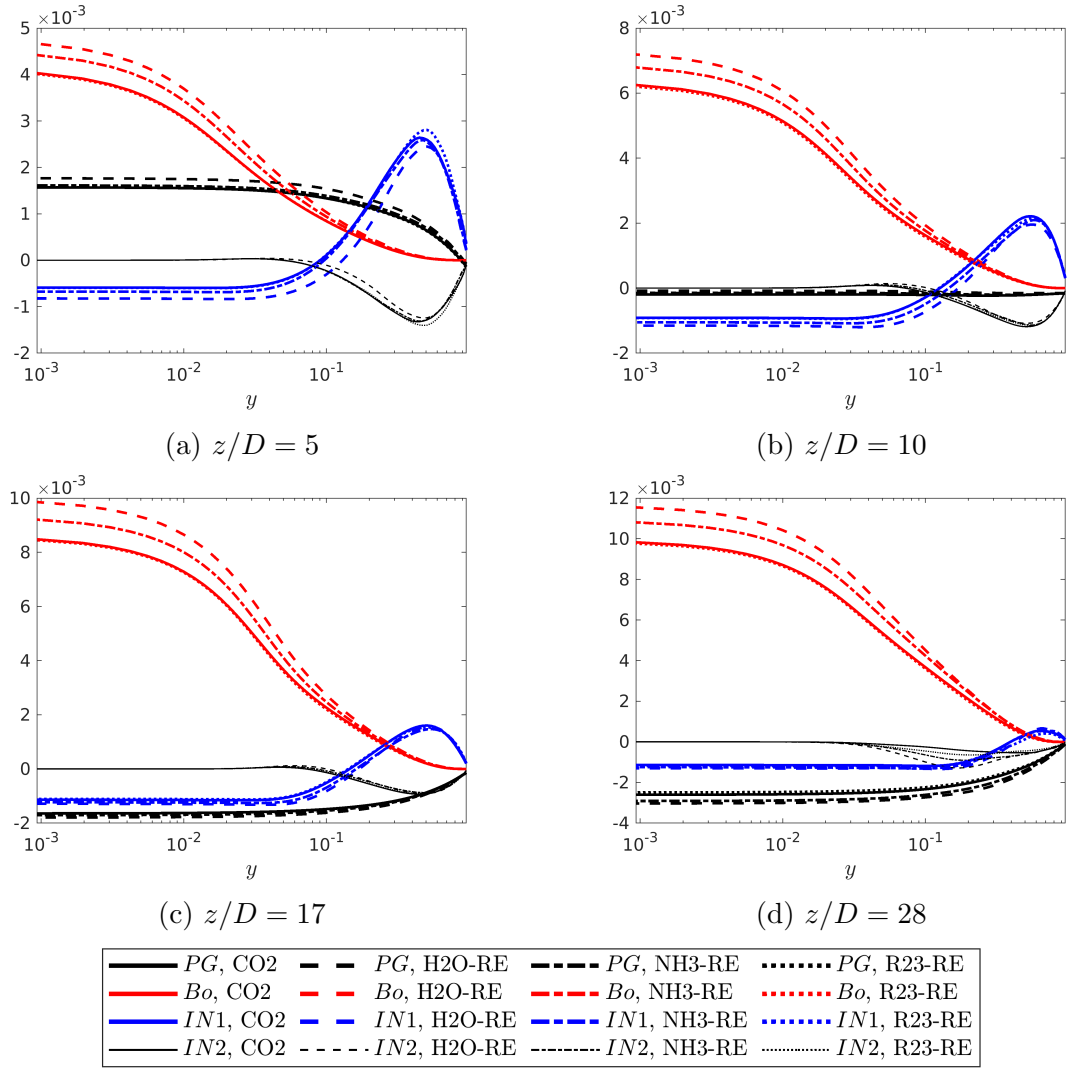

(a) $z/D = 5$ (b) $z/D = 10$

(c) $z/D = 17$ (d) $z/D = 28$

Figure 6.17: Profiles of modified pressure gradient (PG), Buoyancy term (Bo) and inertial terms ($IN1$ & $IN2$) of the integrated momentum equation at chosen locations of the RE-series cases.

i.e., gravity near the wall reduces, then the streamwise pressure gradient $-\frac{\partial \overline{p}}{\partial z}$ reduces as a response, both near the wall and at the main stream.

The near-wall changes (local density or viscosity reductions) affect the mainstream flow mainly through the response of term PG. In these cases, the inertial terms $IN1$ and $IN2$ rise due to the force imbalance caused by the overall reduction of PG, which indicates acceleration and deceleration happens during the laminarization and recovery, reflected in the changes of velocity profiles in Fig. 6.9. From $z/D = 5$ to 10 in each case, PG reduces to zero everywhere as a result of the increasing Bo, then at $z/D = 17$, PG becomes negative. The response of the two inertial terms are also very similar in all cases. The budget terms of the streamwise momentum equation show that the differences of viscosity near the wall in these cases are mainly reflected in the differences in $VS2$ near the wall, which are balanced by the difference in Bo close to the wall. The general developments of $TS2$, PG and the inertia terms of the RE-series cases agree well with each other.

The flow and thermal fields, turbulent quantities and structures of the RE-series cases are very similar, and the significance behind this is that any one of these fluid can be a surrogate fluid of another fluid in experiments. With the support of the current scaling method, the flow and thermal features of the surrogate fluid can be translated to those of the target (prototype) fluid. The second significance is that for flows at these specific configurations, the chosen fixed non-dimensional parameters (N_{TPC}, N_{SPC}, Fr_0, Re_0) and operating pressures are able to characterise the heat transfer and turbulence in such flows. The above comparisons of the RE-series cases provide further understandings and validations of the current scaling method at chosen configurations.

6.3 Results and discussion on PE-series

The above discussions focus on the RE-series cases with Re_0 fixed and good similarity is achieved, in terms of variations in heat transfer and turbulent characteristics. In this section, another potential choice in the scaling method is investigated, in which the inlet Peclect number (Pe_0) rather than the inlet Reynolds number (Re_0) is matched. With Pe_0 fixed, potentially a better similarity in the non-dimensional energy equation can be achieved in the model fluid. However, compared to the RE-series cases, the similarity of the momentum equation will be somehow loosened, and the effect of this will be investigated. Flow and thermal boundary conditions of the "PE" cases and their determination are introduced in section 6.1.

6.3.1 Comparison of heat transfer characteristics

The developments of the bulk enthalpy and temperature in the PE-series cases are shown in Fig. 6.18. They are exactly the same as those of the RE-series cases, as a result of the fixed N_{SPC} and N_{TPC}. h_b^+ in the four cases are consistent and linear. T_b have a same starting point and become more and more different due to the different c_p. With a linear h_b^+, the change rates of T_b reduces along the streamwise direction in each case due to the increasing c_p. Moreover, the bulk thermophysical properties in the PE-series cases are exactly the same as those in the RE-series cases as they are the same fluids: ρ_b and μ_b of CO_2 and R23 nearly collapse with each other, different from those of H_2O and NH_3.

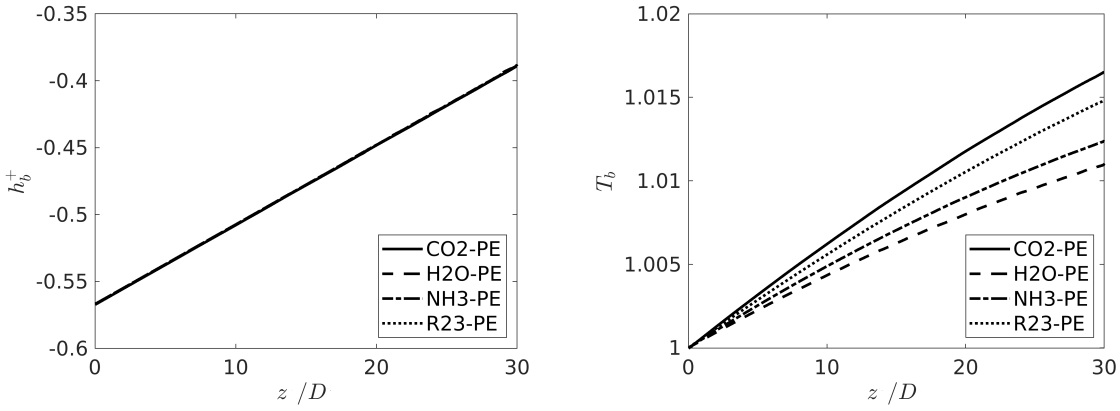

(a) (b)

Figure 6.18: Streamwise developments of (a) bulk enthalpy and (b) bulk temperature in the PE-series cases.

The developments of wall enthalpy $\overline{h_w^+}$ of the PE-series cases are shown in Fig. 6.19a, as well as the wall temperature $\overline{T}_w$ in Fig. 6.19b. Different from the similar $\overline{h_w^+}$ profiles in the RE-series cases, $\overline{h_w^+}$ of the PE-series cases are quite different from each other. The peaks of $\overline{h_w^+}$ appear at different locations: $z/D \approx 17$ for Case H2O-PE, $z/D \approx 18$ for Case NH3-PE & R23-PE and $z/D \approx 20$ for Case CO2. It suggests that the worst heat transfer locates differently in these cases, contrasting the consistency of the RE-series cases. Re_0 of Case CO2, H2O-PE, NH3-PE and R23-PE are respectively 2617, 4444, 3436 and 3573. It is found that a larger Re_0 results in an earlier peak of $\overline{h_w^+}$, i.e., a faster variation in heat transfer. It should be noted that the $\overline{h_w^+}$ profiles for Case NH3-RE and R23-RE nearly collapse with each other, as the values of Re_0 are very close and Pe_0 are the same in these two cases. An excellent similarity is therefore achieved between them.

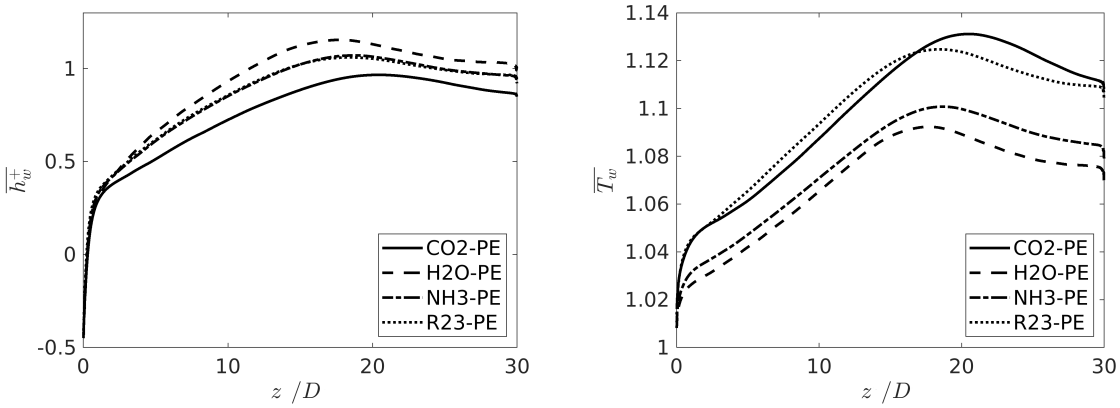

(a) (b)

Figure 6.19: Streamwise developments of (a) wall enthalpy and (b) wall temperature in the PE-series cases.

The developments of wall temperature (Fig. 6.19b) are not as similar as those of $\overline{h_w^+}$, due to the differences in $c_p(h^+)$. Differences in $c_p(h^+)$ also result in larger divergence of $\overline{T}_w$ developments in these cases. However, the sequence of peak $\overline{T}_w$ values in terms of streamwise locations are the same with that in $\overline{h_w^+}$: peak $\overline{T}_w$ locates earlier with a larger Re_0, hear transfer deterioration progress faster.

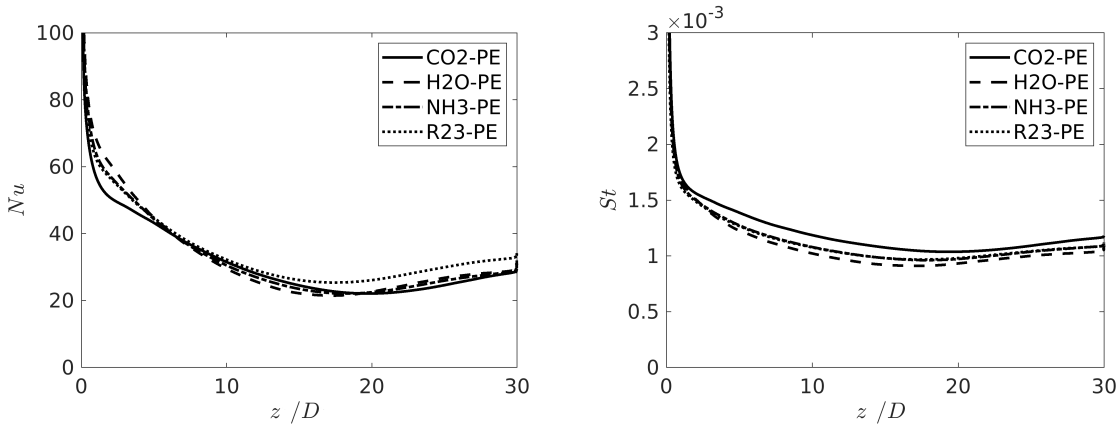

(a) (b)

Figure 6.20: Streamwise developments of (a) Nusselt number and (b) Stanton number in the PE-series cases.

The developments of the Nusselt number and Stanton number in the four cases are shown in Fig. 6.20a & 6.20b. Similar development trends are observed in these four cases. Nusselt numbers in all cases firstly reduce rapidly at the entrance region ($z/D < 2$), then reduce with lower rates, and rise after reaching the minimum at

different locations for difference cases. The locations with the minimum Nu in Case CO2, H2O-RE, NH3-RE and R23-RE are $z/D = 19.8$, 17.33, 18.22 and 17.36, while for the minimum St, the locations are $z/D = 19.34$, 17.06, 17.81 and 17.42. It suggests that for all the "PE" cases the worst heat transfer appears at slightly earlier locations, and also the recoveries are brought forward. It is worth noting that although Case NH3-RE and R23-RE have collapsed developments in h^+ and $\overline{h_w^+}$, their Nusselt numbers are very close at $z/D < 7$, but diverge from each other later. However, the Stanton number in these two cases collapse at all locations, brilliant similarity in heat transfer characteristics between them is reflected in the developments of St. In conclusion, by choosing to fix Pe_0, the general trends of Nu and St are reproduced by the model fluids, but the agreements are weaker than the cases with Re_0 fixed.

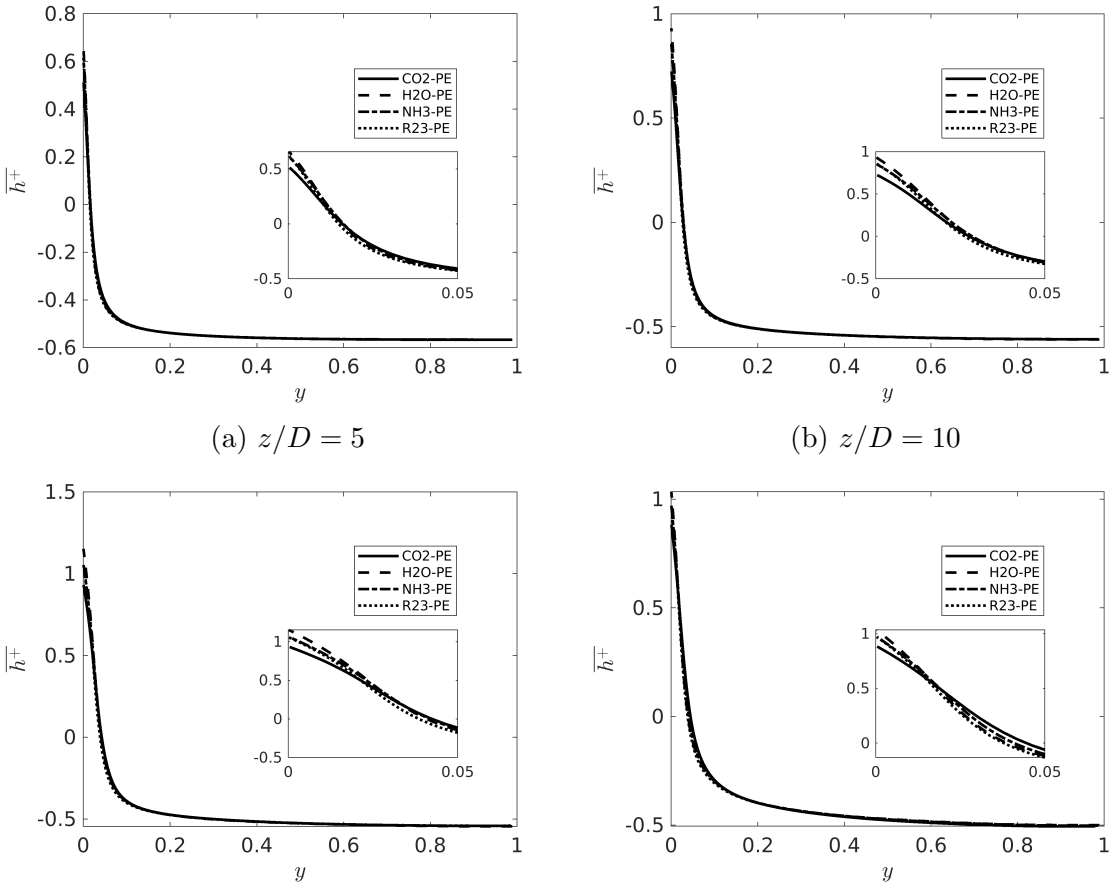

(a) $z/D = 5$ (b) $z/D = 10$

(c) $z/D = 17$ (d) $z/D = 28$

Figure 6.21: Profiles of $\overline{h^+}$ at chosen locations of the PE-series cases.

To compare the thermal fields, radial profiles of $\overline{h^+}$ in the PE-series cases are shown in Fig. 6.21. Although the inlet Reynolds number of theses flows are different,

the enthalpy fields are not largely affected. $\overline{h^+}$ profiles agree well at most part and the main differences are close to the wall.

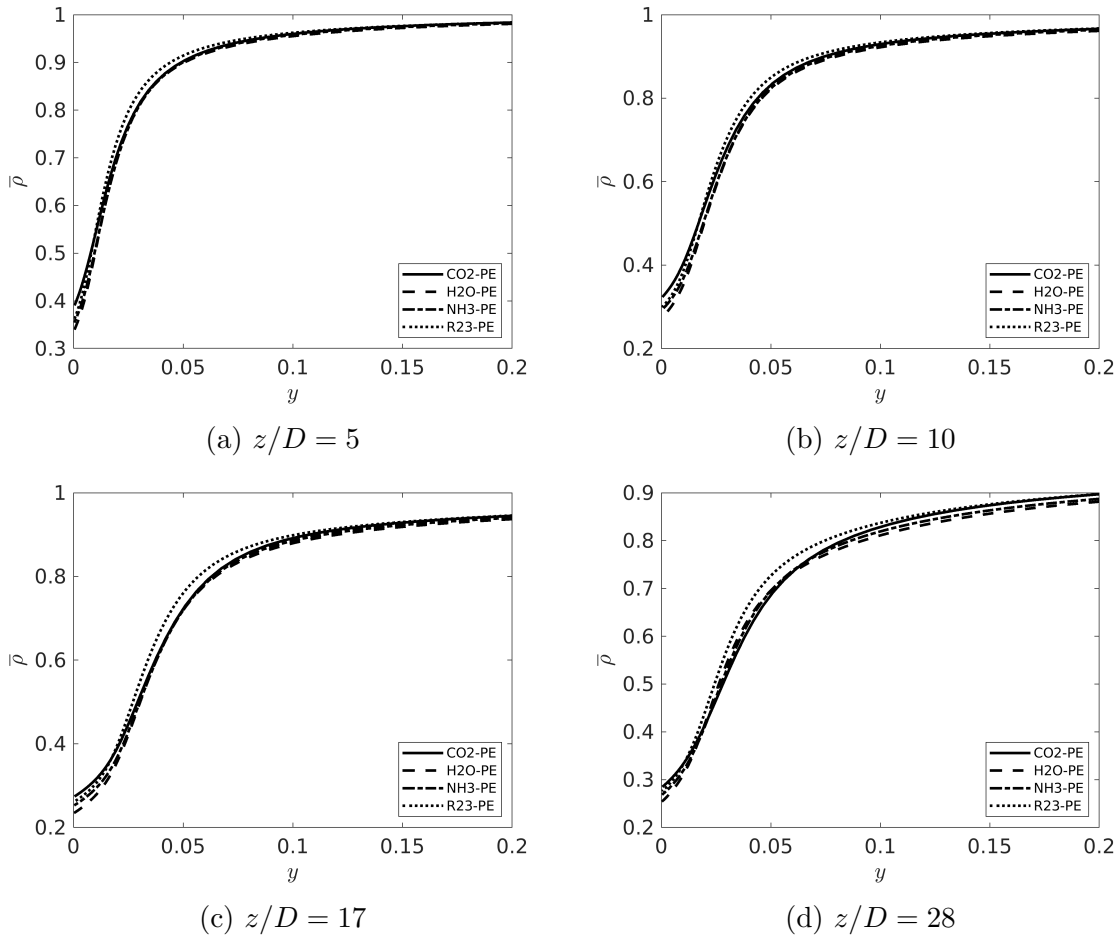

(a) $z/D = 5$ (b) $z/D = 10$

(c) $z/D = 17$ (d) $z/D = 28$

Figure 6.22: Profiles of $\overline{\rho}$ at chosen locations of the PE-series cases.

The density profiles of the PR-series cases are shown in Fig. 6.22. Similar to those in the RE-series cases, the profiles are clipped with $y = 0$ to 0.2, to more clearly show the near-wall region with significant variations. The agreement in $\overline{\rho}$ is slightly better than in the RE-series cases and the advantage of fixing Pe_0 is hence embodied. In all cases, $\overline{\rho}$ rapidly reduces at the near-wall region as the enthalpy reach the pseudocritical value ($h^+ = 0$). When the thermal boundary layers become thicker, density further away from the wall is affected at later streamwise locations.

6.3.2 Comparison of flow behaviours and turbulent characteristics

The comparisons of Nu, St and $\overline{h_w^+}$ developments between the PE-series cases show the variations of heat transfer characteristics are less similar when Pe_0 rather than Re_0 are scaled in the model fluids, and the responses in heat transfer (deterioration and recovery) happen faster when Re_0 is higher. It is known that the changes in heat transfer characteristics is strongly influenced by the variations in turbulence. The comparisons of flow behaviours and variations in turbulent characteristics are therefore presented in this section, to further understand the reason behind the different paces of heat transfer variations in these cases.

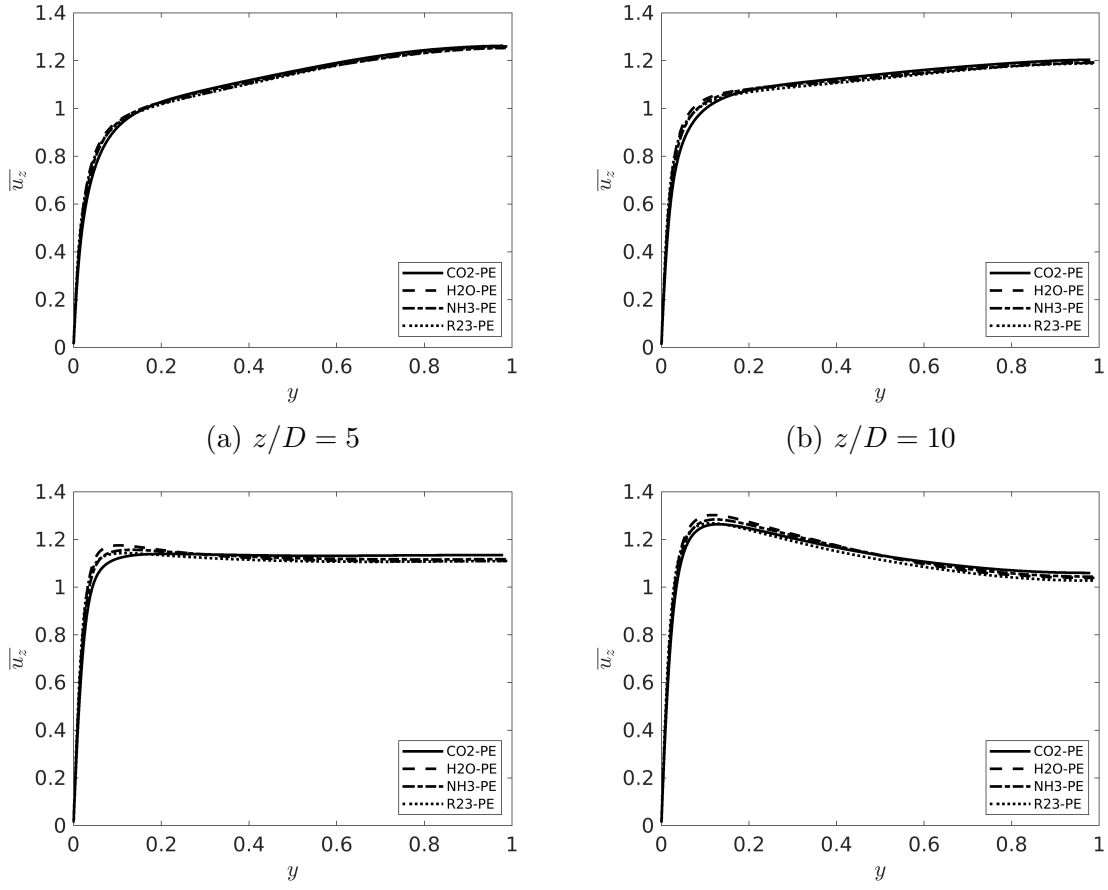

(a) $z/D = 5$ (b) $z/D = 10$

(c) $z/D = 17$ (d) $z/D = 28$

Figure 6.23: Profiles of $\overline{u_z}$ at chosen locations of the PE-series cases.

The streamwise velocity ($\overline{u_z}$) profiles of the PE-series cases at chosen locations are shown in Fig. 6.23. Similar to those in the RE-series cases, with the near-wall accelerations and mainstream decelerations which are mainly caused by the near-wall

reduction of gravity and the overall reduction of modified pressure gradient $(-\left(\frac{\partial \overline{p}}{\partial z}\right), \overline{u_z}+\overline{\rho_c}g\big)$, $\overline{u_z}$ profiles in all cases are firstly flattened, then turn into M-shape profiles. The general variation trends in all cases are the same. At $z/D = 5$, $\overline{u_z}$ profiles of the PE-series cases collapse with each other, later at $z/D = 10$, the near-wall ($y < 0.2$) $\overline{u_z}$ of the "PE" cases are slightly higher than that of Case CO2, and such differences is more obvious at $z/D = 17$, where the $\overline{u_z}$ profile of Case CO2 is just flattened, while the $\overline{u_z}$ profiles of the other three cases are M-shape, with $\overline{u_z}$ higher near the wall and lower at the main stream. At $z/D = 17$ and 28, development of $\overline{u_z}$ in Case H2O-PE is the fastest, followed by those of Case NH3-PE and R23-PE, and development of Case CO2 is the slowest. Such difference is not obvious in the comparisons of $\overline{u_z}$ profiles, and it can be clearly seen in the comparisons of turbulent shear stress ($\overline{\rho u_z'' u_r''}$) profiles.

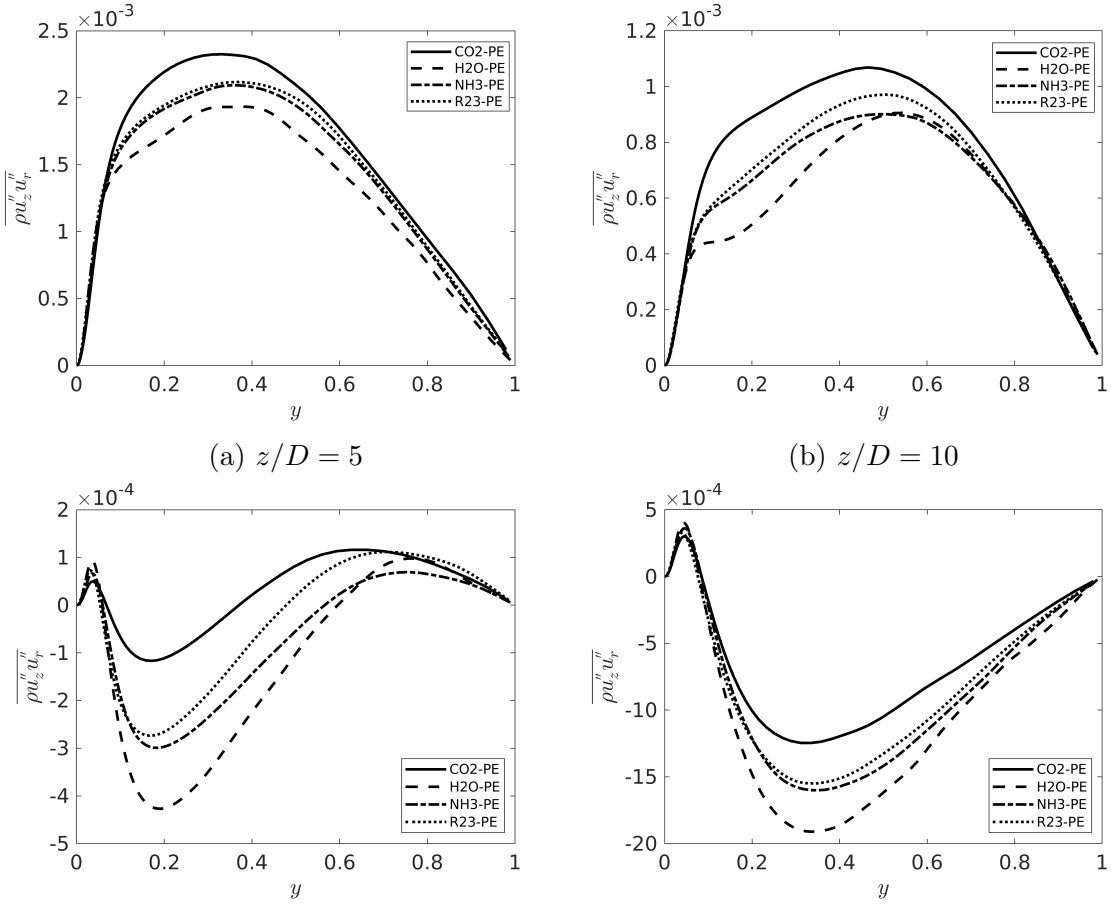

Figure 6.24: Profiles of $\overline{\rho u_z'' u_r''}$ at chosen locations of the PE-series cases.

The profiles of $\overline{\rho u_z'' u_r''}$ at chosen locations of all cases are shown in Fig. 6.24. The developing trends in $\overline{\rho u_z'' u_r''}$ of the PE-series cases are the same as those of the RE-

series cases, i.e., the $\overline{\rho u_z'' u_r''}$ values are all positive at the initial locations, then they gradually reduce, become zeros at most part when the flow is fully laminarized, then it keep reducing with rising magnitudes. When the velocity profile turns M-shape, $\overline{\rho u_z'' u_r''}$ profiles are positive close to the wall and negative at the main stream. In Fig. 6.24, although all cases follow this variation trend, their developing speed is different. $\overline{\rho u_z'' u_r''}$ values of H2O-RE are always the lowest, indicates developing speed of $\overline{\rho u_z'' u_r''}$ in Case H2O-RE is faster. $\overline{\rho u_z'' u_r''}$ profiles of Case NH3-RE and R23-RE are very close, especially at $z/D = 5$ and 28, as their initial Re_0 are relatively close. The development of $\overline{\rho u_z'' u_r''}$ in Case CO2 is the slowest, with the lowest Re_0. Such different development paces of $\overline{\rho u_z'' u_r''}$ are well corresponded with the different developments of responses in heat transfer, i.e., difference in locations of minimum Nu and St.

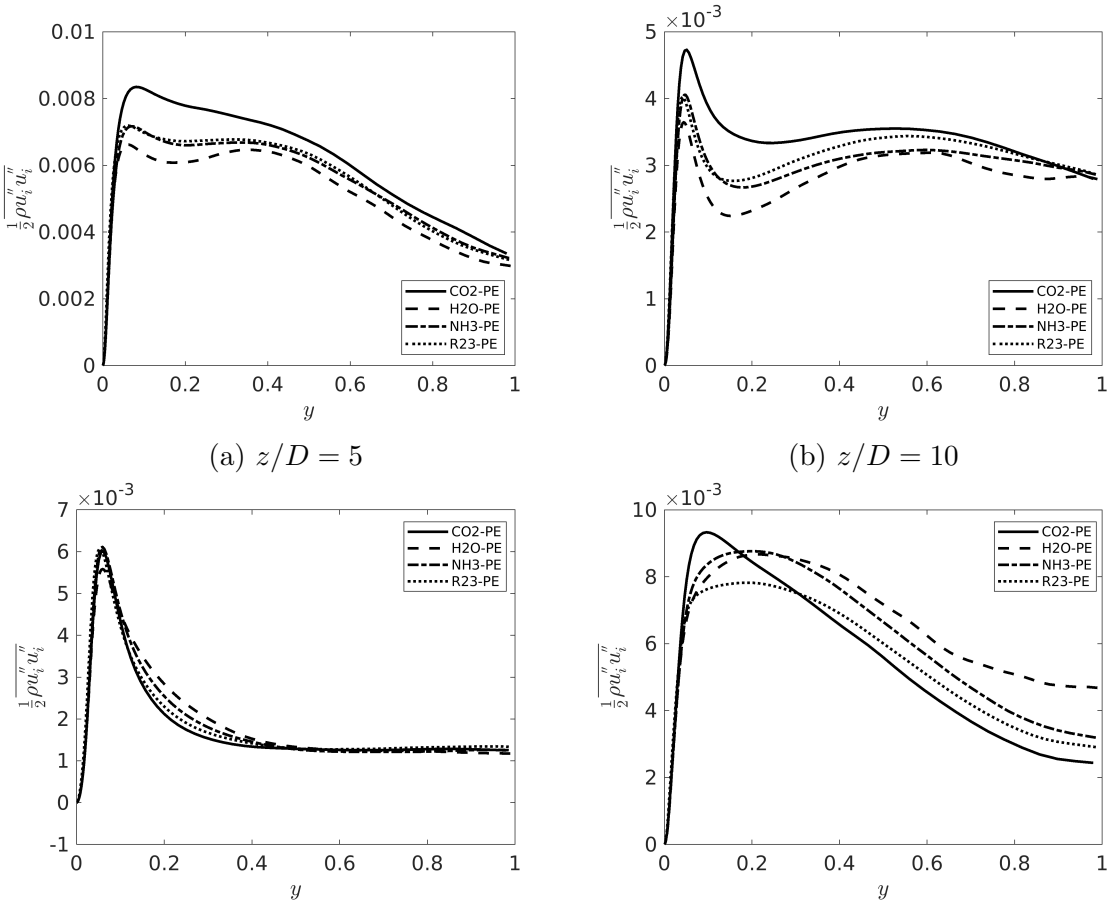

(a) $z/D = 5$ (b) $z/D = 10$

(c) $z/D = 17$ (d) $z/D = 28$

Figure 6.25: Profiles of $\frac{1}{2}\overline{\rho u_i'' u_i''}$ at chosen locations of the PE-series cases.

Finally, developments of turbulent kinetic energy (TKE) profiles in all cases are shown in Fig. 6.25. Similar to the different developments in $\overline{\rho u_z'' u_r''}$ profiles, different

reduction speeds are shown in TKE. From $z/D = 5$ to 17, TKE reduces at most part. From $z/D = 5$ to 10, reductions of TKE at about $y = 0.2$ are heavier in all cases, TKE profiles with two peaks are formed in all cases at about $z/D = 10$. However, for Case H2O-RE, the two-peak TKE profile is already formed at $z/D = 5$, faster than the other cases. With a faster reduction, at $z/D = 10$, Case H2O-RE has the lowest TKE values everywhere. At $z/D = 17$, TKE profiles of all cases agree well, especially at the main stream ($y > 0.4$) and near the wall ($y < 0.1$), then at later location ($z/D = 28$), TKE profiles become different, with peaks located differently. It is worth noting that TKE profiles of Case NH3-RE and R23-RE are very close at $z/D = 5$, 10 and 17, with nearly the same developments, but they diverge during the recovery ($z/D = 28$). The different developments in TKE profiles in these cases are similar those in $\overline{\rho u_z'' u_r''}$ profiles, both agree with the difference in variations of heat transfer, i.e., laminarization and heat transfer deterioration is faster with higher Re_0.

6.4 The effect of inlet Prandtl number

6.4.1 Problem concerned and additional case settings

The above discussions investigate the performances of two scaling options:

$$\begin{aligned} [St,\ u_z] &= f_1(N_{SPC},\ N_{TPC},\ Fr_0,\ Re_0,\ \rho(h^+)) \\ [St,\ u_z] &= f_1(N_{SPC},\ N_{TPC},\ Fr_0,\ Pe_0,\ \rho(h^+)) \end{aligned} \tag{6.19}$$

Excellent success has been achieved using the first scaling option, in terms of similarities St, thermal and flow fields, variations of turbulent quantities and structures, while weaker similarities are achieved using the second option, with similar $\overline{h^+}$ and $\overline{\rho}$ fields reproduced in the model fluids, but different paces of variations in heat transfer and turbulent characteristics.

The success of the first scaling method (RE-series cases) was published in a paper [1], and it has also been discussed by Pucciarelli & Ambrosini [151] and Pucciarelli et al. [152]. Pucciarelli & Ambrosini pointed out that the achieved similarities in the RE-series cases is limited to the cases that the inlet Pr_0 values are similar in the various cases, which is the cases studied in the RE series. They implied that the scaling may not be that successful at conditions with very different Pr_0 in different fluids. As shown in table 6.1, for the RE-series cases, with Re_0 fixed, Pe_0 of Case CO2, H2O-RE, NH3-RE and R23-RE are 7477, 4403, 5695 and 5476 respectively. In Fig. 6.2a, the four $Pr(h^+)$ functions nearly collapse at $h^+ = 0$ (pseudocritical enthalpy, $h^+_{pc} = 0$), and h^+_0 of Case CO2 is close to h^+_{pc}, results in similar inlet Prandtl

numbers between the RE-series cases. Pr_0 of Case CO2, H2O-RE, NH3-RE and R23-RE are 2.86, 1.68, 2.18 and 2.09. If a lower h_0^+ is chosen for the CO_2, Pr_0 will be more different.

To further investigate the effect of Pr_0 on the achieved similarities, a case at lower h_0^+ (lower Pr_0) is set, named CO2-LPR, with $Pr_0 = 2.09$. Another scaled case is set with non-dimensional parameters in the first scaling option of Eq. 6.19 fixed, and H_2O at the same operating pressure as Case H2O-RE is used, named H2O-LPR. Pr_0 of Case H2O-LPR is 0.84. An additional case of CO_2 (at the same operating pressure as Case CO2) with artificially modified $\lambda(h^+)$ functions match the Pr_0 of Case H2O-LPR is also set for comparison, named CO2-MTC. Pr_0 of Case CO2-LPR and H2O-LPR are calculated using the inlet thermophysical properties:

$$\begin{aligned} Pr_{0,CO2-LPR} = 2.09 &= \frac{c^*_{p,0,CO2-LPR}\mu^*_{0,CO2-LPR}}{\lambda^*_{0,CO2-LPR}} \\ Pr_{0,H2O-LPR} = 0.84 &= \frac{c^*_{p,0,H2O-LPR}\mu^*_{0,H2O-LPR}}{\lambda^*_{0,H2O-LPR}} \end{aligned} \tag{6.20}$$

And λ^* of Case CO2-MTC is therefore multiplied by a factor of $\frac{Pr_{0,CO2-LPR}}{Pr_{0,H2O-LPR}} = 2.49$, but all the other thermophysical properties of Case CO2-MTC is the same as Case CO2-LPR, so that the Pr_0 of Case CO2-MTC is adjusted to match Case H2O-LPR:

$$\begin{aligned} \lambda^*_{0,CO2-MTC} &= 2.49 \times \lambda^*_{0,CO2-LPR} \\ Pr_{0,CO2-MTC} = \frac{c^*_{p,0,CO2-MTC}\ \ \mu^*_{0,CO2-MTC}}{2.49\lambda^*_{0,CO2-LPR}} &= Pr_{0,H2O-LPR} \end{aligned} \tag{6.21}$$

Inlet enthalpies, thermophysical properties, pipe diameters and inlet velocities of the three new cases, i.e., CO2-LPR, H2O-LPR, CO2-MTC are listed in table 6.3. And the scaled non-dimensional parameters of each case are listed in table 6.4. As shown in table 6.4, although Case CO2-LPR and H2O-LPR has the same Re_0, their inlet Prandtl numbers are very different, result in very different Peclect numbers, while for Case CO2-MTC, Pr_0 and Pe_0 are adjusted artificially to be the same as Case H2O-LPR. The influences of Pr_0 (or Pe_0) can therefore be quantified by comparing these three cases. The three new cases are grouped and named the LPR-series cases.

6.4.2 Comparison of heat transfer characteristics

Developments of h_b^+ and $\overline{h_w^+}$ in all the three cases are shown in Fig. 6.26a and 6.26b. Same as before, developments of h_b^+ in all cases collapse due to the fixed N_{SPC} and N_{TPC}, while the $\overline{h_w^+}$ profiles diverge. Difference in the radial distributions

Table 6.3: Inlet enthalpies and thermophysical properties of the new cases

Case	h_0^+	ρ_0^* (kg/m^3)	μ_0^* $(Pa \cdot s)$	$c_{p,0}^*$ $(J/kg \cdot K)$	λ_0^* $(W/m \cdot K)$
CO2-LPR	-1.30	1003.1	1.25×10^{-4}	2134.3	0.128
H2O-LPR	-1.30	725.9	8.84×10^{-5}	5352.7	0.565
CO2-MTC	-1.30	1003.1	1.25×10^{-4}	2134.3	0.319

Table 6.4: Scaled non-dimensional parameters of the new cases

Case	N_{SPC}	N_{TPC}	Fr_0	Re_0	Pr_0	Pe_0
CO2-LPR	1.30	0.44	0.18	2617	2.09	5476
H2O-LPR	1.30	0.44	0.18	2617	0.84	2193
CO2-MTC	1.30	0.44	0.18	2617	0.84	2193

of h^+ is expected, due to the different heat transfer characteristics. Bulk and wall temperatures of all cases are also shown in Fig. 6.26c and 6.26d. Case CO2-LPR and CO2-MTC has exactly the same T_b profiles as they have the same $c_p(h^+)$ functions. $\overline{T}_w$ of Case H2O-LPR agree very well with that of Case CO2-MTC before about $z/D = 20$, which is considered as an coincidence as the $\overline{h_w^+}$ developments of these two cases are different. The purpose of the the current tested scaling method is to achieve the similarities in h^+ fields between different fluids, rather than the temperature fields.

Differences in $\overline{h_w^+}$ and $\overline{T}_w$ profiles suggest differences in heat transfer performances in the three flows. The developments of Nusselt number and Stanton number in these cases are shown in Fig. 6.27. The Nusselt number of Case H2O-LPR and CO2-MTC are very similar until $z/D = 15$, then they deviate from each other but still follow the same trend. The Nusselt number of Case CO2-LPR is different from the other two cases, which firstly reduces and reaches a valley at very early stage, then it increases, followed by a continuous reduction. The rapid reductions of Nu before $z/D = 3$ are caused by the entrance effect. Comparisons of the Nusselt number developments in these cases indicate the importance of the inlet Prandtl number in terms of characterising the heat transfer behaviour. For Case CO2-LPR and H2O-LPR, Re_0, Fr_0, h_b^+ are the same, and Pr_0 of these two cases are very different (2.09 & 0.84), while for Case CO2-MTC and H2O-LPR, Re_0, Fr_0, h_b^+ and Pr_0 are the same, and more similar heat transfer performances are achieved in these two cases. In the RE-series cases that discussed in section 6.2, although Pr_0 are different, the differences are much smaller than that of the "-LPR" cases. Therefore the success of the scaling method used in the RE-series cases is limited, only when the chosen inlet Pr_0 of the model fluid is close to that of the prototype fluid, similarity can be

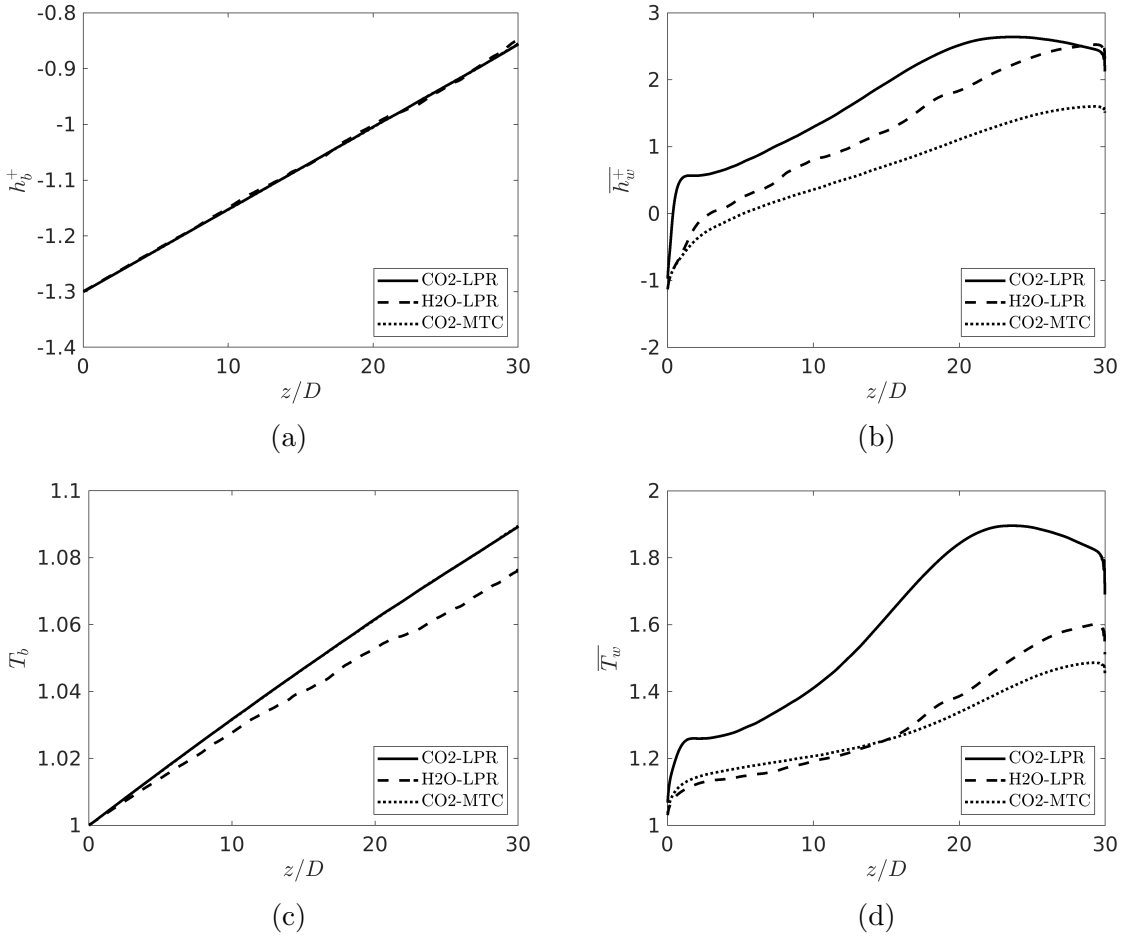

Figure 6.26: Streamwise developments of (a) bulk enthalpy, (b) wall enthalpy, (c) bulk temperature and (d) wall temperature in the LPR-series cases

achieved. The two "-LPR" cases considered here are extreme cases, the inlet h^+ with the most different Pr_0 between the two fluids was chosen.

The developments of the Stanton number in the RE-series cases are very similar (Fig. 6.4d), while for Case H2O-LPR, in which the scaling method same as the RE-series cases was used, St is quite different from that of Case CO2-LPR. Even for Case H2O-LPR and CO2-MTC with the same Pr_0, St developing trends are similar, but St magnitudes are quite different.

6.4.3 Comparison of flow and turbulent features

To investigate the reasons for the differences in heat transfer behaviours, turbulent characteristics in these cases are studied. Firstly profiles of turbulent quantities, i.e., the turbulent shear stress $\overline{\rho u_z'' u_r''}$ and turbulent kinetic energy $\frac{1}{2}\overline{\rho u_i'' u_i''}$ for all cases are

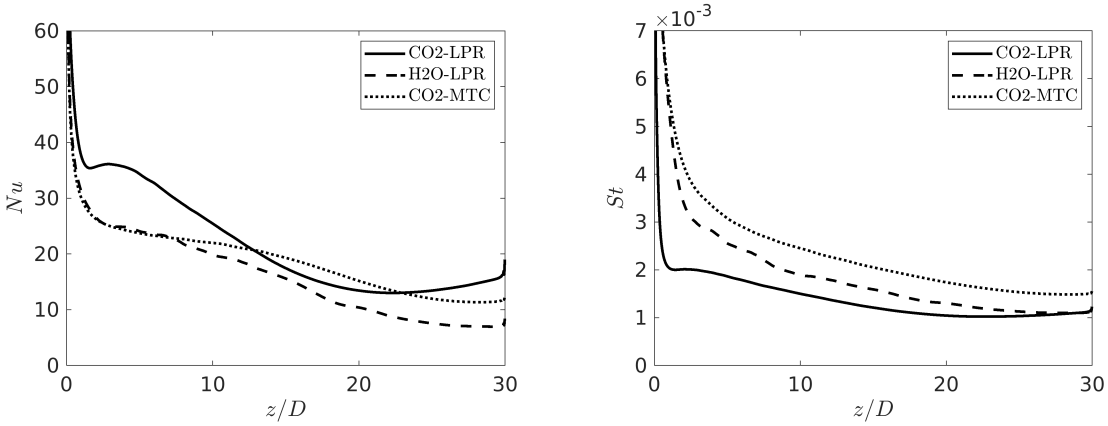

(a) (b)

Figure 6.27: Streamwise developments of the (a) Nusselt number and the (b) Stanton number in the LPR-series cases.

shown (Fig. 6.28 & 6.29), the laminarization and recovery in each flow are clearly reflected in the streamwise variations of these profiles.

The profiles of turbulent shear stress $\overline{\rho u_z'' u_r''}$ at chosen locations of the three cases are shown in Fig. 6.28. Similar to the RE-series cases discussed before, in each case, $\overline{\rho u_z'' u_r''}$ reduces during the laminarization, then becomes negative at most part during the regeneration of turbulence, corresponding to the worsening and enhanced heat transfer at these stages. The development of $\overline{\rho u_z'' u_r''}$ in Case CO2-LPR is faster than the other two cases, and the changes of $\overline{\rho u_z'' u_r''}$ in Case H2O-LPR and CO2-MTC are relatively similar. $\overline{\rho u_z'' u_r''}$ of Case CO2-LPR is significantly reduced before $z/D = 17$, while $\overline{\rho u_z'' u_r''}$ of the other two cases are still relatively high, turbulence of Case CO2-LPR is weaker than the other two. At $z/D = 28$, magnitudes of $\overline{\rho u_z'' u_r''}$ rise in all cases, with positive values near the wall, and negative values at the mainstream, which is the same as the typical regeneration of turbulence in the cases discussed previously (RE- & PE-series cases). $\overline{\rho u_z'' u_r''}$ of Case CO2-LPR has the largest magnitudes everywhere, while for Case H2O-LPR and CO2-MTC, $\overline{\rho u_z'' u_r''}$ magnitudes are relatively low, as the recovery stages just begin.

Similarly but less obviously, different progresses in laminarization and regeneration of turbulence are shown in the variations of turbulent kinetic energy (TKE) profiles, shown in Fig. 6.29. The streamwise development of TKE in Case CO2-LPR is faster than the other two cases. For TKE, laminarization is mainly reflected in the reduction of the near-wall peak, while recovery is mainly reflected in the increase of magnitudes at most part, including those at the mainstream. Before $z/D = 17$, TKE of Case CO2-LPR reduce faster than Case H2O-LPR and CO2-MTC, and at $z/D = 17$, the

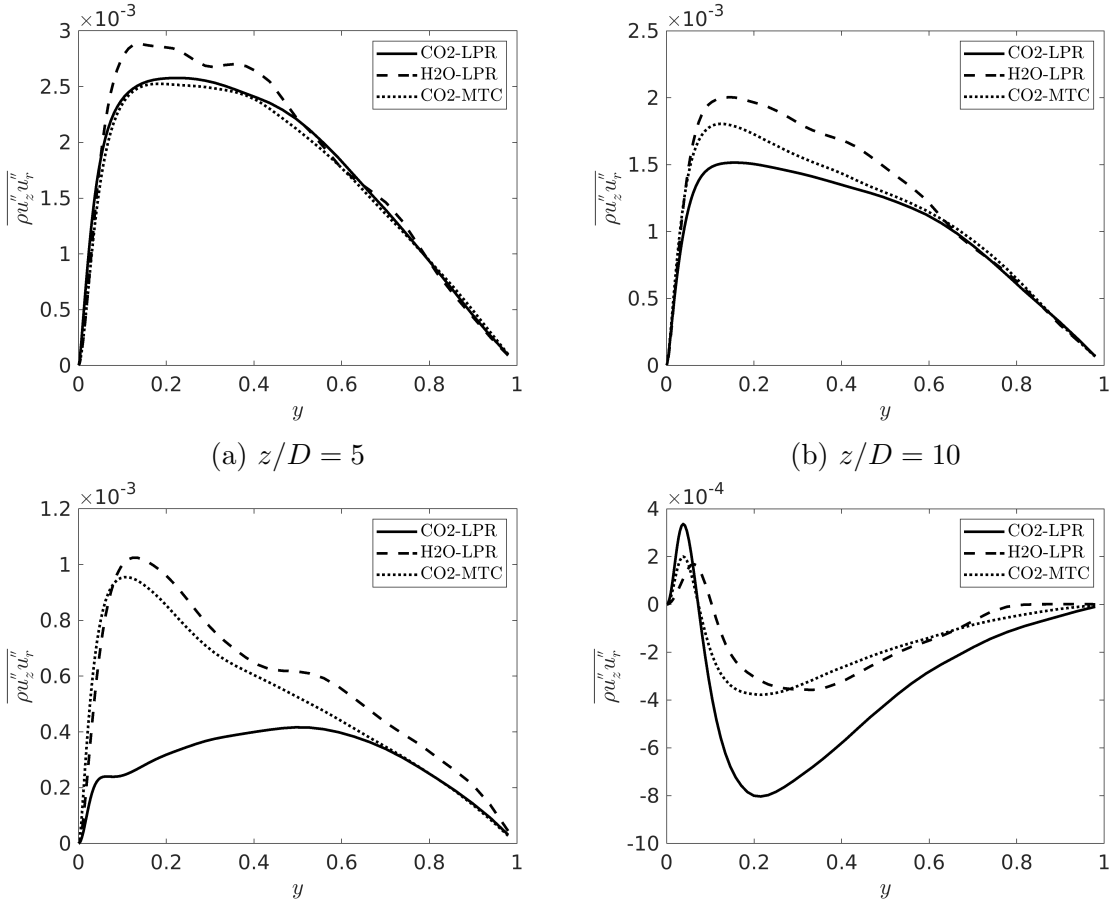

(a) $z/D = 5$ (b) $z/D = 10$

(c) $z/D = 17$ (d) $z/D = 28$

Figure 6.28: Radial profiles of turbulent shear stress $\overline{\rho u_z'' u_r''}$ at chosen locations of the LPR-series cases

near-wall peak of TKE in Case CO2-LPR is only about half of those of the other two cases. At $z/D = 28$, during the recovery, TKE at $y > 0.1$ of Case CO2-LPR is larger than those of the other two cases, while it is still lower than those two at $z/D = 17$, which indicates that the regeneration of turbulence happens earlier in Case CO2-LPR.

Visualizations of vortexes are shown by the isosurfaces of $\lambda 2 = -0.4$ in Fig. 6.30, with vortexes at the main stream coloured in red, vortexes near the wall coloured in grey and vortexes at the middle region coloured in yellow. In all the three cases vortexes gradually disappear along streamwise direction, and similarly, gradually re-generated at late stage ($z/D \sim 30$). For Case CO2-LPR, vortexes become sparser than those at the initial flow from about $z/D = 10$, and most of the red and yellow vortexes disappear at about $z/D = 18$, turbulent activities are significantly reduced. The laminarization in Case H2O-LPR and CO2-MTC is slower, the locations with

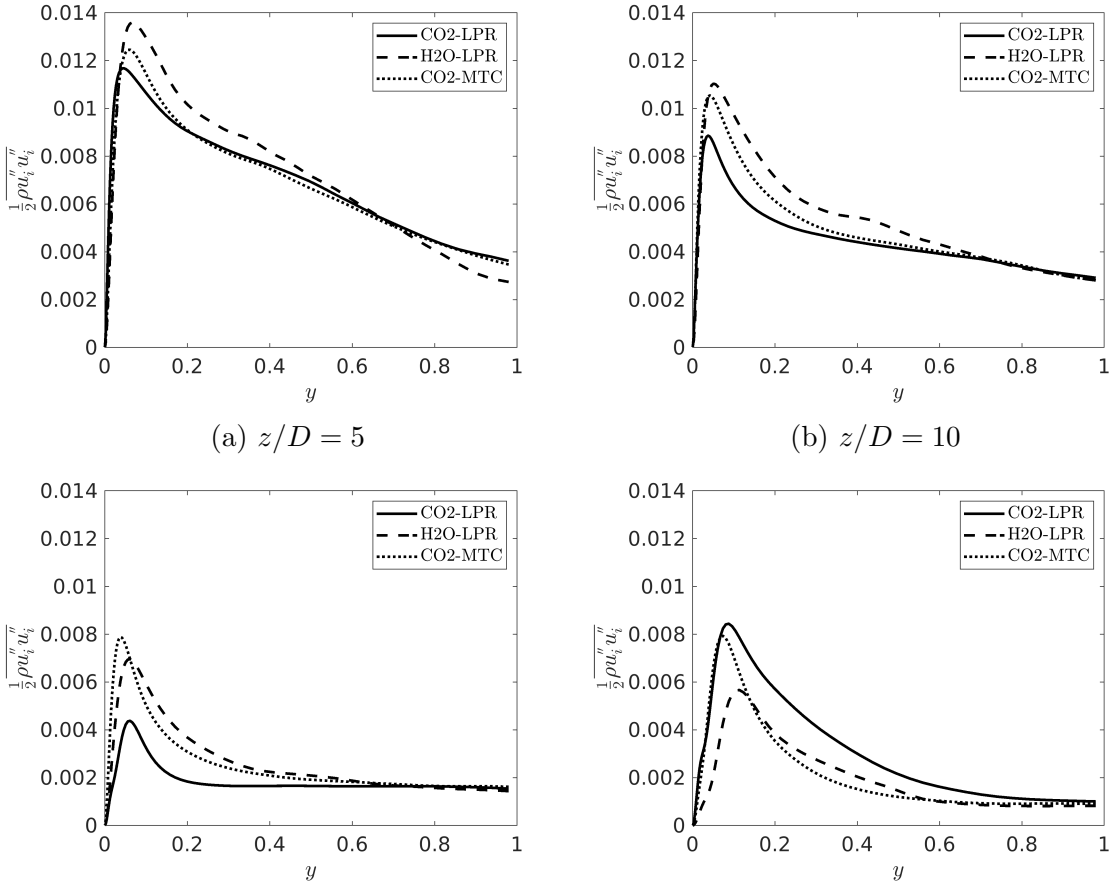

(a) $z/D = 5$ (b) $z/D = 10$

(c) $z/D = 17$ (d) $z/D = 28$

Figure 6.29: Radial profiles of turbulent kinetic energy $\frac{1}{2}\overline{\rho u_i'' u_i''}$ at chosen locations of the LPR-series cases

most of the red and yellow vortexes disappeared are slightly later ($z/D > 20$) than that in Case CO2-LPR, both take longer distances to diminish the vortexes. And at $z/D \approx 27$ of Case CO2-LPR, vortexes at the mainstream (red) and close to the wall (yellow) start generating and become denser again, while for the same location of the other two cases, only very few and coarse near-wall vortexes are regenerated, indicate they are still at the beginning of the recovery stage.

Unlike those between the RE-series cases, the variations of vortexes in the LPR-series cases are not synchronized, such difference in progresses of laminarization and regeneration can also be observed from the variations of streak behaviours in these cases. Instantaneous fluctuations of mass flux $(\rho u_z)'$ at the near-wall planes ($y^{+0} \approx 5$) of the LPR-series cases are shown in Fig. 6.31. In all cases, turbulent spots are spacially frequent after the inlet, then streaks are shaped during the laminarization and broken down during the recovery. For Case CO2-LPR, $(\rho u_z)'$ become less frequent

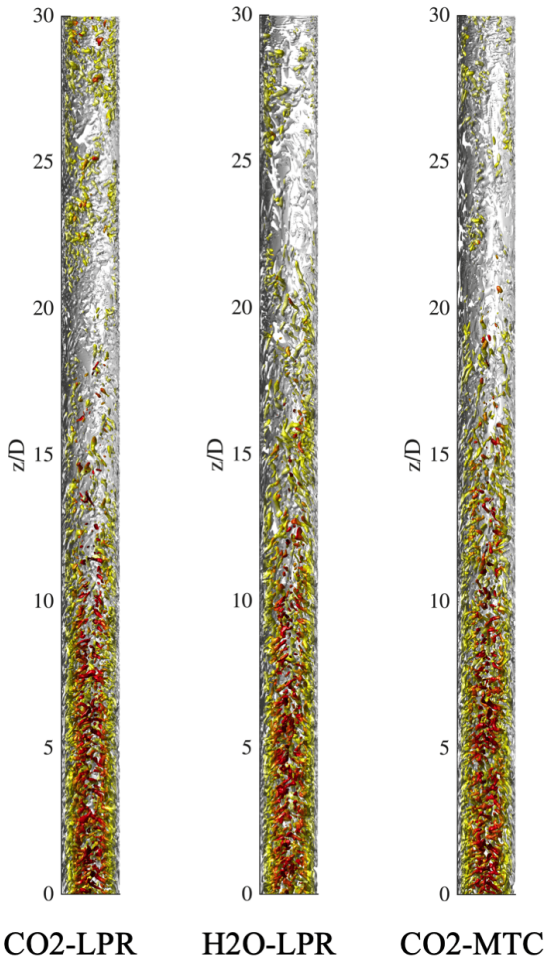

Figure 6.30: Isosurfaces of $\lambda_2 = -0.4$ in the LPR-series cases.

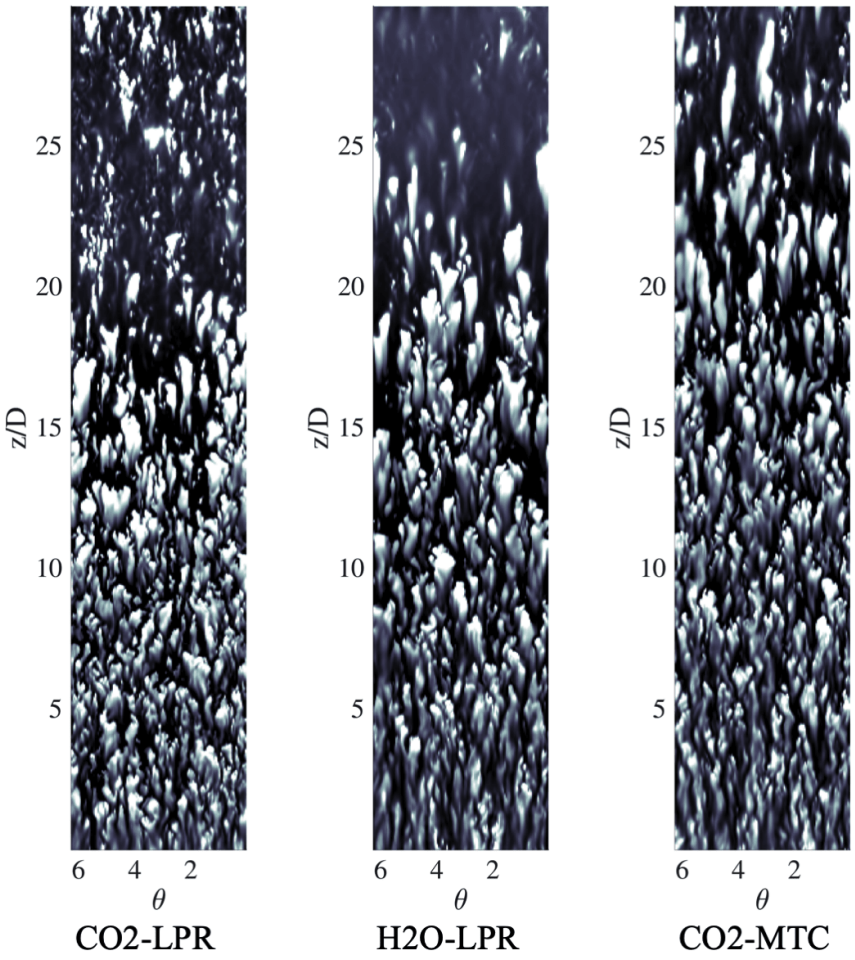

Figure 6.31: Contours of instantaneous $(\rho u_z)'$ at near-wall surfaces ($y^{+0} \approx 5$) of the LPR-series cases.

from about $z/D = 15$, elongated streaks are formed shortly after that, followed by the burst of turbulent spots, these are corresponding to the laminarization and regeneration stages, which progress fast in this case. For Case H2O-LPR, turbulent spots become sparser from about $z/D = 15$, streaks are more clearly observed, then they all disappear after $z/D = 25$, and the burst of turbulent spots is hardly seen near the outlet. Compared to Case CO2-LPR, the full-laminarization stage with most turbulent activities diminished is longer in Case H2O-LPR. Differently, in Case CO2-MTC, such progress is slower, with sparse and long streaks gradually formed at about $z/D = 20$, the burst of turbulent spots is also not clearly observed in this case.

The comparisons of vortexes and streaks behaviours show that the domain length ($30D^*$) can not cover the recovery stage of Case H2O-LPR and CO2-MTC, in which the laminarizations and heat transfer deteriorations take longer distances than Case CO2-LPR, and the regeneration stages are therefore delayed. The success in achieving similarity in the RE-series cases using the scaling correlation $St = f(Re_0, Fr_0, h_b^+)$ (discussed in section 6.2) proved that these parameters are able to characterise the heat transfer performance of such flows, at least at these configurations. In contrast Case H2O-LPR was scaled against Case CO2-LPR using the same scaling correlation, and similarity is not well achieved in heat transfer and turbulence.

Streamwise distributions of bulk density, dynamic viscosity and molecular thermal diffusivity in the LPR-series cases are shown in Fig. 6.32. The bulk viscosity appears in the non-dimensional momentum equation is $\frac{\mu}{Re_0}$, since Re_0 is the same in all these cases, so μ_b is directly compared. $\frac{\lambda}{Pr_0\, c_p}$ is the molecular thermal diffusivity appears in the non-dimensional energy equation, and $\frac{\lambda_b}{Pr_0\, c_{p,b}}$ is its bulk value. In Fig. 6.32, similarity in ρ_b is achieved among all cases, while μ_b of Case H2O-LPR diverges from the other two cases, and $\frac{\lambda_b}{Pr_0\, c_{p,b}}$ of Case CO2-LPR is very different from the other two cases. The bulk thermophysical properties ρ_b, μ_b, λ_b and $c_{p,b}$ are dependent on h_b^+ and the property functions on h^+ ($\rho(h^+)$, $\mu(h^+)$, $\lambda(h^+)$), and the developments of h^+ are determined by the fixed N_{SPC} and N_{TPC}. One-to-one comparisons of each two cases are carried out, with the fixed non-dimensional parameters listed and the

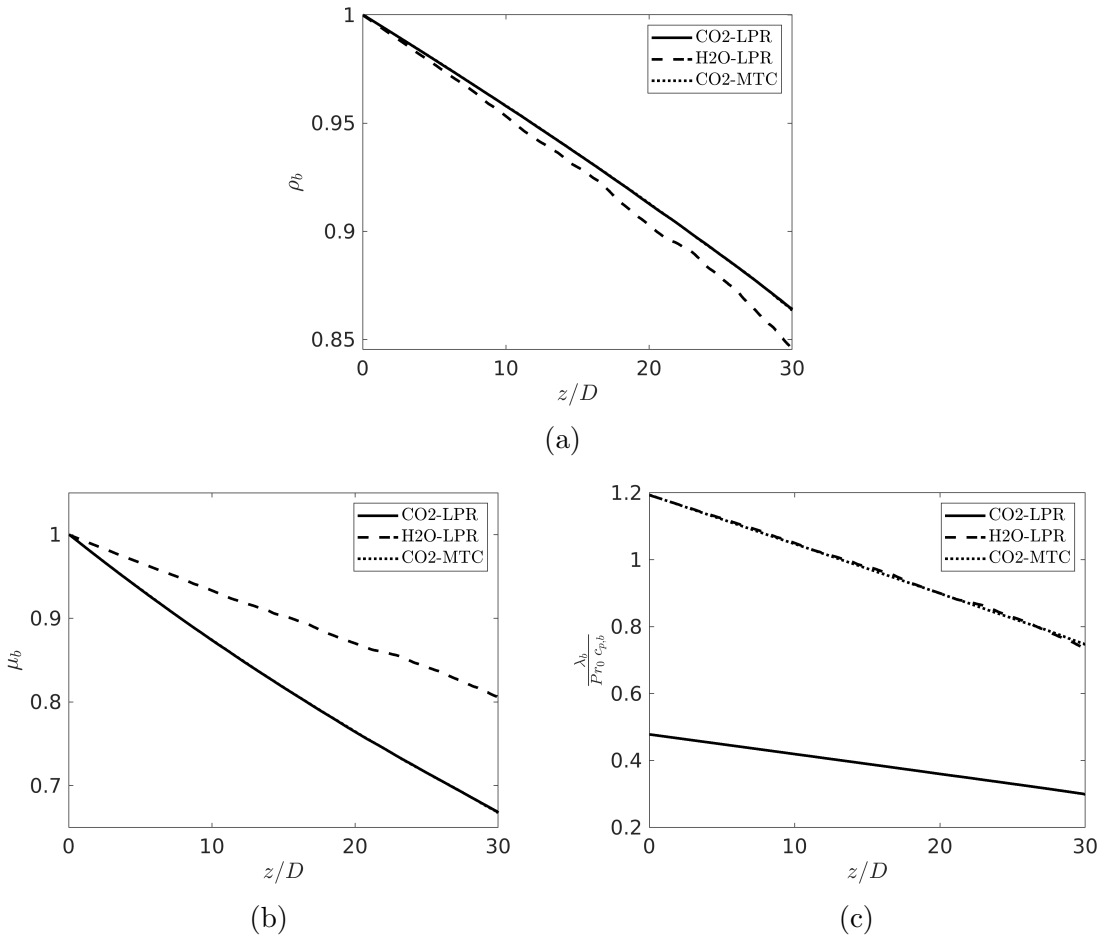

Figure 6.32: Streamwise distributions of bulk density, bulk dynamic viscosity and bulk molecular thermal diffusivity in the LPR-series cases

comparison results were in the following bracket:

CO2-LPR & H2O-LPR: h_b^+, Fr_0, ρ_b (not similar)

CO2-LPR & CO2-MTC: h_b^+, Fr_0, ρ_b, $\frac{\mu_b}{Re_0}$, (not similar)

H2O-LPR & CO2-MTC: h_b^+, Fr_0, ρ_b, $\frac{\lambda_b}{Pr_0\ c_{p,b}}$ (relatively similar)

For all the three cases, h_b^+, Fr_0 are the same and ρ_b are similar, which are the common points across these cases. In addition to that, the above list shows that for Case CO2-LPR and CO2-MTC, although the bulk molecular diffusivities $\frac{\mu_b}{Re_0}$ are the same, the bulk molecular thermal diffusivities $\frac{\lambda}{Pr_0\ c_p}$ are very different, which results in divergence of variations in turbulent and heat transfer characteristics. While for Case H2O-LPR & CO2-MTC, they also share the common points (h_b^+, Fr_0 & ρ_b),

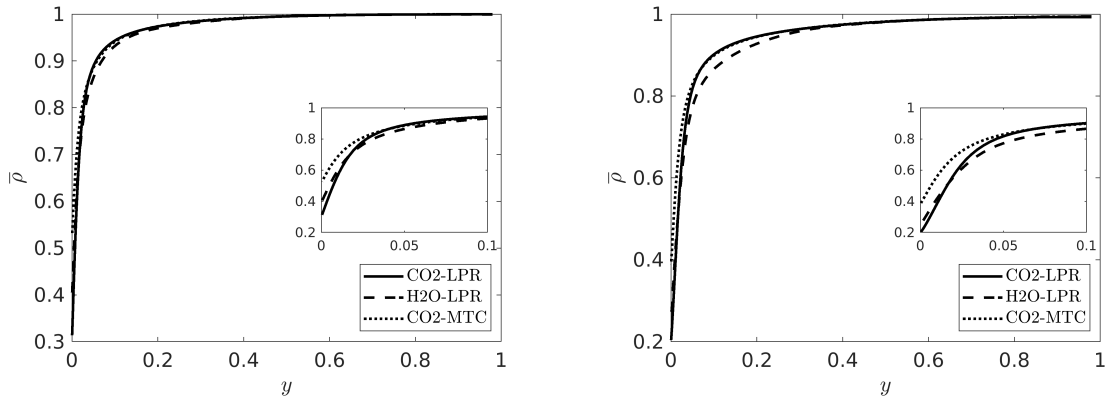

(a) $z/D = 5$ (b) $z/D = 10$

(c) $z/D = 17$ (d) $z/D = 28$

Figure 6.33: Profiles of $\overline{\rho}$ at chosen locations of the LPR-series cases.

and additionally $\frac{\lambda}{Pr_0\ c_p}$ is included, although their $\frac{\mu_b}{Re_0}$ are different, these two flows have relatively similar behaviours in turbulence and heat transfer. Such comparison indicates that at this configuration, differences in $\frac{\lambda}{Pr_0\ c_p}$ is the main reason for the failure of achieving similarity, while $\frac{\mu_b}{Re_0}$ is less efficient here, as similarity is achieved in Case H2O-LPR & CO2-MTC without $\frac{\mu_b}{Re_0}$ fixed.

To look at how different in $\frac{\lambda}{Pr_0\ c_p}$ causing the different developments of turbulent characteristics, we firstly investigate the differences between Case CO2-LPR and CO2-MTC, as in these two cases, h_b^+, Fr_0, ρ_b and $\frac{\mu_b}{Re_0}$ are the same, the only difference is $\frac{\lambda}{Pr_0\ c_p}$ shown in Fig. 6.32c. As we known, for two thermal boundary layers with the same bulk enthalpy, the one with higher thermal diffusivity results in a more uniform distribution of enthalpy, with a lower wall-normal gradient $\frac{\partial h}{\partial r}$ near the wall, and therefore a lower wall enthalpy. This is also agreed by the two cases in comparison, shown in Fig. 6.26b, Case CO2-MTC with a higher bulk thermal diffusivity $\frac{\lambda}{Pr_0\ c_p}$ has lower h_w^+ at all locations. Two main consequences that are relevant to turbulence

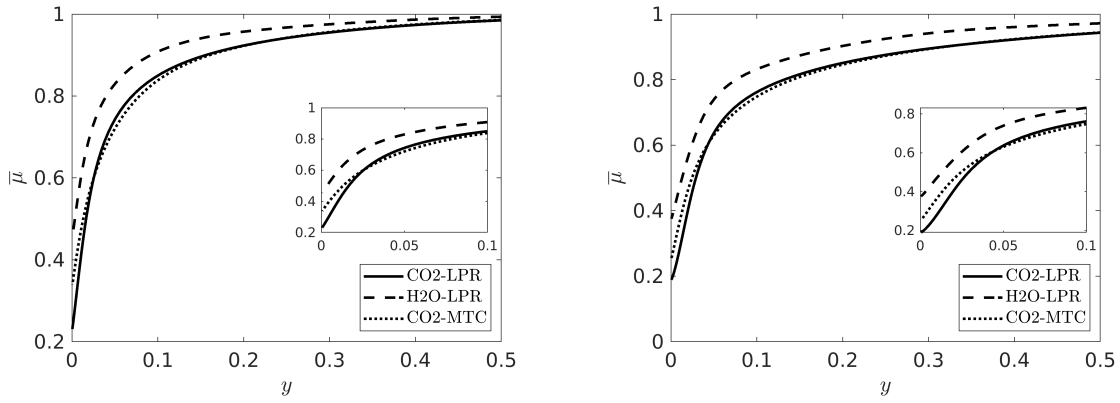

(a) $z/D = 5$ (b) $z/D = 10$

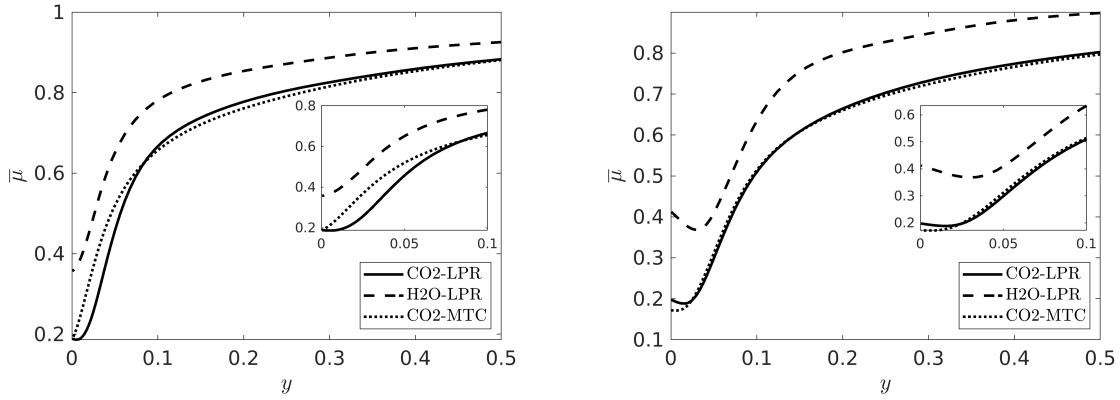

(c) $z/D = 17$ (d) $z/D = 28$

Figure 6.34: Profiles of $\overline{\mu}$ at chosen locations of the LPR-series cases.

characteristics caused by a higher wall enthalpy are lower density and viscosity near the wall. Radial profiles of $\overline{\rho}$ and $\overline{\mu}$ at chosen locations in the three cases are shown in Fig. 6.33 & 6.34. For $y < 0.1$, density and viscosity of Case CO2-MTC are higher than those in Case CO2-LPR, at $z/D = 5$, 10 and 17, near-wall density of Case CO2-MTC is nearly double of that in Case CO2-LPR. For viscosity, at $z/D = 5$ and 10, $\overline{\mu}$ near the wall in Case CO2-MTC is about 50% higher than that of Case CO2-LPR. These differences suggest the laminarization caused by the combined effects of near-wall reduction in viscosity and density (buoyancy) is weaker in Case CO2-MTC, which agrees with the slower laminarization and recovery progresses in this case, which can be quantified by the variations in momentum balance.

Profiles of the the radial viscous and turbulent shear stress ($VS2$ & $TS2$) and the buoyancy (Bo) of the streamwise momentum equation (Eq. 4.7) at chosen locations of all cases are shown in Fig. 6.35. Logarithmic scale is applied to the horizontal axis to clearly show the near-wall differences. At $z/D = 5$, $VS2$ and $TS2$ of Case

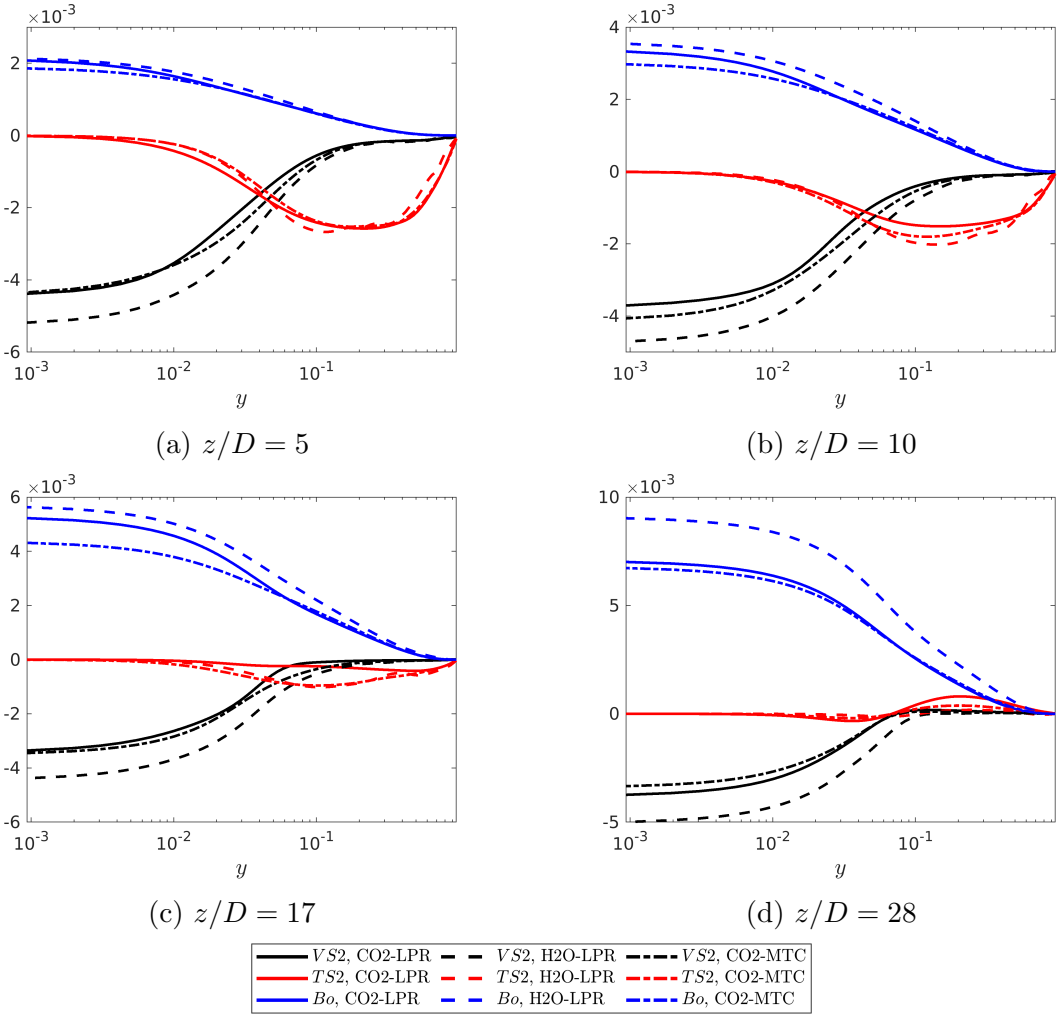

Figure 6.35: Profiles of viscous ($TS2$), turbulent stress term ($VS2$) and buoyancy term (Bo) of the integrated momentum equation at chosen locations of the LPR-series cases.

CO2-LPR and CO2-MTC were very similar especially close to the wall, and the buoyancy in Case CO2-LPR is slightly stronger close to the wall. At $z/D = 10$ & 17, during the laminarizing stage, differences between the two cases were larger, reduction of $VS2$ and the increment of Bo in Case CO2-LPR is larger, as a result of the higher wall enthalpy and lower near-wall density and viscosity. Therefore the laminarization is faster in Case CO2-LPR, with much stronger buoyancy and near-wall viscosity reduction effects. At $z/D = 10$ & 17, differences in term $VS2$ between Case CO2-LPR and H2O-LPR are larger. This is corresponding to the much larger $\overline{\mu}$ in Case H2O-LPR especially close to the wall (Fig. 6.34 & Fig. 6.32b). It suggests that using the operating pressures same as those in the RE-series cases for CO_2 and

H_2O at a lower inlet enthalpy cannot achieve similar $\mu(h^+)$ functions (Fig. 6.32b). However, for $\rho(h^+)$ functions between the two, similarity is maintained even though the inlet enthalpy is lowered (Fig. 6.32a). At $z/D = 10$ & 17, the viscosity reduction close to the wall in Case CO2-LPR is much stronger, while the buoyancy is slightly weaker than that of Case H2O-LPR, which result in a faster laminarization in Case CO2-LPR.

6.5 Conclusions

In this part of work, DNS of four fluid flows (supercritical carbon dioxide, water, ammonia and fluoroform) in a vertical heated pipe are carried out, with the conditions scaled using the fluid-to-fluid scaling correlation of Ambrosini et al. [14], to achieve similar flow and heat transfer features. The scaling parameter group (Re_0, Fr_0, N_{SPC}, N_{TPC}) was firstly chosen to apply. Excellent similarities in both turbulent and heat transfer characteristics have been successfully achieved. To investigate the influence of the matched parameters, another group of parameter (Pe_0, Fr_0, N_{SPC}, N_{TPC}) is applied for the four fluids. Larger differences between the various fluids are found, with different paces of heat transfer deterioration and laminarization observed. Furthermore, to study the applicability of the first group of parameter with a lower inlet enthalpy (and more different Pr_0), two cases with lower h_0^+ were carried out (H_2O & CO_2), and another CO_2 case with an artificially adjusted thermal conductivity were also included. It is found that these flows are less similar when there is larger difference in Pr_0. The reason behind the failure here is investigated. Several conclusions are drawn in the discussion of this sub-topic, which were listed below:

- For the RE-series cases, with parameter group (Re_0, Fr_0, N_{SPC}, N_{TPC}) scaled and the operating pressure tuned to achieve similar enthalpy dependent thermo-physical properties, the thermal and flow fields of the various fluid cases are very similar to each other. Excellent agreement is seen in the developments of wall enthalpy $\overline{h_w^+}$, turbulent heat flux and Stanton number. Stanton number is found to be more representative than the Nusselt number in terms of characterising the similar heat transfer feature for these scaled cases. In all cases, the laminar, turbulent and inhomogeneous contribution to the Nusselt numbers are similar, with the reductions of turbulent being the main contribution responsible for the heat transfer deterioration. The developments of the velocity profile, turbulent shear stress and turbulent kinetic energy progress similarly in all cases. The velocity profiles are flattened and turned M-shape at close locations, and

the turbulent shear stresses reached the lowest value and flipped also at close locations. The forming and breaking down of $(\rho u_z)'$ streaks are similar in all cases, the initial turbulent spots gradually disappeared at about $z/D = 15$ with elongated streaks formed, where the flow is fully-laminarized. Then streaks are broken down with new turbulent spots generated at later stage. The multi-scale vortexes are observed to reduce and be regenerated at similar locations in the RE-series cases.

- For the PE-series cases, with parameter group (Pe_0, Fr_0, N_{SPC}, N_{TPC}) matched, the inlet Reynolds number of the four fluid flows are different. The impact of the Reynolds number is found to be rather significant, which affects the pace of laminarization and therefore the heat transfer deterioration. Weaker similarity between the fluid flows are achieved with this choice. For thermal behaviours, the peaks of the wall enthalpy $\overline{h_w^+}$ in the PE-series cases are different, with larger Re_0 resulting in earlier peak. The development trends of the Nusselt and Stanton numbers in four cases generally agree well, but their minimum values are at different locations. For the flow with a lower Reynolds number, the minimum of Nu and St also appear at an earlier z/D location. This is due to the differences in developments of the velocity profiles and turbulent quantities. For the flow with the largest inlet Reynolds number (H2O-RE), the acceleration close to the wall and deceleration at the core are greater than the other cases and so are the reduction of turbulent shear stress and turbulent kinetic energy.

- When the first group of matched parameters (Re_0, Fr_0, N_{SPC}, N_{TPC}) are applied to the H_2O and CO_2 at a lower inlet enthalpy with a larger difference in Pr_0 (LPR-series cases), similarity in turbulence and heat transfer is not achieved. The laminarisation in CO_2 progress faster, due to a stronger viscosity variation effect. When the inlet condition is changed (compared to those in the RE-series cases), $\rho(h^+)$ functions between the two fluids remain similar, while $\mu(h^+)$ functions are very different. Such difference results in a lower near-wall viscosity in CO_2, causing a faster laminarisation due to the stronger viscosity variation effect. The difference in viscosity variation effects is the reason behind the failure of similarity using the first group of matched parameters.

Chapter 7

The effect of conjugate heat transfer on the flow of supercritical carbon dioxide

In Chapter 6, successful similarity is achieved between vertical pipe flows of different supercritical fluids, with their boundary conditions scaled using the fluid-to-fluid scaling correlation. In this chapter, another interesting and concerned topic on numerical studies of supercritical fluid flows is investigated, that is, the effect of conjugate heat transfer. In most numerical studies of turbulent heat transfer in supercritical fluid flows, ideal thermal boundary conditions, i.e., a spacially uniform and temporally constant wall heat flux was imposed, while the heating in experiments or practical applications is usually non-uniform due to the thermal conduction in the solid pipe wall or container. Two effects were introduced when such solid conduction is considered, i.e., the spatial redistribution of wall heat flux and the damping of temperature/enthalpy fluctuations. For most numerical studies of supercritical fluid flows, these two effects were not considered. In this chapter, simulations of upward pipe flows of supercritical CO_2 with and without the solid wall were carried out and compared, to acquire further understandings on the influences of these effects. The author's contribution on this topic is to implement the conjugate heat transfer function in CHAPSim (described in chapter 3) and carry out initial investigations, which are described here.

7.1 Case settings

Upward pipe flows of CO_2 at 7.6MPa ($p_c^* = 7.38MPa$, $T_{pc}^* = 305.45K$) with strong heating ($63kW/m^2$) are studied in the work described in this chapter. A base case

(NSW) without the solid wall, was carried out with a uniform wall heat flux imposed. A second case with the thermal conduction of the solid wall considered was set (CHT) with a volumetric heat source imposed in the solid wall. In this case (CHT), solid heating begins from $z/D = 5$ rather than from the inlet, to model the backward conduction that happens in practical flows. To acquire a fully-developed turbulent flow, a certain length of pipe without heating is usually set before the heating section in practical flows, and backward (upstream) thermal conduction is expected in the solid. Another case with different treatment of the heating electrode is carried out (Case CHTE). In experiments, heating of the solid pipe is normally imposed by electric current, with electrodes attached at both ends of the metal pipe. For most part of the metal pipe, electrical resistance are uniform, and heating is therefore uniform, however, the heating at the locations that are in contact with the electrodes will clearly be modified. This effect was discussed by Yan et al. [154], as one of the potential effect that might cause uncertainties in numerical simulations. In the current study, such effect is modelled in case (CHTE), after a region of $\Delta z/D = 5$ without solid heating, a region of $\Delta z/D = 10$ with only 10% of the solid heating is modelled before the full heating is applied in the rest solid pipe.

Table 7.1: Properties of the solid pipe

λ^* $(W/m \cdot K)$	c_p^* $(J/kg \cdot K)$	ρ^* (kg/m^3)
16.38	125.6	7900

The inlet Reynolds number in all cases is 1800 (3600 based on diameter), and the wall heat flux of Case NSW (q_w^*) is $63000 W/m^2$, an equivalent volumetric heat source S_q^* was obtained and imposed in the solid domains of the conjugate heat transfer simulations (Cases CHT & CHTE):

$$S_q^* = \frac{q_w^* A_{in}^*}{V_{pipe}^*} = \frac{2R_{in}^* q_w^*}{R_{out}^{*2} - R_{in}^{*2}}, \tag{7.1}$$

in which A_{in}^* is the surface area of the pipe inner wall, and V_{pipe}^* is the volume of the solid pipe, R_{in}^* and R_{out}^* are respectively the inner and outer radius of the solid pipe. Constant solid properties were considered in the conjugate heat transfer simulations (Cases CHT & CHTE) and thermophysical properties for the solid pipe are listed in table 7.1. Configurations of the three studied simulations are listed in table 7.2.

Table 7.2: Configurations of the simulation cases

Case	$Re_{D,0}$	T_0^*/T_{pc}^*	q_w^* (W/m^2)	S_q^* (W/m^3)	D_{in}^* (mm)	D_{out}^* (mm)
NSW	3600	0.97	63000	None	1.906	4.2
CHT	3600	0.97	None	34290	1.906	4.2
CHTE	3600	0.97	None	34290	1.906	4.2

7.2 Results and discussions

7.2.1 Comparison of the heat transfer behaviours

Firstly the general heat transfer behaviours in all cases are compared. Streamwise distributions of wall heat fluxes and developments of wall temperatures are shown in Fig. 7.1. The wall heat fluxes were calculated using the temperature gradient and thermal conductivity at the wall:

$$\overline{q_w^*} = \overline{\lambda^*} \frac{\partial \overline{T^*}}{\partial r^*}\bigg|_w \tag{7.2}$$

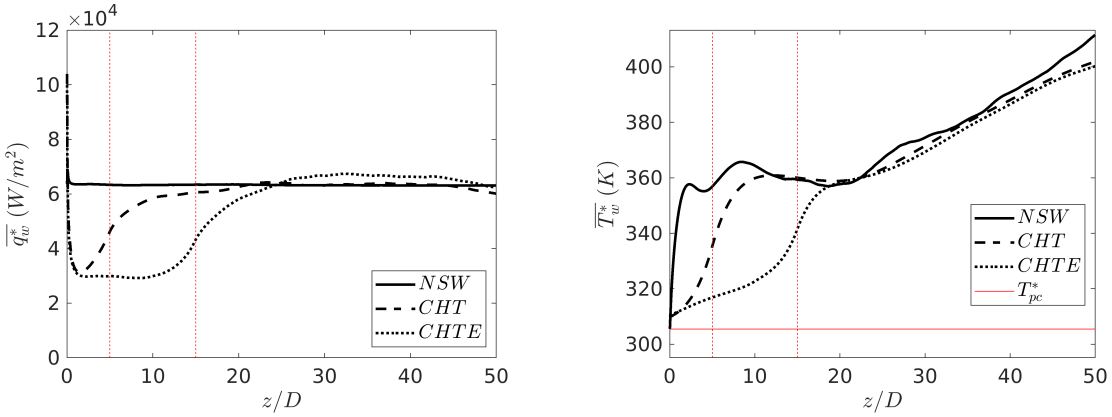

(a) (b)

Figure 7.1: Streamwise developments of (a) wall temperature and (b) surface heat flux at the fluid wall boundary in all cases.

Case NSW is taken as a reference case, in which heating (constant wall heat flux) was imposed starting from $z/D = 0$, and the heating of cases CHT and CHTE were imposed starting from $z/D = 5$ & 15 respectively. As shown in Fig. 7.1a, wall heat flux of case NSW is constant everywhere, while those of Cases CHT & CHTE are non-uniform due to the redistribution. It should be noted that the wall heat flux of Case CHT and CHTE do not strictly start from $z/D = 5$ & 15, due to the backward thermal conduction in the pipe wall and heat flux at the no-heating

region of these two cases are quite significant. Such observation indicates that in experiments of such flows, heatings might not strictly start from the set locations, as they are redistributed due to the solid conduction, and hence heating is significant at the developing region of Case CHT and CHTE. $\overline{q_w^*}$ of the three cases are significantly different before $z/D = 20$, which is also reflected in the developments of the wall temperatures, shown in Fig. 7.1b. Similarly, $\overline{T_w^*}$ of the three cases are very different before $z/D = 20$, and they become closer after this location. This indicates that although the heat inputs before $z/D > 20$ in the three cases are different, their development trends of $\overline{T_w^*}$ are very similar.

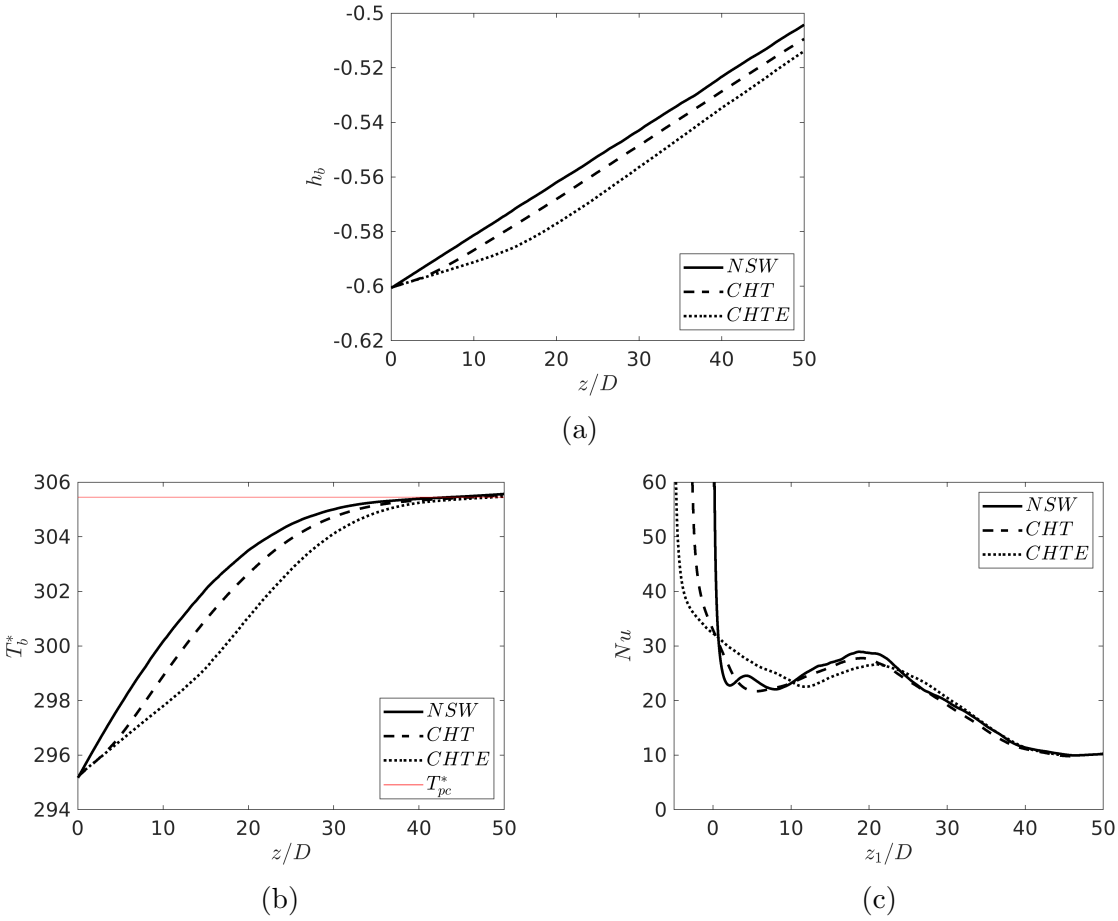

Figure 7.2: Streamwise developments of (a) bulk enthalpy, (b) bulk temperature and (c) Nusselt number in all cases.

The developments of bulk enthalpy in the three cases are shown in Fig. 7.2a. h_b is always linear in NSW but is only linear at a later stage in Cases CHT and CHTE where $\overline{q_w^*}$ is about linear. It can be seen that there is a delay of h_b in Case CHT and CHTE, compared to case NSW, which is due to the differences in the total input heats.

Such delay is about $3D$ for Case CHT, and $5D$ for Case CHTE. In later discussions, locations of Case CHT and Case CHTE are shifted by $3D$ and $5D$ respectively, to match the bulk enthalpy with case NSW. To distinguish with the original locations (z/D), a new streamwise distance unit z_1/D is used, with those in Case CHT and CHTE shifted by $3D$ and $5D$. The bulk temperatures in all cases are shown in Fig. 7.2b, with the critical temperature specified by a thin red line. All the three T_b^* are non-linear as c_p changes significantly when T_b^* approaches the critical value. Along the streamwise direction, T_b^* in the three cases become closer and closer, due to the rapidly increasing c_p. The Nusselt numbers against z_1/D in these cases are shown in Fig. 7.2b. Developments of the Nusselt number are very similar across the three cases. At the begin of each case, Nu reduces rapidly due to the entrance effect, the distances of this process are different in these cases. Then Nu reduce slower in all cases, and reaches a minimum. After this, the Nusselt numbers increase again, but reduce again after reaching the peak.

Although the heat fluxes at the initial stage ($z/D < 20$) are different in these cases, the peaks of Nusselt number in different cases appear at nearly the same h_b, which indicates the effect of conjugate heat transfer is relatively minor for flows at these configurations. References show that with conjugate heat transfer considered, two effects were included, i.e., the redistribution of wall heat flux and the stabilisation of the near-wall temperature/enthalpy fluctuations. The numerical result of Case CHT shows that the wall heat flux is not strictly started from the location where solid heating starts, and there is a shift of h_b compared to case NSW, in which uniform wall heat flux is imposed. The shifted Nu of Case CHT is very similar to that in case NSW, which indicates that the function of $Nu - h_b$ in the two cases are very close and the second effect (stabilisation of the near-wall temperature/enthalpy fluctuation) on the heat transfer characteristic might be relatively minor.

To visualise the stabilised enthalpy fluctuations, the root mean square of the enthalpy and density fluctuations at two near-wall locations ($y^{+0} = 0.08$ and 5.18) in case NSW and CHT are shown in Fig. 7.3a & 7.3b. At $y^{+0} = 0.08$, the enthalpy fluctuations of the two cases are very different: h'_{rms} of case NSW rapidly increases before $z/D = 5$, reaches a peak then reduces, it remain unchanged from about $z/D = 10$. While for Case CHT, h'_{rms} keeps reducing before $z/D = 10$, then remain unchanged later. At $z/D > 10$, h'_{rms} of case NSW is about $20 \sim 30$ times larger than that in Case CHT, while at the location slightly further away ($y^{+0} = 5.18$), the differences between two fluctuations are significantly diminished. This suggests the stabilisation

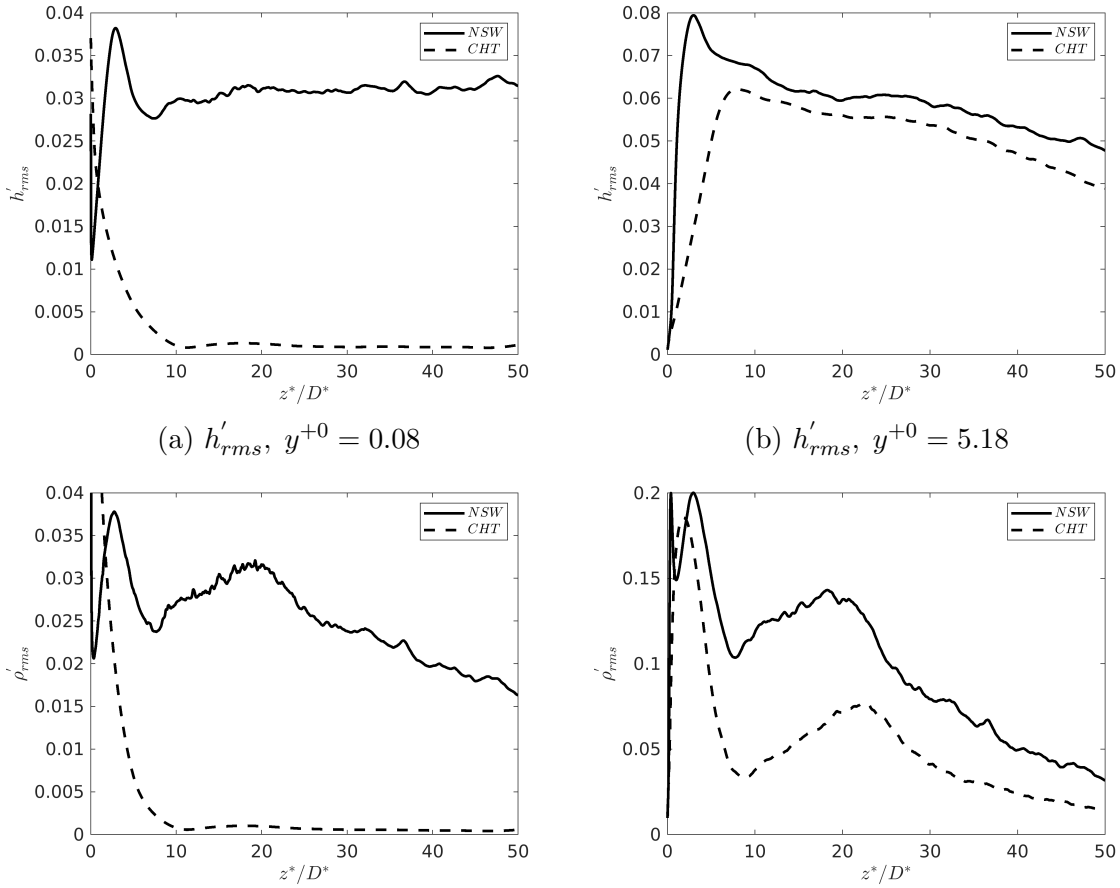

(a) h'_{rms}, $y^{+0} = 0.08$ (b) h'_{rms}, $y^{+0} = 5.18$

(c) ρ'_{rms}, $y^{+0} = 0.08$ (d) ρ'_{rms}, $y^{+0} = 5.18$

Figure 7.3: Root mean square of enthalpy and density fluctuation at $y^{+0} = 0.08$ and 5.18 of case NSW and CHT.

effect is limited close to the wall (at least in these configurations) and the fluctuating intensity of enthalpy beyond $y^{+0} = 5.18$ remains largely unaffected with the consideration of conjugate heat transfer. Same comparisons of the root mean square of density fluctuations are shown in Fig. 7.3c & 7.3d. The behaviours in the two cases are very different: for case NSW at $y^{+0} = 0.08$, two peaks of ρ'_{rms} are formed at about $z/D = 5$ and 20, while ρ'_{rms} of Case CHT reduces before $z/D = 10$, then largely disappears. Differences between ρ'_{rms} in the two cases are relatively large after $z/D = 10$. Similarly, at $y^{+0} = 5.18$, differences between the two are much smaller, both with two peaks. The peak value of ρ'_{rms} at $z/D = 20$ in Case CHT is about half of that in case NSW, after the peaks, ρ'_{rms} in both cases keep reducing. The comparison of ρ'_{rms} at two locations shows the stabilisation of density fluctuation in Case CHT is also limited close to the wall, such effect is diminished rapidly further away from the wall.

Compared to case NSW, fluctuating intensities of enthalpy and thermophysical properties in Case CHT are dampened close to the wall, but such effect is significantly diminished further away. Such stabilisation might affect the heat transfer characteristics by affecting the turbulent heat flux, hence the FIK decomposition (Eq. 6.13) is used here to identify different contributions to the Nusselt number in these cases. Firstly, to validate the FIK decomposition, the total Nu_{FIK} is compared with the Nusselt number in case NSW and CHT (Fig. 7.4a). In both cases, Nu_{FIK} and Nu agree well. Comparisons of the laminar, turbulent and inhomogeneous contributions in thses two cases are shown in Fig. 7.4a 7.4b & 7.4c respectively, in which data for Case CHT are shifted by $3D$ to match the bulk enthalpies in the two cases. The laminar contribution Nu_l in both cases reduce rapidly first, then slightly increase, followed by continuous reduction after $z_1/D = 20$. Nu_l in Case CHT is slightly smaller than that in case NSW at most locations. The laminar contributions in both cases are relatively small in magnitude compared to the turbulent contributions shown in Fig. 7.4b. Before $z_1/D = 10$, Nu_t of the two cases are quite different, due to the different wall heat fluxes in this region. The two Nu_t converge from about $z_1/D = 10$, and both increase until $z_1/D \approx 25$, then reduce continuously. Nu_t in Case CHT is always slightly smaller than that of case NSW after $z_1/D = 10$, differences between the two are not significant. The effect of different fluctuating enthalpies on heat transfer behaviours is reflected in Nu_t, the comparison of Nu_t indicates such effect is minor. Comparison of the inhomogeneous contributions Nu_h are shown in Fig. 7.4d, Nu_h of the two cases agree very well, both with an initial rapid reduction, and reach a minimum at about $z_1/D = 25$, then remain unchanged after $z_1/D = 30$. The differences between Nu_l and Nu_t suggest the variations of the flow fields and turbulent characteristics are different between the two cases, which will be presented and discussed later.

7.2.2 Comparison of turbulent characteristics

In the last section the differences between the near-wall enthalpy and density fluctuations of Cases NSW & CHT are presented, and the effect on heat transfer characteristics is found to be minor at these configurations, as the Nusselt number of the two cases are very similar. However, differences in Nu_l and Nu_t suggest the flow developments and turbulence in these two cases might be different. Such differences might be coming from the differences in the structural effect of density variations, that is, the stabilised ρ'_{rms} in Case CHT might cause reductions in the buoyancy production of the Reynolds stress $\overline{\rho u''_z u''_z}$, and result in lower magnitudes of the turbulent kinetic

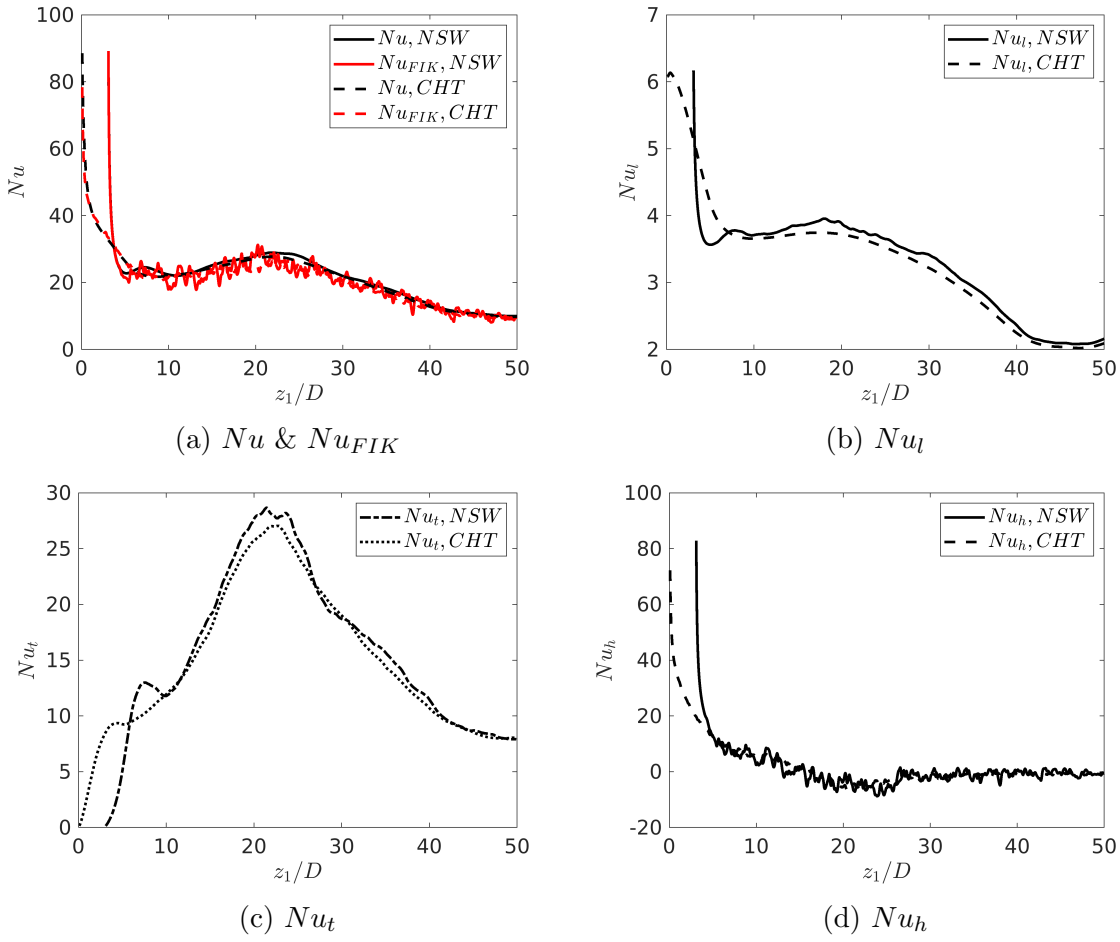

Figure 7.4: Comparisons of (a) Nu_{FIK} and Nu, (b) laminar, (c) turbulent and (d) inhomogeneous contributions of the Nusselt number in case NSW and CTH.

energy. However, Fig. 7.3c & 7.3d show that such stabilisation is limited close to the wall and diminished further away. This will be quantified and investigated later on.

Firstly, developments of the velocity profiles in Cases NSW and CHT are shown in Fig. 7.5. Similarly, locations of the two cases are matched by h_b, with those in Case CHT shifted by $3D$. At each location, the velocity profiles of the two cases are slightly different. General development trends of the velocity profiles in the two cases are very similar, with the near-wall acceleration and mainstream deceleration flattening then turning the profiles to M-shape. When the profiles turn M-shape at about $z_1/D = 20$, the peak velocities are close to the wall ($y \approx 0.1$). At later locations, the near-wall and mainstream velocities keep rising and decreasing respectively. At these locations, velocity gradients become large and larger and the enhancement in turbulent shear production is expected. These changes in $\overline{u_z}$ are very similar in the two cases, with the near-wall velocity of case NSW slightly higher than that in Case CHT at $z_1/D = 15$,

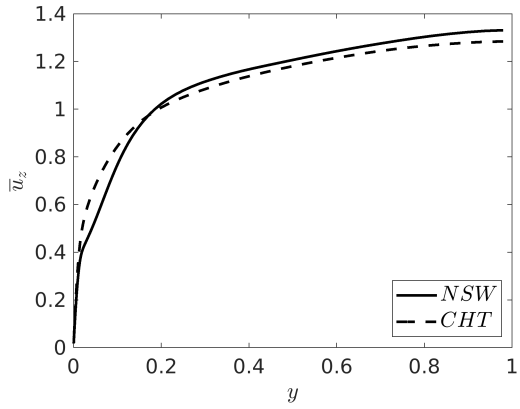

(a) $z_1/D = 6$

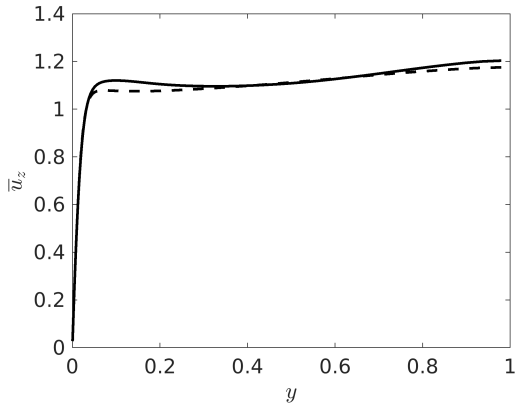

(b) $z_1/D = 15$

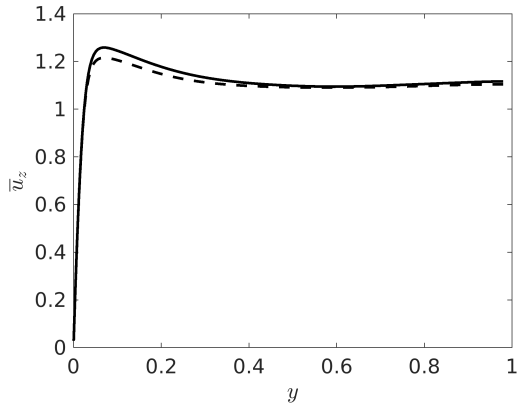

(c) $z_1/D = 20$

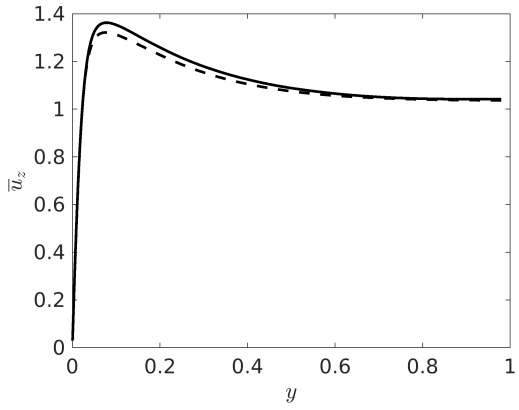

(d) $z_1/D = 25$

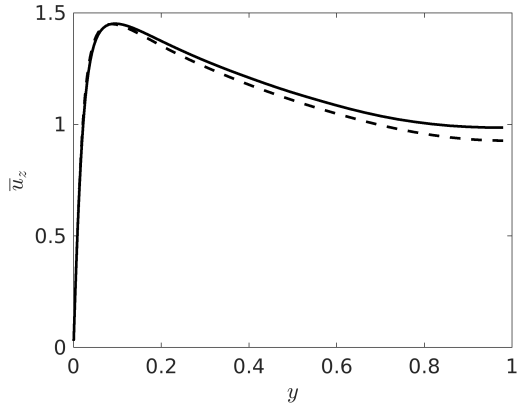

(e) $z_1/D = 35$

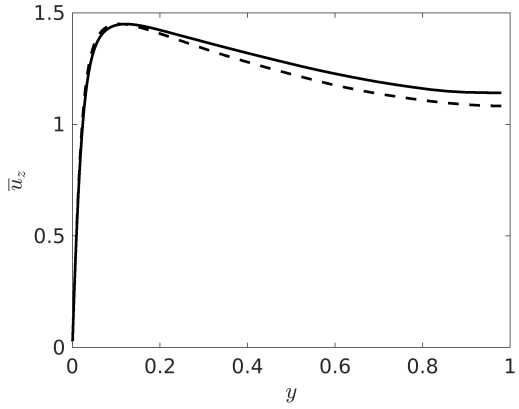

(f) $z_1/D = 45$

Figure 7.5: Streamwise velocity profiles at chosen locations of case NSW and CHT.

20 and 25.

The variations of the turbulent kinetic energy (TKE) in these two cases are shown in Fig. 7.6. At both $z_1/D = 6$ and 15, the peaks of TKE in Case CHT are 1/3 lower than those in case NSW, which indicates the stabilisation of near-wall density in Case CHT significantly affects the turbulent quantities. At further downstream ($z_1/D = 20$ & 25), differences between the peak values of TKE in the two cases are smaller, with those in Case CHT about 1/4 lower than those in case NSW. Then at later locations ($z_1/D = 35$ & 45), they are closer and closer. At $z_1/D = 15$, magnitudes of TKE in both cases are much lower than those at other locations, which is corresponding to the location where the velocity profiles are flattened and shear productions are greatly reduced. Then at later locations, the two flows rapidly recovered, with TKE magnitudes rising at both the near-wall and mainstream regions.

It is worth noting that the differences in TKE between the flows with and without conjugate heat transfer considered (case NSW & CHT) are very similar to those observed previously in the flows simulated by Pucciarelli & Ambrosini [15] using LES, in which the peaks of TKE were very different during the laminarization, with the peak value of TKE in the case without solid wall about two times of that in the case with the solid wall, then differences between the two reduce at later stage when the flow was recovered. Such stabilization in near-wall turbulence affected by the solid wall is well reproduced in the current DNS.

The differences in TKE at the initial stages of case NSW and CHT are presumably due to the differences in the direct effect, that is, differences in density fluctuations close to the wall affecting the buoyancy productions. This was found to be dominant during the laminarization as the shear production is significantly diminished [11, 63]. Changes in the buoyancy production, shear production of TKE and the summation of the two (total production) in the two cases are shown in Fig. 7.7. Initially, at $z_1/D = 6$, the buoyancy production terms are relatively small in both cases and the peak of shear production in Case NSW is about two times of that in Case CHT. Then at further downstream ($z_1/D = 15$), the shear productions in both cases rapidly reduce as a result of the laminarization, while the buoyancy productions rise. At this stage, the buoyancy production is much larger than the shear production, and it is the main contributor. The peak of buoyancy production in Case NSW is about 30% higher than that in Case CHT, which are located at about $y^{+0} = 4.4$, where differences between the density fluctuation in the two cases are rapidly reducing. At further downstream ($z_1/D = 20$ & 25), during the recovery, shear production of the two cases rise again, both with two peaks. The first peak close to the wall in Case

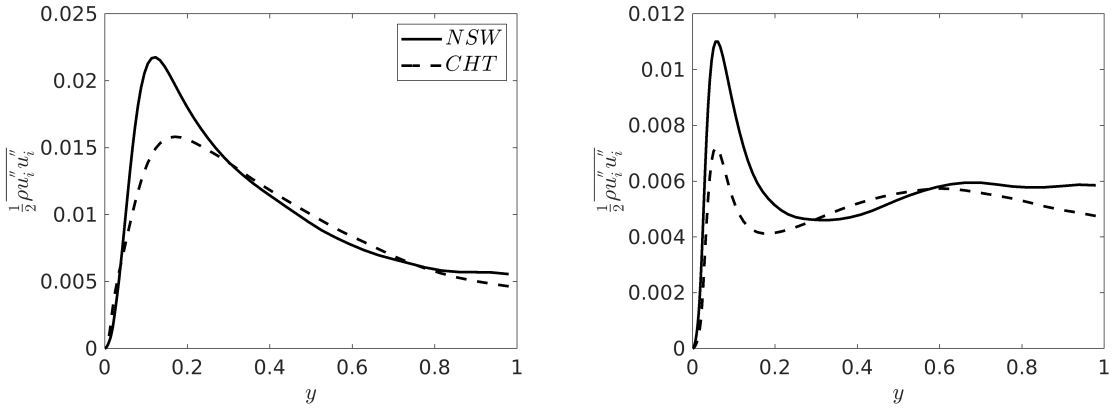

(a) $z_1/D = 6$ (b) $z_1/D = 15$

(c) $z_1/D = 20$ (d) $z_1/D = 25$

(e) $z_1/D = 35$ (f) $z_1/D = 45$

Figure 7.6: Profiles of turbulent kinetic energy at chosen locations of case NSW and CHT.

NSW is about two times of that in Case CHT, while the peaks further away from the wall in the two cases are relatively close. Next at $z_1/D = 35$ and 45, the buoyancy productions in the two cases were very close, the stabilization effect is minor, and the density fluctuation levels in the two cases were similar. Also, the mainstream peaks of the shear productions remain close in the two cases, the main differences of the total production are attributed to the differences in the near-wall peak of the shear production, with that in Case CHT about 40% lower than that in Case NSW.

Comparison of turbulent shear stresses $\overline{\rho u_z'' u_r''}$ in Cases NSW and CHT are shown in Fig. 7.8. Similar variation trends of $\overline{\rho u_z'' u_r''}$ are observed in both cases, with slightly different magnitudes. From $z_1/D = 6$ to 15, magnitudes of $\overline{\rho u_z'' u_r''}$ in both cases reduce significantly, and both turn negative close to the walls. However, the reduction of $\overline{\rho u_z'' u_r''}$ in Case NSW is faster than that in Case CHT. While at the recovery stage ($z_1/D = 20$ to 35), magnitudes of $\overline{\rho u_z'' u_r''}$ in Case NSW is always slightly larger than those in Case CHT. The lower turbulent shear stress and TKE in Case CHT indicate that at the same bulk enthalpy, turbulence in Case CHT is weaker than that in Case NSW, which is corresponding to the slightly lower turbulent contribution (Nu_t, Fig. 7.4c) to the Nusselt number in Case CHT. From $z_1/D = 25$ to 35, $\overline{\rho u_z'' u_r''}$ of both cases are negative at most part, with low-magnitude positive values close to the wall ($y < 0.1$). At this stage, turbulent shear stress in both cases significantly increase, which is during the stage that near-wall $\overline{u_z}$ accelerate after the velocity profiles turning M-shape (Fig. 7.5d & 7.5e), with increasingly larger radial velocity gradients.

The above comparisons between the flow fields and turbulent quantities of Cases NSW and CHT show that the stabilisation effect in conjugate heat transfer simulations is significant close to the wall. Such effect causes more differences in turbulent quantities between the case with and without solid wall during the laminarization process, and it is found to be diminished at the regeneration process. With these features, heat transfer characteristics are not significantly affected: The Nusselt number developments of cases NSW and CHT agree well and the laminar and turbulent contributions of the two cases are only slightly different.

Contours of the instantaneous fluctuations of the streamwise mass flux $(\rho u_z)'$ close to the wall in Case NSW and CHT ($z/D = 0$ to 20) are shown in Fig. 7.9. Fig. 7.9a shows that continuous streaks are rapidly formed and broken down within $z/D = 2$, while in Case CHT (Fig. 7.9b), long streaks are formed from the inlet to $z/D = 5$, then they broke down into fluctuations with a higher frequency. Transition in Case CHT is about $3D$ delayed compared to that in Case NSW, which agrees with the delay in the h_b development.

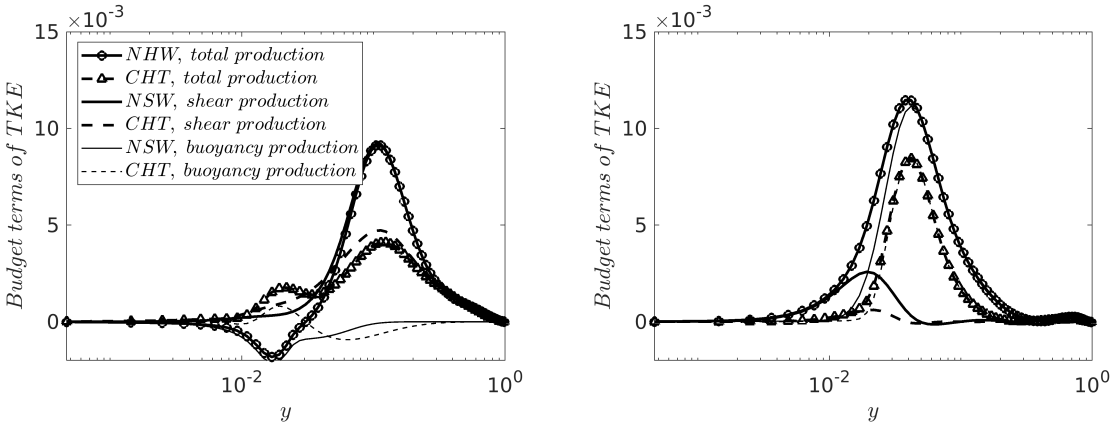

(a) $z_1/D = 6$ (b) $z_1/D = 15$

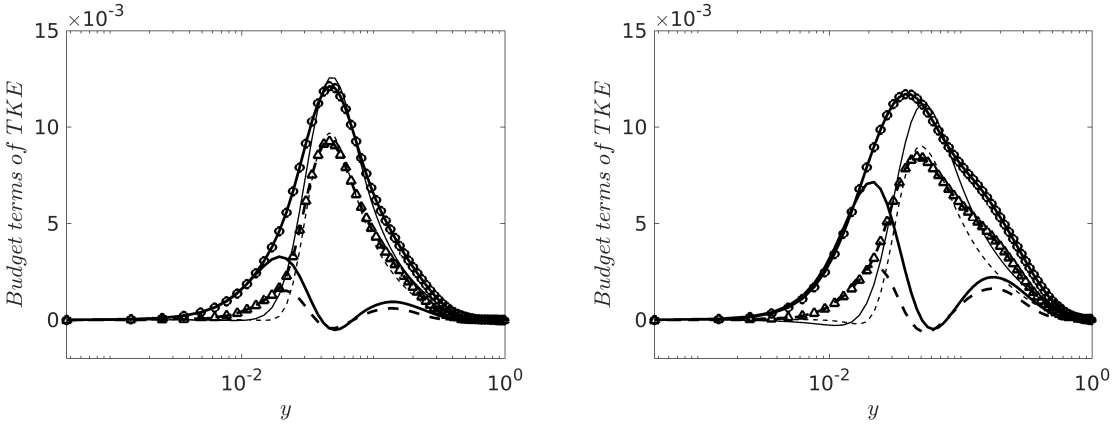

(c) $z_1/D = 20$ (d) $z_1/D = 25$

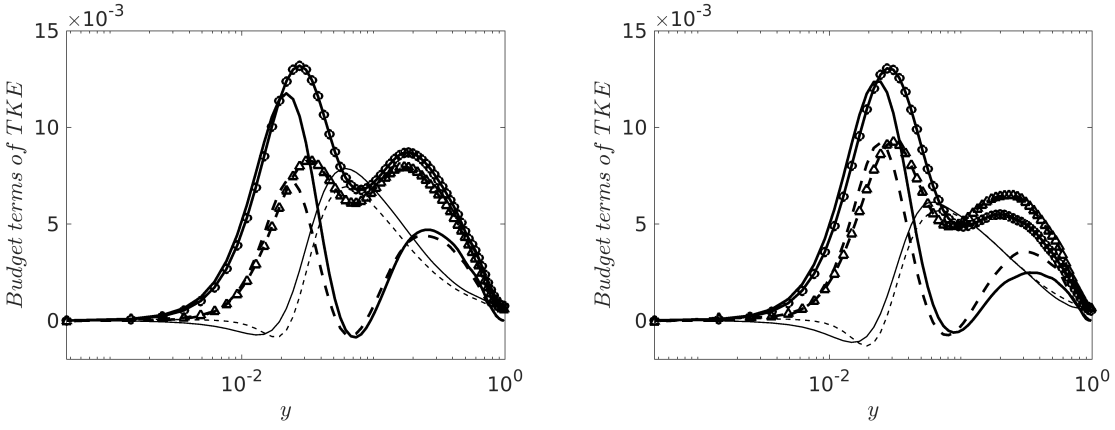

(e) $z_1/D = 35$ (f) $z_1/D = 45$

Figure 7.7: Summation of production and buoyancy production of TKE at chosen locations of Case NSW and CHT.

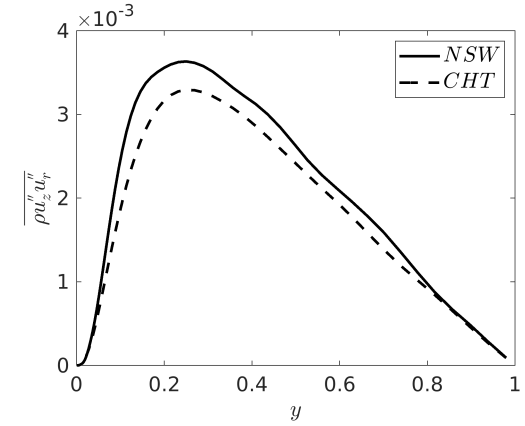

(a) $z_1/D = 6$

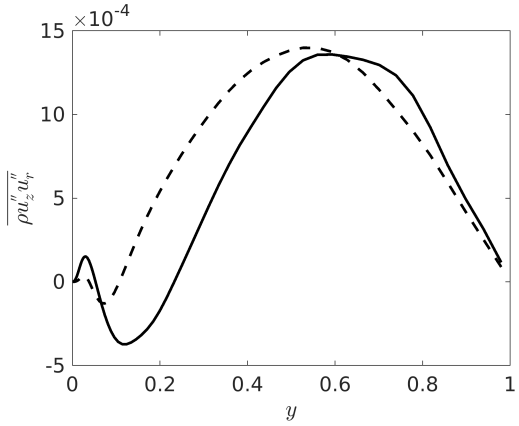

(b) $z_1/D = 15$

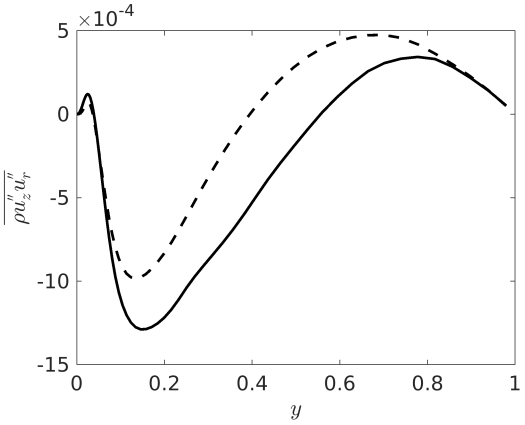

(c) $z_1/D = 20$

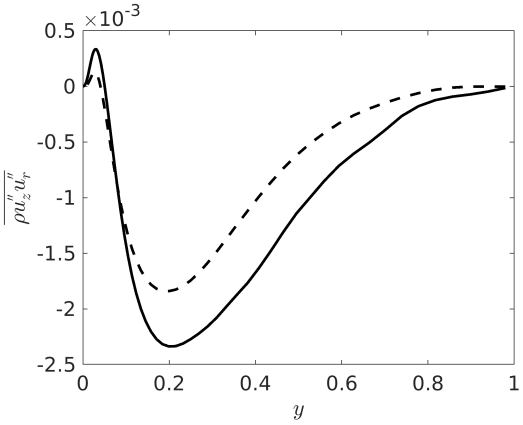

(d) $z_1/D = 25$

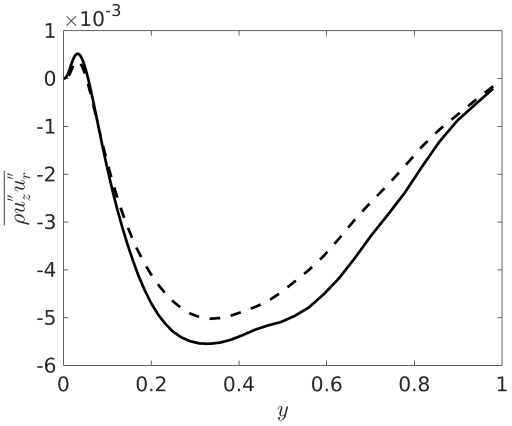

(e) $z_1/D = 35$

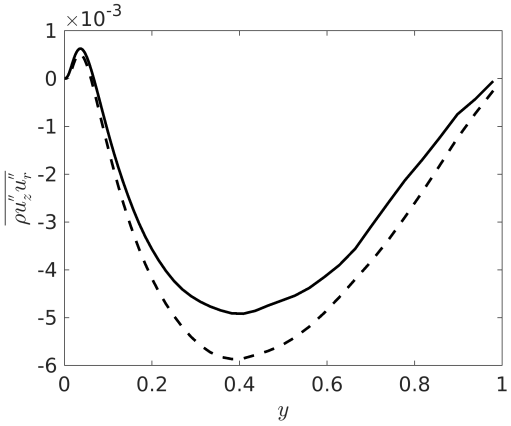

(f) $z_1/D = 45$

Figure 7.8: Profiles of turbulent shear stress at chosen locations of Case NSW and CHT.

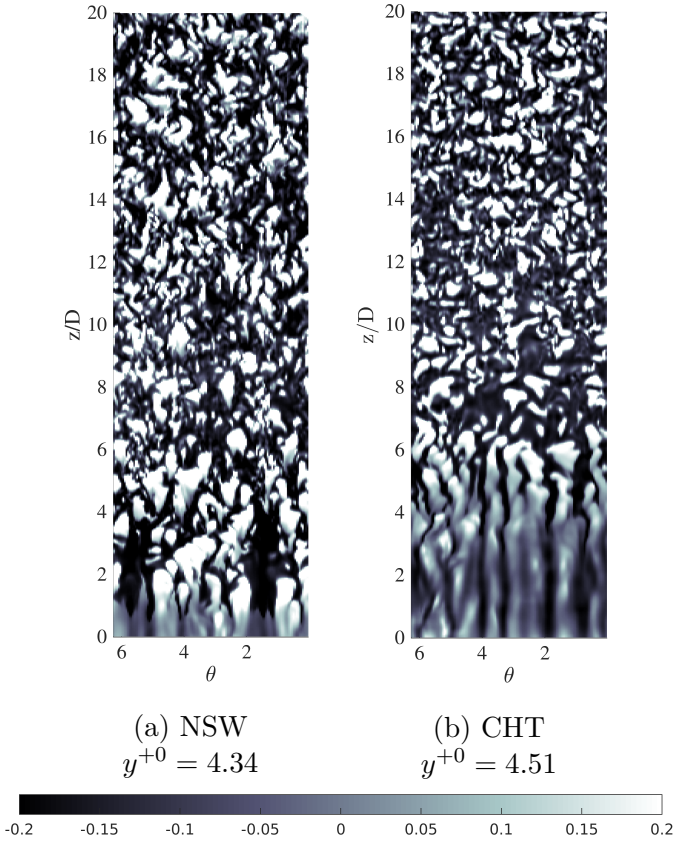

(a) NSW $y^{+0} = 4.34$ (b) CHT $y^{+0} = 4.51$

Figure 7.9: Contours of instantaneous $(\rho u_z)'$ at near-wall surfaces in Case NSW and CHT.

7.3 Conclusions

In the study of this sub-topic, DNS of upward heated flow of supercritical carbon dioxide (7.6 MPa) were carried out, with and without the solid pipe wall (conjugate heat transfer) considered. In conjugate heat transfer simulations, two effects are included, that is, the dampening of fluctuating enthalpy (as well as the fluctuating thermophysical properties) close to the wall, and the axial re-distribution of wall heat flux. Simulations of a case without the solid wall (Case NSW) but with a constant wall heat flux, a case with the solid wall and with a equivalent volumetric heat source starting from $z/D = 5$ (Case CHT) and a case with the solid wall and heating from $z/D = 5$, but the heating at $z/D = 5$ to 15 are adjusted to 1/10 of the target heating are carried out. Conclusions drawn from the result discussions are listed below:

- Cases CHT and CHTE have an 'unheated' section with zero volumetric heating applied in the wall. This allows heat conduction upstream from the heated section to be considered. This conduction often exists in experiments and practical systems. It has indeed been found that the conduction has significantly redistributed the heating influencing the bulk and wall temperatures in the flow.

- The fluctuations of enthalpy and density are much higher (20∼30 times higher) very close to the wall ($y^{+0} \approx 0.08$) in case NSW, but such differences reduce rapidly further away from the wall ($y^{+0} = 5.18$). The damping effect is found to be limited close to the wall but diminished further away.

- The Nusselt numbers in all cases agree well, suggesting the stabilization effect is limited. The laminar and turbulent contributions of Nusselt number in case CHT is slightly lower than those in case NSW, which is mainly affected by the stabilization effect.

- During the laminarization, the peak of turbulent kinetic energy in case CHT is about 1/3 lower than that in case NSW, which is similar to the observations in Pucciarelli & Ambrosini [15]. At further downstream, when the flow is recovered, differences between the two turbulent kinetic energy profiles are much smaller. Initially the peak of shear production in case NSW is much higher than that in case CHT. However, when buoyancy productions in the two cases become dominant with the shear productions rapidly reduced, the differences between the total productions in the two cases become smaller. During the recovery stage, the buoyancy productions as well as the mainstream peak of the shear production in the two cases are very close.

Chapter 8

Conclusions and future work

8.1 Conclusions of the current study

In the current study, numerical investigations on four sub-topics that are relevant to the turbulence and heat transfer characteristics of upward pipe flows of supercritical fluid have been carried out. In the first sub-topic (Chapter 4), the mechanism of the buoyancy, viscosity and density variations affecting the flow development and the laminarization are studied. Simulations with one or more effects isolated or eliminated have been carried out and the contributions from different effects are compared. The processes of laminarization caused by these effects are identified using the momentum balance. In the second sub-topic (Chapter 5), the apparent Reynolds number (ARN) analysis proposed in He et al. [13], based on isothermal flows with artificial body-forces, is extended to the current thermal flows. A unified approach that treats the buoyancy, viscosity and density variation effects as (pseudo-) body forces is proposed and the contributions of these effects are quantified. Expressions are derived to decompose the flow into an equivalent pressure gradient (EPG) flow and a perturbation flow. The turbulent structures in the buoyancy influenced flows are studied. In the next two chapters, two popular topics of supercritical fluid flows are investigated, i.e., the fluid-to-fluid scaling and the effect of conjugate heat transfer. In Chapter 6, the fluid-to-fluid scaling method proposed by Ambrosini & De Rosa [14] are evaluated for four different fluids using DNS. Excellent success of similarity is achieved, and different choices of scaled parameters and inlet conditions are also investigated. In Chapter 7, the effect of conjugate heat transfer on supercritical fluid flows is studied, by comparing simulations with and without the solid wall. The influences of the near-wall stabilization of enthalpy fluctuations and re-distribution of wall heat flux are investigated.

The DNS code CHAPSim used in this study has been validated in a number of previous studies [131, 133, 154]. Additional validations for the particular problems concern herein are presented in Chapter 3.

The main contributions of this study are as follows:

1. Developed important understanding of the mechanisms of flow laminarisation and recovery using DNS of an upward heated flow of supercritical carbon dioxide with individual effect artificially switched off or isolated. Results were published in He et al. [6];

2. Developed a unified theory to explain the various complex factors influencing flow laminarisation in a heated supercritical fluid flow using the apparent Reynolds number approach. A paper has been drafted based on this work which is to be submitted shortly;

3. Produced DNS of flows of four different fluids under conditions of similarity to support the fluid-to-fluid scaling studies. The results were published in He et al. [1]. This is the foundation of two recent publications of collaborators [151, 152];

4. Analysed and clarified the effect of conjugate heat transfer on turbulence and heat transfer in an upward pipe flow of supercritical carbon dioxide using the code implementation developed by the author.

The conclusions drawn from the discussion of each sub-topics are presented in each chapter, they are briefly summarised herein:

1. Effects of buoyancy and thermophysical property variations on the flow of supercritical carbon dioxide

   (a) In a heated vertical pipe flow of supercritical carbon dioxide, the viscosity variation and buoyancy cause flow laminarisation in a similar mechanism.

   (b) The flow inertia is significant, it delays the above effects.

   (c) The Boussineq approximation is able to capture the key flow phenomenon.

2. Further analysis of the supercritical fluid flow using the apparent Reynolds number theory

   (a) The effects of buoyancy, variations of density and viscosity, flow inertia can be explained using a unified explanation based on the apparent Reynolds number (ARN) approach.

(b) In the 'full' laminarisation region, turbulence regeneration cycle has ceased, with significant turbulent kinetic energy.

(c) The recovery region is akin to the bypass transition, with streaks broken down and vortexes regenerated.

3. Fluid-to-fluid scaling for supercritical fluid flows

(a) When Pr_0 is close, excellent similarity is achieved between the four supercritical fluids when the parameter group (Re_0, Fr_0, N_{SPC}, N_{TPC}) is chosen to scale.

(b) The four flows is less similar when parameter group (Pe_0, Fr_0, N_{SPC}, N_{TPC}) is chose. Matching the parameters in the momentum equation is more important.

(c) When Pr_0 is very different, similarity is not achieved even though parameter group (Re_0, Fr_0, N_{SPC}, N_{TPC}) is matched.

4. The effect of conjugate heat transfer on the flow of supercritical carbon dioxide

(a) For the studied flows, the damping effect of enthalpy fluctuation and axial re-distribution of wall heat flux are significant when conjugate heat transfer is considered.

(b) The damping effect is diminished rapidly further away from the wall.

(c) For the studied flow condition, the Nusselt number is not largely affected when conjugate heat transfer is introduced.

(d) The near-wall peak of turbulent kinetic energy is reduced by 1/3 when solid wall is considered, but this is only limited at early streamwise locations.

8.2 Suggestions for future work

The present study focuses on the changes in turbulent and heat transfer features in upward heated flows of supercritical fluids, and they are all buoyancy-aided flows. The flow physics of buoyancy-opposed downward flows are not included in the current study, in which heat transfer enhancement might happen due to the combination of several effects. The mechanism causing the turbulence and heat transfer enhancement could be studied using a similar analysis, that is the momentum balance analysis used to find the reason behind these phenomena. The apparent Reynolds number

analysis can also be applied to the buoyancy-opposed flows, to characterise the flow and heat transfer features. The capability of the proposed unified theory in terms of describing buoyancy-opposed flows is also interesting: for buoyancy-opposed flows, the body force contributed by buoyancy is opposite to those caused by the viscosity and density variations. This could be a potential topic for future studies in this field, as an extensions of the present study.

Furthermore, in some of the experiments of upward heated flows in mini-tubes, it was found that the acceleration effect (density variation) was much stronger than the buoyancy, the main contributor of the laminarization was the density variation effect. With the newly derived unified theory, the body forces contributed by buoyancy, viscosity and density variations in these flows can be quantified.

For the fluid-to-fluid scaling of supercritical fluids, DNS has been used to test some of the correlations in the present study. Similar assessment could be carried out to study the capabilities of the other scaling correlations developed in the literature, to compare their performances at different configurations (Re_0, T_0^*, q_w^*, D^*...). An overall benchmark (database) for different scaling methods can be made, with example scaling cases using different fluids and conditions, to provide numerical references for experiments that surrogate fluids are needed.

For the effect of conjugate heat transfer on simulations of supercritical fluid flows, comparisons between flows with and without solid wall conduction should be extended to more conditions. It is possible that for flows at other configurations, with a larger thermal conductivity or specific heat of the solid wall, the stabilization of enthalpy fluctuations is much stronger, which may possibly affect the flow more significantly than in the cases in the present study.

Appendices

Appendix A

Derivation of the Reynolds-averaged and Favre-averaged Navier-Stokes equations

A.1 Reynolds-averaged Navier-Stokes equations

The Reynolds-averaged Navier-Stokes (RANS) simulations are not used in the current study, however, the concept of RANS equations, eddy viscosity and turbulent heat flux are key points in the result discussion. The derivation of RANS equations and its modelling are introduced in this part.

The concept of Reynolds-average was proposed by Osborne Reynolds [155], who decomposed the instantaneous velocity into the time averaged and fluctuating components (Eq. A.1). The former is the averaged value within certain amount of sample time points (Eq. A.2), with the same interval (time step).

$$\phi_i = \overline{\phi} + \phi^{'} \tag{A.1}$$

$$\overline{\phi} = \frac{\sum_{i=1}^{n} \phi^i}{n} \tag{A.2}$$

The Reynolds-averaged Navier-Stokes (RANS) equations (Eq. A.3, A.4, A.5) are derived by substituting the instantaneous variables with the summation of their time averaged and fluctuating values ($u_i = \overline{u_i} + u_i^{'}$, $h = \overline{h} + h^{'}$), then time average the equation. After some manipulation with consideration of the properties of Reynolds-averaged values ($\overline{\phi'} = 0$, $\overline{a \pm b} = \overline{a} \pm \overline{b}$), the form of these equations are largely

maintained, with an additional shear stress $\rho\overline{u_i'u_j'}$ appeared in the momentum equation, and an additional heat flux $\rho\overline{u_i'h'}$ in the energy equation. The RANS equations describe the situation when thermophysical properties (ρ, μ, λ, c_p) are constant.

$$\frac{\partial\rho\overline{u_i}}{\partial x_i} = 0 \tag{A.3}$$

$$\frac{\partial\rho\overline{u_i}}{\partial t} + \frac{\partial\rho\overline{u_iu_j}}{\partial x_j} = -\frac{\partial\overline{p}}{\partial x_i} + \frac{1}{Re}\frac{\partial}{\partial x_j}\Big(\mu\big(\frac{\partial\overline{u_i}}{\partial x_j} + \frac{\partial\overline{u_j}}{\partial x_i}\big) - Re\rho\overline{u_i'u_j'}\Big) - \rho g \tag{A.4}$$

$$\frac{\partial\rho\overline{h}}{\partial t} + \frac{\partial\rho\overline{u_i}\overline{h}}{\partial x_i} = \frac{1}{RePr}\frac{\partial}{\partial x_i}\big(\frac{\lambda}{c_p}\frac{\partial\overline{h}}{\partial x_i} - RePr\rho\overline{u_i'h'}\big) \tag{A.5}$$

For stationary laminar flows, fluctuations of velocities are neglectable ($u_i \approx \overline{u_i}$), analytical solutions of flow/thermal field can be easily obtained with closed RANS equations. The turbulent shear stress $-\rho\overline{u_i'u_j'}$ and turbulent heat flux $-\rho\overline{u_i'h'}$ are new unknowns and need to be modelled to close the equations. To tackle the closure problem of the RANS momentum equation, the concept of eddy viscosity μ_t was proposed by Boussinesq [156], and most of the RANS turbulence models are based on modelling the eddy viscosity:

$$-\rho\overline{u_i'u_j'} = \mu_t\Big(\frac{\partial\overline{u_i}}{\partial x_j} + \frac{\partial\overline{u_i}}{\partial x_j}\Big) - \frac{2}{3}k\delta_{ij} \tag{A.6}$$

And the turbulent heat flux can also be modelled by the turbulent Prandtl number Pr_t:

$$-\rho\overline{u_i'h'} = \frac{\mu_t}{Pr_t}\frac{\partial h}{\partial x_i}, \tag{A.7}$$

where σ_t is the turbulent Prandtl number which is normally taken as a constant. Numerous turbulent models have been developed to model the eddy viscosity. Example of turbulence models include the one-equation Spalart-Allmaras turbulence model [157], the standard $k-\epsilon$ model [158], and the low Reynolds number turbulence model, the Wilcox $k-\omega$ model [159].

A.2 Favre-averaged Navier-Stokes equations

In the derivation of the RANS equations, density is assumed to be constant, so that the RANS equations maintain the same form as the Navier-Stokes equations, which greatly simplifies the modelling work. For the situation with density variations, the a density weighted averaged algorithm, i.e., Favre-averaged treatment is used. The Favre-averaged value of variable ϕ and the Favre-averaged fluctuation is defined as:

$$\widetilde{\phi} = \frac{\overline{\rho\phi}}{\overline{\rho}}, \quad \phi'' = \phi - \widetilde{\phi}, \tag{A.8}$$

with properties:

$$\overline{\rho\phi''} = 0, \quad \overline{\widetilde{\phi}} = \widetilde{\phi}, \quad \overline{\widetilde{\phi}a} = \widetilde{\phi}\overline{a} \tag{A.9}$$

The Favre-averaged Navier-Stokes (FANS) equations can be obtained by substituting variables with the summations of their Favre-averaged and fluctuating values ($u_i = \widetilde{u}_i + u_i''$, $h = \widetilde{h} + h''$) into the Navier-Stokes equations, then time averaging every term:

$$\frac{\partial \overline{\rho}\widetilde{u}_i}{\partial x_i} = 0 \tag{A.10}$$

$$\frac{\partial \overline{\rho}\widetilde{u}_i}{\partial t} + \frac{\partial \overline{\rho}\widetilde{u}_i\widetilde{u}_j}{\partial x_j} = -\frac{\partial \overline{p}}{\partial x_i} + \frac{1}{Re_0}\frac{\partial}{\partial x_j}\Big(\mu\big(\frac{\partial \overline{u_i}}{\partial x_j} + \frac{\partial \overline{u_j}}{\partial x_i}\big) - Re_0\overline{\rho u_i'' u_j''}\Big) - \overline{\rho}g \tag{A.11}$$

$$\frac{\partial \overline{\rho}\widetilde{h}}{\partial t} + \frac{\partial \overline{\rho}\widetilde{u}_i\widetilde{h}}{\partial x_i} = \frac{1}{Re_0 Pr_0}\frac{\partial}{\partial x_i}\Big(\lambda\frac{\partial \overline{T}}{\partial x_i} - Re_0 Pr_0\overline{\rho u_i'' h''}\Big) \tag{A.12}$$

With the Favre-averaged treatment, the form of the FANS equations is largely the same as RANS equations. $-\overline{\rho u_i'' u_j''}$ is the turbulent shear stress, and $\overline{\rho u_i'' h''}$ is the turbulent heat flux.

Appendix B

Mesh sensitivity test on CHAPSim

To test the grid independence of the results in the current study, a mesh sensitivity test for DNS code CHAPSim is performed. Case A & E from Chapter 4 is chosen ($Re_{D0} = 5234$, $Re_{\tau 0} = 180$). The mesh size used in the present study is $1024 \times 64 \times 128$ (streamwise×radial×spanwise direction), and the mesh resolution is: $\Delta y^+ = 0.17 \sim 7.46$, $\Delta r\theta^+ = 8.91$, $\Delta z^+ = 14.19$. Simulations of cases A & E with the streamwise and radial mesh size doubled ($2048 \times 128 \times 128$) are carried out, with a mesh resolution of $\Delta y^+ = 0.21 \sim 2.88$, $\Delta r\theta^+ = 8.73$, $\Delta z^+ = 6.95$. The comparison of the streamwise velocity and turbulent shear stress profiles are shown in Fig. B.1 & B.2.

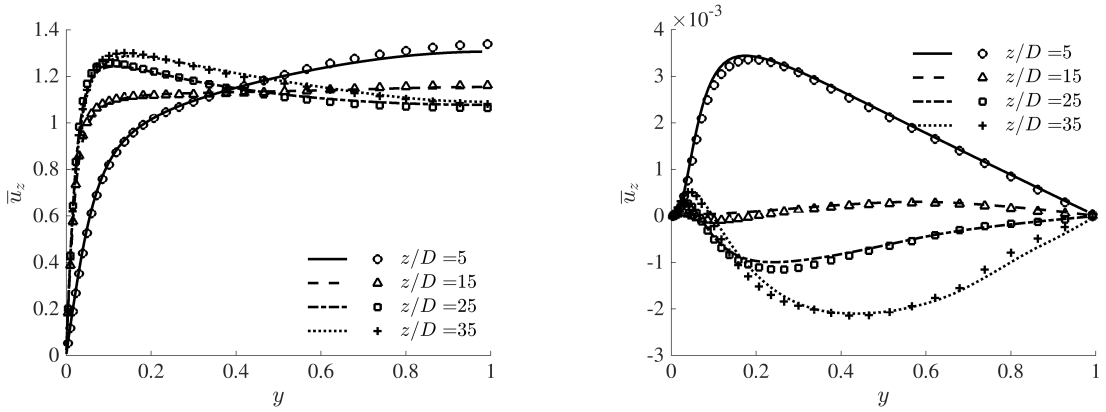

Figure B.1: Comparison of the streamwise velocity and turbulent shear stress profiles of case A with different mesh resolutions (lines: original mesh, markers: refined mesh).

In Fig. B.1 & B.2, the averaged velocity profiles and turbulent shear stress profiles at different locations agree well between the cases with the original and refined mesh. The flow with a mesh size of $1024 \times 64 \times 128$ can capture the same flow feature as that in the refined mesh case, i.e., the velocity profile is firstly flattened, then turns into a M-shape profile, turbulent shear stress reduces and flips negative. The mesh

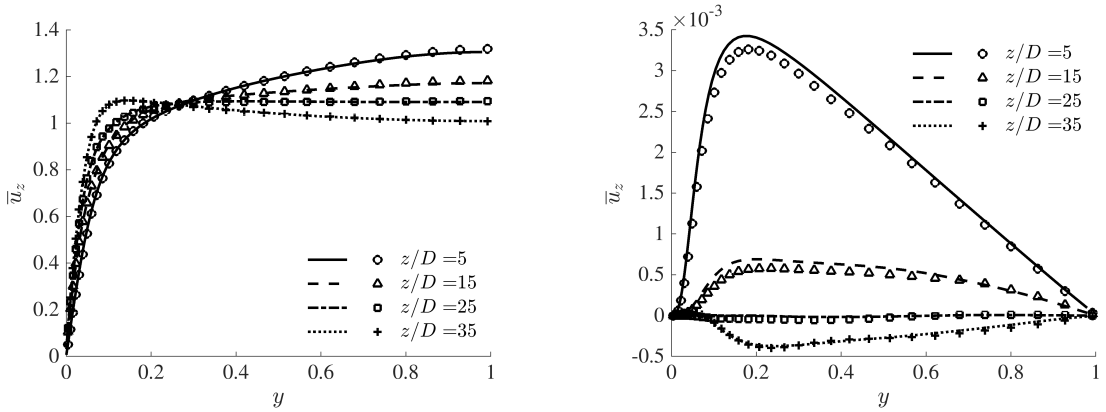

Figure B.2: Comparison of the streamwise velocity and turbulent shear stress profiles of case E with different mesh resolutions (lines: original mesh, markers: refined mesh).

sensitive test of the two cases shows the current used mesh resolution is sufficient for the concerned flows.

Appendix C

Fluctuating velocities in Cases A to F

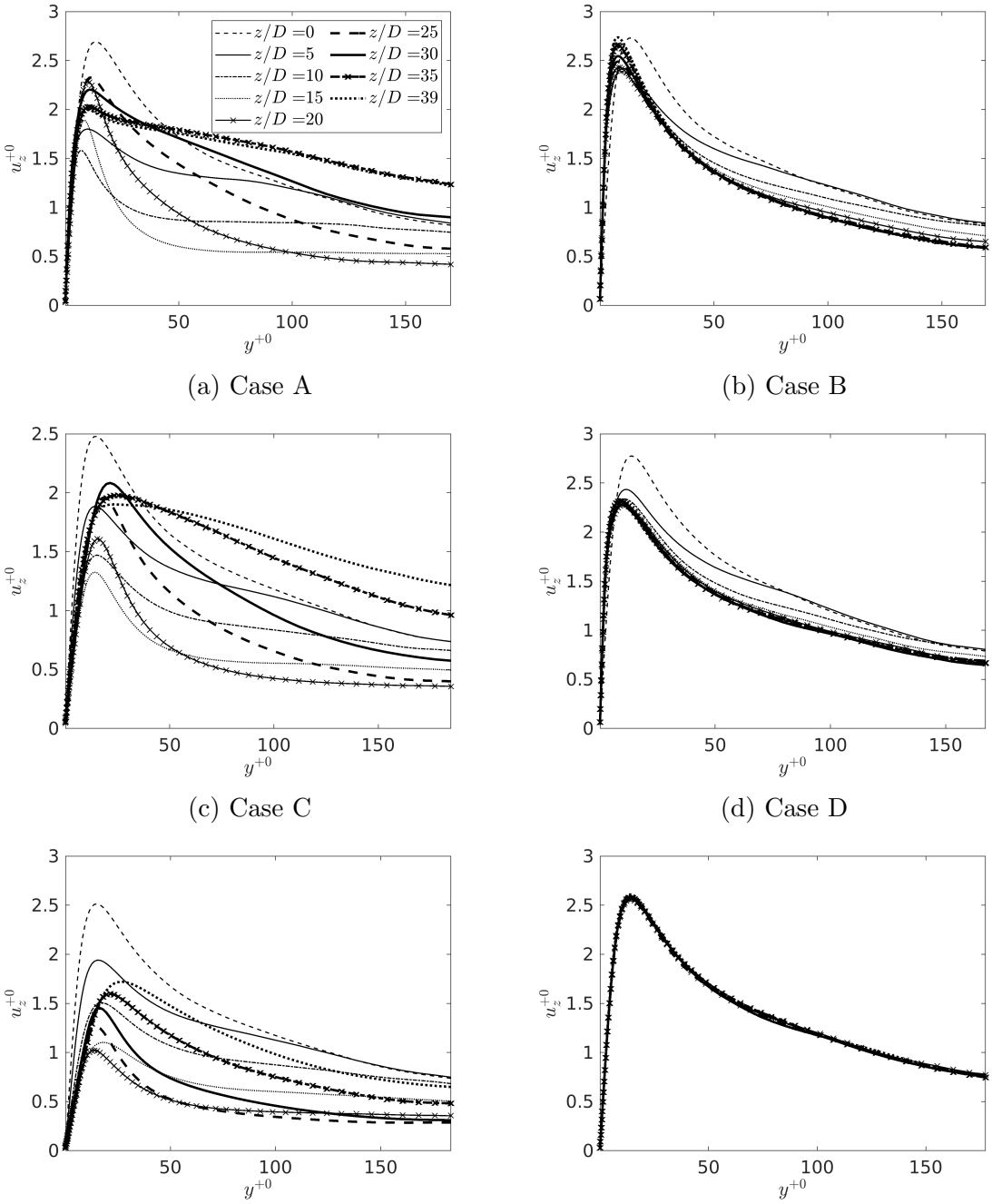

(a) Case A

(b) Case B

(c) Case C

(d) Case D

(e) Case E

(f) Case F

Figure C.1: Profiles of the streamwise fluctuating velocity u_z^{+0} against y^{+0} in case A to F.

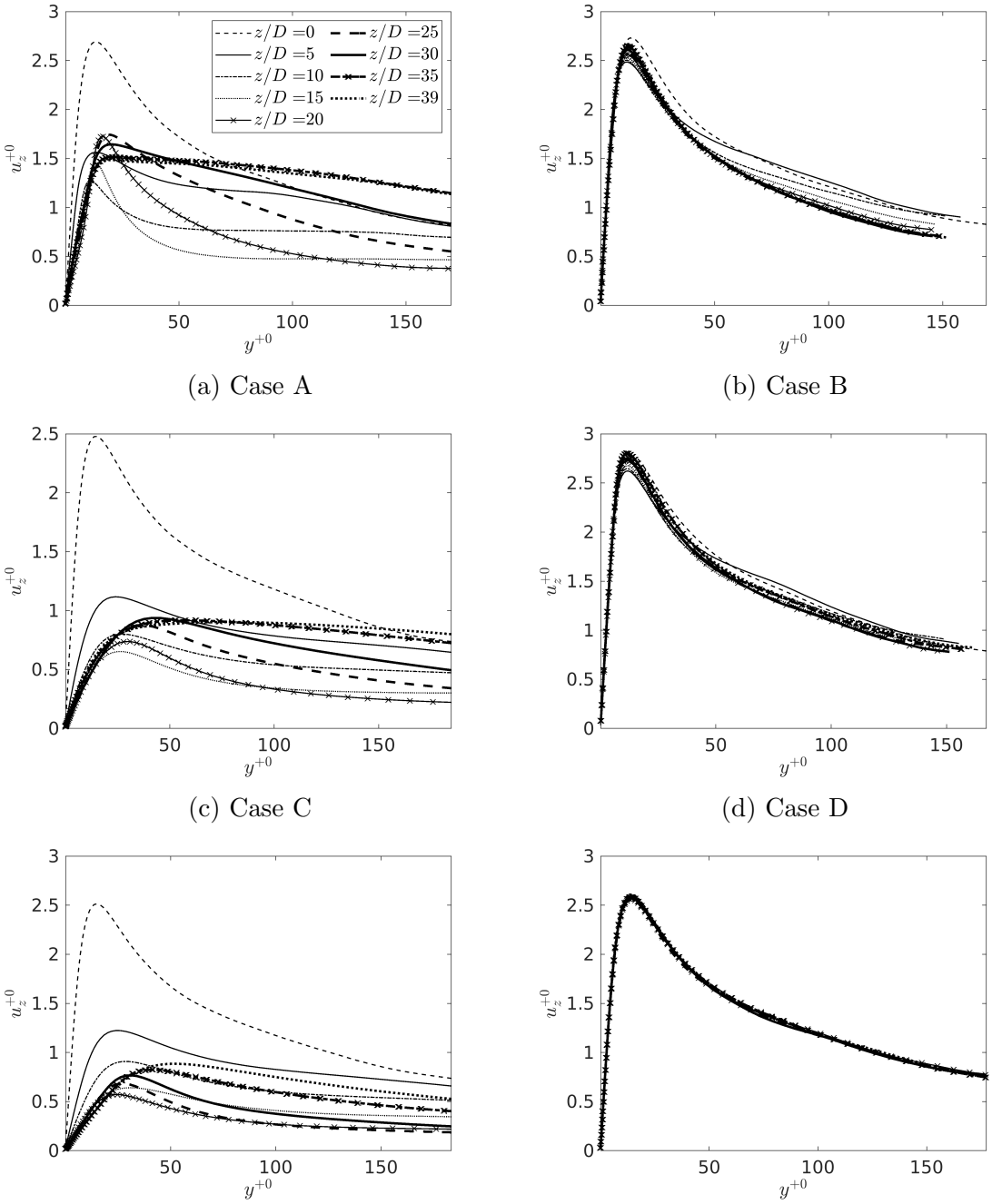

(a) Case A

(b) Case B

(c) Case C

(d) Case D

(e) Case E

(f) Case F

Figure C.2: Profiles of the streamwise fluctuating velocity u_z^+ against y^+ in case A to F.

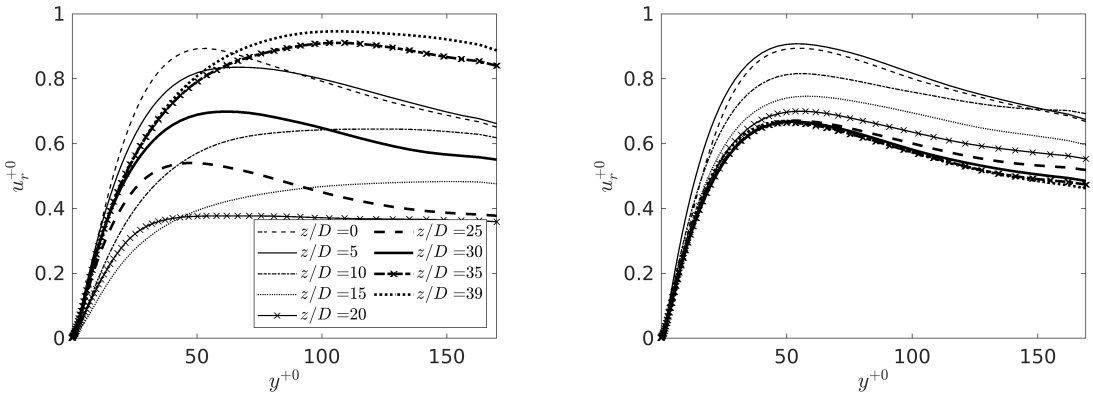

(a) Case A

(b) Case B

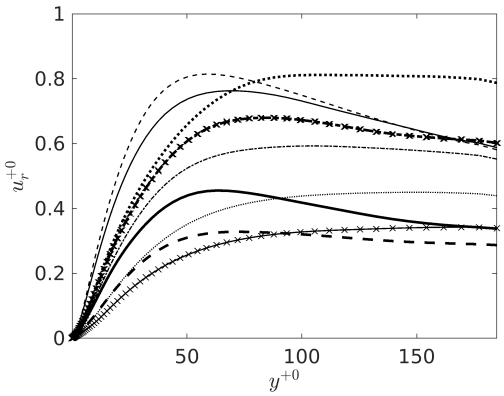

(c) Case C

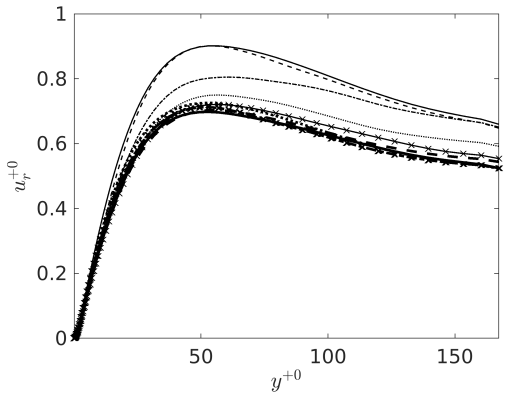

(d) Case D

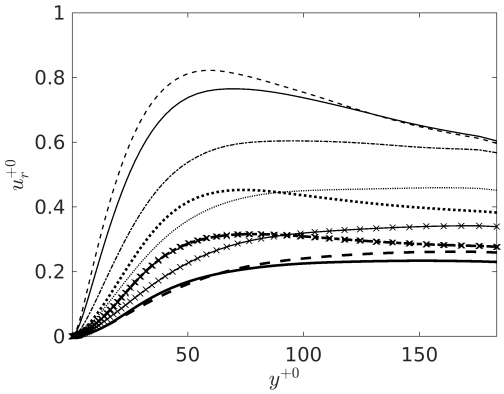

(e) Case E

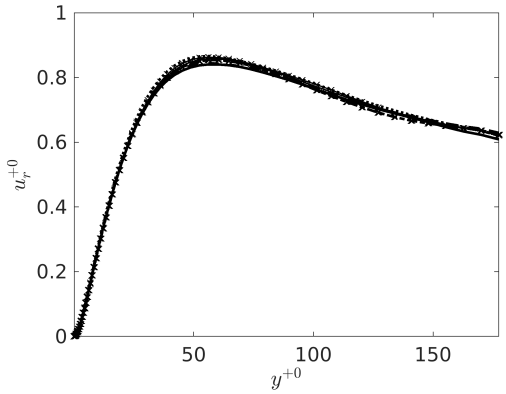

(f) Case F

Figure C.3: Profiles of the radial fluctuating velocity u_r^{+0} against y^{+0} in case A to F.

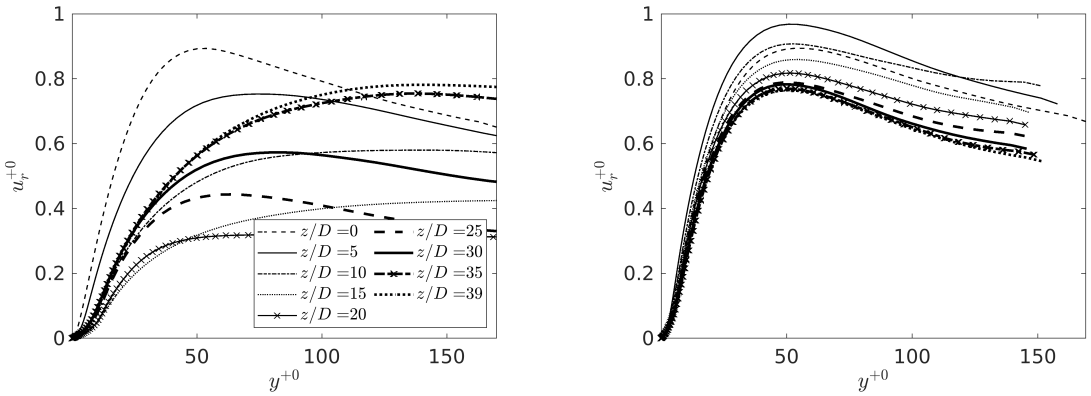

(a) Case A

(b) Case B

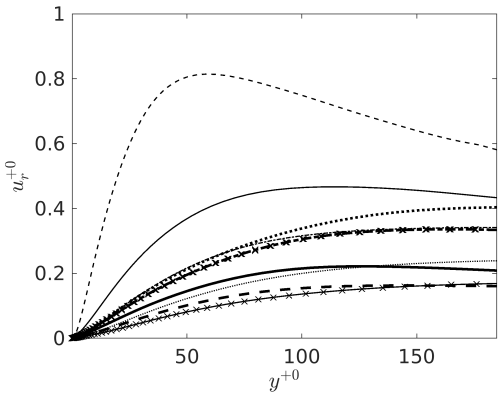

(c) Case C

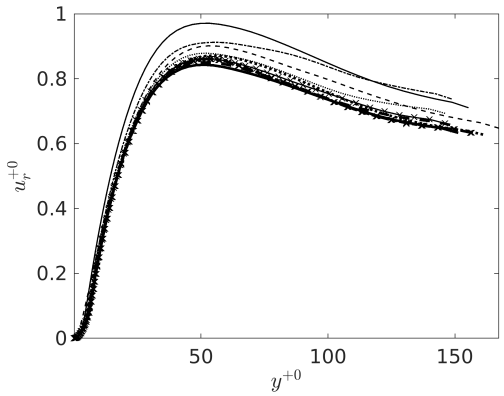

(d) Case D

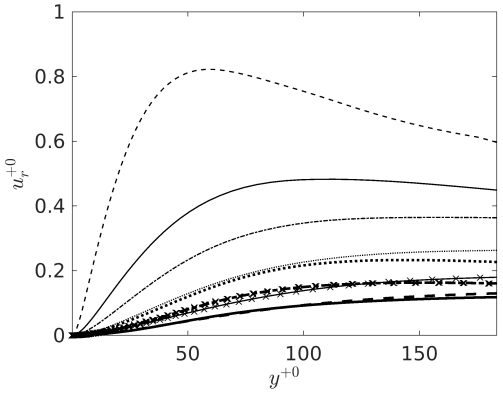

(e) Case E

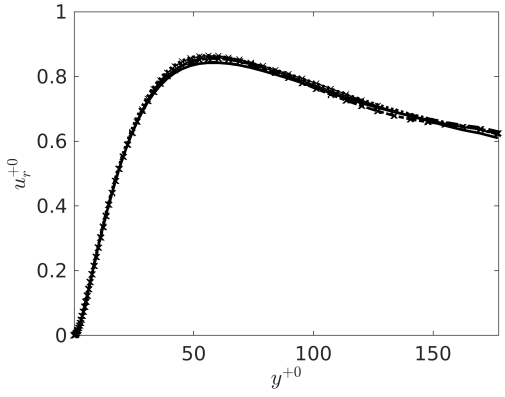

(f) Case F

Figure C.4: Profiles of the radial fluctuating velocity u_r^+ against y^+ in case A to F.

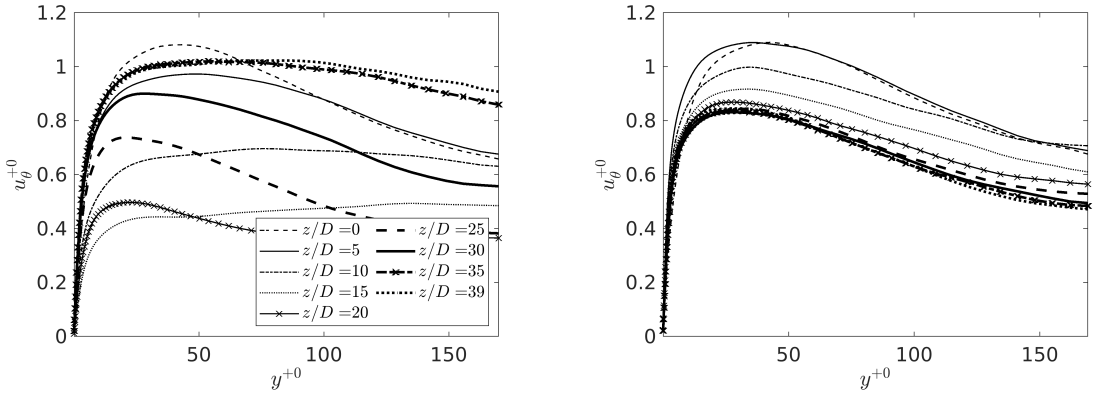

(a) Case A (b) Case B

(c) Case C (d) Case D

(e) Case E (f) Case F

Figure C.5: Profiles of the spanwise fluctuating velocity u_θ^{+0} against y^{+0} in case A to F.

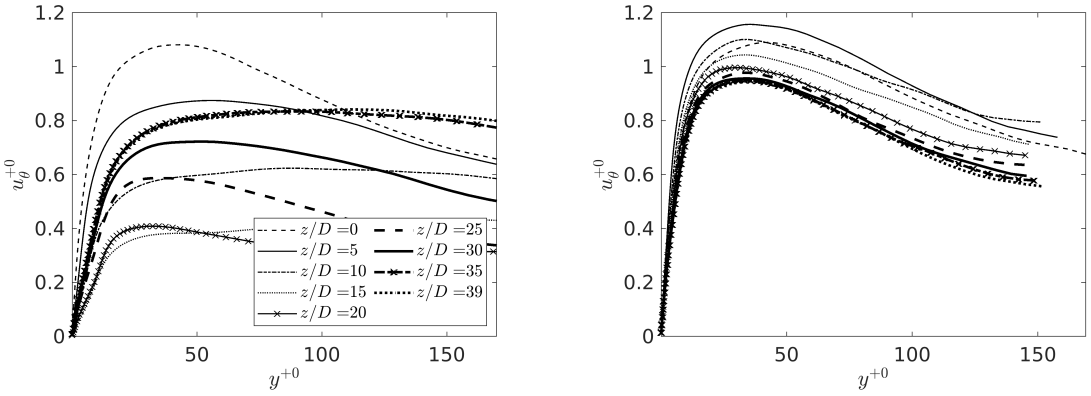

(a) Case A

(b) Case B

(c) Case C

(d) Case D

(e) Case E

(f) Case F

Figure C.6: Profiles of the spanwise fluctuating velocity u_θ^+ against y^+ in case A to F.

Appendix D

Momentum balances in Cases A to E

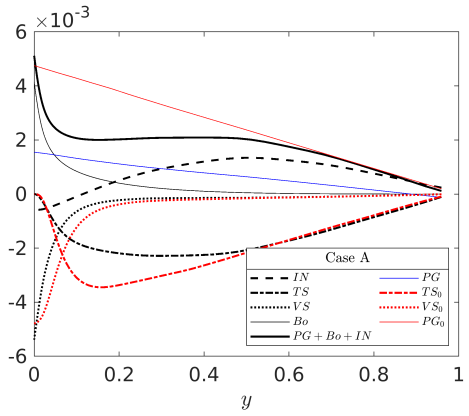

(a) $z/D = 5$

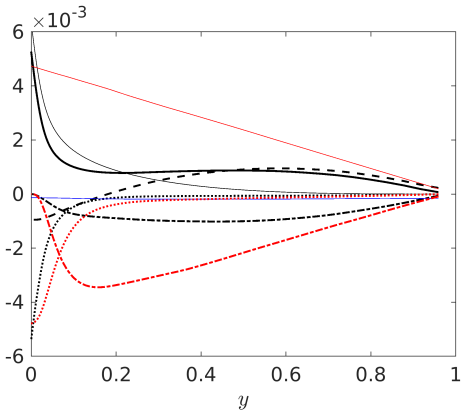

(b) $z/D = 10$

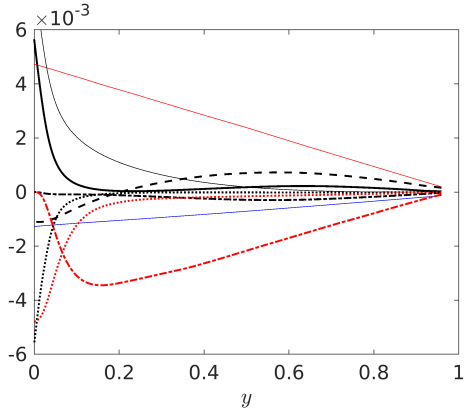

(c) $z/D = 15$

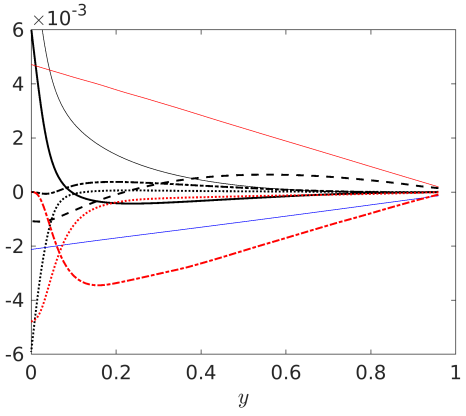

(d) $z/D = 20$

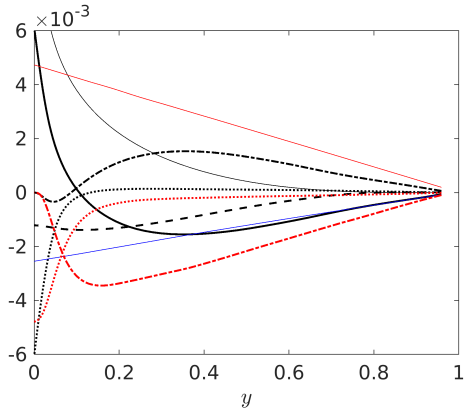

(e) $z/D = 30$

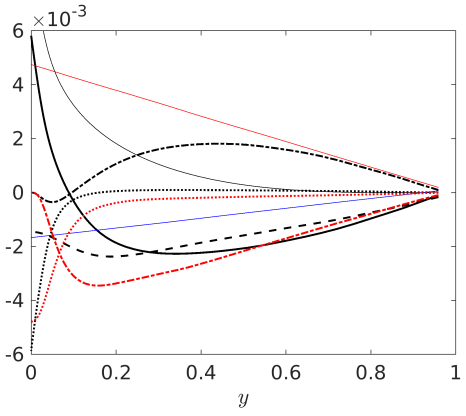

(f) $z/D = 38$

Figure D.1: Momentum balance at chosen locations of case A.

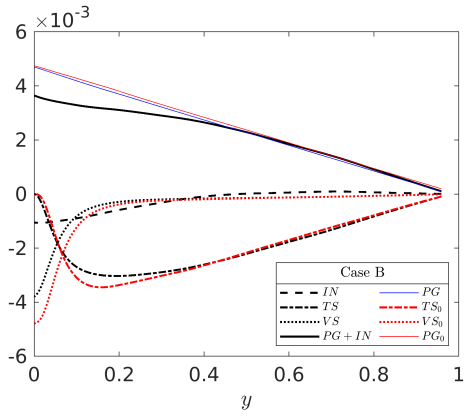

(a) $z/D = 5$

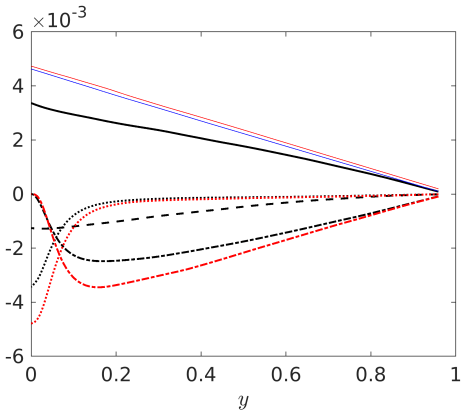

(b) $z/D = 10$

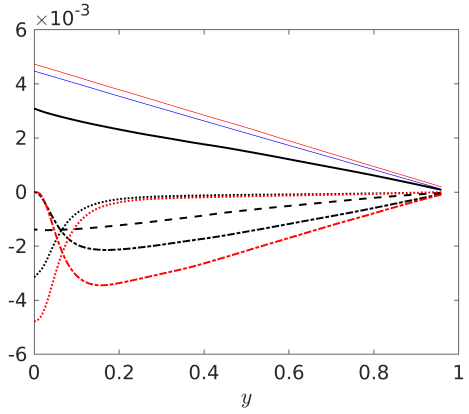

(c) $z/D = 15$

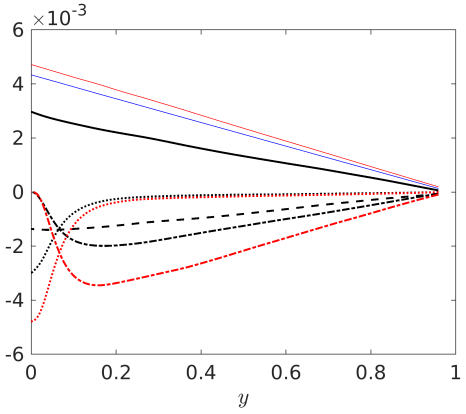

(d) $z/D = 20$

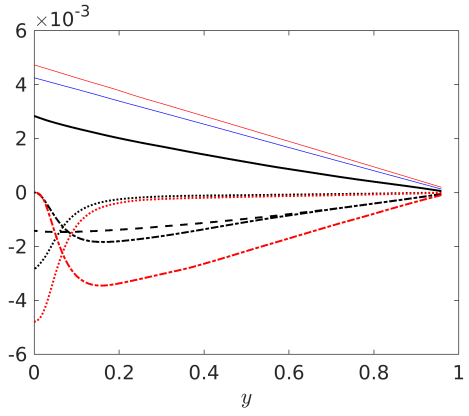

(e) $z/D = 30$

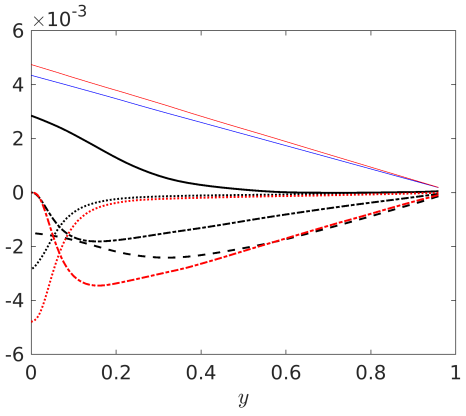

(f) $z/D = 38$

Figure D.2: Momentum balance at chosen locations of case B.

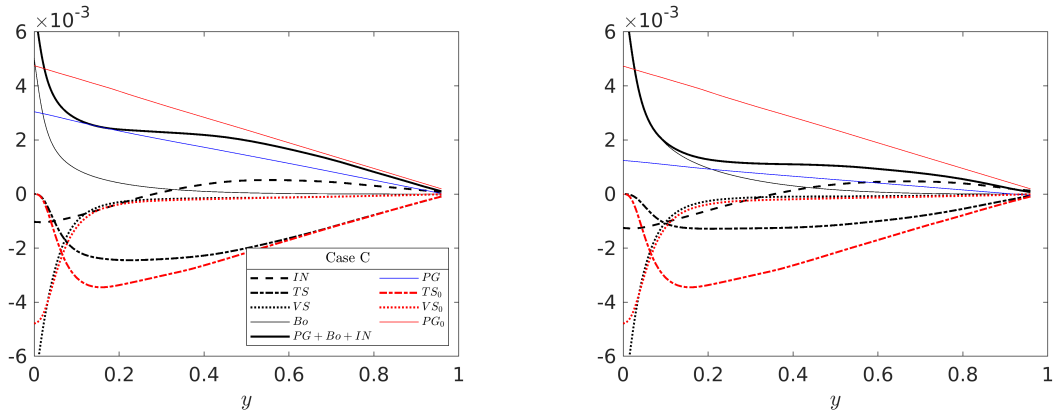

(a) $z/D = 5$ (b) $z/D = 10$

(c) $z/D = 15$ (d) $z/D = 20$

(e) $z/D = 30$ (f) $z/D = 38$

Figure D.3: Momentum balance at chosen locations of case C.

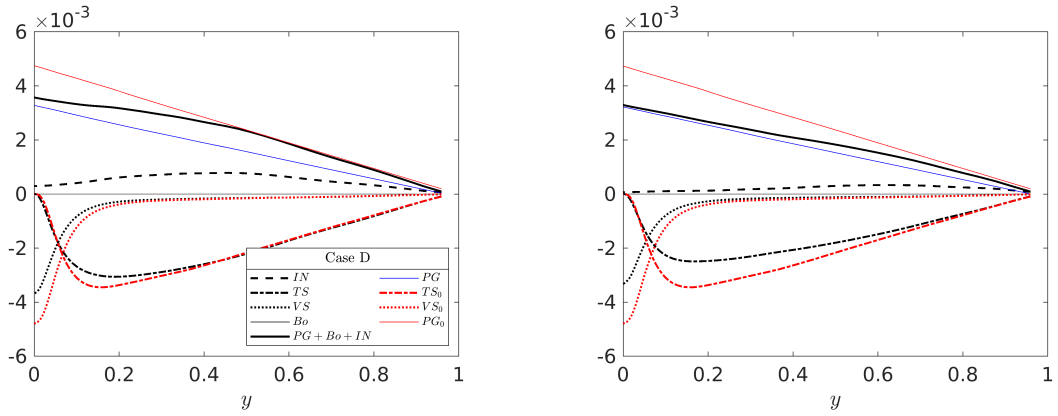

(a) $z/D = 5$ (b) $z/D = 10$

(c) $z/D = 15$ (d) $z/D = 20$

(e) $z/D = 30$ (f) $z/D = 38$

Figure D.4: Momentum balance at chosen locations of case D.

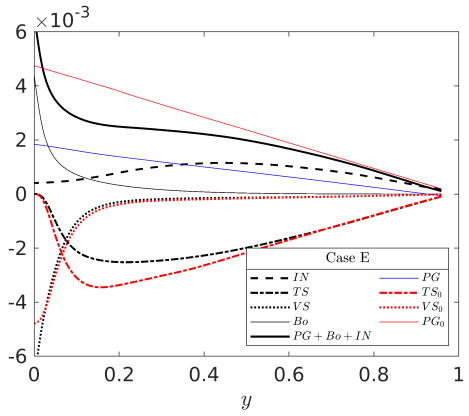

(a) $z/D = 5$

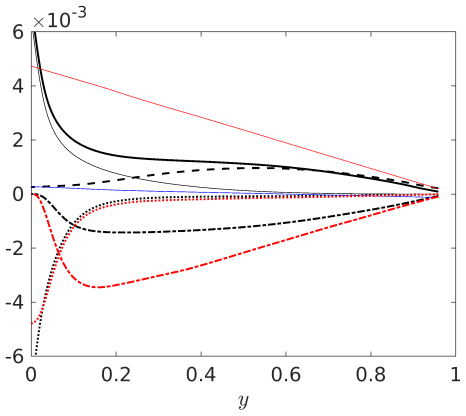

(b) $z/D = 10$

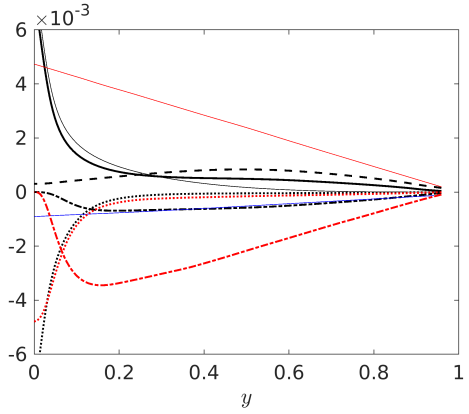

(c) $z/D = 15$

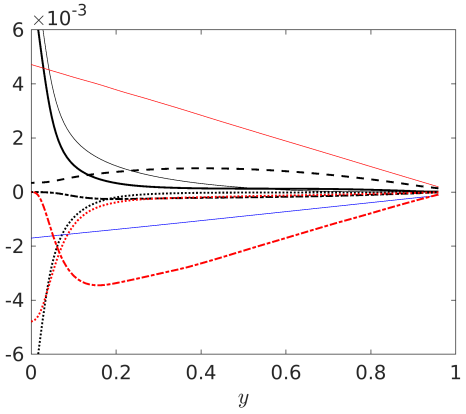

(d) $z/D = 20$

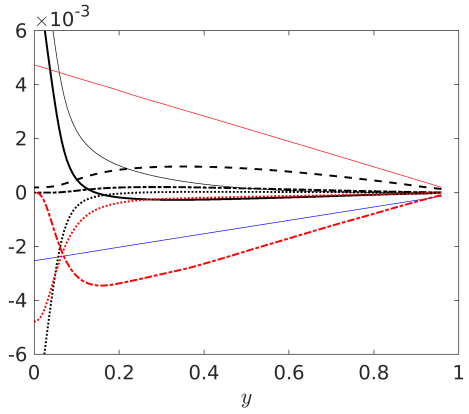

(e) $z/D = 30$

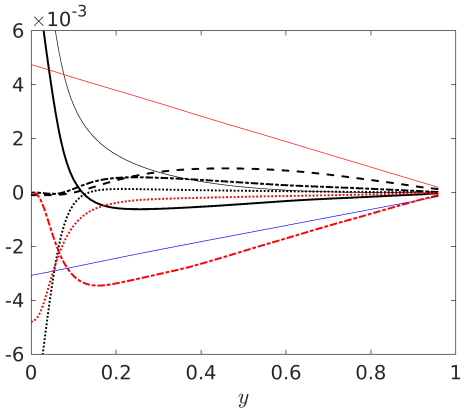

(f) $z/D = 38$

Figure D.5: Momentum balance at chosen locations of case E.

Bibliography

[1] Jundi He, Junjie Yan, Wei Wang, and Shuisheng He. Direct numerical simulation study for fluid-to-fluid scaling for fluids at supercritical pressure. In *International Heat Transfer Conference Digital Library*. Begel House Inc., 2018.

[2] Jundi He, Shuisheng He, and Bing Xu. Effect of channel distortion and different graphite thermal conductivity models on the prediction of graphite temperatrue. In *6th EDF Energy Nuclear Graphite Conference*, 2018.

[3] Shuisheng He, A Lozano-Durán, Jundi He, and Minjeong Cho. Turbulent-turbulent transition of a transient three-dimensional channel flow. In *Center for Turbulence Research–Proceedings of the Summer Program*, pages 257–266, 2018.

[4] Jundi He, Shuisheng He, and Bing Xu. CFD studies of effect of fuel channel/stringer eccentricity in the core of an advanced gas-cooled reactor. In *18th International Topical Meeting on Nuclear Reactor Thermal Hydraulics (NURETH-18)*, 2019.

[5] Jundi He, Junjie Yan, Wei Wang, and Shuisheng He. A DNS study of turbulence structures of flow of fluid at supercritical pressure. In *11th International Symposium on Turbulence and Shear Flow Phenomena*, 2019.

[6] Jundi He, Junjie Yan, Wei Wang, Peixue Jiang, and Shuisheng He. Effects of buoyancy and thermophysical property variations on the flow of supercritical carbon dioxide. *International Journal of Heat and Fluid Flow*, 86:108697, 2020.

[7] Jundi He, Ran Tian, Peixue Jiang, and Shuisheng He. Turbulence in a heated pipe at supercritical pressure. *Journal of Fluid Mechanics*, 2021.

[8] Jundi He, Bing Xu, and Shuisheng He. The effect of conjugate heat transfer on the flow of supercritical carbon dioxide. In *17th UK Heat Transfer Conference*, 2021.

[9] K Yamagata, K Nishikawa, S Hasegawa, T Fujii, and S Yoshida. Forced convective heat transfer to supercritical water flowing in tubes. *International Journal of Heat and Mass Transfer*, 15(12):2575–2593, 1972.

[10] JD Jackson. Fluid flow and convective heat transfer to fluids at supercritical pressure. *Nuclear Engineering and Design*, 264:24–40, 2013.

[11] Joong Hun Bae, Jung Yul Yoo, and Haecheon Choi. Direct numerical simulation of turbulent supercritical flows with heat transfer. *Physics of fluids*, 17(10):105104, 2005.

[12] Hassan Nemati, Ashish Patel, Bendiks Jan Boersma, and Rene Pecnik. Mean statistics of a heated turbulent pipe flow at supercritical pressure. *International Journal of Heat and Mass Transfer*, 83:741–752, 2015.

[13] S He, K He, and M Seddighi. Laminarisation of flow at low Reynolds number due to streamwise body force. *Journal of Fluid Mechanics*, 809:31–71, 2016.

[14] Walter Ambrosini and Mattia De Rosa. Application of similarity principles for heat transfer and fluid-dynamics to different fluids at supercritical pressure. *Proc. of the 5th Int. Sym. SCWR (ISSCWR-5), Vancouver, British Columbia, Canada*, 2011.

[15] Andrea Pucciarelli and Walter Ambrosini. On the effect of conjugate heat transfer on turbulence in supercritical fluids: Results from a LES application. *Annals of Nuclear Energy*, 111:340–346, 2018.

[16] JD Jackson, MA Cotton, and BP Axcell. Studies of mixed convection in vertical tubes. *International journal of heat and fluid flow*, 10(1):2–15, 1989.

[17] FC Lai and FA Kulacki. Experimental study of free and mixed convection in horizontal porous layers locally heated from below. *International journal of heat and mass transfer*, 34(2):525–541, 1991.

[18] JV Vilemas, PS Poškas, and VE Kaupas. Local heat transfer in a vertical gas-cooled tube with turbulent mixed convection and different heat fluxes. *International journal of heat and mass transfer*, 35(10):2421–2428, 1992.

[19] SM Liao and TS Zhao. Measurements of heat transfer coefficients from supercritical carbon dioxide flowing in horizontal mini/micro channels. *J. Heat Transfer*, 124(3):413–420, 2002.

[20] Bong-Jin Ko, Won Jae Lee, and Bum-Jin Chung. Turbulent mixed convection heat transfer experiments in a vertical cylinder using analogy concept. *Nuclear engineering and design*, 240(12):3967–3973, 2010.

[21] T Aicher and H Martin. New correlations for mixed turbulent natural and forced convection heat transfer in vertical tubes. *International journal of heat and mass transfer*, 40(15):3617–3626, 1997.

[22] JeongIk Lee, P Hejzlar, P Saha, MS Kazimi, and DM McEligot. Deteriorated turbulent heat transfer (dtht) of gas up-flow in a circular tube: Heat transfer correlations. *International journal of heat and mass transfer*, 51(21-22):5318–5326, 2008.

[23] Ali Arefmanesh and Mostafa Mahmoodi. Effects of uncertainties of viscosity models for al2o3–water nanofluid on mixed convection numerical simulations. *International journal of Thermal sciences*, 50(9):1706–1719, 2011.

[24] A Akbarinia and A Behzadmehr. Numerical study of laminar mixed convection of a nanofluid in horizontal curved tubes. *Applied Thermal Engineering*, 27(8-9):1327–1337, 2007.

[25] Farhad Talebi, Amir Houshang Mahmoudi, and Mina Shahi. Numerical study of mixed convection flows in a square lid-driven cavity utilizing nanofluid. *International Communications in Heat and Mass Transfer*, 37(1):79–90, 2010.

[26] Khalil M Khanafer, Abdalla M Al-Amiri, and Ioan Pop. Numerical simulation of unsteady mixed convection in a driven cavity using an externally excited sliding lid. *European Journal of Mechanics-B/Fluids*, 26(5):669–687, 2007.

[27] MA Cotton and JD Jackson. Vertical tube air flows in the turbulent mixed convection regime calculated using a low-reynolds-number $k - \epsilon$ model. *International journal of heat and mass transfer*, 33(2):275–286, 1990.

[28] Brian Edward Launder and BI Sharma. Application of the energy-dissipation model of turbulence to the calculation of flow near a spinning disc. *Letters in heat and mass transfer*, 1(2):131–137, 1974.

[29] Joseph Boussinesq. *Théorie de l'écoulement tourbillonnant et tumultueux des liquides dans les lits rectilignes a grande section*, volume 1. Gauthier-Villars, 1897.

[30] AD Carr, MA Connor, and HO Buhr. Velocity, temperature, and turbulence measurements in air for pipe flow with combined free and forced convection. *Journal of heat transfer*, 95(4):445–452, 1973.

[31] Jongwoo You, Jung Y Yoo, and Haecheon Choi. Direct numerical simulation of heated vertical air flows in fully developed turbulent mixed convection. *International Journal of Heat and Mass Transfer*, 46(9):1613–1627, 2003.

[32] Pinghui Zhao, Jiaming Liu, Zhihao Ge, Yuanjie Li, Nian Zhao, and Yuanxi Wan. Direct numerical simulation of strongly heated air flows in a vertical pipe using a thermophysical property table. *International Journal of Heat and Mass Transfer*, 124:1181–1197, 2018.

[33] Koji Fukagata, Kaoru Iwamoto, and Nobuhide Kasagi. Contribution of reynolds stress distribution to the skin friction in wall-bounded flows. *Physics of Fluids*, 14(11):L73–L76, 2002.

[34] Koji Fukagata, Kaoru Iwamoto, and Nobuhide Kasagi. Novel turbulence control strategy for simultaneously achieving friction drag reduction and heat transfer augmentation. In *Fourth International Symposium on Turbulence and Shear Flow Phenomena*. Begel House Inc., 2005.

[35] EW Lemmon, ML Huber, and MO McLinden. Nist standard reference database 23: Reference fluid thermodynamic and transport properties-refprop, version 8.0. national institute of standards and technology, standard reference data program. *Standard Reference Data Program, Gaithersburg*, 2018.

[36] PJ Bourke, DJ Pulling, LE Gill, and WH Denton. Forced convective heat transfer to turbulent CO2 in the supercritical region. *International Journal of Heat and Mass Transfer*, 13(8):1339–1348, 1970.

[37] JW Ackerman. Pseudoboiling heat transfer to supercritical pressure water in smooth and ribbed tubes. *Journal of Heat Transfer*, 92(3):490–497, 1970.

[38] B Shiralkar and P Griffith. The effect if swirl, inlet conditions, flow direction, and tube diameter on the heat transfer to fluids at supercritical pressure. *Journal of Heat Transfer*, 92:490–497, 1970.

[39] CJ Sanders and JP Holman. Franz grashof and the grashof number. *International Journal of Heat and Mass Transfer*, 15(3):562–563, 1972.

[40] VA Kurganov and AG Kaptil'Ny. Velocity and enthalpy fields and eddy diffusivities in a heated supercritical fluid flow. *Experimental thermal and fluid science*, 5(4):465–478, 1992.

[41] VN Popov, VM Belyaev, and Valueva EP. Calculation of heat transfer and resistance by turbulent flow in a circular pipe of fluids with various types of temperature dependence of physical properties. *Teplofiz. Vys. Temp*, 15(6):1220–1229, 1977.

[42] JD Jackson, KE Lutterodt, and R Weinberg. Experimental studies of buoyancy-influenced convective heat transfer in heated vertical tubes at pressures just above and just below the thermodynamic critical value. In *Proceedings of the Joint International Conference on Global Environment and Nuclear Energy System/Advanced Power Plants*, pages 15–19, 2003.

[43] Igor L Pioro, Hussam F Khartabil, and Romney B Duffey. Heat transfer to supercritical fluids flowing in channels—empirical correlations (survey). *Nuclear engineering and design*, 230(1-3):69–91, 2004.

[44] Romney B Duffey and Igor L Pioro. Experimental heat transfer of supercritical carbon dioxide flowing inside channels (survey). *Nuclear Engineering and Design*, 235(8):913–924, 2005.

[45] Pei-Xue Jiang, Yi-Jun Xu, Jing Lv, Run-Fu Shi, Shuisheng He, and JD Jackson. Experimental investigation of convection heat transfer of CO2 at super-critical pressures in vertical mini-tubes and in porous media. *Applied Thermal Engineering*, 24(8-9):1255–1270, 2004.

[46] EA Krasnoshchekov. Experimental study of heat exchagne in carbon dioxide in the supercritical range at high temperature drops. *High Temperature*, 4:375–382, 1966.

[47] Pei-Xue Jiang, Yu Zhang, Chen-Ru Zhao, and Run-Fu Shi. Convection heat transfer of CO2 at supercritical pressures in a vertical mini tube at relatively low reynolds numbers. *Experimental Thermal and Fluid Science*, 32(8):1628–1637, 2008.

[48] Pei-Xue Jiang, Bo Liu, Chen-Ru Zhao, and Feng Luo. Convection heat transfer of supercritical pressure carbon dioxide in a vertical micro tube from transition

to turbulent flow regime. *International journal of heat and mass transfer*, 56(1-2):741–749, 2013.

[49] Zhi-Hui Li, Pei-Xue Jiang, Chen-Ru Zhao, and Yu Zhang. Experimental investigation of convection heat transfer of CO2 at supercritical pressures in a vertical circular tube. *Experimental thermal and fluid science*, 34(8):1162–1171, 2010.

[50] J D_ Jackson. Consideration of the heat transfer properties of supercritical pressure water in connection with the cooling of advanced nuclear reactors. In *The 13th pacific basin nuclear conference. Abstracts*, 2002.

[51] Pei-Xue Jiang, Chen-Ru Zhao, Run-Fu Shi, Yang Chen, and Walter Ambrosini. Experimental and numerical study of convection heat transfer of CO2 at supercritical pressures during cooling in small vertical tube. *International journal of heat and mass transfer*, 52(21-22):4748–4756, 2009.

[52] Junjie Yan, Yinhai Zhu, Ran Zhao, Shuai Yan, and Peixue Jiang. Experimental investigation of the flow and heat transfer instabilities in n-decane at supercritical pressures in a vertical tube. *International Journal of Heat and Mass Transfer*, 120:987–996, 2018.

[53] Peixue Jiang, Zelong Lu, Yuxuan Guo, and Yinhai Zhu. Experimental investigation of convective heat transfer of hydrocarbon fuels at supercritical pressures within rotating centrifugal channel. *Applied Thermal Engineering*, 147:101–112, 2019.

[54] Ran Tian, Yue Zhang, Yuezheng Ma, Hui Li, and Lin Shi. Experimental study of buoyancy effect and its criteria for heat transfer of supercritical R134a in horizontal tubes. *International Journal of Heat and Mass Transfer*, 127:555–567, 2018.

[55] Ran Tian, Dabiao Wang, Yue Zhang, Yuezheng Ma, Hui Li, and Lin Shi. Experimental study of the heat transfer characteristics of supercritical pressure R134a in a horizontal tube. *Experimental Thermal and Fluid Science*, 100:49–61, 2019.

[56] F. W. Dittus and L. M. K. Boelter. Heat transfer in automobile radiators of the tubular type. *International Communications in Heat and Mass Transfer*, 12:3–22, 1985.

[57] CP Bellmore and RL Reid. Numerical prediction of wall temperatures for near-critical para-hydrogen in turbulent upflow inside vertical tubes. *Journal of Hear Transfer*, 105(3):536–541, 1983.

[58] S Koshizuka, Naoki Takano, and Y Oka. Numerical analysis of deterioration phenomena in heat transfer to supercritical water. *International Journal of Heat and Mass Transfer*, 38(16):3077–3084, 1995.

[59] Sang Ho Lee and John R Howell. Turbulent developing convective heat transfer in a tube for fluids near the critical point. *International Journal of Heat and Mass Transfer*, 41(10):1205–1218, 1998.

[60] Shuisheng He, Pei-Xue Jiang, Yi-Jun Xu, Run-Fu Shi, WS Kim, and JD Jackson. A computational study of convection heat transfer to CO2 at supercritical pressures in a vertical mini tube. *International journal of thermal sciences*, 44(6):521–530, 2005.

[61] S He, WS Kim, and JH Bae. Assessment of performance of turbulence models in predicting supercritical pressure heat transfer in a vertical tube. *International Journal of Heat and Mass Transfer*, 51(19-20):4659–4675, 2008.

[62] M Behnia, S Parneix, and Paul A Durbin. Prediction of heat transfer in an axisymmetric turbulent jet impinging on a flat plate. *International journal of heat and mass transfer*, 41(12):1845–1855, 1998.

[63] WS Kim, S He, and JD Jackson. Assessment by comparison with DNS data of turbulence models used in simulations of mixed convection. *International journal of heat and mass transfer*, 51(5-6):1293–1312, 2008.

[64] Z Yang and Tsan-Hsing Shih. New time scale based $k - \epsilon$ model for near-wall turbulence. *AIAA journal*, 31(7):1191–1198, 1993.

[65] Andrea Pucciarelli, Irene Borroni, Medhat Sharabi, and Walter Ambrosini. Results of 4-equation turbulence models in the prediction of heat transfer to supercritical pressure fluids. *Nuclear Engineering and Design*, 281:5–14, 2015.

[66] K Abe, T Kondoh, and Y Nagano. A new turbulence model for predicting fluid flow and heat transfer in separating and reattaching flows—ii. thermal field calculations. *International Journal of Heat and Mass Transfer*, 38(8):1467–1481, 1995.

[67] Baoqing Deng, Wenquan Wu, and Shitong Xi. A near-wall two-equation heat transfer model for wall turbulent flows. *International journal of heat and mass transfer*, 44(4):691–698, 2001.

[68] Andrea Pucciarelli, Medhat Sharabi, and Walter Ambrosini. Prediction of heat transfer to supercritical fluids by the use of algebraic heat flux models. *Nuclear Engineering and Design*, 297:257–266, 2016.

[69] Keke Xu, Bo Ruan, and Hua Meng. Validation and analyses of RANS CFD models for turbulent heat transfer of hydrocarbon fuels at supercritical pressures. *International Journal of Thermal Sciences*, 124:212–226, 2018.

[70] Pei-Xue Jiang, Zhen-Chuan Wang, and Rui-Na Xu. A modified buoyancy effect correction method on turbulent convection heat transfer of supercritical pressure fluid based on RANS model. *International Journal of Heat and Mass Transfer*, 127:257–267, 2018.

[71] Joong Hun Bae, Jung Yul Yoo, and Donald M McEligot. Direct numerical simulation of heated co 2 flows at supercritical pressure in a vertical annulus at re= 8900. *Physics of Fluids*, 20(5):055108, 2008.

[72] Joong Hun Bae, Jung Yul Yoo, Haecheon Choi, and Donald M McEligot. Effects of large density variation on strongly heated internal air flows. *Physics of Fluids*, 18(7):075102, 2006.

[73] Gilbert Accary, Isabelle Raspo, Patrick Bontoux, and Bernard Zappoli. An adaptation of the low Mach number approximation for supercritical fluid buoyant flows. *Comptes Rendus Mécanique*, 333(5):397–404, 2005.

[74] Xinliang Li, Katsumi Hashimoto, Mamoru Tanahashi, and Toshio Miyauchi. Numerical study of heat transfer mechanism in turbulent supercritical CO2 channel flow. In *ASME/JSME 2007 Thermal Engineering Heat Transfer Summer Conference collocated with the ASME 2007 InterPACK Conference*, pages 247–256. American Society of Mechanical Engineers Digital Collection, 2007.

[75] Xu Chu and Eckart Laurien. Flow stratification of supercritical CO2 in a heated horizontal pipe. *The Journal of Supercritical Fluids*, 116:172–189, 2016.

[76] Hassan Nemati, Ashish Patel, Bendiks J Boersma, and Rene Pecnik. The effect of thermal boundary conditions on forced convection heat transfer to fluids at supercritical pressure. *Journal of Fluid Mechanics*, 800:531–556, 2016.

[77] Jung Yul Yoo. The turbulent flows of supercritical fluids with heat transfer. *Annual review of fluid mechanics*, 45:495–525, 2013.

[78] Jurriaan WR Peeters, Rene Pecnik, Martin Rohde, THJJ Van Der Hagen, and Bendiks Jan Boersma. Turbulence attenuation in simultaneously heated and cooled annular flows at supercritical pressure. *Journal of Fluid Mechanics*, 799:505–540, 2016.

[79] JD Jackson. Fluid flow and convective heat transfer to fluids at supercritical pressure. *Nuclear Engineering and Design*, 264:24–40, 2013.

[80] Donald M McEligot, Xu Chu, Joong Hun Bae, Eckart Laurien, and Jung Yul Yoo. Some observations concerning" laminarization" in heated vertical tubes. *International Journal of Heat and Mass Transfer*, 163:120101, 2020.

[81] Boris S Petukhov and AF Polyakov. *Heat transfer in turbulent mixed convection*. Hemisphere Publishing Corporation, New York, 1988.

[82] JWR Peeters, Rene Pecnik, Martin Rohde, THJJ van der Hagen, and Bendiks Jan Boersma. Characteristics of turbulent heat transfer in an annulus at supercritical pressure. *Physical Review Fluids*, 2(2):024602, 2017.

[83] Chukwudi Azih and Metin I Yaras. Effects of spatial gradients in thermophysical properties on the topology of turbulence in heated channel flow of supercritical fluids. *Physics of Fluids*, 30(1):015108, 2018.

[84] Shawn K Reinink and Metin I Yaras. Study of coherent structures of turbulence with large wall-normal gradients in thermophysical properties using direct numerical simulation. *Physics of Fluids*, 27(6):065113, 2015.

[85] Edward R Van Driest. Turbulent boundary layer in compressible fluids. *Journal of the Aeronautical Sciences*, 18(3):145–160, 1951.

[86] Gary N Coleman, John Kim, and RD Moser. A numerical study of turbulent supersonic isothermal-wall channel flow. *Journal of Fluid Mechanics*, 305:159–184, 1995.

[87] PC Huang, GN Coleman, and P Bradshaw. Compressible turbulent channel flows: DNS results and modelling. *Journal of Fluid Mechanics*, 305:185–218, 1995.

[88] Alexander J Smits and Jean-Paul Dussauge. *Turbulent shear layers in supersonic flow*. Springer Science & Business Media, 2006.

[89] L Duan, I Beekman, and MP Martin. Direct numerical simulation of hypersonic turbulent boundary layers. part 2. effect of wall temperature. *Journal of Fluid Mechanics*, 655:419, 2010.

[90] Maher Lagha, John Kim, JD Eldredge, and Xiaolin Zhong. A numerical study of compressible turbulent boundary layers. *Physics of Fluids*, 23(1):015106, 2011.

[91] Youhei Morinishi, Shinji Tamano, and Koichi Nakabayashi. Direct numerical simulation of compressible turbulent channel flow between adiabatic and isothermal walls. *Journal of Fluid Mechanics*, 502:273, 2004.

[92] Ashish Patel, Jurriaan WR Peeters, Bendiks J Boersma, and Rene Pecnik. Semi-local scaling and turbulence modulation in variable property turbulent channel flows. *Physics of Fluids*, 27(9):095101, 2015.

[93] Andrew Trettel and Johan Larsson. Mean velocity scaling for compressible wall turbulence with heat transfer. *Physics of Fluids*, 28(2):026102, 2016.

[94] Ashish Patel, Bendiks J Boersma, and Rene Pecnik. The influence of near-wall density and viscosity gradients on turbulence in channel flows. *Journal of Fluid Mechanics*, 809:793–820, 2016.

[95] Ashish Patel, Bendiks J Boersma, and Rene Pecnik. Scalar statistics in variable property turbulent channel flows. *Physical Review Fluids*, 2(8):084604, 2017.

[96] Rene Pecnik and Ashish Patel. Scaling and modelling of turbulence in variable property channel flows. *Journal of Fluid Mechanics*, 823, 2017.

[97] Peter C Ma, Xiang IA Yang, and Matthias Ihme. Structure of wall-bounded flows at transcritical conditions. *Physical Review Fluids*, 3(3):034609, 2018.

[98] Teng Wan, Pinghui Zhao, Jiaming Liu, Chaozheng Wang, and Mingzhun Lei. Mean velocity and temperature scaling for near-wall turbulence with heat transfer at supercritical pressure. *Physics of Fluids*, 32(5):055103, 2020.

[99] Jiaming Liu, Pinghui Zhao, Mingzhun Lei, Suo Yang, and Hassan Nemati. Numerical investigation of spatial-developing turbulent heat transfer in forced convections at different supercritical pressures. *International Journal of Heat and Mass Transfer*, 159:120128, 2020.

[100] Elena Marensi, Shuisheng He, and Ashley P Willis. Suppression of turbulence and travelling waves in a vertical heated pipe. *arXiv preprint arXiv:2008.13486*, 2020.

[101] SY Ahmad. Fluid to fluid modeling of critical heat flux: a compensated distortion model. *International Journal of Heat and Mass Transfer*, 16(3):641–662, 1973.

[102] R Van de Graaf, THJJ Van der Hagen, and RF Mudde. Two-phase flow scaling laws for a simulated bwr assembly. *Nuclear engineering and design*, 148(2-3):455–462, 1994.

[103] T Ortega Gómez, A Class, RT Lahey Jr, and T Schulenberg. Stability analysis of a uniformly heated channel with supercritical water. *Nuclear Engineering and Design*, 238(8):1930–1939, 2008.

[104] Walter Ambrosini and Medhat Sharabi. Dimensionless parameters in stability analysis of heated channels with fluids at supercritical pressures. In *14th International Conference on Nuclear Engineering*, pages 881–888. American Society of Mechanical Engineers, 2006.

[105] Walter Ambrosini. Dimensionless parameters in stability analysis of heated channels with supercritical fluids at imposed heating flux and wall temperature conditions. In *IAEA Technical Meeting on Heat Transfer, Thermal-Hydraulics and System Design for Supercritical Water Reactors*, 2010.

[106] Igor´ Leonardovich Pioro and Romney B Duffey. *Heat-Transfer Enhancement at Supercritical Pressures*. ASME Press, 2007.

[107] J. D. Jackson and W. B. Hall. Forced convection heat transfer to fluids at supercritical pressure. *Turbulent forced convection in channels and bundles*, 2:563, 1979.

[108] S Zwolinski, M Anderson, M Corradini, and J Licht. Evaluation of fluid-to-fluid scaling method for water and carbon dioxide at supercritical pressure. In *5th*

International Symposium on Supercritical Water-Cooled Reactors (SCWR5), Vancouver, Canada, 2011.

[109] X Cheng, XJ Liu, and HY Gu. Fluid-to-fluid scaling of heat transfer in circular tubes cooled with supercritical fluids. *Nuclear Engineering and Design*, 241(2):498–508, 2011.

[110] Urmi S Tejaswini, Dipankar N Basu, and Manmohan Pandey. Improved scaling analysis for heat transfer in a circular tube with various supercritical fluids using computational fluid dynamics simulations. *Heat Transfer Engineering*, 38(2):149–161, 2017.

[111] H Zahlan, DC Groeneveld, and S Tavoularis. Fluid-to-fluid scaling for convective heat transfer in tubes at supercritical and high subcritical pressures. *International Journal of Heat and Mass Transfer*, 73:274–283, 2014.

[112] Guojun Yu, Chaofei Jiang, Liu Wang, GH Su, and SZ Qiu. A new method on fluid-to-fluid scaling for heat transfer in tubes at supercritical pressures. *International Journal of Heat and Mass Transfer*, 126:809–822, 2018.

[113] Ran Tian, Florian Feuerstein, Xiaoye Dai, and Lin Shi. Fluid-to-fluid scaling of heat transfer to mixed convection flow of supercritical pressure fluids. *International Journal of Energy Research*, 42(10):3361–3377, 2018.

[114] Walter Ambrosini. Discussion of similarity principles for fluid-to-fluid scaling of heat transfer behaviour at supercritical pressures. *Nuclear Engineering and Design*, 241(12):5149–5173, 2011.

[115] M Rohde and THJJ van der Hagen. Downscaling the hplwr to an experimental facility by using a scaling fluid. In *Proceedings of the 4th international symposium on supercritical water-cooled reactors, Heidelberg, Germany*, 2009.

[116] Ning Zhou and Anantha Krishnan. Numerical simulation of coupled heat transfer characteristics for flows at supercritical pressure [aircraft fuel flow]. In *IECEC 96. Proceedings of the 31st Intersociety Energy Conversion Engineering Conference*, volume 2, pages 1471–1476. IEEE, 1996.

[117] Kuei-Yuan Chien. Predictions of channel and boundary-layer flows with a low-reynolds-number turbulence model. *AIAA journal*, 20(1):33–38, 1982.

[118] Leilei Wang, Zunjing Chen, and Hua Meng. Numerical study of conjugate heat transfer of cryogenic methane in rectangular engine cooling channels at supercritical pressures. *Applied Thermal Engineering*, 54(1):237–246, 2013.

[119] J. D. Jackson and W. B. HALL. Influences of buoyancy on heat transfer to fluids flowing in vertical tubes under turbulent conditions. *Turbulent forced convection in channels and bundles*, 2:613–640, 1979.

[120] Zhenxing Zhao and Defu Che. Numerical investigation of conjugate heat transfer to supercritical CO2 in a vertical tube-in-tube heat exchanger. *Numerical Heat Transfer, Part A: Applications*, 67(8):857–882, 2015.

[121] Zhenxing Zhao, Defu Che, Jun Wu, Shiwei Yao, Kelong Zhang, Yuansheng Lin, and Hanbing Ke. Numerical investigation on conjugate cooling heat transfer to supercritical CO2 in vertical double-pipe heat exchangers. *Numerical Heat Transfer, Part A: Applications*, 69(5):512–528, 2016.

[122] K Abe, T Kondoh, and Y Nagano. A new turbulence model for predicting fluid flow and heat transfer in separating and reattaching flows—i. flow field calculations. *International journal of heat and mass transfer*, 37(1):139–151, 1994.

[123] Z Yang and TH Shih. A $k - \epsilon$ calculation of transitional boundary layers. In *Instability, Transition, and Turbulence*, pages 611–620. Springer, 1992.

[124] Zhenxing Zhao, Defu Che, Yun Zhang, Shiwei Yao, Kelong Zhang, and Yuansheng Lin. Numerical investigation on conjugate heat transfer to supercritical CO2 in membrane helical coiled tube heat exchangers. *Numerical Heat Transfer, Part A: Applications*, 69(9):977–995, 2016.

[125] Xing Sun, Keke Xu, Hua Meng, and Yao Zheng. Buoyancy effects on supercritical-pressure conjugate heat transfer of aviation kerosene in horizontal tubes. *The Journal of Supercritical Fluids*, 139:105–113, 2018.

[126] Keke Xu, Xing Sun, and Hua Meng. Conjugate heat transfer, endothermic fuel pyrolysis and surface coking of aviation kerosene in ribbed tube at supercritical pressure. *International Journal of Thermal Sciences*, 132:209–218, 2018.

[127] Javad Khalesi and Nenad Sarunac. Numerical analysis of flow and conjugate heat transfer for supercritical CO2 and liquid sodium in square microchannels. *International Journal of Heat and Mass Transfer*, 132:1187–1199, 2019.

[128] Javad Khalesi, Nenad Sarunac, and Zahra Razzaghpanah. Supercritical CO2 conjugate heat transfer and flow analysis in a rectangular microchannel subject to uniformly heated substrate wall. *Thermal Science and Engineering Progress*, page 100596, 2020.

[129] M Pizzarelli, S Carapellese, and Francesco Nasuti. A quasi-2-d model for the prediction of the wall temperature of rocket engine cooling channels. *Numerical Heat Transfer, Part A: Applications*, 60(1):1–24, 2011.

[130] Wiesław Zima and Marzena Nowak-Ocłoń. A new one/two-dimensional model of the conjugate heat transfer in waterwall tubes of the supercritical steam boiler combustion chamber. *Heat Transfer Engineering*, 39(13-14):1272–1282, 2018.

[131] Mehdi Seddighi. *Study of turbulence and wall shear stress in unsteady flow over smooth and rough wall surfaces*. PhD thesis, University of Aberdeen, 2011.

[132] S He and M Seddighi. Turbulence in transient channel flow. *Journal of Fluid Mechanics*, 715:60–102, 2013.

[133] Wei Wang and Shuisheng He. Mechanisms of buoyancy effect on heat transfer in a horizontal flow. In *Proceedings of the 7th International Symposium on Supercritical Water-Cooled Reactors (ISSCWR-7)*, pages 15–18, 2015.

[134] Anders Lundbladh, Dan S Henningson, and Arne V Johansson. An efficient spectral integration method for the solution of the navier-stokes equations. *STIN*, 93:29009, 1992.

[135] Paolo Orlandi. *Fluid flow phenomena: a numerical toolkit*, volume 55. Springer Science & Business Media, 2012.

[136] Richard Courant, Kurt Friedrichs, and Hans Lewy. Über die partiellen differenzengleichungen der mathematischen physik. *Mathematische annalen*, 100(1):32–74, 1928.

[137] Vaidehi Ambatipudi. Simple solver for driven cavity flow problem. Citeseer, 2006.

[138] CHARLES D PIERCE and Parviz Moin. Progress-variable approach for large-eddy simulation of non-premixed turbulent combustion. *Journal of fluid Mechanics*, 504:73, 2004.

[139] George K El Khoury, Philipp Schlatter, Azad Noorani, Paul F Fischer, Geert Brethouwer, and Arne V Johansson. Direct numerical simulation of turbulent pipe flow at moderately high Reynolds numbers. *Flow, turbulence and combustion*, 91(3):475–495, 2013.

[140] Christie J Geankoplis. *Transport processes and separation process principles:(includes unit operations)*. Prentice Hall Professional Technical Reference, 2003.

[141] A Malhotra and SS Kang. Turbulent prandtl number in circular pipes. *International journal of heat and mass transfer*, 27(11):2158–2161, 1984.

[142] Wiliam M Kays. Turbulent prandtl number. where are we? *ATJHT*, 116(2):284–295, 1994.

[143] Stuart W Churchill. A reinterpretation of the turbulent prandtl number. *Industrial & engineering chemistry research*, 41(25):6393–6401, 2002.

[144] NC Markatos, MR Malin, and G Cox. Mathematical modelling of buoyancy-induced smoke flow in enclosures. *International Journal of Heat and Mass Transfer*, 25(1):63–75, 1982.

[145] Soonil Nam and Robert G Bill Jr. Numerical simulation of thermal plumes. *Fire Safety Journal*, 21(3):231–256, 1993.

[146] S He and M Seddighi. Transition of transient channel flow after a change in reynolds number. *Journal of Fluid Mechanics*, 764:395–427, 2015.

[147] Stephen B Pope. *Turbulent flows*. IOP Publishing, 2001.

[148] Paul Andersson, Luca Brandt, Alessandro Bottaro, and Dan S Henningson. On the breakdown of boundary layer streaks. *Journal of Fluid Mechanics*, 428:29, 2001.

[149] RG Jacobs and PA Durbin. Simulations of bypass transition. *Journal of Fluid Mechanics*, 428:185, 2001.

[150] Jens HM Fransson, Masaharu Matsubara, and P Henrik Alfredsson. Transition induced by free-stream turbulence. *Journal of Fluid Mechanics*, 527:1–25, 2005.

[151] Andrea Pucciarelli and Walter Ambrosini. A successful general fluid-to-fluid similarity theory for heat transfer at supercritical pressure. *International Journal of Heat and Mass Transfer*, 159:120152, 2020.

[152] Andrea Pucciarelli, Shuisheng He, and Walter Ambrosini. A successful local fluid-to-fluid similarity theory for heat transfer to supercritical pressure fluids: merits and limitations. *International Journal of Heat and Mass Transfer*, 157:119754, 2020.

[153] T Gomez, V Flutet, and P Sagaut. Contribution of reynolds stress distribution to the skin friction in compressible turbulent channel flows. *Physical Review E*, 79(3):035301, 2009.

[154] Junjie Yan, Wei Wang, Pei-Xue Jiang, and Shuisheng He. Direct numerical simulation of convective heat trasfner in a vertical pipe for supercritical pressure CO2. In *International Heat Transfer Conference Digital Library*. Begel House Inc., 2018.

[155] Osborne Reynolds. Iv. on the dynamical theory of incompressible viscous fluids and the determination of the criterion. *Philosophical transactions of the royal society of london.(a.)*, 186:123–164, 1895.

[156] Joseph Boussinesq. *Thōrie analytique de la chaleur mise en harmonie avec la thermodynamique et avec la thōrie mcanique de la lumi_re: Refroidissement et chauffement par rayonnement, conductibilit des tiges, lames et masses cristallines, courants de convection, thōrie mcanique de la lumi_re*, volume 2. Gauthier-Villars, 1903.

[157] Philippe Spalart and Steven Allmaras. A one-equation turbulence model for aerodynamic flows. In *30th aerospace sciences meeting and exhibit*, page 439, 1992.

[158] Brian Edward Launder and Dudley Brian Spalding. The numerical computation of turbulent flows. In *Numerical prediction of flow, heat transfer, turbulence and combustion*, pages 96–116. Elsevier, 1983.

[159] David C Wilcox. Formulation of the kw turbulence model revisited. *AIAA journal*, 46(11):2823–2838, 2008.